

Cranfield University

Cheung Chi Shing

**An investigation of chirped fibre Bragg gratings Fabry-Perot
interferometer for sensing applications**

Optical Sensors Group
Centre for Photonics and Optical Engineering
School of Engineering



PhD Thesis

Cranfield University

Optical Sensors Group

Centre for Photonics and Optical Engineering

School of Engineering

PhD Thesis

Academic year 2004

Cheung Chi Shing

An investigation of chirped fibre Bragg gratings Fabry-Perot for sensing applications

Supervisors: Dr. S. W. James
Prof. R. P. Tatam

March 2005

This thesis is submitted in partial fulfilment of the requirement for the degree of Doctor of Philosophy of Cranfield University, on March 2005.

©Cranfield University, 2005. All rights reserved. No part of this publication may be reproduced without the written permission of the copyright holder.

Abstract

Fibre interferometer configurations such as the Michelson and Fabry-Perot (FP) have been formed using uniformed and chirped Fibre Bragg Gratings (FBG) acting as partial reflectors. As well as increasing the dynamic range of the interferometer, chirped FBGs are dispersive elements which can allow tuning of the response of the interferometers to measurements such as strain and temperature. In a chirped FBG, the resonance condition of the FBG varies along the FBG's length. Each wavelength is reflected from different portion of the FBG, which imparts a different group delay to the different components of the incident light. The implication of the wavelength dependence resonance position is that there is a large movement of the resonance position when the incident wavelength is changed. A chirped FBG FP can be configured in which the large movement of the reflection positions in the respective FBGs forming the cavity changes in such a way that the sensitivity of the cavity can be enhanced or reduced. The FP filter response can be tailored through the extent of chirp.

In this project a theoretical model of the in fibre interferometers formed using chirped FBGs is presented. The model indicates that it is possible to form FP cavities with varying sensitivity to strain and temperature by appropriate choice of chirp parameters and cavity length. An experimental demonstration of a chirped FBG FP cavity with reduced sensitivity to strain. This scheme offers flexibility in determining the sensitivity of the FP sensor to strain, not only through the gauge length but also via the parameters of the chirped FBG pairs, allowing the use of long or short gauge length sensors. It is possible to configure the system to exhibit enhanced sensitivity to strain or alternatively, to have reduced or even zero strain sensitivity. This ability to tailor the sensitivity of the FP via the FBG parameters will enhance the capabilities of FP sensor system.

Acknowledgement

I would like to express my sincere gratitude to Prof. Ralph Tatam for giving me the opportunity to pursue a PhD and thank you is also due to Cranfield University which has provided me with the support for this period.

I am thankful to Dr. Steve James and Prof. Ralph Tatam for their help and ideas and tolerance when I break things which I shouldn't have done! I am greatly indebted to Dr. Steve James for his vast wealth of knowledge and numerous input and advice together with his quiet patience in going through my thesis with meticulous care. A big Thank You!

I must also thank Dr. Chen-Chun Ye for taking his valuable time to write the chirped FBGs for me, Dr. Edmond Chehura for his advice and discussion in the subject of optics and besides and Dr Roger Groves for my first induction into optics and fibre optics. Special thanks are also due for Stephen Steines for his immaculate conceptions of his trademark precision engineering with electronics to boot not to mention all the little things he has done for my car. Thanks goes to past and present members of the Optical Sensors Group in particular Dr. Gerald Byrne for showing me the way, and Dr. Nick Rees and Dr. Sarfraz Khaliq getting me to put pen to paper in a very unconventional way.

My gratitude goes to my mum and dad for their unfailing support and understanding. Extra special thanks to my brother, and sisters, uncle and my aunty and not to forget my little niece for just being there.

謹獻給親愛的爸爸媽媽

To:

My mum and dad

Contents

Contents	i
Glossary of symbols and abbreviations	iv
List of figures and tables	vi
1 Introduction	1
1.1 Scope of thesis	5
References	
2 The Fibre Bragg Gratings	10
2.1 Introduction	10
2.2 Uniform FBG	11
2.3 Linearly chirped FBG	12
2.4 Fabrication of fibre optic Fibre Bragg Grating	15
2.4.1 Holographic method	15
2.4.2 Phase Mask technique	17
2.4.3 Chirped FBG fabrication	19
2.5 Summary	26
References	
3 Review of FBG sensors and filters	30
3.1 Introduction	30
3.2 Uniform FBG sensors	30
3.2.1 FBG Sensor systems	34
3.2.2 Interferometric demodulation	35
3.3 Linearly Chirped FBG sensors	37
3.4 Uniform FBG Fabry-Perot filters	47
3.5 Uniform FBG Fabry-Perot sensor	52
3.6 Dispersive Bulk type Fabry-Perot filter	55
3.7 Dispersive Optical delay line interferometer	62
3.8 Chirped FBG Fabry-Perot and Michelson interferometer filter	63
3.9 Dissimilar chirped FBG Fabry-Perot and Michelson interferometer filter	68
3.10 Chirped FBG Michelson interferometric sensor	73
3.11 Strain enhancement of chirped FBG Michelson and large path-length scanning Fabry-Perot interferometer	76
3.12 Summary	83
References	
4 Theory of Fibre Optic Bragg Grating and Fabry-Perot Interferometers	95
4.1 Introduction	95
4.2 Theory of light propagation in optical fibre	95
4.2.1 Propagation modes in optical fibres	95

4.2.2	LP modes and cut off	97
4.2.3	Dispersion of light in propagation	99
4.2.4	Phase matching and Bragg condition	100
4.2.5	FBG parameters	101
4.2.6	Chirped FBG and the grating phase shift	103
4.3	Theory of the Fabry-Perot interferometer	104
4.3.1	The bulk Fabry-Perot Etalon	107
4.4.2	Dispersive Bulk Fabry-Perot	110
4.3.3	Fibre Bragg Grating Fabry-Perot	113
4.3.3.1	Uniform Period Fibre Bragg Grating Fabry-Perot	113
4.3.3.2	Chirped Fibre Bragg Grating Fabry-Perot	114
4.3.3.3	Co-propagating chirped FBG Fabry-Perot cavity	120
4.3.3.4	Contra-propagating chirp FBG FP: The reduced Configuration	122
4.3.3.5	Contra-propagating chirped FBG FP: The enhanced Configuration	129
4.3.3.6	Phase response of the insensitive chirped FBG FP	131
4.4	Summary	136
References		
5	Variable Strain and Temperature sensitive chirped FBG FP cavity	139
5.1	Introduction	139
5.2	Strain sensitivity of chirped FBG Fabry-Perot	139
5.3	The phase response to strain of the chirped FBG FP	144
5.4	The phase response of the chirped FBG FP to temperature	148
5.5	Summary	150
References		
6	FBG and FBG FP Simulation	152
6.1	Introduction	152
6.2	The Transfer Matrix Method	154
6.3	Penetration and transmission depth	157
6.4	TMM simulation of FBG	159
6.1.1	Uniform FBG	160
6.4.2	Positively chirped FBG	163
6.1.1	Negatively chirped FBG	166
6.5	Modelling the strain effect on the chirped FBG	169
6.5.1	The change in the penetration depth of the chirped FBG with strain	170
6.5.2	The change in length of the chirped FBG with strain	174
6.5.3	Strain response of the chirped FBG FP: A semi TMM approach	175
6.5.4	Strain insensitive chirped FBG FP cavity	176
6.6	Summary	179

References		
7	Details and specifications of devices used in the design of experiment	181
7.1	Introduction	181
7.2	Experimental set up	181
7.3	The light source	183
7.4	Calibration of the piezo-actuator	186
7.5	Wavelength monitoring for the 800nm source	188
7.6	Temperature measurement	189
7.7	Summary	190
References		
8	Calibrations of chirped FBG Fabry-Perots	191
8.1	Introduction	191
8.2	Observation of reduced strain sensitivity	191
8.3	Chirped FBG FP with chirp rate of 25nm mm ⁻¹ and cavity length of 97mm	196
8.3.1	The strain response	198
8.3.2	Temperature response	204
8.3.3	The wavelength response	206
8.4	Dissimilar chirped FBG FP formed between a chirped FBG with chirp rate of 25nm/mm and a cleaved end of an optical fibre	209
8.4.1	Wavelength response of the dissimilar chirped FBG	210
8.4.2	Straining the dissimilar chirped FBG	217
8.4.3	Wavelength response of dissimilar chirped FBG FP with the chirp in the FBG created by applying a strain gradient along the length of FBG	222
8.5	Overlapping cavity chirped FBG FP	227
8.5.1	Wavelength response of the overlapping cavity	229
8.5.2	Strain response of the overlapping cavity	231
8.5.3	Temperature response of the overlapping	234
8.6	Summary	237
References		
9	Conclusion	243
9.1	Future work	246
List of publications		248
Appendix A		a-d
Appendix B		e
Appendix C		f
Appendix D		g
Appendix E		h
Appendix F		k
Appendix G		m
Appendix H		o

Glossary of symbols and abbreviations

Symbols

α	Coupling constant
B	Backward propagating mode
β	propagation constant
b	Positional detuning with wavelength in chirped FBG
c	free space velocity of light
$^{\circ}\text{C}$	degrees centigrade
$\Delta\beta$	differential propagation constant
$\delta\lambda$	detuned wavelength
Δ	relative difference in the core-cladding refractive index
Δn	Difference in the core-cladding refractive index
$\Delta\lambda_c$	Total chirp
$\Delta\lambda_0, \Delta\nu_0, \Delta\lambda_{\text{FSR}}, \Delta\nu_{\text{FSR}}$	Free spectral range
$\Delta\lambda$	Bandwidth of the grating
ΔL	path length mismatched in the Michelson interferometer
$\Delta\phi(\lambda)$	the differential phase
δ	Detuning parameter
δl	differential section of the grating
E	electric field distribution
$\xi(\omega)$	amplitude of the component of the plane wave
ε	Permittivity
$d\varepsilon$	Strain
ξ	Strain responsivity
ζ	temperature responsivity
F	Forward propagating mode
I_T	transmitted intensity
I_R	Reflected intensity
n	Refractive index
n_0	Initial refractive index
n_{eff}	Effective refractive index
n_1	Refractive index of optical fibre core
n_2	Refractive index of optical fibre cladding
λ_0	central wavelength
λ_B	Bragg wavelength
$l(\lambda)$	wavelength dependent cavity length
l_g, L_g	grating length
$l_0, l(\lambda_0)$	Cavity length of the centre wavelength
L	Cavity length measure between the edges of the gratings
L_c	Coherent length
p_{11} and p_{12}	Pockels coefficients
R	Reflectivity
R_{FP}	reflectivity of the FP
R_p	Complex reflectivity

θ	Phase
ψ	cumulative phase
φ	Incident angle
φ_c	critical angle of internal reflection
φ_A	Coupling angle
$\phi(z)$	additional phase applied to the sinusoidal refractive modulation
k	wave number
K	Special frequency
Γ	Complex transmission
dT	change in temperature
τ	time delay
V	Visibility
ν	Poisson ratio
ω	angular frequency
χ	susceptibility
z	Distance along the fibre/grating

Abbreviations

DAQ	Data Acquisition
dB	Decibels
EMI	Electromagnetic Interference
FBG	Fibre Bragg Grating
FFT	Fast Fourier Transform
FP	Fabry-Perot
FSR	Free Spectral Range
FWHM	full-width half maximum
Ge	Germania
MZ	Mach Zehnder
NA	Numerical Aperture
OCT	Optical Coherence Tomography
OPL	Optical Path Length
OSA	Optical Spectrum Analyser
PZT	Piezo stack
RTPS	Round Trip Phase Shift
RSOD	Rapid Scanning Optical Delay line
TMM	Transfer Matrix Method
Ti	Titanium
UV	ultra-violet
WDM	Wavelength Division Multiplex
WKB	Wentzel-Kramers-Brillouin

List of Figures

Figure 2.1	The formation of FBG by UV light.	Page 11
Figure 2.2	Schematic diagram of a FBG illustrating that only the wavelength of light, λ_B , that satisfies the Bragg condition, is reflected.	Page 12
Figure 2.3	Response of chirped Bragg grating where: a) Illustration of the spectral response of the chirped grating. b) the variation of the resonance condition with grating length.	Page 13
Figure 2.4	illustration of the chirped FBG with position detuned Bragg wavelength where the detuning is, a) driven by the position dependence periodicity, $\Lambda(z)$ and b) is driven by the varying mode index with position $n_{\text{eff}}(z)$.	Page 14
Figure 2.5	Two beam transverse interferometer.	Page 16
Figure 2.6	Illustration of the fabrication of FBGs using a phase mask.	Page 18
Figure 2.7	Holographic writing technique using a phase mask as a beam splitter a) using mirror and b) using a prism to vary the angle between the two interfering beams.	Page 19
Figure 2.8	shows the configuration for writing linearly chirped FBG by bending the optical fibre [13].	Page 20
Figure 2.9	writing chirped FBGs with interference of different wavefronts by using lens of different focus at the respective beam paths [14].	Page 20
Figure 2.10	shows the configuration for writing a linearly chirp FBG using a uniform phase mask [17].	Page 21
Figure 2.11	illustrations of writing a chirped FBG using a chirped phase mask.	Page 22

Figure 2.12	an illustration of the stepped chirped FBG produced by using a stepped phase mask. Each section consisted of constant period with a progressively increasing period from section to section [19].	Page 22
Figure 2.13	chirped FBG created using a tapered fibre[33].	Page 24
Figure 3.1	shows a schematic diagram of a FBG illustrating that only the wavelength of light, λ_B , that satisfies the Bragg condition, is reflected.	Page 31
Figure 3.2	shows a schematic effect of perturbed FBG response with the corresponding wavelength shift.	Page 32
Figure 3.3	illustrates a basic wavelength division multiplexed FBG based sensor system with reflective detection.	Page 35
Figure 3.4	illustration of the grating sensor system with interferometric wavelength discrimination using an unbalanced MZ	Page 35
Figure 3.5	illustration of the grating laser sensor system where the wavelength sensitivity can be increased because of the improved signal linewidth.	Page 36
Figure 3.6	illustrates the position dependence of each wavelength component for a linearly chirped FBG with a linear variation of the period.	Page 37
Figure 3.7	shows a schematic of the timed signal for measuring the group delay [52]	Page 38
Figure 3.8	the group delay measurement demonstrating the different delay of each wavelength due to the wavelength dependence of the reflection position [52].	Page 39
Figure 3.9	Schematic of the synthetic wavelength technique [55] for measuring the group delay	Page 39
Figure 3.10	illustrates the results of the group delay measurement using the synthetic wavelength technique [55]. The results demonstrate that different wavelength are reflected from different positions along the chirped FBG	Page 40

- Figure 3.11** illustrates a chirped FBG imparts delay to different wavelength component in a pulse. Depending on the parameter of the chirp FBG, the slower component can catch up with the faster component on reflection, changing the shape of the pulse. **Page 41**
- Figure 3.12** the effect of stretching a chirped FBG, showing the shift in the central wavelength, $\Delta\lambda_B$ accompanied by the redistribution of the period. The chirp gradient is constant and thus there is no broadening of the reflected spectrum[61]. **Page 42**
- Figure 3.13** Schematic diagram of the identical broadband chirped grating interrogation[62]. **Page 43**
- Figure 3.14** illustrates the effect of increasing the strain gradient on the FBG, the effect broaden the spectrum of the FBG as well as shifting the central wavelength due to the increasing average strain [69] **Page 45**
- Figure 3.15** Schematic of the intensity based intra-grating sensing [73] where the nonlinear strain field changes the distribution of the period in the Chirp FBG resulting in a modified reflected spectrum. **Page 46**
- Figure 3.16** diagram showing a uniform FBGs pair forming a fibre FP. The bandwidth of the 2 FBGs overlap in wavelength [76]. **Page 48**
- Figure 3.17** a), b) shows the spectral profile of the 2 uniform FBGs. The interference fringe in the profile is caused by the result of spurious cavity formed within the interrogation system with a fibre connector. c), the FP spectrum with a cavity length of $\sim 5\text{cm}$, giving a $\text{FSR} = 0.016\text{nm}$. (FBGs are written and FP characterised in-house at Cranfield) **Page 49**
- Figure 3.18** the result of the TMM of a FP filter formed between 2 identical uniform FBGs. The FSR/cavity resonance spacing is determined by the cavity length between the gratings centre (The coding of the simulation was done under Matlab which was undertaken for the Phd project). **Page 50**

- Figure 3.19** a) wavelength, b) strain and c) temperature scanning of the same uniform FBGs FP filter formed using 2 FBGs in the region of 1560.5nm. The uneven spacing of the fringes in b) is due to the non-linear scanning of the piezo-actuator used (FBGs are written and FP characterised in-house at Cranfield). **Page 51**
- Figure 3.20** schematic diagram of the low coherence interrogation of multiplexed FBG FP formed with different Bragg wavelengths. The path length imbalance of the MZ matches that of the FP to within cm as the effective L_c is determined by the bandwidth of the uniform FBGs ($\sim 0.3\text{nm}$)[85]. **Page 54**
- Figure 3.21** Fabry-Perot Etalon **Page 56**
- Figure 3.22** illustration of the experiment use to record the frequency response of a bulk FP containing a dispersive material. The inset shows the refractive index together with the index gradient with wavelength [88] **Page 58**
- Figure 3.23** experimental measurement of the FSR of a FP cavity containing a dispersive medium. The FSR varied by 75%, depending on the temperature of the cavity [88] **Page 59**
- Figure 3.24** the spontaneous emission spectra from $\text{GaAs}_{1-x}\text{P}_x$ driven below threshold, showing varying FSR/resonance mode spacing [89] **Page 60**
- Figure 3.25** Mach-Zehnder interferometer to measure the dispersion of the optical fibre and the results of the wavelength response where there is a change of FSR [90]. **Page 61**
- Figure 3.26** diagram of the rapid scanning optical delay line which consists of a bulk grating which transform the light in frequency domain. The lens focuses the dispersed light into the scanning mirror which impart a linear phase ramp to the frequency of the light[91]. **Page 62**
- Figure 3.27** Coherent interrogation of a reflective surface using the optical delay line scanning technique. Dispersion causes the broadening of the auto- correlations of the source and also alters the carrier frequency inside the envelope (characterised in-house at Cranfield). **Page 63**

- Figure 3.28** Chirped FBG FP filter with chirp oriented in the same direction, such that the cavity length, $l(\lambda)$ is the same for all wavelengths. **Page 64**
- Figure 3.29** shows the reflection profile of the chirped FBG and the spectral response of the chirped FBG FP with the cavity resonance lies within the envelope of the chirped FBG reflection profile, giving a broad band response. The response was calculated using a TMM model of a pair of chirp FBGs (@1550nm, 2mm, 5nm) with a cavity length of 5mm, giving a FSR= 0.16nm. **Page 64**
- Figure 3.30** shows the measured transmission response of a chirped FBG FP filter with cavity length of 8 mm. The corresponding FSR = 0.1nm over a 0.4nm wavelength range around 1536nm is shown [94] **Page 65**
- Figure 3.31** measured transmissivity of the chirped FBGs FP filter with the cavity length = 0.5mm. The top trace is for the entire spectrum where the bottom trace shows the same results over a reduced wavelength range. The measured FSR is 1.5nm [94] **Page 66**
- Figure 3.32** the spectral response of a Michelson filter consisting of 2 chirped FBGs (@1550nm, grating length of 5mm and bandwidth of 10nm) with length mismatch, $\Delta l = 1.724\text{mm}$ which corresponds to a measured FSR of $\sim 0.47\text{nm}$, from the graph[99] **Page 67**
- Figure 3.33** illustration of a Michelson filter consisting of 2 chirped FBGs with the chirps orientated in the opposite direction to each other [101]. **Page 69**
- Figure 3.34** shows a Michelson interferometer filter consisting of 2 chirped FBGs centred @1541nm with chirp of 7.8nm and cavity length of 96mm with the minimum cavity length of 20mm and maximum cavity length of 210mm[102] **Page 70**
- Figure 3.35** measured frequency response for the dissimilar chirped FBGs Michelson interferometer[102]. a) FSR of the various available cavities accessed by different wavelength and b) a plot of FSR with wavelength. Using the relationship of the detuned wavelength with position, the cavity length measured in terms of wavelength shows an inverse relationship with cavity length. **Page 71**

- Figure 3.36** illustrates the loop mirror interferometer configuration, where the cavity length is given by the path difference of the two reflected waves. The filter response for 2 different chirped FBGs used is also shown [104]. **Page 72**
- Figure 3.37** illustration of the phase based Bragg intragrating distributed strain measurement based on the dissimilar chirped FBG Michelson interferometer where one arm of the interferometer is terminated with a mirror with a broadband response[105]. **Page 74**
- Figure 3.38** illustration of arbitrary stain profile measurement based on the dissimilar chirped FBGs Michelson interferometer where the path matching is determined by the amount of stretching and the wavelength is determined by the maximum return signal when matching wavelength [108]. **Page 75**
- Figure 3.39** the effect of a perturbation upon a periodically chirped FBG showing the change in the resonance position. **Page 76**
- Figure 3.40** illustration of the Michelson interferometer used to demonstrate the strain magnification using a chirped FBG in one arm and a mirror end in the other[51]. **Page 77**
- Figure 3.41** illustration of the dissimilar chirped FBG FP setup, a) non dispersive where the dispersion is cancelled, b) dispersion in the FP is not cancelled and there is the residual dispersive effect and c) other types of dispersive FP configurations. **Page 79**
- Figure 3.42** a), illustrates the coherence interrogation configuration which consists of a reference interferometer and a sensing interferometer. b) the theoretical plot of the autocorrelation of the source, c) is the dispersion free configuration consists of 2 chirped FBGs but the scan revealed that there is still residual dispersion as the autocorrelation is broaden and d) 2nd interferometer configuration consisting of only a single chirped FBG and the scan produced a less broadened autocorrelation [111]. **Page 81**
- Figure 3.43** illustration of the heterodyne interrogation of a chirped FBG FP resonator. A carrier of frequency ω_c is created by ramping the injection current [113]. **Page 82**

Figure 4.1	illustration of light in ray diagram undergoing internal reflection when the angle of incident to the core/cladding surface is greater than the critical angle φ_c	Page 96
Figure 4.2	a plot of normalised refractive index against normalised frequency, V for the LP modes [2]	Page 98
Figure 4.3	schematic of the grating with the boundary conditions as shown.	Page 101
Figure 4.4	arrangement of the FP configuration.	Page 105
Figure 4.5	illustrates a FP cavity formed between a fibre end and a mirror.	Page 105
Figure 4.6	illustrates a FP cavity formed between 2 fibre ends with supporting members.	Page 106
Figure 4.7	illustrates a FP cavity formed by fusion splicing piece of fibres together with a reflective surface to form reflective mirrors.	Page 106
Figure 4.8	a), schematic diagram showing a fibre FP cavity consisting of a section of an optical fibre forming a cavity with its' ends cleaved such that $R \sim 4\%$. b) showing the transmission response with a small visibility but high intensity throughput where as in c) the reflection response has a high visibility but a low intensity throughput.	Page 109
Figure 4.9	uniform FBG grating FP	Page 113
Figure 4.10	shows the FBG FP wavelength response shown the cavity resonance mode modulated by the FBG stopband.	Page 114
Figure 4.11	shows a chirped FBG FP, which consists of 2 chirped FBGs separated by cavity length, where $l(\lambda)$ is a wavelength dependent cavity length and the total chirps, $\Delta\lambda = \lambda_1 - \lambda_0$ where $\lambda_1 > \lambda_0$.	Page 115

- Figure 4.12** illustration of the chirped FBG FP cavity with FBG having the same central wavelength, λ_0 , where the cavity length for the, λ_0 , is the distance between the grating centres, $l(\lambda_0)=l_0$. The cavity length, $l(\lambda)$, changes with different illumination wavelength. **Page 118**
- Figure 4.13** diagram showing the tendency to change the cavity length, l by the effect of movement of the resonance points within the grating, $+b$ to increase the cavity length and $-b$ to decrease the cavity length. **Page 119**
- Figure 4.14** shows the co-propagating cavities of chirped FBG FP with chirps of the FBG oriented in the same direction as shown in a) and in the b) but in the opposite sense. When the wavelength is increased, the movement of the reflection point moves in the direction of the increasing chirp. The net effect in the 2 chirped FBGs cancels out each other such that there is no change in the cavity length. **Page 121**
- Figure 4.15** shows the reduced configuration of the contra-propagating chirped FBG cavity which consists of 2 identical chirped FBGs separated by a distance with the direction of the increasing chirped oriented away from the centre of the cavity. Increasing the wavelength will have a corresponding increase in the cavity length. **Page 122**
- Figure 4.16** a plot of the equation (4.55) for 3 wavelengths, 1550nm, 1300nm and 800nm. **Page 125**
- Figure 4.17** a) the FSR variation of the insensitive cavity configuration compared to the Bulk FP response and b) using the relationship of the positional dependence of wavelength, the equivalent FSR with wavelength is plotted using equation (4.56). **Page 127**
- Figure 4.1** shows the enhanced configuration of the contra-propagating chirped FBG cavity where there is a decreased in the cavity length, l with wavelength. **Page 130**
- Figure 4.19** a plot of equation (4.63) with λ_0 of 1550 nm and chirp rate of 25nm mm^{-1} . **Page 133**

- Figure 5.1** illustrates a chirped FBG FP cavity configured to have reduced sensitivity to strain. The cavity consists of 2 chirped FBGs with the direction of increasing chirp oriented away from the centre of the cavity λ_0 . The cavity is interrogated with a wavelength, λ and has a cavity length, $l(\lambda)$, measured between the resonance positions. The total chirp, $\Delta\lambda = \lambda_2 - \lambda_1$ where $\lambda_2 > \lambda_1$. **Page 140**
- Figure 5.2** a plot of the cavity length vs chirp rate required to construct a chirped FBG FP cavity that is insensitive to strain. The line is calculated using equation (5.5), assuming that, $\alpha=0.80$ and $\lambda = 1550\text{nm}$. **Page 142**
- Figure 5.3** a plot of the strain sensitivity of equation (5.9) as a function of wavelength. **Page 144**
- Figure 5.4** illustrating a chirped FBG FP cavity that consists of 2 chirped FBGs with arbitrary chirp, with a central Bragg wavelength, λ_0 . The cavity is interrogated at a wavelength, λ , with a corresponding the cavity length, $l(\lambda)$, measured between the appropriate resonance positions. The total chirp, $\Delta\lambda = \lambda_2 - \lambda_1$ where $\lambda_2 > \lambda_1$. **Page 145**
- Figure 6.1** schematic diagram showing the input and output fields at the start and the end of the section. **Page 155**
- Figure 6.2** the division of a FBG into section to facilitate the use of the TMM. Each section has constant FBG parameters to form a composite grating of varying period, to model a stepped chirped grating. **Page 156**
- Figure 6.3** the intensity and the phase response of a chirped FBG. **Page 158**
- Figure 6.4** illustration of the time delay for the reflected and transmitted beam in a FBG through, a) positional dependent reflection point and b) through a difference in the group velocity **Page 159**
- Figure 6.5** illustrates a uniform FBG where the Bragg wavelength, λ_B is strongly reflected and the off resonance wavelength is less so allowed a deeper penetration into the grating. **Page 160**
- Figure 6.6** illustrates the reflection spectrum of a uniform FBG centred at wavelength of 1550nm having length of 4mm. (a) reflectivity, (b) phase and (c) the penetration depth. **Page 161**

- Figure 6.7** shows the transmission profile for a uniform FBG having length of 4mm. (a) the transmittivity, (b) the phase response and (c) the path traversed. **Page 162**
- Figure 6.8** illustrates a positively chirped FBG where the light is incident from the left. The longer wavelength, λ_2 is reflected from a position in the FBG further to the right (positive in the right direction) compared to the shorter wavelength, λ_1 in a Cartesian coordinate system. **Page 163**
- Figure 6.9** illustrates the reflection response for a chirped FBG having length of 4mm with a chirp of +10nm. (a) the reflectivity, (b) the phase response and (c) the penetration depth. **Page 164**
- Figure 6.10** illustrates the transmission response for a chirped FBG having a length of 4mm and a total chirp of +10nm. (a) the transmission (b) the phase response and (c) the path traversed which is the grating length. **Page 165**
- Figure 6.11** illustrates a negatively chirped FBG where light is incident on the grating from the left. The longer wavelength, λ_2 is reflected from a point near on the left hand side of the FBG (more negative towards the left) compared to the shorter wavelength, λ_1 in a Cartesian coordinate system. **Page 166**
- Figure 6.12** illustration of the reflection response for a negatively chirped FBG having a length of 4mm and total chirp of -10nm. (a) the reflectivity, (b) the phase response and (c) the penetration depth. **Page 167**
- Figure 6.13** illustrates the transmission response for a negatively chirped FBG of 1550nm central wavelength, having a grating length of 4mm and a total chirp of -10nm. (a) the transmission profile, (b) the phase response and (c) the distance travelled across the grating. **Page 168**
- Figure 6.14** showing the movement of the central wavelength with strain for a 4mm FBG with a total chirp of +10nm. **Page 170**
- Figure 6.15** illustrates a positively chirped FBG experiencing axial strain and being interrogated at wavelength, λ . The displacement of the reflection point goes against the direction of chirp and hence reduces the penetration depth in this positively chirped FBG. **Page 171**

- Figure 6.16** showing what the increasing strain has on the penetration depth of the reflected wave in the positive chirped 4mm FBG. **Page 171**
- Figure 6.17** shows the variation of the penetration depth as a function of axial strain for a FBG of length 4mm with total chirp of +10nm illuminated at the central wavelength. **Page 172**
- Figure 6.18** showing the rate of change of reflection point w.r.t strain as a function of grating length, l_g for different total chirp in the FBGs at the central wavelength of 1550nm **Page 173**
- Figure 6.19** showing the rate of change of the grating length with strain for the FBG as a function of the total chirp, $\Delta\lambda_c$ for different grating length for the central wavelength. **Page 174**
- Figure 6.20** illustration of an arbitrary chirped FBG FP cavity demonstrating the aggregate changes in the reflection position and the length traversed in the grating which determines the strain sensitivity of the cavity. **Page 176**
- Figure 6.21** illustration of an arbitrary chirped FBG FP cavity demonstrating the aggregate changes in the reflection position and the length traversed in the grating which determines the strain sensitivity of the cavity. **Page 177**
- Figure 6.22** shows the cavity length required for a strain insensitive chirped FBG FP cavity employing two identically chirped FBGs in the reduced configuration shown in figure (6.21). **Page 178**
- Figure 6.23** using the results in figure (6.22), a plot of cavity length required to achieve a strain insensitive cavity against chirp rate for the central wavelength @1550nm, using the Semi-TMM approach together with equation (5.5), using $\xi = 0.8 \text{ } \epsilon^{-1}$. **Page 178**
- Figure 7.1** shows the experimental setup which uses 3dB fibre couplers to split and direct light to interrogate cavities simultaneous or individually with wavelength scanning or with a calibrated strain. **Page 182**
- Figure 7.2** the implementation of the strain rig with travelling stages where the width between the two travelling stages forming a cavity can be varied by means of a travelling vernier and a piezo-actuator to apply the extension to the cavity. **Page 183**
- Figure 7.3** A diagram illustrating the ring cavity configuration of the tuneable Ti:sapphire laser configured in the figure of 8. **Page 184**

Figure 7.4	diagram illustrating the design of the external cavity tuneable laser.	Page 185
Figure 7.5	illustrates how a bulk optics FP is used to monitor the extension of the straining rig. The cavity is formed between a cleaved fibre end and the mirror surface. It is attached onto an adjacent moving stage, which shared the moving mechanism.	Page 186
Figure 7.6	illustrates the monitoring FP response with the applied voltage showing the sinusoidal response.	Page 187
Figure 7.7	shows the variation of the extension as a function of applied voltage produced by the piezo-actuator. The graph demonstrates the expansion and contraction of the piezo-actuator in response to a sawtooth signal, driven at 30mHz. The hysteresis can be seen clearly.	Page 188
Figure 7.8	shows a scan of the FP where the separation of the two peaks provides the value of the FSR together with the voltage ramp to scan the mirror with.	Page 189
Figure 7.9	shows a photograph of the tube furnace.	Page 190
Figure 8.1	schematic of a reduced strain sensitivity chirped FBG FP cavity where the movement of the resonance positions, $\frac{\delta b}{\delta \epsilon}$ opposes the increase in cavity length caused by application of axial strain.	Page 191
Figure 8.2	the reflection profile of the two chirped FBGs used to form the FP cavity (parameters detailed in table (8.1))	Page 193
Figure 8.3	the implementation of the strain rig with a manual travel to impart strain on both of the cavities in question. The lead screw is twisted back and forth to create the extension and the signal from D1 and D2 are captured simultaneously.	Page 193
Figure 8.4	the strain response of the two cavities is simultaneously captured using a storage oscilloscope. The chirped FBG FP, shows a reduced strain sensitivity, as compared with the FP formed between the uniform period FBG FP	Page 194
Figure 8.5	shows the grating profiles used in the experiment where the reflectivity for all gratings used <4%. The scan is achieved by sweeping the scanning wavelength of the Photonetics laser from 1506 to 1610nm in steps of 0.05nm.	Page 197

- Figure 8.6** illustrating the effect that strain has on chirped FBG FP cavities in a) the normal configuration where the movement of the reflection points in one grating acts to increase, in the other, act to decrease the cavity length, hence effect is nulled and the FP response will be that of the cavity length response to strain, b) the reduced configuration where the movement of the reflection points with strain reduces the effect strain has on the cavity and c) the enhanced configuration when the movement of the reflection point with strain in the grating enhances the effect of strain has on the cavity length. **Page 199**
- Figure 8.7** the experiment configuration which involved the use of fibre couplers so that the cavities can be interrogated and monitored with a computer controlled software. The signal is captured in detector D1. **Page 200**
- Figure 8.8** Strain response of the chirped FBG FP in the normal configuration. a) the driving voltage of the piezo, b) the intensity output from the monitoring bulk FP used in strain calibration and c) the strain response of the chirped FBG FP in the normal configuration interrogated at 1510nm. The calibrated strain level is $\sim 730\mu\epsilon$ giving ~ 100 fringe cycles. **Page 201**
- Figure 8.9** shows the plot of the strain sensitivity as a function of the inverse of the illuminating wavelength a) for normal, b) reduced strain sensitivity and c) enhanced strain sensitivity configurations. The linear relationships demonstrate that the strain sensitivity is proportional to the cavity length only and is not dependent upon the orientation of the chirp of the FBGs in the FP formations **Page 202**
- Figure 8.10** shows the temperature response of the chirped FBG FP arranged in the reduced strain sensitivity configuration with the FBGs having a chirp rate of ~ 25 nm/mm and cavity length of 97mm, a) the temperature response at an illuminating wavelength of 1520nm and b) the temperature sensitivity at different illuminating wavelengths. **Page 204**
- Figure 8.11** illustration of the reduced configuration of the chirped FBG FP cavity which consist of 2 chirped FBG with grating length ~ 4 mm, total chirp, $\Delta\lambda_c \sim 100$ nm with the orientation of chirp going away from each other and having a cavity length between the grating centre ~ 97 mm **Page 206**

- Figure 8.12** the wavelength response of the chirped FBG FP in the reduced configuration with no reduction of the sensitivity observed, b) a FSR $\sim 0.008\text{nm}$ is shown in the wavelength region of 1560nm and this cavity has a uniform wavelength response across the bandwidth and c) using the non dispersive chirped FP FSR response, equation (4.59), the detuned cavity length, $l(\lambda)$ can be determined using the FSR values. The detuned cavity length can be distinguished with $l(\lambda_2) > l(\lambda_1)$ for $\lambda_2 > \lambda_1$ which is consistent with the chirped FBGs arranged in the reduced configuration, figure (8.11). **Page 207**
- Figure 8.13** Schematic diagram of a dissimilar chirped FBG FP configuration employing a chirped FBG as one reflector and a cleaved fibre end as the other with a wavelength dependent cavity length, $l(\lambda)$. **Page 210**
- Figure 8.14** shows the reduced wavelength sensitive dissimilar chirped FBG FP configuration, where the direction of the increasing chirp is aligned away from the centre of the cavity. **Page 211**
- Figure 8.15** a) shows the wavelength response of the dissimilar chirped FBG FP which consists of a chirped FBG and a cleaved end of the fibre forming a cavity with the length of $\sim 7\text{mm}$, measured from the centre of the FBG to the fibre end. b) a plot of the variation of the FSR with wavelength and c) a plot of wavelength detuned cavity length, $l(\lambda)$ as a function of wavelength defined from equation (4.47). **Page 212**
- Figure 8.16** shows the enhanced wavelength sensitive dissimilar chirped FBG FP configuration, where the direction of the increasing chirp is aligned towards the centre of the cavity. **Page 213**
- Figure 8.17** a) shows the wavelength response of the dissimilar chirped FBG FP which consists of a chirped FBG and a cleaved end of the fibre. The cavity length is $\sim 7\text{mm}$, measured from the centre of the FBG to the fibre end. b) a plot of the variation of the FSR with wavelength and c) a plot of cavity length as a function of wavelength defined from equation (4.47). **Page 214**
- Figure 8.18** showing the dissimilar chirped FBG FP with a very short cavity length with the chirped FBG having a chirp rate of $\sim 25\text{nm/mm}$ and cavity length $\sim 2\text{mm}$ measured from the centre of the grating to the cleaved end **Page 215**

- Figure 8.19** a) shows the wavelength response of the dissimilar chirped FBG FP which consists of a chirped FBG and a cleaved end of the fibre forming a cavity with the length of $\sim 2\text{mm}$, measured from the centre of the FBG to the fibre end. b) a plot of the variation of the FSR with wavelength and c) a plot of cavity length as a function of wavelength defined from equation (4.47). **Page 216**
- Figure 8.20** experimental arrangement to strain only the grating of the chirped FBG FP. The shift in the RTSP with the application of strain is monitored. **Page 218**
- Figure 8.21** a) the voltage ramp, b) the calibrating HeNe wavelength at which ~ 5 fringes appeared giving an extension of $\sim 1.5\mu\text{m}$ in a grating of $\sim 4\text{mm}$ which corresponds to an applied strain of $\sim 375\mu\epsilon$. A progressing increasing strain sensitivity with increasing illuminating wavelength can be seen from c) to g) with wavelength in the range of 1565nm to 1575nm in steps of 2nm . The maximum observed phase change $\sim 2\pi$ radian @ 1575nm . **Page 220**
- Figure 8.22** illustrates the setup used to apply a strain gradient to a uniform period FBG to induce a chirp. This system was used to form the chirped FBG reflector in the FP cavity. **Page 222**
- Figure 8.23** a) the wavelength response of the uniform period FBG FP which consists of a uniform FBG forming a FP with a fibre end and cavity length $\sim 20\text{mm}$. b) – d) shows the same cavity when the chirp of the FBG is progressively increased. The bandwidth of the wavelength response is progressively broadened but the change of the chirp rate has no affect on the measured FSR. **Page 224**
- Figure 8.24** a) the reflection profile of the 2 chirped FBG written by using a continuous phase mask method, b), the wavelength response @ 1547nm and the corresponding FSR, c) the wavelength response @ 1549nm and d) the wavelength response @ 1555nm . The measured FSR for all wavelengths corresponds to a cavity length $\sim 65\text{mm}$ of a non dispersive FP cavity. **Page 226**
- Figure 8.25** a), illustration of an overlapping cavity where the respective resonance positions provide the cavity length $l(\lambda)$. b) there exist 2 wavelengths, λ_1 and λ_2 which shares the same cavity length. For a perfectly overlapping chirped FBG FP, the central wavelength will see a cavity length of zero between the reflection points in the respective FBGs. **Page 228**

- Figure 8.26** a) the wavelength response of the overlapping chirped FBG FP cavity where the FSR is the highest at ~ 1526 and decreases on either side, b) the measured FSR is plotted together with equation (8.6) and c) using the FSR data and using equation (8.6) the wavelength detuned cavity length, $l(\lambda)$ is plotted as a function of wavelength. The wavelength at ~ 1526 nm corresponds to a cavity length of zero. A linear fit gives a chirp rate ~ 27 nm. Notice that for a cavity length $l(\lambda)$, can be accessed by 2 illuminating wavelength. **Page 230**
- Figure 8.27** shows the strain response of the overlapping chirped FBG FP cavity measured at illuminating wavelength of, a) $\lambda=1535$ nm, b) $\lambda=1545$ nm and c) $=15650$ nm. **Page 232**
- Figure 8.28** a) shows the plot of the measured phase shift as a function of the applied strain for different illuminating wavelength and b) is the strain sensitivity of the overlapping cavity as a function of wavelength. **Page 233**
- Figure 8.29** measured temperature responses of the overlapping chirped FBG FP cavity with wavelengths a) @1535nm, b) @1540nm, c) @1550nm. **Page 235**
- Figure 8.30** a) shows the plot of the measured phase shift as a function of the temperature for different illuminating wavelengths and b) is the temperature sensitivity of the overlapping chirped FBG FP cavity as a function of wavelength. **Page 237**

List of Tables

Table 2.1	Methods of creating chirp in FBGs	Page 25
Table 3.1	Strain and temperature response of FBGs at different wavelengths	Page 33
Table 3.2	Characteristics of interferometers involving the used of chirped FBGs	Page 83
Table 4.1	Table indicating the insensitive length required for the wavelength for 800nm, 1300nm and 1500nm from equation (4.55).	Page 125
Table 4.2	FP response of interferometers involving the used of chirped FBGs	Page 134
Table 5.1	Strain response of FP interferometers involving the used of chirped FBGs	Page 149
Table 8.1	The parameters of the two FPs	Page 191
Table 8.2	characteristics of interferometers involving the used of chirped FBGs	Page 239

1 Introduction

Advances in laser and fibre optic technologies are having a significant impact on the development of optical instrumentation systems for sensor and telecommunication applications. For sensor systems, the main research interest areas have been concerned with the production of a wide range of optical fibre based configurations and signal processing techniques that may be used in a variety of sensing and control schemes [1, 2, 3, 4]. Fibre optic sensors and devices have several advantages over their conventional electrical counterpart in that they are compact in size, robust, chemically inert, non-conductive and are immune to electromagnetic interference (EMI).

In general, fibre sensor schemes are based on an interaction of the measurand with the fibre that changes the intensity, frequency, phase, wavelength, modal distribution, or polarisation of the light propagating within the fibre. Fibre optic sensors have been shown to offer performance that compares well with those of well-established conventional sensors. However commercial exploitation of fibre optic sensors has largely been limited to low volume markets, and they are still perceived to be costly to implement and difficult to handle. Consequently, fibre sensors are generally exploited in niche areas where their attributes are most needed. Examples include the Sagnac configuration for optical gyroscopes [5] for sensitive rotation measurement, optical fibre hydrophones [6] for applications in high sensitivity measurement for the detection of weak acoustic fields and applications in hazardous and hostile environments such as encountered in the oil and gas industries and other specialised areas where there is the need for passive and very light weight device with minimal intrusion for tackling difficult measurement situations. One clear advantage of fibre sensors is the relative ease with which elements can be multiplexed into arrays using a common input and output fibre, offering the possibility of quasi-distributed sensing [7] and remote monitoring. Multiplexing allows the sharing of the light source, detection and signal processing system, which can reduce the cost of the sensor system.

Fibre optic technology is finding increasing use in the field of distributed and embedded sensors in applications in the civil and aerospace industries [8]. Much of the work in embedded sensors has been in the development of the fibre Bragg grating (FBG). FBGs are simple sensing elements, which can be photo-inscribed into a silica fibre by UV irradiation [9]. This process creates periodic refractive modulation directly into the fibre core, forming a highly resonant device. In addition they are compatible with the telecommunications and optoelectronics industries which are driving the development of new optoelectronic devices and forcing prices down.

FBG based sensors provide absolute wavelength encoding of information and their performance may be configured to be independent of the overall system light levels. The wavelength is dependent upon measurands such as strain and temperature. The wavelength selectivity of the FBGs allows arrays of FBGs to be encoded at different wavelengths to be addressed in serial or in parallel using Wavelength Division Multiplex technique (WDM) or having the FBGs array sharing a common wavelength and located at different vicinities, to be addressed using Time Division Multiplex (TDM) techniques or a combination of both techniques can be used with different multiplex architectures [10]. Their usage has been demonstrated for a wide range of sensing applications providing measurements of physical quantities such as pressure [11], ultrasound [12], acceleration [13] and magnetic field. Their small size, light weight and flexibility of deployment are attributes commensurate with embedded and surface mounted sensing schemes, making them the ideal candidate for use in quasi-distributed sensing. Embedded fibre sensors can be used for a variety of applications. One of the most important potential applications of FBG sensors is as the sensory elements in Smart Structures for self monitoring. A significant limitation to their mass exploitation is the requirement for temperature compensation of strain measurement errors caused by thermal fluctuations.

A large number of techniques for demodulating the wavelength have been demonstrated and reported, eg scanning filters such as the tuneable FP [14] and acoustic-optic tuneable filter (AOTF)[15], using passive filters such as band-edge of a spectral filter[16] and wavelength division couplers[10], matched gratings pair [17]. All of these techniques

have their advantages and limitations. For high sensitivity measurement, fibre-optical interferometric sensors based on the optical phase change detection offer much higher resolution. Fibre equivalent interferometers such as the Michelson and Fabry-Perot have been formed using FBGs acting as mirrors.

The Fabry-Perot (FP) interferometer is a key component for optical applications. It has already been demonstrated in the all fibre Fabry-Perot filter [18], which could be used as filters and sensors. The fabrication of such a device in the fibre form requires the introduction of highly reflective mirrors inside the fibre or terminating the ends with highly reflective materials, to form the cavity. The FBG inscription technique allows the creation of intrinsic reflectors without the need to physically intrude into the core and compromise the physical integrity and light guiding properties of the fibre. A pair of uniform period FBGs has been used to form the narrow band reflectors in the Fabry-Perot configuration [19]. The optical frequency response of in-fibre FBG Fabry-Perot filters have been studied theoretically and compared with experimentally measured data [20]. Such configurations have been demonstrated in the measurement of strain, temperature and vibration [21]. The inherent cross sensitivity between strain and temperature still exist for FBGs in the FP configuration. Many schemes have been reported to separate the strain and temperature responses, the most popular of which is to multiplex one or more reference FBGs in the system. The reference FBGs are kept isolated from strain but experience the same thermal environment as the active FBG sensor elements. Furthermore, it is difficult to distinguish between strain and temperature-induced wavelength shifts for which various techniques have been explored [22] which compromise the simplicity of multiplexed sensor arrays.

To ensure good spectral overlap between these two gratings it is necessary to make the FBG as broadband as possible, hence the use of chirped FBG. Chirped FBGs are dispersive elements and they have been used as dispersion compensation elements [23] in communications systems. With this type of structure, the pitch of the grating is varied along the grating length, and a different wavelength is reflected from different portions of the gratings. They offer a wider bandwidth than uniform FBGs, as well as imparting

different group delay to different components of the light. In order to increase the dynamic range and bandwidth, FPs were formed using identical chirped FBGs with chirp oriented the same way [24, 25, 26]. Improvement in the fabrication technique increased the reflectivity of the chirped FBGs to the effect of achieving high Finesse and contrast for WDM applications in communication systems [24]. A broadband FBG FP with the chirps of the 2 FBGs oriented the same way has the same characteristics as that of the uniform FBG FP, and they have been employed in sensing purposes. The sensitivity of sensors based on such a cavity configuration depends on the separation of the FBGs in the FP arrangement. FBG FP sensors with arbitrary gauge length can be made by writing two FBGs in an optical fibre with a separation equal to the desired gauge length. However there will be restrictions on the difference in the strain and temperature experienced at the two grating locations. Long gauge length sensors have a greater likelihood of encountering changes in material of structural behaviour than a number of small strain gauges. Long gauge length sensors tend to average local strain concentrations. Small gauge length sensors are suited to point sensing and quasi-distributed sensing and in the context of the FBG FP, small gauge length ensured that the two gratings can be located in close proximity to each other thereby ensuring they are exposed to the same local strain and temperature with little difference in the environment they are measuring.

As well as providing a wider bandwidth than uniform FBGs, chirped FBG imparts different group delay to different components of the light. The implication of the wavelength dependence of the reflection positions is that when a chirped FBG is subjected to axial strain, the reflection point for a particular wavelength changes within the grating length. Depending on the chirp rate, the application of strain to a typically chirped FBG of length of orders mm can induce a large path length change for the reflected light, which is equivalent to straining a piece of fibre of centimetres in length [27]. Given the ability of the chirped FBG to form partial broadband reflectors and utilising the large movement of the reflection position with wavelength in chirped FBG, a chirped FBG FP can be configured in which the large movement of the reflection positions in the respective FBGs forming the cavity, changes in such a way that the

sensitivity of the cavity can have an enhanced or reduced nature. The sensitivity of the chirped FBG FP depends on the chirping parameters of the FBGs. The sensor and filter response can be tailored through the extent of chirp. Variable strain sensitised chirped FP with long or short gauge length would be a great asset. The novel configurations of using chirped FBG FP produce very interesting properties.

In this thesis a novel configuration involving the use of chirped FBG pairs in the formation of fibre Fabry-Perot is considered. The aim of this work is to realise chirped FBG FP cavities with reduced or enhanced wavelength sensitivity which could be determined by the chirped parameters of the FBG and not so much by the cavity length. This scheme offers flexibility in determining the sensitivity of the sensor/filter to wavelength, strain and temperature via the parameters of the chirped FBG pairs, for long or short gauge length device. It is possible to configure the system to exhibit enhanced sensitivity to strain or alternatively, to have reduced or even zero strain sensitivity. This ability to tailor the sensitivity of the cavity to the effect of wavelength, strain and temperature, within the scope of FBG configuration will enhance the capabilities of FBG for use in structural monitoring, sensing and optical devices.

1.1 Scope of thesis

The large group delay experienced by the wavelengths which resulted in the reported strain magnification [27] and in the observed large path-length scanning in the matched path-length interferometric interrogation [28] involving the use of chirped FBGs are evident of the dispersive effect of the chirped FBG. This effect attributed to dispersion in the chirped FBG is not obvious in many of the reported literature on the use of chirped FBGs in the interferometric configuration. Many of which behaved in a non dispersive manner. The thesis will try to dispel the notion that the position dependent of the resonance position of wavelengths inside the chirped FBGs does not automatically make them dispersive when they are used in the interferometric configuration.

In chapter 2, the methods with which uniformed period FBGs and chirped FBGs are fabricated together with their physical difference will be outlined and the effect the chirp has on the reflected grating spectrum is described. Besides providing a broadband response, a chirped FBG imparts a wavelength dependent delay to the reflected signal and this has implications on the performance of the interferometers involving the use of these gratings. Chapter 3 attempts to provide a comprehensive review of the use of chirped FBG in the interferometric configuration and their performance and characteristics are explained.

The dispersion inside the cavity affects the performance of the bulk FP interferometer by modifying the round trip phase shift(RTPS) of the cavity. When chirped FBGs are used in the FP configuration, the effect of dispersion will change the characteristics of these cavities. In order to gain more insight into the mechanism of the effect of dispersion has on chirped FBG FP, a theoretical model is developed in chapter 4, by drawing on analogy with the dispersive bulk FP interferometer, where the dispersion affects the cavity characteristics, analysis of the RTPS will be performed on the chirped FBGs FP with the aim of explaining the possibility of creating chirped FBG FP cavities with sensitivity which could be altered by the chirp parameters of the FBG with a range sensitivities and devices gauge lengths can be configured.

Chapter 5 will try to establish the strain and temperature sensitivity of the chirped FBG FP to the wavelength sensitivity of the cavity. Dispersion in chirped FBG modifies the FSR of the cavity response and because of the relationship between the wavelength detuning with strain in FBGs, the strain sensitivity is also related to the wavelength sensitivity of the dispersive chirped FBG FP. By looking at the movement of the reflection point of the illuminating wavelength under the application of strain, the change in the RTSP of the cavity will be presented to show a relationship between the chirp rate and the length of the cavity required to configure a strain insensitive cavity.

The general aim of chapter 6 is to present the different modelling techniques that have been applied to the FBG. Using the transfer matrix method (TMM), a model of FBGs and

FBG FPs will be developed to simulate the cavities response to wavelength and strain which will complement the theory put forward in chapter 4 and 5. Chapter 7 aims to detail the experimental setup used in the characterisation of the FBG FP sensitivity to wavelength, strain and temperature. A discussion of the operation and performance of the devices used is presented and the implementation of the monitoring systems and their calibration is discussed.

Chapter 8 will present the experimental characterization of the chirped FBG FP of different configurations, formed with chirped FBGs fabricated via a range of techniques, to verify the predictions made in chapter 4 and 5. The properties of the cavities are investigated using a variety of methods including the application of axial strain, scanning the wavelength of the illuminating source and varying the temperature. Finally, the results are summarized, conclusions are drawn and future research directions discussed.

References:

- 1 T. G. Giallorenzi, J. A. Bucaro, A. Dandridge, G. H. Siegel Jr. J. H. Cole, S. C. Rashleigh and R. G. Priest, 'Optical fiber Sensor Technology', IEEE Journal of Quantum Electronics, **18**, 625-665, 1982.
- 2 D. A. Jackson, 'Monomode optical fibre interferometers for precision measurement', J. Phys. E: Sci. Instrum., **18**, 981-998, 1985.
- 3 K. T. V. Grattan and T. Sun, 'Fiber sensor technology: an overview', Sensors and Actuators, **82**, 40-61, 2000.
- 4 A. D. Kersey, 'A Review of recent Developments in Fiber Sensor Technology', Optical Fiber Technology, **2**, 291-317, 1996.
- 5 B. Culshaw and I. P. Giles, 'Frequency Modulated heterodyne Optical fiber Sagnac Interferometer', IEEE Journ. of Quan. Elect., **18**, 690-693, 1982.
- 6 P. G. Cielo, 'Fiber optic hydrophone: improved strain configuration and environmental noise protection', Applied optics, **18**, 2933-2937, 1979.
- 7 A. Dandridge and A. D. Kersey, 'Signal processing for Optical Fiber Sensors', Proc. of SPIE, **798**, 158-165, 1987.

- 8 P. D. Foote, 'Optical fibre Bragg grating sensors for aerospace smart structure', In: Optical Fibre Gratings and Their Applications, IEE Colloquium on Optical Fibre Gratings, 14/1-14/6, 1995.
- 9 G. Meltz, W. W. Morey and W. H. Glen, 'Formation of Bragg gratings in optical fibers by a transverse holographic method', Opt. Lett. **14**, 823-825, 1989.
- 10 A. D. Kersey, M. A. Davis, H. J. Patrick, M. LeBlanc, K. P. Koo, C. G. Askins, M. A. Putnam and E. J. Friebele, 'Fiber Grating Sensors', Journ. of Light. Tech., **15**, 1442-1463, 1997.
- 11 M. G. Xu, L. Reekie, Y. T. Chow and J. P. Dakin, 'Optical in-fibre grating high pressure sensor', Elect. Lett., **29**, 398-399, 1993.
- 12 Y. J. Rao, 'Recent progress in applications of in-fibre Bragg grating sensors', Optics and Lasers in Engineering, **31**, 297-324, 1999.
- 13 S. Theriault, K. O. Hill, F. Bilodeau, D.C. Johnson, J. Albert, G. Drouin and A. Beliveau, 'High-g accelerometer based on an in-fibre Bragg grating sensor; a novel detection scheme', Proc. of SPIE, **3491**, 926-930, 1998.
- 14 M. A. Davis, A. D. Kersey, J. Sirkis and E. J. Friebele, 'Fiber Optic Bragg Grating Array for Shape and Vibration Mode Sensing', Proc. of SPIE, **2191**, 94-101, 1994.
- 15 M. G. Xu, H. Geiger and J. P. Dakin, 'Multiplexed Point and Stepwise-Continuous fibre Grating Based Sensors: Practical Sensor for Structural Monitoring', Proc. of SPIE, **2294**, 69-80, 1994.
- 16 M. Serge, Melle, L. Kexing Liu and R. M. Measure, 'A Passive Wavelength Demodulation system for Guided-Wave Bragg Grating Sensors', IEEE Photon. Tech. Lett., **4**, 516-518, 1992.
- 17 M. A. Davis and A. D. Kersey, 'Matched-filter interrogation technique for fibre Bragg grating arrays', Elect. Lett., **31**, 822-823, 1995.
- 18 D. Hogg, D. Janzen, T. Valis and R. M. Measures, 'Development of a fiber Fabry-Perot strain gauge', Proc. of SPIE, **1588**, 300-307, 1991.
- 19 W.W. Morey, T. J. Bailey, W. H. Glenn and G. Meltz, 'Fiber Fabry-Perot interferometer using side exposed fiber Bragg Gratings', Proc. of OFC, WA2, 96, 1992.
- 20 Legoubin, M. Douay, P. Bernage and P. Niay, 'Free spectral range variations of grating-based Fabry-Perot filters photo written in optical fibers', J. Opt. Soc. Am. A, **12**, 1687-1694, 1995.

- 21 Y. J. Rao, M. R. Cooper, D. A. Jackson, C. N. Pannell and L. Reekie, 'Absolute strain measurement using an in-fibre-Bragg-grating-based Fabry-Perot sensor', *Elect. Lett.*, **36**, 708-709, 2000.
- 22 S. W. James, M. L. Dockney and R. P. Tatam, 'Simultaneous independent temperature and strain measurement using in-fibre Bragg grating sensors', *Elect. Lett.*, **32**, 1133-1134, 1996.
- 23 J. A. R. Williams, I. Bennion, K. Sugden and N. J. Doran, 'Fibre dispersion compensation using a chirped in-fibre Bragg grating', *Elect. Lett.*, **30**, 985-987, 1994.
- 24 X. Peng and C. Roychoudhuri, 'Design of high finesse, wideband Fabry-Perot filter based on chirped fiber Bragg grating by numerical method', *Opt. Eng.*, **39**, 1858-1862, 2000.
- 25 G. E. Town, K. Sugden, J. A. R. Williams, I. Bennion and S. B. Poole, 'wide-Band Fabry-Perot-Like in Optical Fiber', *IEEE Photon. Tech. Lett.*, **7**, 78-80, 1995.
- 26 H. Cho, I. Yokoto and M. Obara, 'Free spectral range variation of a broadband, high-finesse, multi-channel Fabry-Perot filter using chirped fiber Bragg gratings', *Jpn. J. Appl. Phys.*, **36**, 6382-6387, 1997.
- 27 A. D. Kersey and M. A. Davis, 'Interferometric fiber sensor with a chirped Bragg Grating sensing element', *Proc. of SPIE.*, **2360**, 319-322, 1994.
- 28 C. Yang, S. Yazdanfar and J. Izatt, 'Amplification of optical delay by use of matched linearly chirped fiber Bragg Gratings', *Optics Lett.*, **29**, 685-687, 2004.

2 The Fibre Bragg Gratings

2.1 Introduction

The discovery of photosensitivity in optical fibres [1] has had a large impact on telecommunications and on sensor systems with the effect being used to develop devices for many applications [2]. The formation of a Fibre Bragg Grating (FBG) is generally based on the photo-sensitivity of silica fibre doped with germanium. When illuminated by UV radiation, the fibre exhibits a permanent change in the refractive index of the core. Meltz et al [3] demonstrated the first production of Bragg gratings by the side exposure method, in which a spatially modulated intensity interference pattern was used to photo-inscribe a periodic refractive index grating.

The side exposure of the fibre by the interference of two intersecting beams of UV radiation allows fabrication of FBGs with user defined central wavelength, independent of the wavelength of the writing laser, figure (2.1). This UV exposure of the fibre imprints a regular structure of periodicity half the required Bragg wavelength into the fibre core over lengths in the range of millimetres to centimetres. The flexibility of this method allows Bragg wavelengths from the visible region to well beyond the telecommunications wavelength of 1550nm to be written[1].

The FBG has a periodicity of the order of wavelength of length. FBG interacts with the propagating wave in the core creating the diffraction phenomena analogous to that of wave interaction with regular structures in crystals and bulk optical gratings. The interaction with the propagating wave allows the coupling of the forward mode to the backward mode with characteristics depending on the properties of the FBG. FBGs have found applications in routing [4], filtering control and amplification of optical signals [5], as the feedback element in fibre lasers [6], in dispersion compensation [7] and in sensing applications [8].

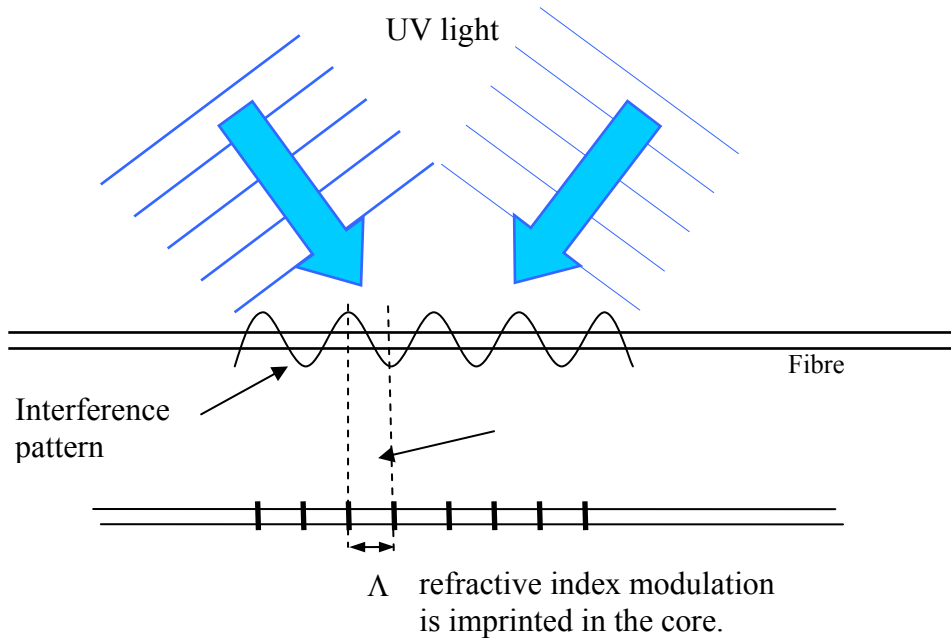


Figure 2.1 The formation of FBG by UV light.

For a FBG of typical length 5mm and period $0.5\mu\text{m}$, the grating comprises of thousands of periods. These highly regular and partially reflective modulation planes reflect a set of waves, which then interfere. This interference is in general destructive but for the wavelength that satisfies the Bragg condition, the reflected light will add constructively. So the FBG acts as a mode coupler, coupling the forward propagating mode to a backward propagating mode only when the resonant condition is satisfied.

2.2 Uniform FBG

For a uniform FBG, the period Λ remains constant throughout the length and the reflection is the strongest at the Bragg wavelength, λ_B . The Bragg resonant wavelength is a function of the period, Λ and the mode effective index (n_{eff}) which is given by [9];

$$\lambda_B = 2n_{\text{eff}}\Lambda \quad (2.1)$$

Light at the Bragg wavelength, λ_B , propagates in the fibre undergoes reflection and the rest of the light is transmitted through the grating unimpeded. The spectral characteristics depend on the grating's parameters, such as the amplitude of the refractive modulations, grating length, the coupling strength and the overlap integral

of the forward and backward propagating modes. A typical reflection spectrum of a uniform FBG is shown in figure (2.2)

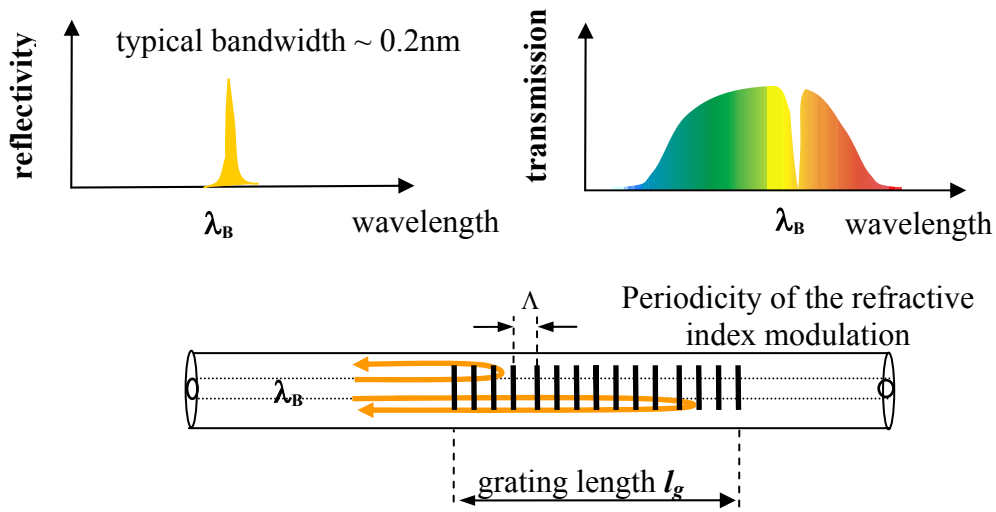


Figure 2.2, Schematic diagram of a FBG illustrating that only the wavelength of light, λ_B , that satisfies the Bragg condition, is reflected.

2.3 Linearly Chirped FBG

A chirped FBG has a Bragg condition, equation (2.2) which varies as a function of position along the grating. This is achieved by ensuring that the periodicity, Λ , varies as a function of position, or that the mode index, n_{eff} varies as a function of position along the FBG [10, 11], or through a combination of both. The Bragg condition for the chirp FBGs can be written as;

$$\lambda_B(z) = 2n_{eff}(z)\Lambda(z) \tag{2.2}$$

where z is the position along the grating. With this type of structure, the resonance condition is no longer localised but is position dependent. Each position has its' own resonance condition and reflects its own wavelength. This can also be interpreted as each wavelength having a different reflection point along the grating. The chirp in the FBG's period gives rise to a broadened reflected spectrum as illustrated in figure (2.3).

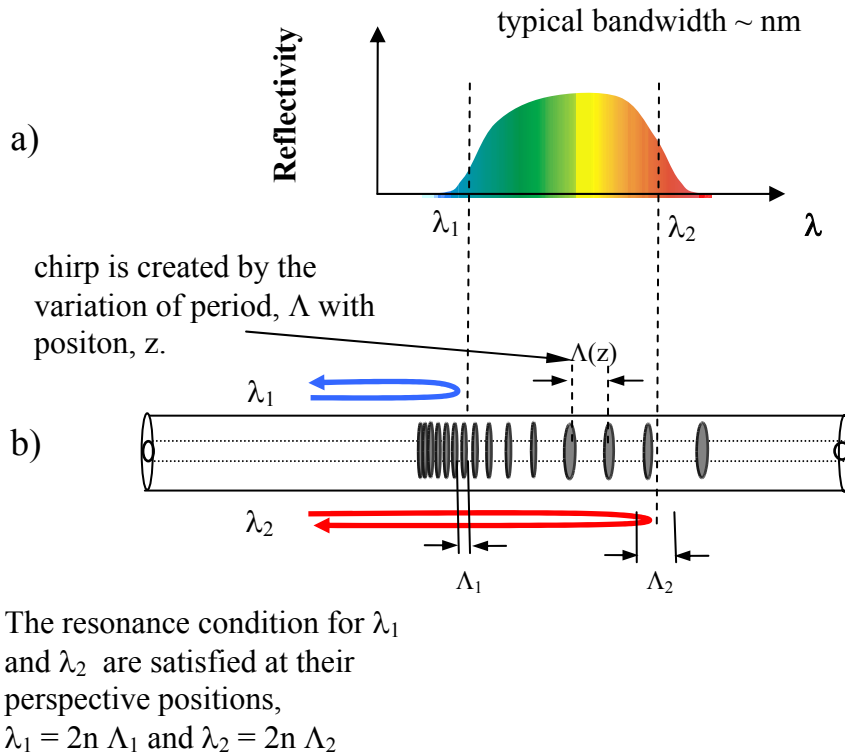


Figure 2.3 Response of chirped Bragg grating where:

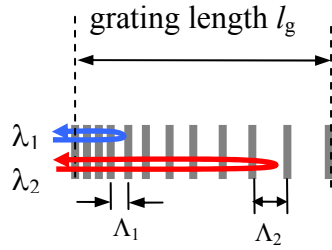
- a) Illustration of the spectral response of the chirped grating.
- b) the variation of the resonance condition with grating length.

The wider bandwidth offered by chirp FBGs provides a larger spectral range to operate within. In a linearly periodic chirped FBG, the dependence of the period of the refractive modulation upon the axial position along the FBG can be expressed as [12];

$$\Lambda(z) = \Lambda_o + \frac{(\Lambda_{lg} - \Lambda_o)}{l_g} z \quad (2.3)$$

where Λ_o is the period at the start of the grating, Λ_{lg} is the period at the end of the grating and l_g is the grating length. The equation (2.3) describing the dependence of periodicity upon position is illustrated in figure (2.4a). This provides a varying Bragg condition along the length of the grating.

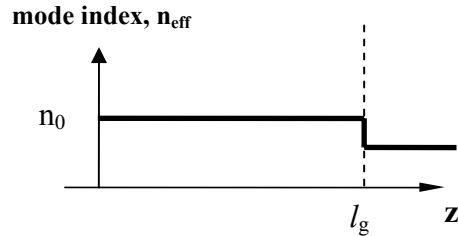
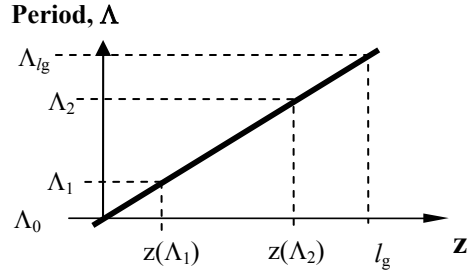
a)



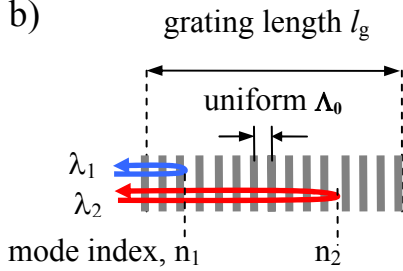
Bragg condition: $\lambda_B(z) = 2n_0 \cdot \Lambda(z)$,
and λ_1, λ_2 is given by;

$$\lambda_1 = 2n_0 \Lambda_1$$

and $\lambda_2 = 2n_0 \Lambda_2$



b)



Bragg condition: $\lambda_B(z) = 2n_{\text{eff}}(z) \cdot \Lambda_0$
and λ_1, λ_2 is given by;

$$\lambda_1 = 2n_1 \Lambda_0$$

and $\lambda_2 = 2n_2 \Lambda_0$

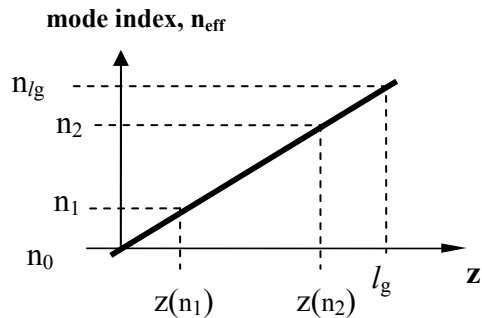
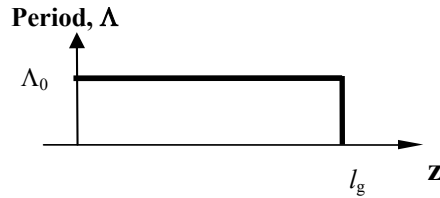


Figure 2.4, illustration of the chirped FBG with position detuned Bragg wavelength where the detuning is, a) driven by the position dependence periodicity, $\Lambda(z)$ and b) is driven by the varying mode index with position $n_{\text{eff}}(z)$.

The resonance condition is also dependent on the mode index. This provision of chirp in the FBG can also be realised by creating a varying mode index along the length of the FBG. Figure (2.4b), demonstrates how a variation in Bragg wavelength with position is possible by introducing a mode index variation with grating length while keeping the periodicity constant. The dependence of the mode refractive index upon the axial position along the FBG can be written similarly to equation (2.3);

$$n(z) = n_o + \frac{(n_{lg} - n_o)}{l_g} z$$

where n_o is the mode index at the start of the grating, n_{lg} is the mode index at the end of the grating. The practical methods of generating a chirped FBG using these two means are discussed in the chirp fabrication section (2.4.3).

2.4 Fabrication of Fibre Bragg Grating

This section discusses the methods used to generate a periodic modulation of the optical properties of the fibre and evaluates their merits and disadvantages. In particular, the methods used to fabricate the FBGs exploited in this thesis are detailed.

2.4.1 Holographic method

The fabrication of FBGs relies upon the introduction of a periodic modulation of the refractive index in the core of the fibre. The resulting regular structure acts as a means for coupling between modes. The change in the refractive index when exposed to UV radiation is made possible by the nonlinear effect, termed ‘photosensitivity’, occurring in the germanium doped fibre, which was first observed in the ‘Hill gratings’[1]. This permanent index modulation is imprinted in the core of the fibre by a standing wave formed within the core between counter-propagating modes of light in the blue-green, ~488nm, region of the optical spectrum. This intensity dependent refractive index change of the fibre core is a result of the absorption feature associated with germania-related defects @240nm, which is a 2 photon process for illumination at 488nm. This method produced FBG of restricted use, as the resulting FBGs were limited to operation at the wavelength of the laser used to fabricate them. As the fibres do not exhibit photosensitivity in the near IR region of the spectrum, this fabrication process is not suitable for producing FBGs for telecom applications.

The current level of interest in FBGs was initiated by the work of Meltz et al [3], who developed a side exposure holographic technique, in which the optical fibre is side exposed to the spatially structured illumination pattern formed by 2 interfering UV laser beams at a wavelength of approximately 240nm. The photosensitivity is based

upon the absorption peak of the germania-related defects of the fibre centred at 220nm. At these wavelengths, the refractive index change is a single photon process, making this approach more efficient.

The Bragg wavelength of FBGs fabricated using this technique is determined by the geometry of the interfering beams, providing flexibility in the characteristics of the FBG allowing a wide range of Bragg wavelengths to be produced. This technique allows the fabrication of FBGs with characteristics suitable for telecom and sensor applications. The interferometric setup for the side exposure technique is shown in Figure (2.5).

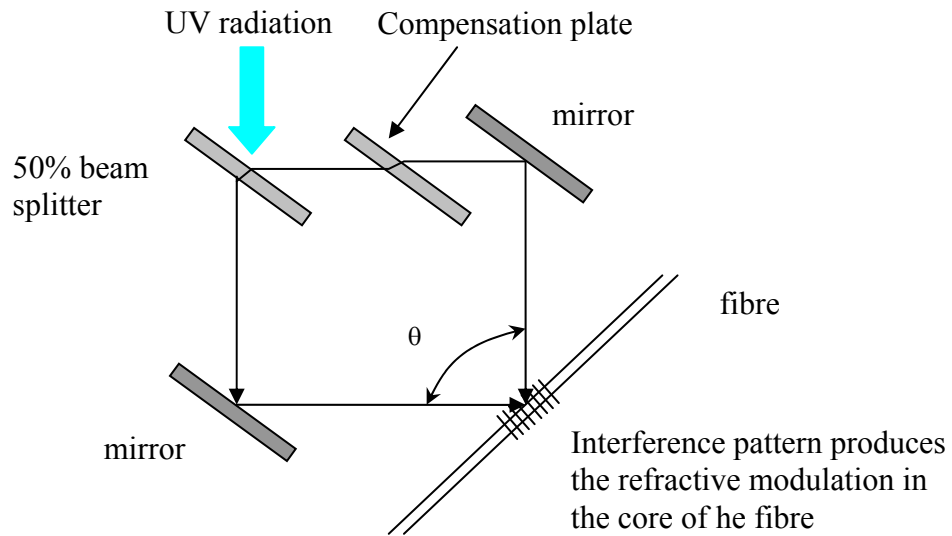


Figure 2.5 Two beam transverse interferometer.

A typical fabrication system is shown in figure (2.5). The UV beam is split into two at the 50/50 beam splitter. The two beams are brought together to interfere at the location of the fibre using mirrors, allowing control over the intercepting beams mutual angle θ . The Bragg wavelength of the FBG produced in the side exposure method is given by [9];

$$\lambda_{Bragg} = \frac{n_{eff} \lambda_{uv}}{n_{uv} \sin\left(\frac{\theta}{2}\right)} \quad (2.4)$$

where λ_{Bragg} is the Bragg wavelength, n_{eff} is the effective mode index of the fibre, n_{uv} is the refractive index of the silica when exposed to the UV light at λ_{uv} and θ is the mutual angle as seen in Figure (2.5). Variation of θ , or of the writing λ_{uv} , allows a wide range of Bragg wavelength to be written. The interference pattern produced at the intersection of the two beams imprints a regular pattern into the fibre. When using a low coherence UV source, the path difference between the two beams must be matched to produce a high visibility fringe pattern. Vibration and temperature changes that occur during exposure of the fibre, which may be as high as $\pm 1^\circ\text{C}$, can influence the path length difference and ultimately deteriorate the quality of the interferogram. Operating the writing light source with short exposure time (10s of seconds) will minimise the effect.

In writing FBGs, accurate placement of the fibre is critical to avoid the production of slanted FBGs which can couple light into other modes. Whilst the holographic side exposure technique is capable of producing Bragg wavelengths of arbitrary value by appropriate selection of the mutual angle between the converging beams, an alternative method based on the phase mask is commonly used. The use of phase mask allow highly repeatable fabrication of FBGs with a given Bragg wavelength defined by properties of the phase mask, however, this wavelength properties can not be tuned significantly.

2.4.2 Phase Mask technique

Phase masks are fabricated using lithography techniques. A silica plate is exposed to electron beams, and using techniques such as plasma etching, a one-dimensional periodic surface relief pattern is produced with well defined spacing and etched depth. The phase mask works in transmission. When a UV beam is incident normally to the phase masks surface, the beam is diffracted into the -1, 0 and +1 orders. Appropriate choice of etch depth allows the intensity of the zero order to be as low as $< 5\%$, such that up to 40% of the UV energy is diverted in the ± 1 orders [9]. The operation of the phase mask is shown in figure (2.6). The overlap between the ± 1 orders close to the phase mask, produces the interference pattern that is inscribed into the fibre, as illustrated in figure (2.6).

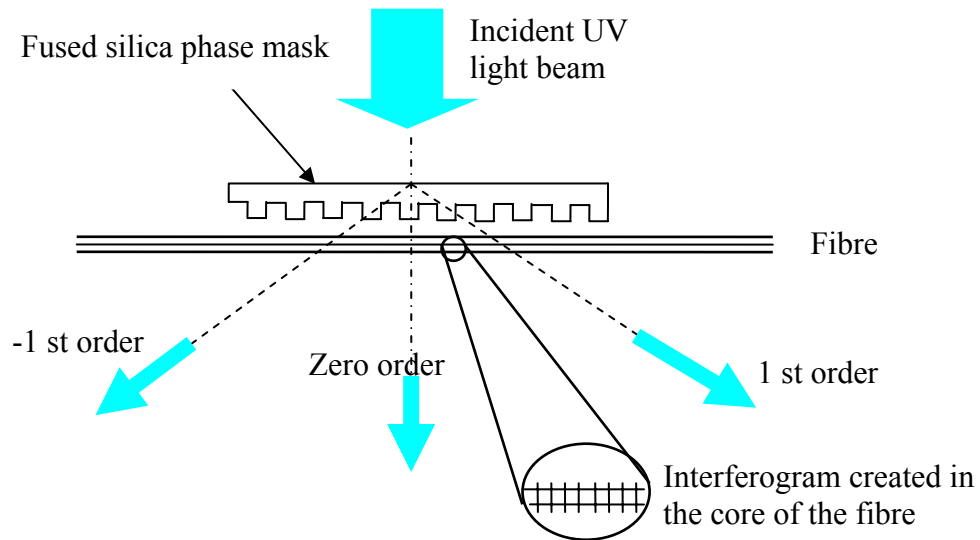


Figure 2.6, Illustration of the fabrication of FBGs using a phase mask.

Using the phase mask in close proximity to the fibre as shown, the inscribed period is equal to half of the period of the phase mask. The use of the phase mask allows highly reproducible fabrication of FBGs with fixed characteristics determined by the phase mask properties. The disadvantages of this method include the fact that a particular phase mask fabricated is use with a specific writing UV wavelength. When used at UV wavelengths other than the design wavelength, the diffraction efficiency is reduced and thus the zero order can influence the final Bragg wavelength. A different phase mask is required for each different Bragg wavelength. The phase mask technique offers easier alignment and imposes a less stringent requirement on the coherence of the writing source. A degree of flexibility in varying the Bragg wavelength can be achieved by application of strain to the optical fibre before the FBG is fabricated. The phase mask can also be used as a component of a 2 beam the interferometric set up as illustrated in figure (2.7).

The phase mask can be used in a way similar to a beam splitter as shown in figure (2.7). The use of a phase mask in this way simplifies the alignment of the fabrication system. In figure (2.7a), the Bragg wavelength can be varied by tuning of the mutual angle, or by varying the UV writing wavelength. Whereas the prism used in the configuration shown in figure (2.7b) can be very compact and stable. Variations of the above scheme have been used to write FBGs.

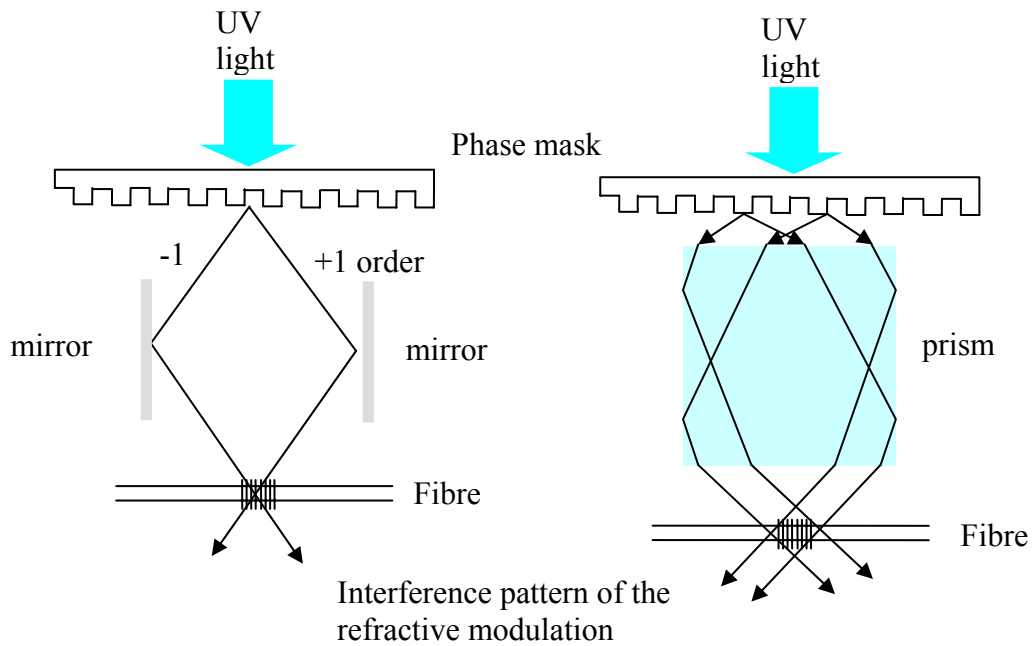


Figure 2.7, Holographic writing technique using a phase mask as a beam splitter a) using mirror and b) using a prism to vary the angle between the two interfering beams.

2.4.3 Chirped FBG fabrication

The previous section dealt with the formation of uniform period FBGs, in which an interferogram of uniform period is created by the intersection of two UV beams. Chirped FBGs require a variation of the period or a variation of the effective refractive index along the length of the grating. Period chirped FBGs may be fabricated by bending [13] the fibre with respect to the interferogram, figure (2.8), where the projection of the interference pattern onto the curved fibre creates a variation in the period. Bending the fibre creates a functional dependence of the grating period upon the radius of curvature, so that a linear or a quadratic chirp may be created. FBGs with bandwidths from 7.5nm to 15nm, and reflectivity as high as 99% have been reported [13].

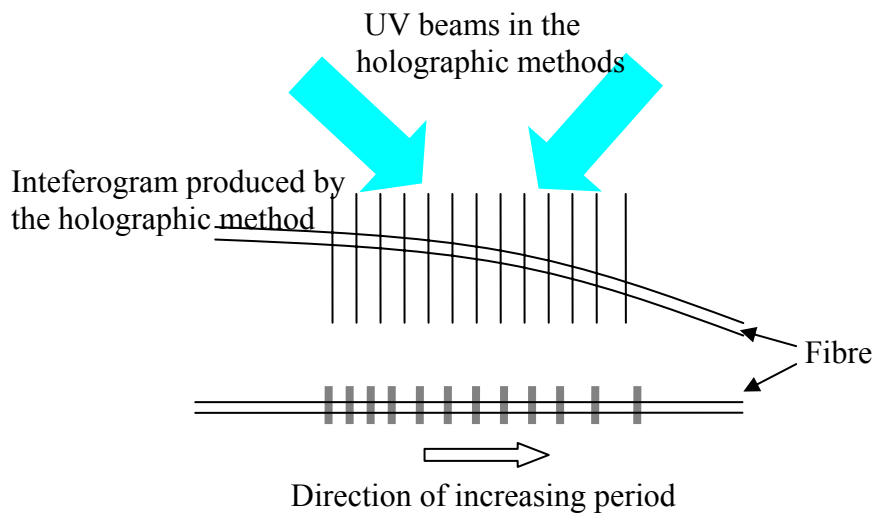


Figure 2.8, shows the configuration for writing linearly chirped FBG by bending the optical fibre [13].

A more flexible technique for fabricating chirped FBGs, which is capable of producing Braggs reflection with wide bandwidth, exploits the interference of beams with dissimilar wavefronts [14]. The setup is shown in figure (2.9).

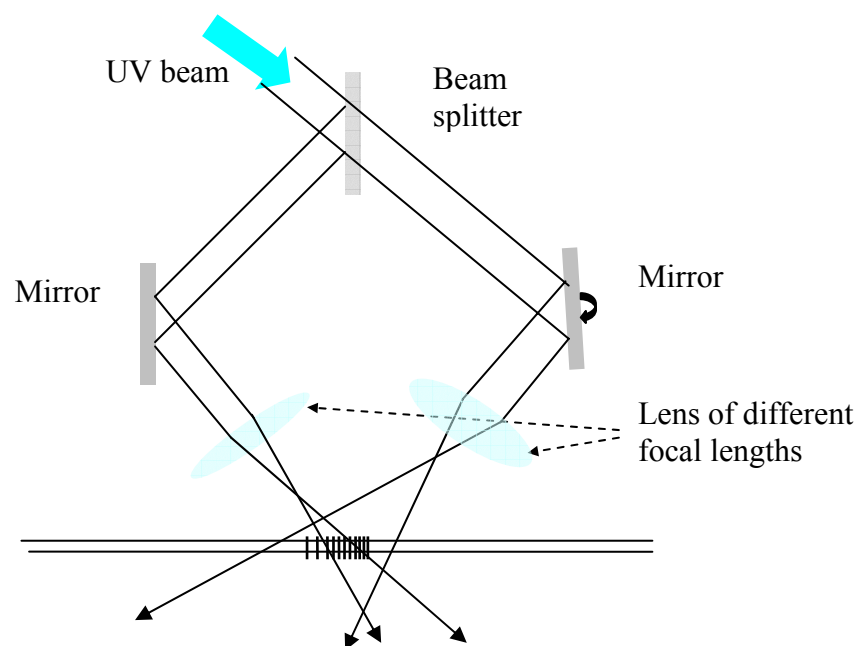


Figure 2.9, writing chirped FBGs with interference of different wavefronts by using lens of different focus at the respective beam paths [14].

By introducing lenses of different focal length into the paths of the 2 beams in the holographic arrangement, the wavefront curvatures will differ at the fibre. When the two beams are brought together to interfere, the resulting interferogram will no longer

have constant period, the period varies as a function of distance along the axis of the fibre. Using this technique, chirped FBGs with bandwidths of $\sim 10\text{nm}$ [15] and 44nm [14] and in excess of 140nm [16], with reflectivities as high as $\sim 80\%$ have been reported.

Phase masks of constant period may also be used to impart chirp to an FBG, as is shown in figure (2.10)[17]. When the fibre is placed parallel to a phase mask, a constant period is inscribed into the core of the fibre. When the fibre is tilted, the period inscribed is a function of the incident angle. The angle of incident of the collimated UV beam can be changed by the introduction of a lens as shown in figure (2.10). The method produces a varying periodicity with grating length and the chirp imposed is determined by the mask's period, the inclined angle α and the characteristics of the lens. Using this technique, an FBG of bandwidth $\sim 6\text{nm}$ has been reported, and a theoretical value of bandwidth of 100nm is possible [17].

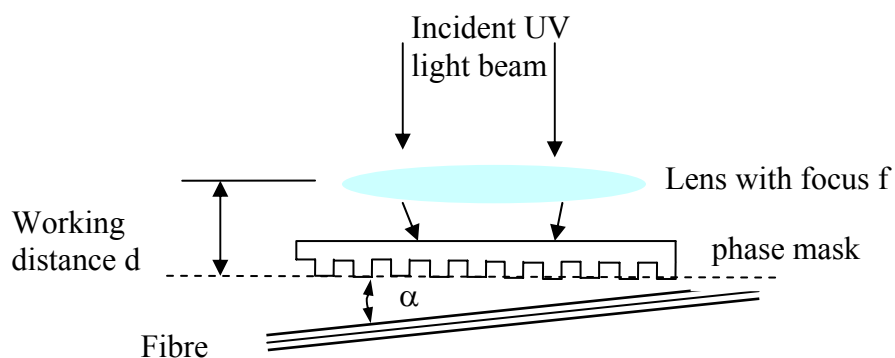


Figure 2.10, shows the configuration for writing a linearly chirp FBG using a uniform phase mask [17].

The phase mask technique is known for its repeatability and ease of use, but suffers from a lack of tuneability of the Bragg wavelength when compared to the holographic method. Chirped phase masks have also been used to inscribe a continuously chirped period FBGs [18]. The chirp phase mask consists of a continuously varying mask period, as is shown in figure (2.11). In this case, the writing process requires the fibre to be in close proximity to the phase mask, but does not require that the fibre is tilted. A bandwidth of $\sim 2\text{nm}$ for a FBG length with length of 5cm has been reported [18].

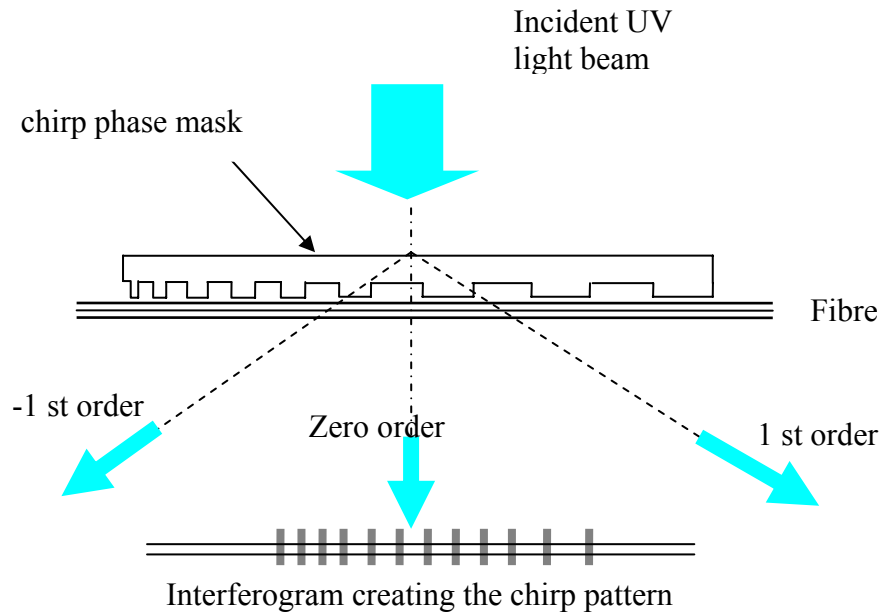


Figure 2.11, illustrations of writing a chirped FBG using a chirped phase mask.

Linearly and non-linearly chirped FBGs have been written using a stepped phase masks [19]. This so called ‘stitched’ phase mask is composed of a series of sections of uniform period, with each section having a different period to its neighbour (step chirp) as shown in figure (2.12).

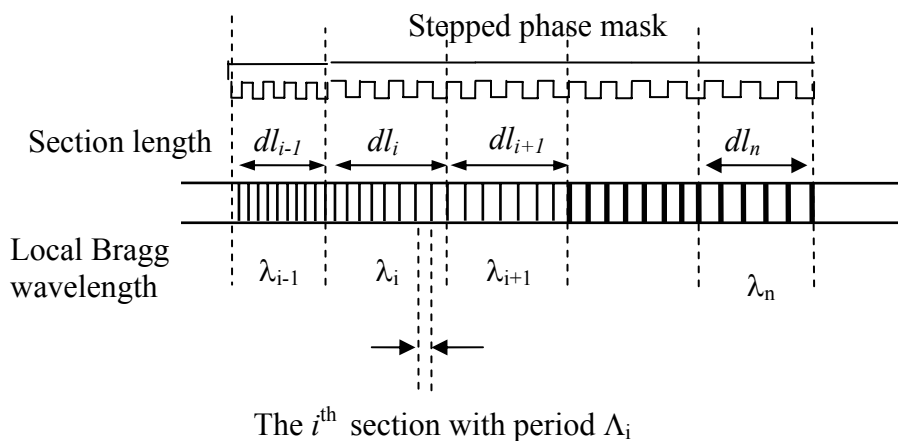


Figure 2.12, an illustration of the stepped chirped FBG produced by using a stepped phase mask. Each section consisted of constant period with a progressively increasing period from section to section [19].

Using this method, gratings with bandwidths of between 0.5nm and 15nm have been fabricated [19]. A stepped chirped grating can also be created by using a simple

stretch and write technique [20]. A uniform phase mask is used with this technique and by shifting the writing beam along the mask while applying a progressively increasing strain to the fibre with every step, gratings with bandwidth of up to 10nm have been demonstrated [20].

Limited tuning of the Bragg wavelength can be achieved in the holographic writing method by pre-stretching the fibre prior to writing, and relaxing following fabrication. This idea can also be used in the fabrication of chirp FBGs. By introducing a non uniform strain profile such as a strain gradient along a uniform grating, chirped FBGs can be created using the same principle. According to equation (2.2), the effect of strain will modulate the effective refractive index and the period, the resonance wavelength at the position along the grating, z is given by [21];

$$\lambda(z) = \lambda_0 + \lambda_0 \xi \varepsilon(z) \quad (2.5)$$

where λ_0 is the Bragg wavelength, ξ is the strain responsivity of the fibre and ε is the local strain. A strain gradient can be imposed by mounting a uniform FBG in a medium, such as an adhesive, with a variable degree of yielding when the adhesive have cured. The two ends of the fibre are loaded with different tension [22], thereby imposing a variation in period along the length of the grating. The central Bragg wavelength shift, which is related to the average of the strain across the grating, is determined by the strain response of the fibre used and the bandwidth is determined by the strain gradient created by the loading and characteristics of the adhesive. A Bragg wavelength shift of 7nm and bandwidths of 0.25nm to 2nm have been demonstrated [22]. Encapsulating a uniform FBG in a tapered elastic plate [23] or mounting on a tapered steel plate [24] where the area of the plate along its' length decreases gradually, will have the same effect when the plate is strained.

The strain gradient can also be achieved by straining a plate with a uniform FBG attached near to a hole drilled in the plate [25]. The deformation due to pressure of a circular diaphragm maybe used to impose a stain gradient [26], as may the use of a the cantilever beam [27, 28, 29, 30 31 32]. By mounting the uniform or pre chirped FBG to the surface of the cantilever, the effect of loading will create a non-linear

change in shape of the cantilever, thus transferring a strain gradient onto the FBG which modifies the period along the FBG's length.

Previous sections have shown that a period chirp can be created by the inscription of a refractive index of modulation of period that varies along the FBG. Chirped FBGs can also be realised by varying the effective refractive index of the propagation mode along the FBG. This may be achieved by changing the guiding properties along the length of the grating such as varying the diameter of the cladding of the fibre to a taper. This tapered fibre can be created by differential etching using a timed chemical etching technique where the fibre becomes a tapered section as shown in figure (2.13). The tapered fibre is designed at which there is a smooth change in the fibre diameter from $125\mu\text{m}$ to a value of $50\mu\text{m}$ over a length of 10mm. By exposing this gradual tapered region to an interferogram generated by the holographic method, a uniform periodic refractive index modulation is imprinted onto the core of the tapered region, thus forming a chirped FBG as shown in figure (2.13). The tapering of the fibre creates a varying mode index along the FBG which together with the uniform periodicity of the refractive index modulation establishes a varying Bragg condition along the FBG's length. Using this method a bandwidth of 2.7nm has been created in a 10mm FBG [33].

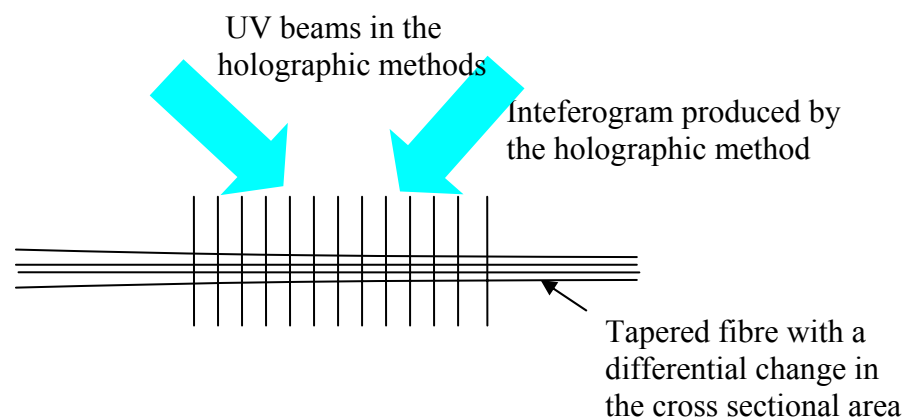


Figure 2.13, chirped FBG created using a tapered fibre[33].

The taper can be created by chemical etching [34, 35] or by stretching the fibre when exposure to the arc of a fusion splicer [36]. Writing a uniform periodic refractive

index modulation in the core of the tapered section then creates the chirped FBG. By stretching the fibre, the differential change in the cross sectional area of the tapered fibre translates this strain to one of differential strain/strain gradient across the FBG, thus modifying the period along the FBG's length. This coupled with the changes to the already varying mode index, via the strain optic effect changes the chirping further. A tuneable total chirp of 4.5 ± 4 nm has been demonstrated in this way [36].

Etching the surface of the fibre surface can modify the refractive index of the mode through the alteration to the propagating properties of the fibre. Etching can also be to directly create a periodic refractive index modification in the core of the fibre. Chirped FBGs have been fabricated with a bandwidth of 20nm over a grating length of 1cm, using the electron-beam etching method [37].

Table 2.1

Methods of creating chirp in FBGs	
method	bandwidth reported
bending the fibre[13]	7.5nm to 15nm
interference of different wavefront[14]	10nm, 44nm and in excess of 140nm
uniform period phase mask tilting fibre [17]	6nm (theoretical 100nm)
chirped phase mask [18]	2nm, 10nm
stepped phase mask [19]	10nm
strain gradient [22, 27,28,29,30,31,32]	0.25-2nm
temperature gradient [38] [39]	0.5nm
taper fibre[33]	2.7nm
direct writing using e-beam etching [37]	20nm

Change in the local temperature changes the Bragg wavelength by modifying both the physical period and the refractive index via the thermo-optic effect. Just as chirp can be created by imposing a strain gradient along the FBG, chirp can also be established by applying a temperature gradient along the grating length [38]. A thermal gradient can be generated by using two peltier thermo-electric elements at either end of a uniform period FBG [39], thus establishing a linear temperature gradient. Using this method the spectral bandwidth of a uniform FBG 0.2nm of a uniform FBG has been

shown to broaden from 0.2nm to 0.5nm with a temperature difference $\sim 70^{\circ}\text{C}$ between the 2 ends of the grating.

2.5 Summary

A brief introduction to the formation of FBG has been provided. When a photosensitive optical fibre is exposed to spatially allocated UV light, a refractive index modulation is induced into the core of the fibre. The operation of a FBG as a mode coupler, causing coupling between the forward and backward modes and promotes the reflection of light which satisfies the Bragg condition. The difference between uniform period FBGs and the chirped FBGs was outlined and their spectral characteristics described. Methods used to inscribe FBGs have been detailed and methods used for fabricating chirped FBGs have been tabulated, table 2.1.

In the theory section that follows, it can be seen that the exact chirp of the FBGs is not so important for the observation of dispersive effect in the FP interferometric response of the cavity. The specification of the chirped FBGs used in this work is mostly constrained by what is practically achievable in the chirped FBG writing process in our laboratory or limited by what is available commercially without incurring great cost. Based upon the finding in the theory sections, low reflectivity in the FBG reflectors in the formation of the FP will give a high visibility on reflections so low reflectivity ($\sim 4\%$) is suffice for the gratings and it is also much more difficult to achieve high reflectivity in chirped FBG in the writing process because of the wide band response of the chirped FBGs.

References:

- 1 K. O. Hill, Y. Fujii, D. C. Johnson and B. S. Kawasaki, 'Photo-sensitivity in optical fiber waveguides: Application to reflection filter fabrication', *App. Phys. Lett.*, **32**, 647-649, 1978.
- 2 K. T. V. Grattan and T. Sun, 'Fiber sensor technology: an overview', *Sensors and Actuators*, **82**, 40-61, 2000.
- 3 G. Meltz, W. W. Morey and W. H. Glen, 'Formation of Bragg gratings in optical fibers by a transverse holographic method', *Opt. Lett.*, **14**, 823-825, 1989.

- 4 T. Blair and S. A. Cassidy, 'Wavelength Division multiplexed sensor Network using Bragg Fibre Reflection Gratings', *Elect. Lett.*, **28**, 1734-1735, 1992.
- 5 C. R. Giles, 'Lightwave Applications of fiber Bragg Gratings', *Journ. of Light Tech.*, **15**, 1391-1404, 1997.
- 6 K. P. Koo and A. D. Kersey, 'Bragg grating-based laser sensors systems with interferometric interrogation and wavelength division multiplexing', *Journ. of Light Tech.*, **13**, 1243-1249, 1995.
- 7 J. A. R. Williams, I. Bennion, K. Sugden and N. J. Doran, 'Fibre dispersion compensation using a chirped in-fibre Bragg grating', *Elect. Lett.*, **30**, 985-987, 1994.
- 8 Y. J. Rao, 'Recent progress in applications of in-fibre Bragg grating sensors', *Optics and Lasers in Engineering*, **31**, 297-324, 1999.
- 9 R. Kashyap, *Fiber Bragg Gratings*, Academic Press, chapter 4, 153, 1999.
- 10 J. Mora, J. Villatoro, A. Diez, J. L. Cruz and M. V. Andres, 'Tunable chirp in Bragg gratings written in tapered cored fibers', *Optics Comm.*, **210**, 51-55, 2002.
- 11 J. Kwan, S. Chung, Y. Jeong and B. Lee, 'Group Delay tailored Chirped fiber Bragg Gratings Using a Tapered Elastic Plate', *IEEE Photon. Tech. Lett.*, **14**, 1433-1435, 2002.
- 12 S. LaRochelle, V. Mizrahi, K. D Simmons and G. I. Stegeman, 'Photosensitive optical fibers used as vibration sensors', *Optics lett.* **15**, 399-401, 1990.
- 13 Sugden, I. Bennion, a. Moloney and N. J. Copner, 'Chirped grating produced in photosensitive optical fibres by fibre deformation during exposure', *Elect. Lett.*, **30**, 440-441, 1994.
- 14 M. C. Farries, K. Sugden, D.C. J. Reid , I. Bennion, A. Molony and M. J. Goodwin, 'Very Broad reflection bandwidth (44nm) chirped fibre gratings and narrow bandpass filters produced by the use of an amplitude mask', *Elect. Lett.*, **30**, 891-892, 1994.
- 15 R. W. Fallon, L. Zhang, A. Gloag and I. Bennion, 'Identical broadband chirped grating interrogation technique for temperature and strain sensing', *Elect. Lett.*, **33**, 705-707, 1997.
- 16 G. E. Town, K. Sugden, J. A. R. Williams, I. Bennion and S. B. Poole, 'Wide-Band Fabry-Perot-Like Filters in Optical fiber', *IEEE Photon. Tech. Lett.*, **7**, 78-80, 1995.

-
- 17 Y. Painchaud, A. Chandonnet and J. Lauzon, 'Chirped fibre gratings produced by tilting the fibre', *Elect. Lett.*, **31**, 171-172, 1995.
 - 18 A. E. Willner, K. M. Feng, J. Cai, S. Lee, J. Peng and H. Sun, 'Tunable Compensation of Channel Degrading effects Using Nonlinearly Chirped Passive fiber Bragg Gratings', *IEEE Journ. of Selected Topics in Quant. Elect.*, **5**, 1298-1311, 1999.
 - 19 R. Kashyap, P. F. McKee, R. J. Campbell and D. L. Williams, 'Novel method of producing all fibre photoinduced chirped gratings', *Elect. Lett.*, **30**, 996-998, 1994.
 - 20 K. C. Byron and H. N. Rourke, 'Fabrication of chirped fibre gratings by novel stretch and write technique', *Elect. Lett.*, **31**, 60-61, 1995.
 - 21 S. Huang, M. M. Ohn and R. M. Measures, 'Phase-based Bragg intragrating distributed strain sensor,' *Applied Optics*, **35**, 1135-1142, 1996.
 - 22 P. C. Hill and B. J. Eggleton, 'Strain gradient chirp of fibre Bragg gratings', *Elect. Lett.*, **30**, 1172-1174, 1994.
 - 23 J. Kwon, S. Chung, Y. Jeong and B. Lee, 'Group Delay Tailored Chirped Fiber Bragg Gratings Using a Tapered Elastic Plate', *IEEE Photon. Tech. Lett.*, **14**, 1433-1435, 2002.
 - 24 Y. Zhu, P. L. Swart and B. M. Lacquet, 'Chirp tuning of a fiber Bragg grating by using different tapered transducers and loading procedures: an application in the accelerometer', *Opt. Eng.*, **40**, 2092-2096, 2001.
 - 25 M. LeBlanc, S. Y. Huang, M. Ohn and R. M. Measures, 'Distributed strain measurement based on a fiber Bragg grating and its reflection spectrum analysis', *Optics Lett.*, **21**, 1405-1407, 1996.
 - 26 C. Chang and S. T. Vohra, 'Spectral broadening due to non-uniform strain fields in fibre Bragg grating based transducers', *Elect. Lett.*, **34**, 1778-1779, 1998.
 - 27 R. M. Measures, M. M. Ohn, S. Y. Huang, J. Bigue and N. Y. Fan, 'Tunable laser demodulation of various fiber Bragg grating sensing modalities', *Smart. Mater. Struct.*, **7**, 237-247, 1997.
 - 28 P. L. Fuhr, S. J. Spammer and Y. Zhu, 'A novel signal demodulation technique for chirped Bragg grating strain sensors', *Smart. Mater. Struct.*, **9**, 85-94, 2000.
 - 29 Y. Zhu, P. Shum and C. Lu, M. B. Lacquet, P. L. Swart, A.A. Chtcherbakov and S. J. Spammer, 'Temperature insensitive measurements of static displacements using a fiber Bragg grating', *Optics Express*, **11**, 1918-1924, 2003.

-
- 30 C. S. Goh, S. Y. Set, K. Taira, S. K. Khijwania and K. Kikuchi, 'Nonlinearly Strain-Chirped Fiber Bragg Grating with an Adjustable Dispersion Slope', *IEEE Photon. Tech. Lett.*, **14**, 663-665, 2002.
 - 31 X. Dong, B. guan, s. Yuan, X. dong and H. Tam, 'Strain gradient chirp of uniform fiber Bragg grating without shift of central Bragg wavelength', *Optics Comm.*, **202**, 91-95, 2002.
 - 32 Z. Wei, L. Qin, H. Li, Q. Wang, W. Zheng and Y. Zhang, 'Fabrication of high quality chirped fiber Bragg grating by establishing strain gradient', *Optical and Quant. Elect.*, **33**, 55-65, 2001.
 - 33 K. C. Byron, K. Sugden , T. Bricheno and I. Bennion, 'Fabrication of chirped Bragg Gratings in Photosensitive fibre', *Elect. Lett.*, **39**, 1659-1660, 1993.
 - 34 L. Dong, J. L. Crux, L. Reekie and J. L. Archambault, 'Tuning and chirping fiber Bragg Gratings by Deep Etching', *IEEE Photon. Tech.*, **7**, 1433-1435, 1995.
 - 35 M. A. Putnam, G. M. Williams and E. J. Friebele, 'Fabrication of tapered , strain-gradient chirped fibre Bragg gratings', *Elect. Lett.*, **31**, 309-310, 1995.
 - 36 J. Mora, J. Villatoro, A. Diez, J. L. Crux, and M. V. Andres, 'Tunable chirp in Bragg gratings written in tapered core fibers', *Optics Comm.*, **210**, 51-55, 2002.
 - 37 C. Yang, S. Yazdanfar and J. Izatt, 'Amplification of optical delay by use of matched linearly chirped fiber Bragg gratings', *Optics Lett.*, **29**, 685-687, 2004.
 - 38 S. Barcelos, M. N. Zervas, R. I. Laming and D. N. Payne, 'Interferometric fibre grating characterization', *IEE Colloquium on Optical Fibre Gratings and Their Applications (Digest No.1995/017)*, p5/1-7, 1995.
 - 39 A. D. Kersey and M. A. Davis, 'Interferometric fiber sensor with a chirped Bragg grating sensing element', *Proc. of SPIE*, **2360**, 319-322, 1994.

3 Review of FBG sensors and filters

3.1 Introduction

An FBG consists of a refractive index modulation formed inside the core of an optical fibre. The FBG creates diffraction phenomena when light propagating in the fibre core interacting with the FBG. The interaction with the propagating wave allows the coupling of the forward mode to the backward mode with characteristics depending on the properties of the FBGs. The distinguishing feature of FBGs is the flexibility to achieving desired spectral characteristics of the reflected and transmitted wave. FBGs are simple devices and they are found in key applications such as sensor elements [1], partially reflective mirrors for the formation of fibre Fabry-Perot (FP) interferometers [2] and as wavelength filters [3]. The reflected spectral bandwidth of the uniform period FBGs generally lies in the range $\sim 0.02\text{nm}$ to 0.3nm [4] but bandwidths of up to 1.5nm [5] have been reported. The bandwidth of the reflected spectra can be increased considerably by chirping the FBGs achieved through a positional dependence of the period or mode refractive index. This broadband response can increase the operational bandwidth of FBG when employed as a reflective element in, for example an intrinsic FP interferometer. Chirped FBG may also be used to impose dispersion on wavelengths lying within the bandwidth, as the Bragg condition changes as a function of the position along the grating length, so that different components of the light travel different distances. For the past decade, an intense research effort, and large body of published material, has been devoted to the use of FBG as sensors and telecom devices, they have been thoroughly reviewed [6, 7, 8, 9,10,11,12].

3.2 Uniform FBG sensors

Fibre sensors are usually classified as either extrinsic or intrinsic. Extrinsic sensors carry light to and from some non-fibre element that modulates the light response to the measurand perturbation, whereas intrinsic sensors have the sensing element as the integral part of the fibre itself. FBGs belong to the latter as the interaction of the

measurand with the fibre perturbs the characteristics of the FBG, and thus of the light propagating within its sensing region.

Optical sensor systems involving a FBG sensing element usually work by injecting the output from a spectrally broadband source into the fibre. The resulting signal on reflection has a narrow band spectral component at λ_B the Bragg wavelength. The transmission spectrum is the complement of the reflection as shown in figure (3.1). A FBG operates as a bandpass filter in reflection and notch filter in transmission.

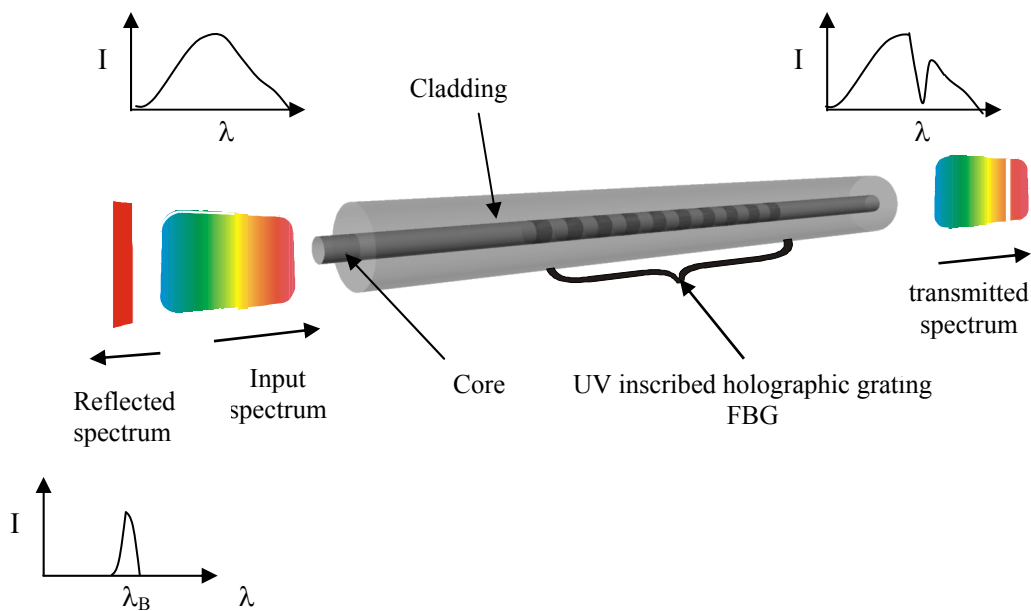


Figure 3.1, shows a schematic diagram of a FBG illustrating that only the wavelength of light, λ_B , that satisfies the Bragg condition, is reflected.

The use of these elements as a sensor is derived by the ability of these FBGs to shift the wavelength through the change in Bragg condition, equation (2.1). Under the influence of strain or temperature, the modulation of the FBG parameter will manifest itself through a change of the resonance condition and thus produce a shift in the Bragg wavelength. A simple illustration of the effect of the change in the physical dimension of the FBG on the spectra of the FBG is shown in figure (3.2).

The perturbation arising from strain or temperature changes the geometry and the effective refractive index of the propagating mode of the FBG through the elasto-optic

and thermo-optic effects. This in turn creates a different coupling condition for the propagating modes, and the interaction of the FBG with the light will give different characteristics. Under the influence of strain and temperature, the sensor responds via a shift in the Bragg wavelength, $\Delta\lambda_B$ according to,

$$\Delta\lambda_B = 2n\Lambda \left[\left\{ \frac{1}{\Lambda} \left(\frac{d\Lambda}{d\varepsilon} \right) + \frac{1}{n} \left(\frac{dn}{d\varepsilon} \right) \right\} \Delta\varepsilon + \left\{ \frac{1}{\Lambda} \left(\frac{d\Lambda}{dT} \right) + \frac{1}{n} \left(\frac{dn}{dT} \right) \right\} \Delta T \right] \quad (3.1)$$

where $\Delta\varepsilon$ is the applied strain, n is the effective refractive index of the propagating mode, Λ is the grating period and the ΔT is the temperature change.

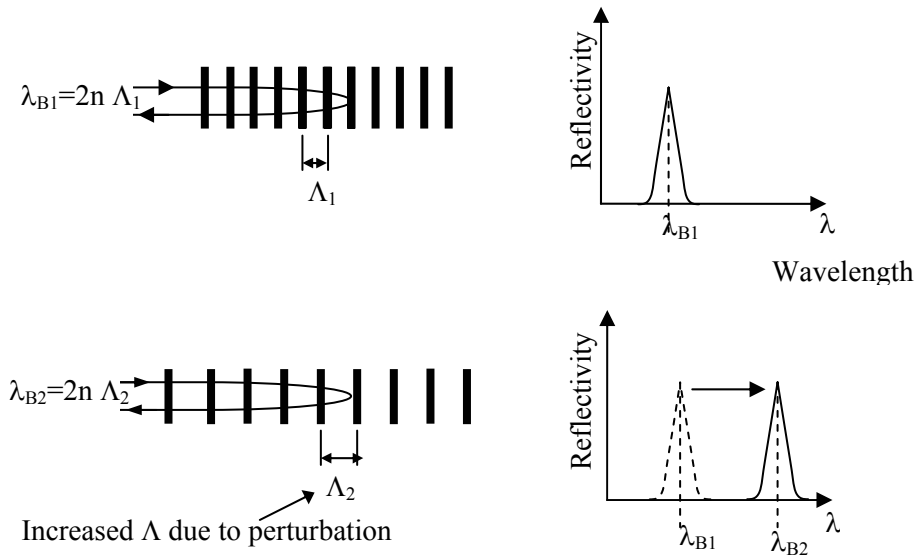


Figure 3.2, shows a schematic effect of perturbed FBG response with the corresponding wavelength shift.

The strain response arises from both the physical elongation of the grating, thus the corresponding fractional change in Λ , and from the change in the mode refractive index due to $\left(\frac{dn}{d\varepsilon} \right)$, the photo-elastic effect. The thermal response arises from the thermal expansion of the fibre material and the temperature dependence of the mode refractive index $\left(\frac{dn}{dT} \right)$, the so called thermo-optic effect. The thermal response is dominated by the thermo-optic effect, which accounts for 95% of the observed wavelength shift [7].

Equation (3.1) can be separated into the strain and temperature contributions [7]:

$$\Delta\lambda_B = \Delta\lambda_\varepsilon + \Delta\lambda_{\Delta T}$$

where

$$\Delta\lambda_\varepsilon = \lambda_B(1-p_e)\Delta\varepsilon \quad \Leftrightarrow \quad \frac{d\lambda}{d\varepsilon} = \lambda\xi$$

and

$$\Delta\lambda_{\Delta T} = \lambda_B(\alpha + \zeta)\Delta T \quad \Leftrightarrow \quad \frac{d\lambda}{dT} = \lambda\zeta \quad (3.2)$$

where, $p_e \sim 0.22$ [10], is the photo-elastic coefficient for fused silica, ξ is strain responsivity with a typical value of $0.75\varepsilon^{-1}$. α is the thermal expansion with a typical value of $0.55 \times 10^{-6} \text{ }^\circ\text{C}^{-1}$ [13], $\zeta \sim 6.67 \times 10^{-6} \text{ }^\circ\text{C}^{-1}$ [1] is the thermo-optic coefficient and ζ is the temperature responsivity with a typical value of $8.3 \times 10^{-6} \text{ }^\circ\text{C}^{-1}$ [13], for germanium-doped fibres. Table (3.1) summarizes the temperature and strain sensitivities represented in the text.

Table 3.1 Strain and temperature response of FBGs at different wavelengths

wavelength range, λ	$d\lambda/d\varepsilon$	$d\lambda/dT$
800nm	$0.52 \text{ pm}/\mu\varepsilon @ 820 \text{ nm}$ [14] $0.67 \text{ pm}/\mu\varepsilon @ 837 \text{ nm}$ [15]	$6.64 \text{ pm}/^\circ\text{C}$ [13] $7.4 \text{ pm}/^\circ\text{C}$ Corning Flexicore@824 [16] $4.3 \text{ pm}/^\circ\text{C}$ Andrew PM@833nm [16] $7.36 \text{ pm}/^\circ\text{C} @ 837 \text{ nm}$ [13] $6.35 \text{ pm}/^\circ\text{C} @ 810 \text{ nm}$ [17]
1300nm	$1.0 \text{ pm}/\mu\varepsilon$ [18]	$8.67 \text{ pm}/^\circ\text{C}$ [13] $10.85 \text{ pm}/^\circ\text{C}$ [19]
1550nm	$1.15 \text{ pm}/\mu\varepsilon$ [20]	$10.45 \text{ pm}/^\circ\text{C} @ 1533 \text{ nm}$ [21] $13 \text{ pm}/^\circ\text{C}$ [16]

The exact value of the thermal and strain response depends on the composition of the fibre used. The composition of the fibre and a built in strain during the FBG inscription [22], can have influence on the material characteristics. The strain response is temperature dependent [23,24] but remains constant from room

temperature to around 500 °C [25] whereas the temperature response is very much constant (room temperature to ~200°C but increases in value at high temperature [10].

One of the most significant limitations facing the wide scale deployment of FBG sensors in real world application is their simultaneous sensitivity to both temperature and strain. The application of the FBG sensors can be complicated by the complicity of strain and temperature especially in the measurement of quasi-DC strain in engineering environments. Temperature variations along the fibre path can lead to anomalous thermal apparent strain readings. A number of techniques for overcoming this limitation have been reported and demonstrated, including the use of dual wavelength gratings [26], cancellation of the thermal response of the grating [23], the use of a reference grating which is shielded from stain and only measures temperature [27, 28] with the latter technique being perhaps the most widely used. The reference FBGs are kept isolated in a strain free environment but experience the same thermal environment as the active FBG sensor elements [29]. This facilitates the separation of the FBG response due to temperature.

3.2.1 FBG Sensor systems

The FBG sensor systems are useful for a variety of applications, in particular smart structures[30], where FBGs are embedded into the structural material to allow real time evaluation of load, strain, temperature, vibration etc. for in-service and real-time monitoring of the integrity of the measurement of structural components. They can also be found in various applications such as strain measurement [31,32,33], temperature [34, 35], vibration [36], acceleration [37], ultrasound [38, 39], magnetic field [40] and pressure [41, 42]. They can also be used as optical filters, for tuning the lasing wavelength of laser diode [43] and reflectors in fibre Fabry-Perot etalon filters and interferometers. FBGs have also been deployed in routing [44], filtering control and amplification of optical signals [45], as feedback element in fibre lasers [46], and in dispersion compensation [47].

FBG sensor systems rely upon the measurement of the measurand induced shift in the Bragg wavelength. The detection of the shift in the measurement of λ_B allows the

magnitude of the measurand to be determined. This is done by injecting a broadband light into the fibre which contains the FBG, and monitoring the change in the λ_B as shown in figure (3.3).

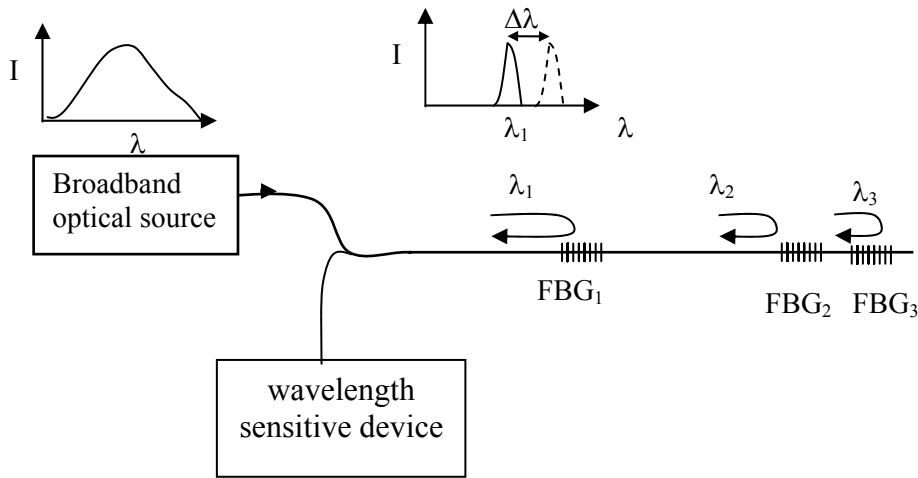


Figure 3.3, illustrates a basic wavelength division multiplexed FBG based sensor system with reflective detection.

3.2.2 Interferometric demodulation

The sensitivity of the FBG sensor system can be increased using interferometric detection. Unbalanced interferometers, such as the Mach-Zehnder (MZ) [48] can be used. This processing interferometer serves as a wavelength sensitive element and converts the shift in wavelength of the optical signal into a change of phase of the interferometric signal, producing a cosinusoidal intensity output with change in wavelength as shown in figure (3.4).

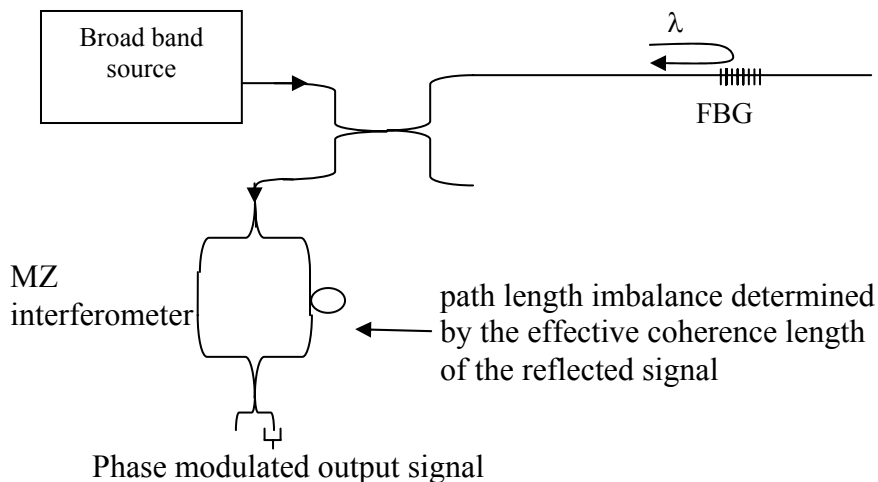


Figure 3.4, illustration of the grating sensor system with interferometric wavelength discrimination using an unbalanced MZ

The sensitivity of this wavelength readout device is limited by the maximum path length unbalance of the MZ, which is determined by the effective coherence length of the reflected bandwidth of the FBGs typically of order 0.2nm [48]. This corresponds to a maximum path length unbalance of $\sim 1\text{cm}$. The phase excursion for a given wavelength shift can be increased by having a larger path length imbalance to the MZ processing interferometer. This is achieved in the demodulation technique which employs a laser sensor concept, where a FBG is used as a feedback element for tuning and linewidth narrowing of a semiconductor laser diode device [43,49] or a pair of matched FBGs are used to form a cavity around a section of Erbium doped fibre [31,50] as shown in figure (3.5).

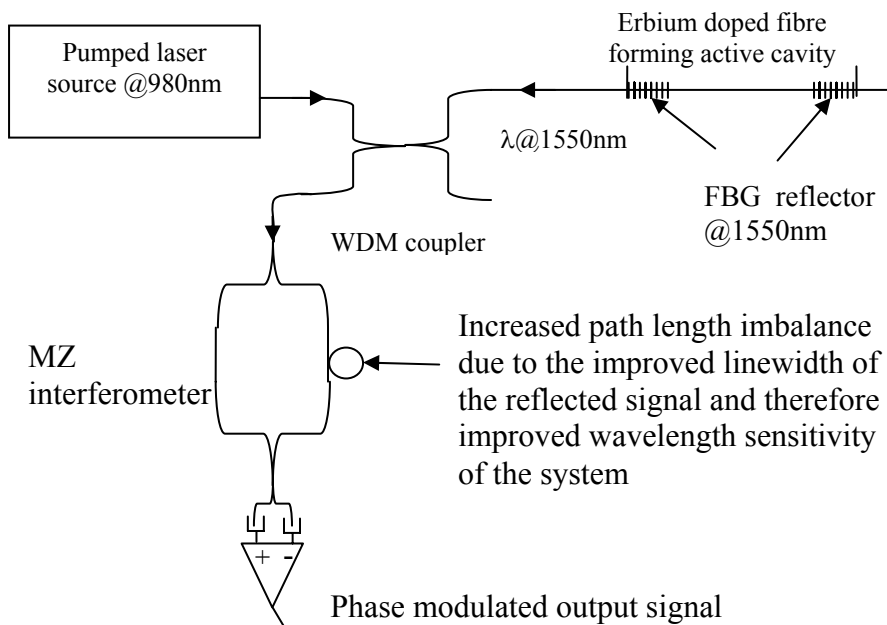


Figure 3.5, illustration of the grating laser sensor system where the wavelength sensitivity can be increased because of the improved signal linewidth.

FBGs are exposed to the measurand field which changes the lasing wavelength. The longer coherence length of the laser allows a longer path length unbalance in the processing interferometer from 1cm to an increased to 96m giving an amplification factor 1920 with an achieved resolution of $5.6 \times 10^{-14} \text{ RMS Hz}^{-1/2}$.

3.3 Linearly Chirped FBG sensors

The uniform FBG acts as a narrow band optical reflector. The characteristics of the narrow spectrum can be varied through external perturbations interacting with the grating and provide a shift in wavelength. When operating as sensors, they can provide real-time strain, temperature and structural integrity information. Chirped FBGs can be used in a similar fashion to provide information on the wavelength shift of the central wavelength. The non-localised Bragg condition of the chirped FBGs gives rise to a variation in the Bragg condition along the grating length. The Bragg condition can be expressed as a function of the position along the grating length given in equation (2.2). Not only do the chirped FBGs offer a broader reflected spectrum of light, but also the position dependence of the Bragg wavelength impose a different time delay to each wavelength component. As the illuminating wavelength increases, depending on the magnitude and the sign of the chirping coefficient, the light propagates further into the grating before reaching its resonant position and undergoing reflection. This effect imposes a varying group delay upon the reflected signal across the spectral bandwidth of the grating as illustrated in figure (3.6).

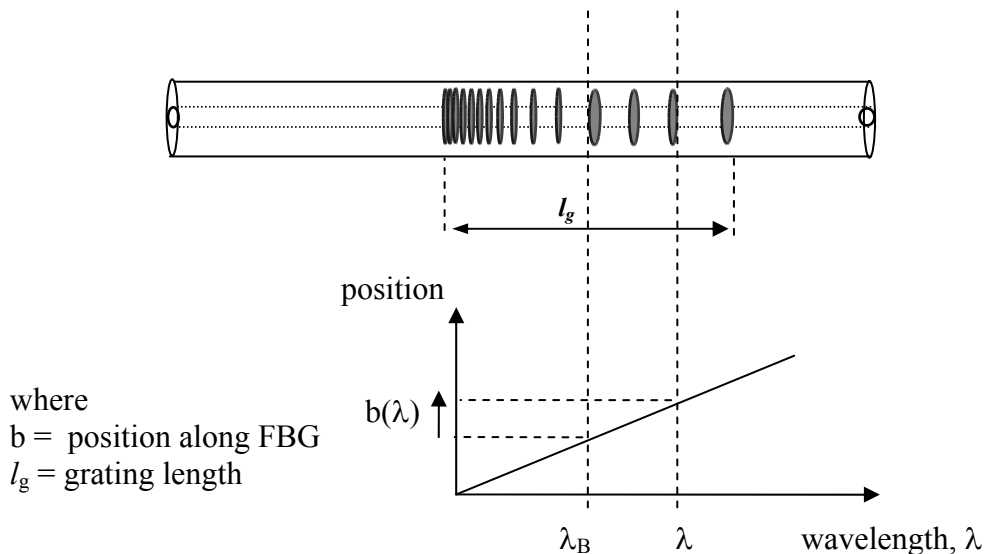


Figure 3.6, illustrates the position dependence of each wavelength component for a linearly chirped FBG with a linear variation of the period.

The wavelength dependent position, $b(\lambda)$, about the centre wavelength, λ_B can be expressed as a linear equation with wavelength [51];

$$b(\lambda) = \frac{\lambda - \lambda_B}{\Delta\lambda_c} l_g \quad (3.3)$$

where $\Delta\lambda_c$ is the total chirp, l_g is the grating length. The difference in distance travelled by each different wavelength creates a time delay. The group delay thus imparted to each wavelength component could be determined by measuring the time elapse for light within the bandwidth of the chirped FBGs to travel to its resonance position, using the time of flight technique [52] as illustrated in figure (3.7). The broadband source is pulsed and the wavelength is selected by a tuneable Fabry-Perot (FP) as shown. The time elapsed between the generation to the detection of the light pulse when it is reflected from its' resonance position, is measured.

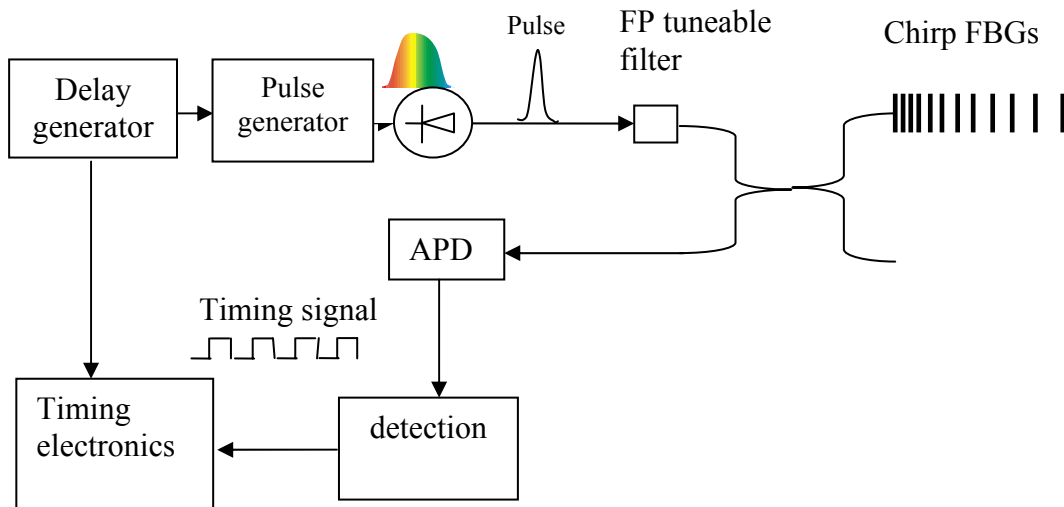


Figure 3.7, shows a schematic of the timed signal for measuring the group delay [52]

The result of this group delay measurement is shown in figure (3.8) and demonstrates that different wavelengths are reflected from different positions along the grating length.

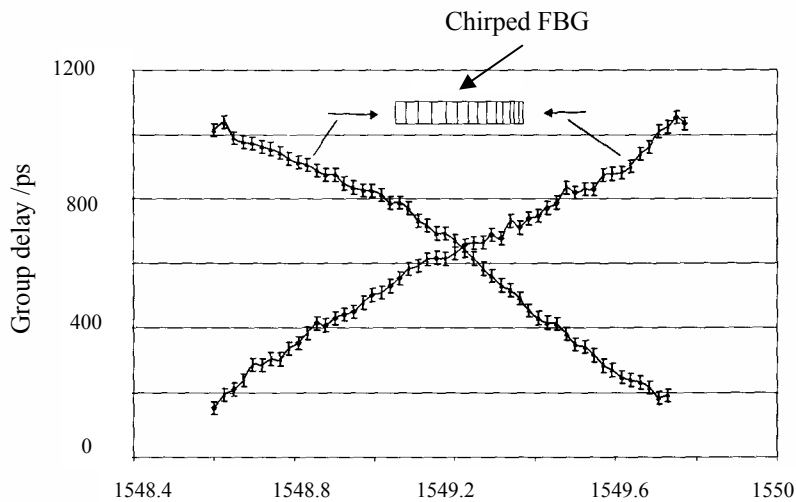


Figure 3.8, the group delay measurement demonstrating the different delay of each wavelength due to the wavelength dependence of the reflection position [52].

Several methods have been used to demonstrate the non localised nature of the reflection of the individual wavelengths. They are either based on direct phase detection using interferometric techniques [53] or using a synthetic wavelength technique [54,55]. In the synthetic wavelength technique, a continuous wave modulation is used to measure the group delay using the synthetic phase information as illustrated in figure (3.9)[55].

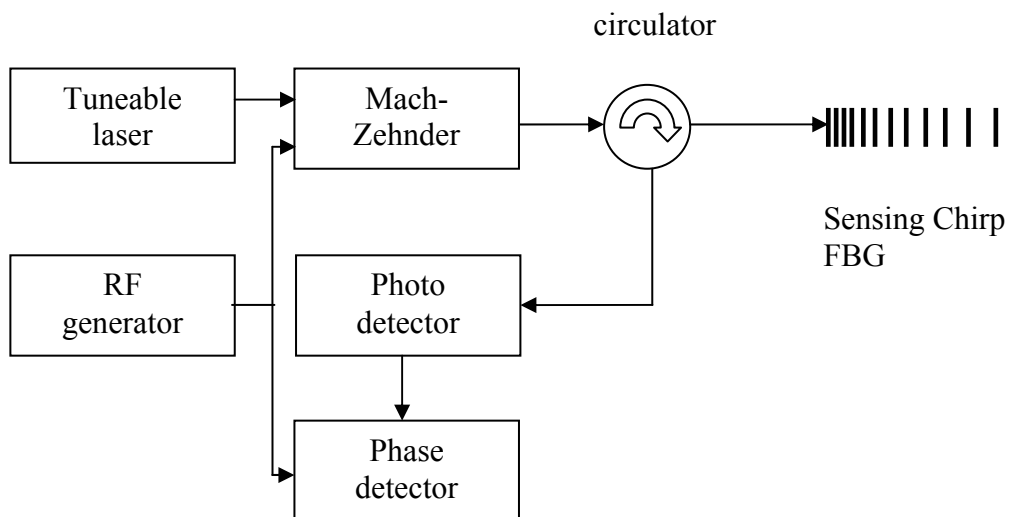


Figure 3.9, Schematic of the synthetic wavelength technique [55] for measuring the group delay

The intensity of the output from the tuneable source operating at a particular wavelength, λ is modulated in the RF frequency range, Ω_s using the MZ modulator. This generates a continuous wave with a synthetic wavelength, Λ_s given by [55];

$$\Lambda_s = \frac{2\pi c}{\Omega_s n}$$

where c is the free space speed of light and n is the refractive index of the material.

The phase of this synthetic wavelength, Λ_s , is detected using a phase detector when light of wavelength, λ is reflected from its respective resonance position. By changing the interrogating wavelength, λ the delay for each wavelength can be mapped out as shown in figure (3.10).

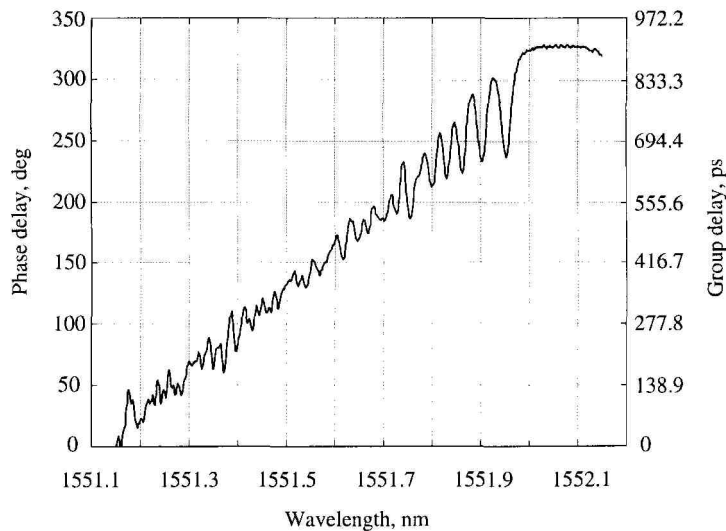


Figure 3.10, illustrates the results of the group delay measurement using the synthetic wavelength technique [55]. The results demonstrate that different wavelength are reflected from different positions along the chirped FBG

The accuracy of the phase measurement technique in determining the group delay depends on the sensitivity of the phase meter and the synthetic wavelength used.

Chirped FBGs offer an attractive solution to the problem of chromatic dispersion in optical fibre systems. A chirped FBG can be used to provide a wavelength dependent delay to the reflected optical signal. In this sense the chirped FBG acts as a dispersive

device where this dispersion or difference in delay of each component can be made to counteract the dispersive effect of the host materials. The wavelength dependence of the reflected position alters the optical path length travelled by each wavelength. The amount of dispersion depends on the shape of the group delay curve which is given by the chirp coefficient of the grating. Dispersion causes broadening [56] in an optical pulse because different wavelengths travel at different group velocities and arrive at different times, which changes the shape of the pulse in time domain. This effect is detrimental in communication systems where data bits will not be resolved. Chirped FBGs have been proposed for dispersion cancellation [57]. Figure (3.11) demonstrates the effect a chirped FBG upon a pulse that has travelled through a dispersive medium.

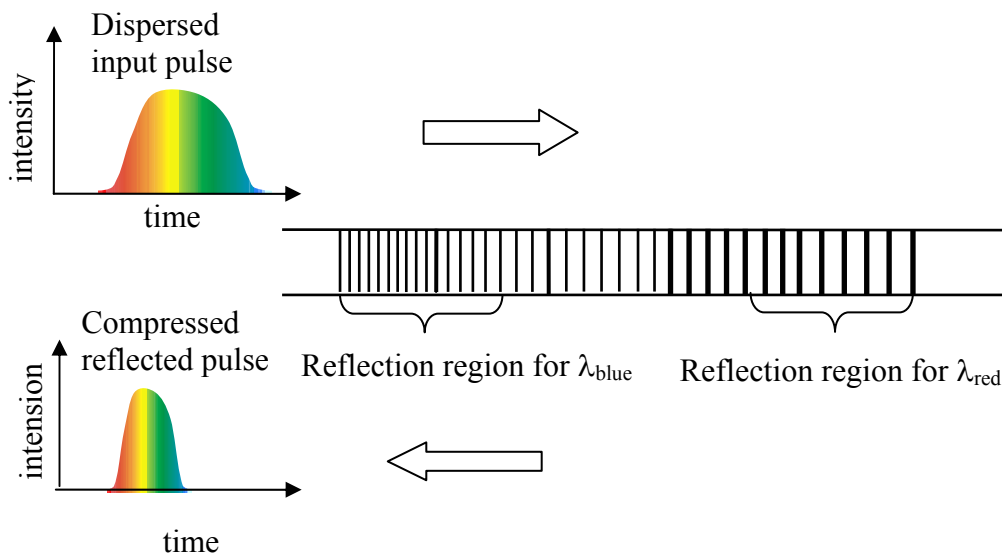


Figure 3.11, illustrates a chirped FBG imparts delay to different wavelength component in a pulse. Depending on the parameter of the chirp FBG, the slower component can catch up with the faster component on reflection, changing the shape of the pulse.

This is achieved by imposing a longer optical path on the leading components of the pulse. Thus the slower component is allowed to catch up with the faster component of the pulse, reshaping it. Chirped FBGs have been demonstrated for pulse compression [58,59,60] in all fibre applications. They allow a large amount of relative group delay to be compensated for in a very compact way. Furthermore, by changing the dispersion slope through the chirp parameters of the FBGs, they can be tailored to

match specific needs. Besides offering wider bandwidth and dispersion cancelling, chirped FBGs can also be used as sensor elements.

When a linearly chirped FBG is subjected to axial strain, there is a redistribution of the period as well as a change in the refractive index due to the photo-elastic effect. If the strain field is uniform, the whole of the chirped bandwidth is simply shifted to the longer wavelength region with increasing strain, figure (3.12). The bandwidth of the reflected spectra remains the same [61], as there is a uniform change of each grating pitch/period and of the refractive index along the grating. This, in accordance with the usual effect of strain/temperature, causes a shift in the Bragg wavelength while the effective bandwidth remains unaffected.

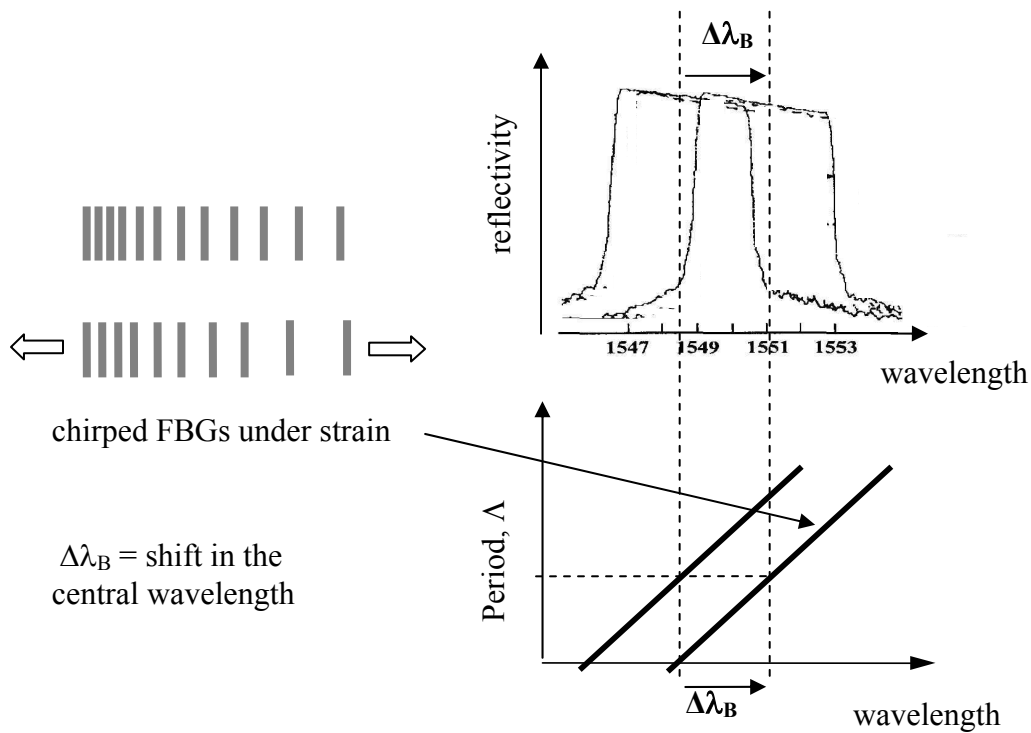


Figure 3.12, the effect of stretching a chirped FBG, showing the shift in the central wavelength, $\Delta\lambda_B$ accompanied by the redistribution of the period. The chirp gradient is constant and thus there is no broadening of the reflected spectrum[61].

The shift of the entire bandwidth of a chirped FBG has been used to detect strain [62]. The interrogation techniques developed for uniform FBGs such as those based on optical filtering and interferometric techniques will no longer be appropriate because of the broad bandwidth of the reflection, which decreases the coherence of the effective source. The technique involving matched gratings as a receiving device to

track the movement of the Bragg wavelength of the reflection from uniform period FBG has been adapted for the use with chirped FBG sensors [62]. The technique involves deliberately mismatching two identical broadband chirped gratings when under the influence of temperature or strain, figure (3.13).

The setup is shown in figure (3.13) where a broadband source is launched into a circulator/coupler. The light is reflected from the sensor and directed to the identical receiving/reference chirped FBG (~10nm). Instead of tracking the wavelength change, the receiver/reference chirped FBG acts as a rejection filter. When no temperature or strain is applied, the correlation function of the two identical chirped FBGs pair will result in a minimum intensity at the detector.

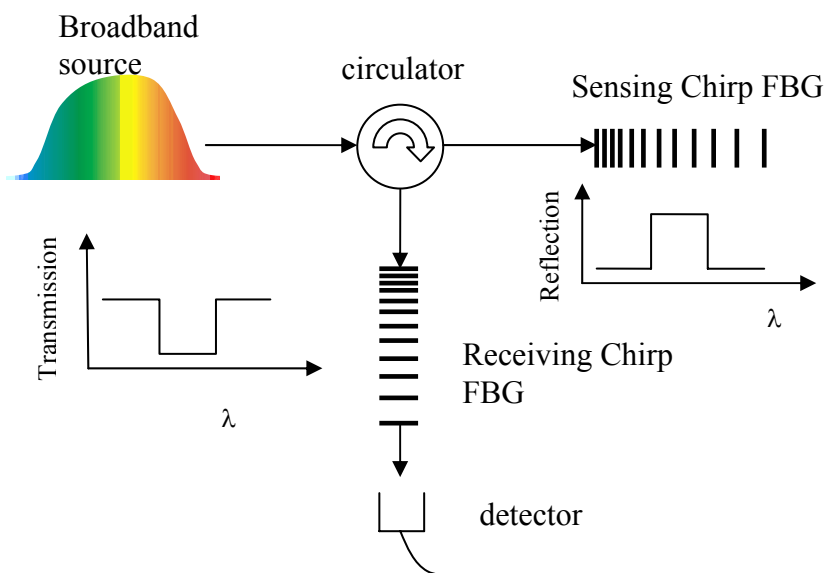


Figure 3.13, Schematic diagram of the identical broadband chirped grating interrogation[62].

When strain or temperature is applied, the shift of the sensor bandwidth (top hat function) will no longer be overlapped with that of the receiver/reference grating's so more light will pass through. As strain and temperature increases/decreases, more power will be detected. The response of the technique is termed, as the cross correlation between the reflection profile of the sensor (top hat function) with the transmission profile of the receiving/reference FBG(inverse of the top hat), will be triangular in shape. The responsivity to strain and temperature of this system will be that of the uniform FBG, namely that of equation (3.2). The dynamic range is given by the bandwidth or the breaking strain of the fibre (~0.1%) which ever comes first.

This enables direct measurement of strain/temperature encoded in transmitted light intensity without the need for a filter or piezoelectric tracking system. The technique has the advantage of being simpler, faster and more cost effective. The system can incorporate more than one sensing/receiving pair, making multiplexing possible [63].

Theoretical studies of FBG filter responses using the coupled mode analysis [64] and the Transfer Matrix Method (TMM) technique [65], have shown that whether chirping is achieved through period or refractive index, the reflection spectrum becomes broadened and the reflectivity decreases with increasing chirp.

Nonlinear/differential strain applied to an FBG has the effect of increasing/decreasing the chirp in the FBG. This is due to the fact that the application of a nonlinear/differential strain along the length, z , of FBG redistributes the pitch/period, Λ , according to the local strain, $\varepsilon(z)$ given by;

$$\Lambda(z) = \Lambda_o(1 + \varepsilon(z)) \quad (3.4)$$

and the effective refractive index is given by;

$$n(z) = n_o(1 - p_\varepsilon(z))\varepsilon(z) \quad (3.5)$$

where Λ_0 and n_0 are the original period/pitch and effective mode index respectively and p_ε is the photo-elastic contribution [10]. Together with the Bragg condition, equation (2.1), the resonance condition can be approximated and becomes dependent on the local strain [66];

$$\lambda(z) = \lambda_o(1 + p_\varepsilon(z))\varepsilon(z) \quad (3.6)$$

The effect of the application of a non-linear/differential strain on a FBG will provide the grating with non-uniform pitch/period. It has been demonstrated, theoretically and experimentally that nonlinear/differential strain will shift the central wavelength and the amount of shift is related to the average strain [67] while the degree of broadening of the reflection profile is related to the strain gradient applied [67,68]. Figure (3.14),

shows the shift of and the broadening of the FBG when a nonlinear strain is applied across it [69]. There is a gradual broadening of the profile as well as the shift of the central wavelength because of the increase in the average strain. Using the dependence of bandwidth on the applied strain gradient, strain has been measured independently of temperature by monitoring the normalised total reflected intensity using a tapered chirped FBG [70] and a period chirped FBG [71], under the assumption that the reflectivity of the chirped FBG remains unchanged under strain, while the profiles broadened.

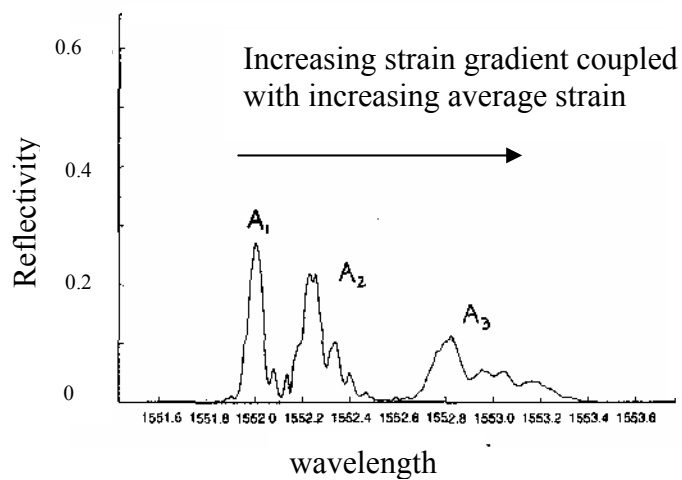


Figure 3.14, illustrates the effect of increasing the strain gradient on the FBG, the effect broaden the spectrum of the FBG as well as shifting the central wavelength due to the increasing average strain [69]

The redistribution of the period under the influence of strain, and the associated modification of the reflected spectrum, has been used in the measurement of disturbances along the grating length. This effect has been used to monitor localised pressure and to locate regions of point forces along the grating length from analysis of the reflection profile [72]. This principle has also been applied to achieve distributed strain measurement along the length of a FBG [73]. Figure (3.15) shows a schematic of this intensity based intra-grating sensing.

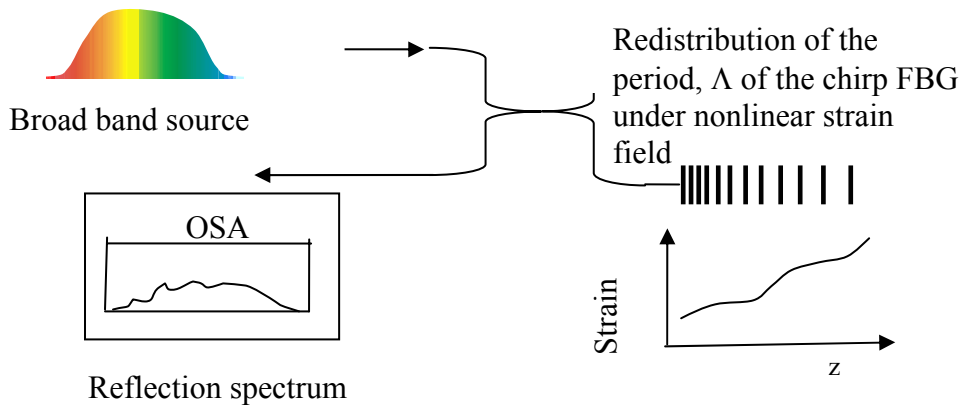


Figure 3.15, Schematic of the intensity based intra-grating sensing [73] where the nonlinear strain field changes the distribution of the period in the Chirp FBG resulting in a modified reflected spectrum.

Under the influence of a non-uniform strain field such as a strain gradient, the pitch/period $\Lambda(z)$ at position, z along the grating will be modified according to the local strain and will be accompanied by an associated change in the effective index $n(z)$. In the studies of filter characteristics [74], the wavelength reflectivity of the chirped FBG is related to the local periodicity of the grating. By analysis of the reflection spectrum, the positional dependence of the phase matching condition can be derived [74]. A differential form of the normalised coupling length (related to the period Λ) is related to the product of the coupling strength, κ and the wavelength reflectivity, $R(\lambda)$ at the phase matching region given by [74];

$$\frac{d\left(\frac{\delta\Lambda}{\Lambda}\right)}{dz} = -\frac{\lambda_0}{2} \frac{|\kappa|^2}{\log\left[1 - R\left(-\frac{\delta\Lambda}{\Lambda}\right)\right]} \quad \text{at } z = z_{(\delta\beta)}$$

where $\delta\beta = \frac{\Delta\beta}{\beta}$ and $\beta = \frac{2\pi}{\lambda}$ is the propagation constant.

From the above relationship, and assuming the coupling strength, κ is constant (related to the amplitude of the refractive index modulation), the period/pitch (and thus the strain field, ε) is determined by the corresponding wavelength, λ by the

Bragg condition and thus the reflection position, z can be written in an integral form using the measured spectral reflectivities [75];

$$z = -\frac{2n_o}{\lambda_o^2 K^2} \int_{\lambda_{\min}}^{\lambda} \ln(1 - R(\lambda)) d\lambda$$

and

for $0 \leq z \leq l_g$

$$z = +\frac{2n_o}{\lambda_o^2 K^2} \int_{\lambda_{\max}}^{\lambda} \ln(1 - R(\lambda)) d\lambda$$

where l_g is the grating length. This provides a relationship between the period, Λ , and thus the local strain field, ε with distance along the grating length z . This method has been used to determine the strain profile around a circular hole in an aluminium plate placed under tension. The method is only valid for monotonically increasing or decreasing strain profiles because of the wavelength reflectivity complicity when wavelength is reflected from more than one point, which will happen when the strain field is not monotonically increasing or decreasing.

3.4 Uniform FBG Fabry-Perot filters

The advent of the holographic method for FBG inscription has made fibre grating devices readily available for the fibre communications and sensing applications. Fibre Fabry-Perot filters are an important component in optical systems, as they are compatible with WDM based fibre communication systems, and may be used as tuneable filters for sensor demodulation. Using a FBG pair to form a fibre FP has been advocated, to allow an increase in the sensitivity of FBG based sensors. The transmission response of such a grating pair FP has been demonstrated to have the FP like characteristics [76] and theoretical analysis has shown that FP cavity resonances will appear within the bandwidth of the FBG [76]. The simplest type of all fibre FP filters is that of a uniform FBG pair inscribed in the fibre core with the length of the cavity determined by the spacing of the FBGs, as illustrated in figure (3.16).

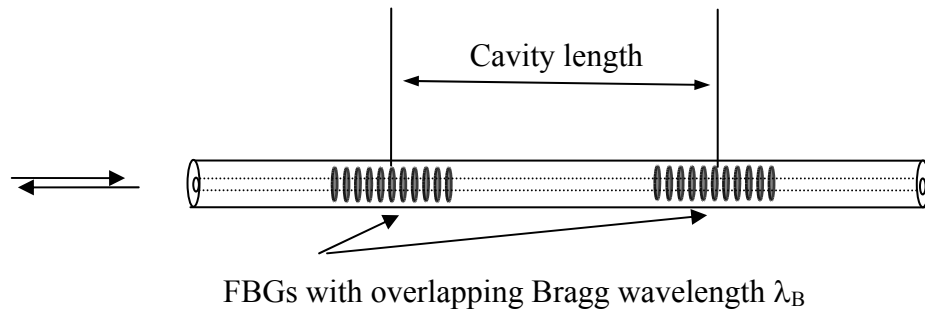


Figure 3.16, diagram showing a uniform FBGs pair forming a fibre FP. The bandwidth of the 2 FBGs overlap in wavelength [76].

High sensitivity can be achieved in this interferometric configuration using phase measurement techniques. Figure (3.17) shows the spectrum of a FP formed by a pair of uniform FBGs (peak reflectivity $\sim 30\%$ @1541.6, bandwidth $\sim 0.3\text{nm}$, written and characterised in-house at Cranfield) with a cavity length of $\sim 5\text{cm}$, giving an equivalent cavity resonance spacing or Free Spectral Range (FSR) of $\sim 0.016\text{nm}$, figure (3.17c).

The wavelength response of uniform FBG FP filters have been theoretical analysed and the predictions compared to experimental values [77]. Their response is identical to that of the bulk FP interferometers, except that the FBG mirrors are distributed reflectors with a narrow band response. The reflectivity of these filters is given by [78];

$$R_{FP} = \frac{4R}{(1+R)^2} \quad (3.7)$$

where R is the reflectivity of the FBG. The FSR/cavity resonance is given by the conventional FP response [78];

$$FSR(\lambda) = \frac{c}{2n_{eff}(\lambda)l(\lambda)} \quad (3.8)$$

where c is the free space speed of light, n_{eff} is the effective refractive index of the mode and $l(\lambda)$ is the cavity length.

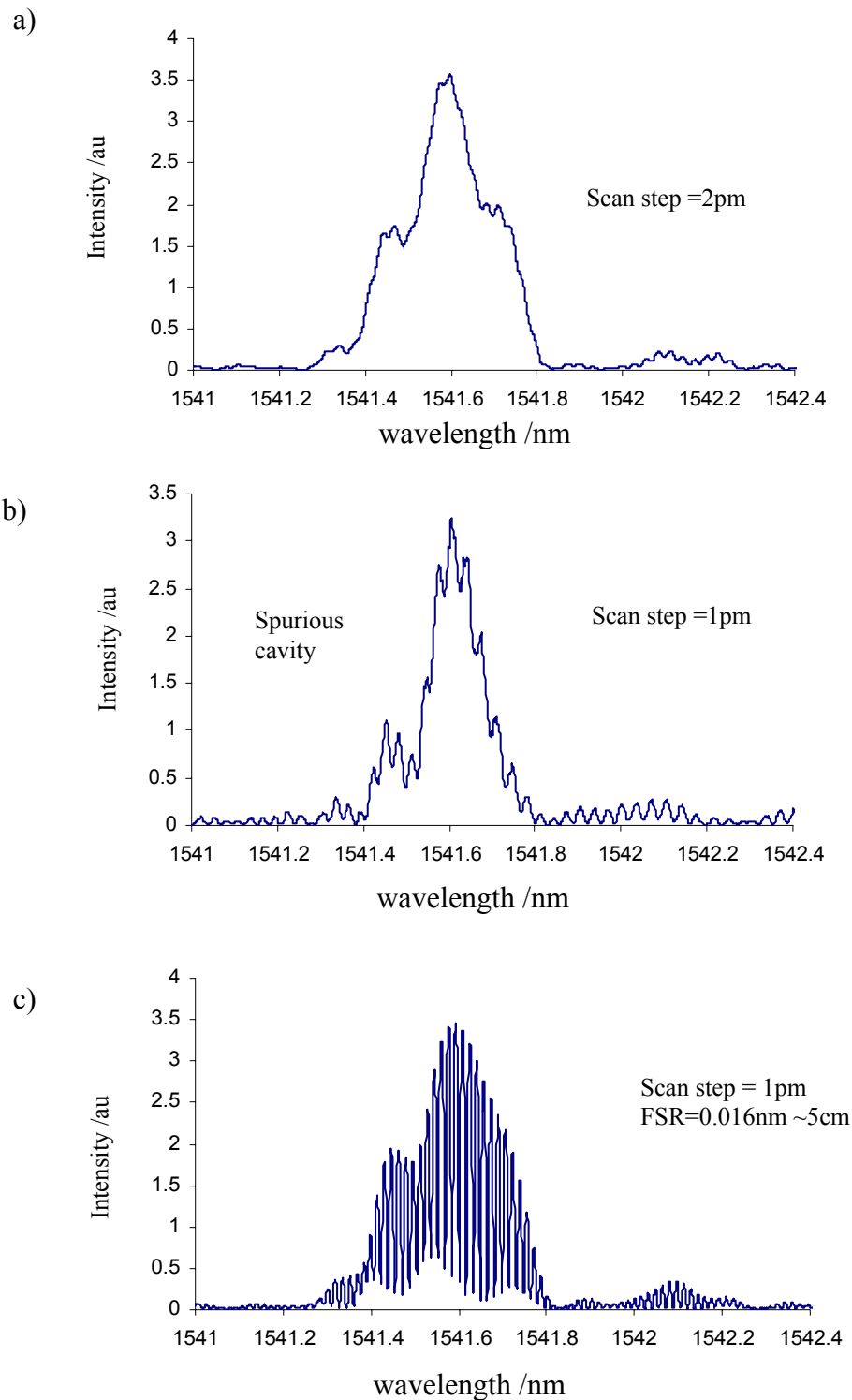


Figure 3.17a), b) shows the spectral profile of the 2 uniform FBGs. The interference fringe in the profile is caused by the result of spurious cavity formed within the interrogation system with a fibre connector. c), the FP spectrum with a cavity length of ~ 5 cm, giving a $FSR = 0.016$ nm. (FBGs are written and FP characterised in-house at Cranfield)

The distributed reflective nature of the FBG modifies the bulk FSR response with off-resonance wavelengths penetrating further into the FBG because they are scattered less, thus experience a longer cavity length than the on-resonance wavelength between the reflection points in the FBGs. An order of 10% variation of the FSR has been observed between the on and off resonance wavelengths [77]. Figure (3.18) shows the predicted reflection spectrum of a uniform FBG FP result, calculated using the Transfer Matrix Method (TMM).

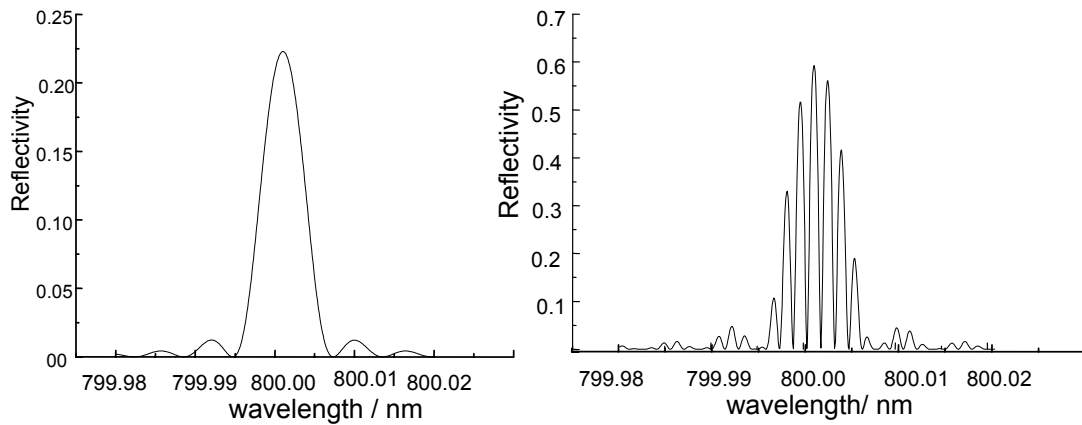


Figure 3.18, the result of the TMM of a FP filter formed between 2 identical uniform FBGs. The FSR/cavity resonance spacing is determined by the cavity length between the gratings centre (The coding of the simulation was done under Matlab which was undertaken for the Phd project).

The multiple bandpass response of the FP resonances has been shown experimentally using a pair of uniform period FBGs to form a FP cavity [78,79]. A FP was formed between 2 uniform FBGs (bandwidth 0.3 nm, peak reflectivity 95.5%) with an overlap of the two FBGs spectrum to within ~ 0.04 nm, with a cavity of length 10cm. The Free Spectral Range (FSR) was 1GHz (~ 6 pm@1300nm) with a finesse of 67 [79]. A finesse as high as 5000 has been reported for such a filter [80]. Similar types of uniform FBG FP filters have been fabricated and the filter response adhere to the conventional Bulk FP response namely that the FSR is inversely proportion to the cavity length, equation (3.8). With stronger gratings and thus higher reflectivity, the visibility improves as in the case of bulk FPs but with these filters the dynamic range is limited by the bandwidth of the uniform FBG reflectors.

The characteristics of the FBG FP filter response can be measured using an optical spectrum analyser (OSA) [78] or by wavelength scanning [79].

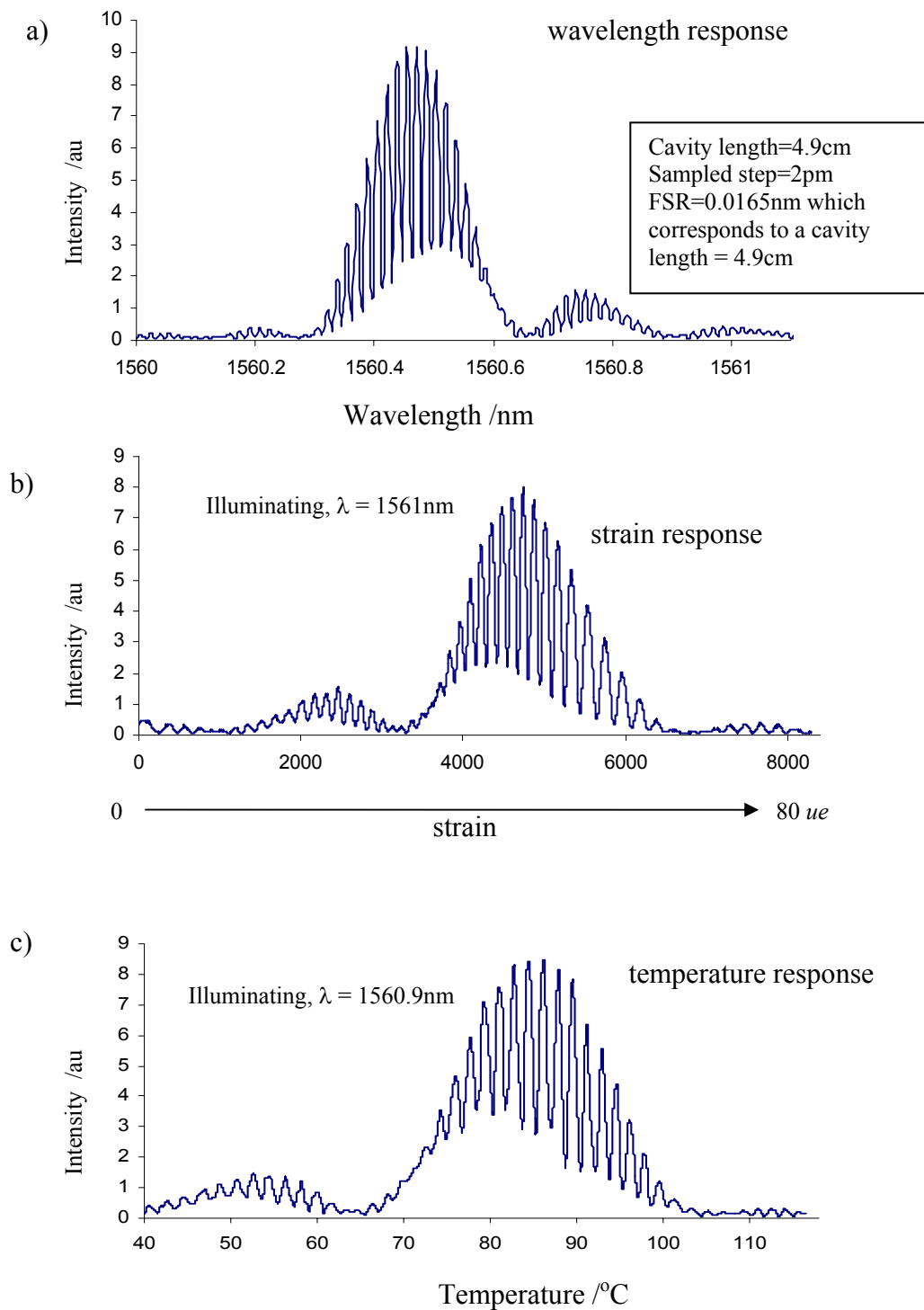


Figure 3.19a) wavelength, b) strain and c) temperature scanning of the same uniform FBGs FP filter formed using 2 FBGs in the region of 1560.5nm. The uneven spacing of the fringes in b) is due to the non-linear scanning of the piezo-actuator used (FBGs are written and FP characterised in-house at Cranfield).

It can also be stretch scanned [79], in which the output from a laser operating at a wavelength in the longer wavelength region of the FBGs' spectra is used to illuminate the FP. The cavity is subjected to axial strain, so that the FBG spectrum is scanned across the laser wavelength, according to the FBGs sensitivity to strain from equation (3.2). The wavelength sensitivity is given by the FSR of the filter which in turn is determined by the cavity length, equation (3.8). The normalised wavelength shift, $\Delta\lambda/\lambda$, of the FBGs is $\sim 74\%$ of the applied strain under tension and this is translated to the equivalent wavelength shift so that the wavelength response can be determined [79]. When stretch-tuned, both the Bragg wavelength and the interferometer fringes shift together at the same rate [79], an effect that is utilised in FBG based laser sensor systems. The same could be achieved by temperature scanning, as is shown in figure (3.19). Figure (3.19a) shows the wavelength response of a uniform period FBG FP formed by 2 overlapping FBG with central wavelength of 1560.5nm, bandwidth $\sim 0.3\text{nm}$ separated by a cavity length of $\sim 4.9\text{cm}$ (written in-house at Cranfield) and figure (3.19b) shows the FP response when the FBG FP is subjected to strain and figure (3.19c) shows the FP response when the FBG FP is experiencing change in temperature.

3.5 Uniform FBG Fabry-Perot sensor

The operation of a uniform FBG FP as a sensor relies on the measurement of the measurand-induced change in the optical length of the interferometer. The change of optical path translates into a change in the phase of the output from the interfering light signal. The operational range is determined by the bandwidth of the overlapping FBGs. As can be seen in the FBG FP's strain and temperature responses, in section (3.4), where the change in the optical path length, due to strain or temperature, is accompanied with the change in phase in the detected interfering signal. Phase measurement demodulation schemes can offer high resolution.

Unlike the use of a FBG as a point sensor, the FBG FP, with a longer cavity length, can be used to average the local strain concentration over the length of the device. The long gauge length FBG FP sensors can be interrogated by scanning the wavelength of the laser [81, 82] and they have been used to monitor the circumferential deforming of concrete structures [82] and to perform temperature measurement [81]. In the later,

the current of a Distributed Feedback (DFB) laser was modulated to provide a wavelength sweep of 0.15nm to interrogate an FBG FP sensor. The cavity, of length 14.5mm (FSR~0.058nm) was formed between two broadband FBGs (1.8nm) [81] thermally enclosed in a controlled environment. The sweep of the laser wavelength produced ~2.6 interferometric fringes. Changes in temperature produced a change in the cavity length, accompanied with the phase change in the interferometric signal, together with the change in visibility because of the shift of the FBG bandwidth with respect to the interrogating wavelength. The change of visibility/amplitude gave a gross indication of temperature change whereas the phase measured provided a high resolution measurement of temperature.

The averaging of strain fields of a structure, for example such as concrete columns in buildings and bridges, requires the use of long gauge length device such as a fibre FP, however FPs with long cavity length suffer from phase noise. A long cavity length sensing fibre FP, formed between a FBG and a reflective end, has been applied to the monitoring of the deformation of concrete columns [82]. The cavity illuminated by a tuneable laser source and interrogated using a reference fibre Michelson interferometer. The length of the path imbalance of the Michelson interferometer is matched to the sensor FP to within 10s of centimetres. When the wavelength is scanned, the interferometric signal is the sum of the signal derived from the long cavities (small FSR, high frequency in wavelength domain) of the FP and the Michelson but also signals from the composite cavities involving the sum (small FSR, high frequency in wavelength domain) and the differences (large FSR, low frequency in wavelength domain) of the two interferometers, and the phase noise involved if the laser suffers from frequency jitter. Using a low pass filter, only the low frequency signal is captured and knowing the length of the reference Michelson interferometer, the extension of the sensing FP is determined [82].

Low coherence interferometry [83,84,85] has been used to interrogate multiplexed FBG FP sensors. This approach reduces interferometric noise and allows high resolution to be achieved. This technique has been deployed to measure strain, temperature and vibration. Figure (3.20) shows the setup of the low coherence interferometry setup which consisted of the sensing interferometer (FBG FP) and a processing/reference interferometer (MZ)[85].

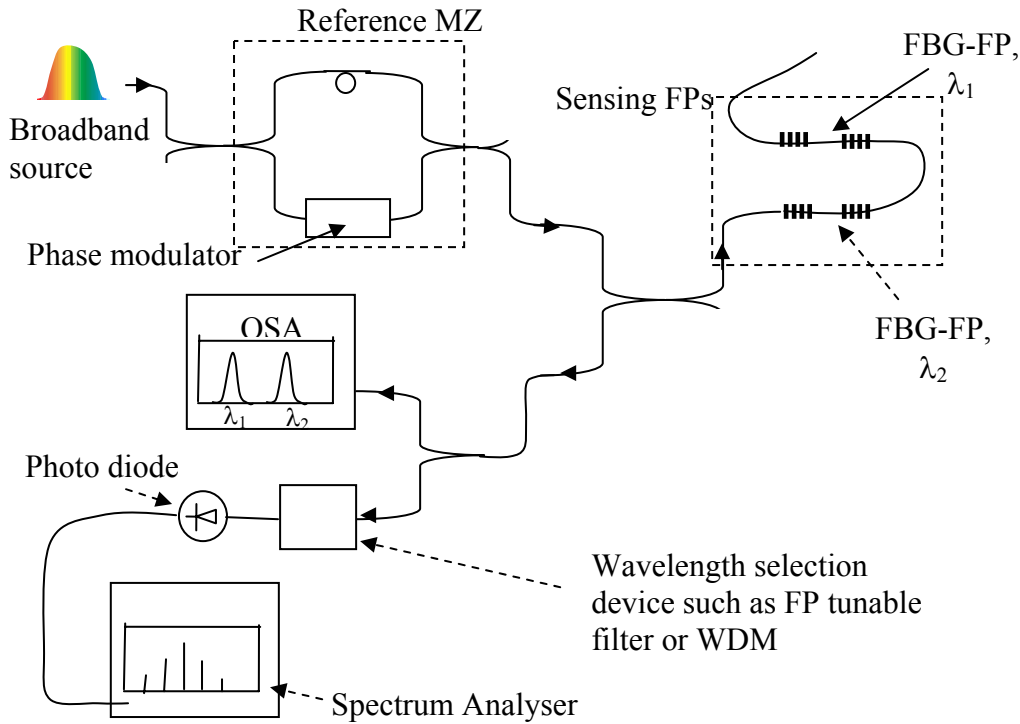


Figure 3.20, schematic diagram of the low coherence interrogation of multiplexed FBG FP formed with different Bragg wavelengths. The path length imbalance of the MZ matches that of the FP to within cm as the effective L_c is determined by the bandwidth of the uniform FBGs ($\sim 0.3\text{nm}$)[85].

By ensuring that the path length imbalance of the reference interferometer is within the coherence length ($\sim 1\text{cm}$) of the FBGs used to form the FPs, interference fringes can be observed at the detector. Quasi-static strain and temperature may be determined by measurement of the shift of the Bragg wavelength of the individual FP pair with the use of an OSA, which has a low resolution (\sim sub nm), so that the interference fringes will not be resolved. This provides a gross measurement. By modulating one arm of the MZ to produce a 2π phase change in the reference MZ, with a serrodyne signal of high frequency, a carrier frequency is created. In this heterodyne signal processing scheme, the carrier is phase modulated by the measurand. A wavelength selection device, such as a FP tuneable filter or a WDM device with a reasonable bandwidth which covers the FBG bandwidth ensures there is no cross talk between the various FBG FPs. Dynamic strain is encoded in the signal with the change in signal phase while the temperature and slowly varying strain is encoded as a change in Bragg wavelength. The magnitude of the vibration is determined by the amplitude of the side-band component about the carrier frequency, as detected by the spectrum analyser. The sensitivities of the FBG FP sensors is determined by the cavity length (FSR) used.

Signal demodulation using the Fast Fourier Transform (FFT) algorithm has been used on multiplexed FBG FPs with various cavity length, but using the same Bragg wavelength bandwidth, such that the signal is collocated in the same wavelength regions[86]. The reflected signal is that of the FBG reflection spectrum modulated by the various FSR created by the different cavities used. The transform of the spectrum will provide information on the FP cavities' spacing.

3.6 Dispersive Bulk type Fabry-Perot filter

Chirped FBGs are dispersive element and when they are used as partial reflectors to form FP, the consequence of dispersion need to be considered. Dispersion causes the different components of wavelength to travel different optical path lengths whether it is through dispersion in material, where the refractive index changes with wavelength, or through a wavelength dependent position of the reflection point such as in the chirped FBG. The dispersion inside the cavity affects the performance of the bulk FP interferometer and parallel can be drawn with the chirped FBG FP.

The bulk optical Fabry-Perot (FP) cavity, figure (3.21) which consists of a pair of optically flat surfaces arranged to form a resonance device has been studied extensively. The two inner surfaces are coated with a highly reflective material. When light enters into the FP etalon, it experiences multiple reflections between the highly reflective surfaces. When the multiple reflections are brought together by a focusing lens, they interfere coherently and narrow fringes are observed. These FP etalons are used in spectroscopy, as spectrometers and filters for wavelength division multiplex (WDM).

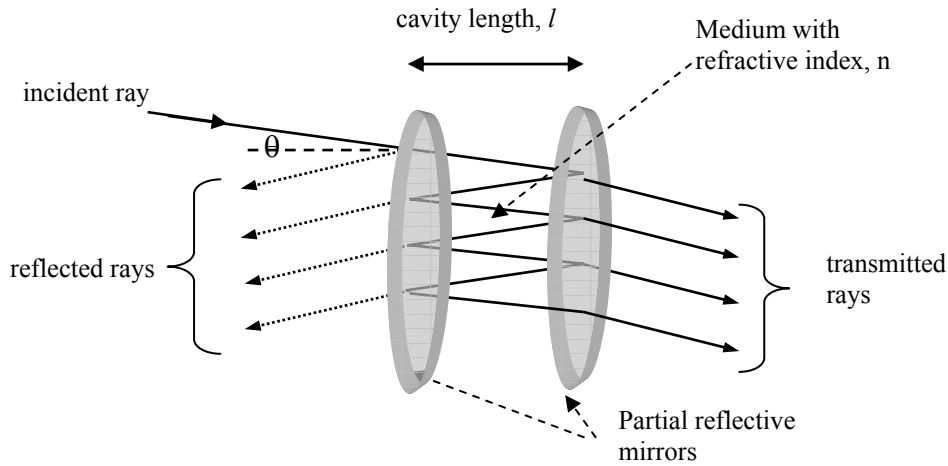


Figure 3.21, Fabry-Perot Etalon

The optical delay incurred by each reflection on traversing the cavity gives rise to an additional phase difference for successive reflections. The total phase difference corresponds to a double passage of the cavity. For a wavelength, λ of a single polarisation at normal incidence, the round trip phase shift (RTPS) of the cavity is given by;

$$\theta_{RTPS} = \frac{4\pi nl}{\lambda} \quad (3.9)$$

where n is the refractive index of the media in the cavity and l is the cavity length. When there is dispersion involved, the change in phase arising from a change in wavelength is given by the differential equation [87];

$$d\theta = \frac{2\pi}{\lambda}(ndl + ldn) - \frac{2\pi nl}{\lambda^2} d\lambda$$

so

$$\frac{d\theta}{d\lambda} = \frac{2\pi}{\lambda} \left(n \frac{dl}{d\lambda} - l \frac{dn}{d\lambda} \right) - \frac{2\pi nl}{\lambda^2} \quad (3.10)$$

For a dispersive material, each different wavelength will experience a different optical path, nl . The dispersion term $\frac{d(nl)}{d\lambda}$ will modify the phase delay for the different wavelengths. When there is no dispersion involved, or it is insignificant, such as in air and in non dispersive fibre, the usual change of phase is derived;

$$\frac{d\theta}{d\lambda} = -\frac{2\pi nl}{\lambda^2} \quad (3.11)$$

When the phase delay is simply an integer multiple of 2π , the reflected waves interfere constructively and when they are of odd multiples of 2π , then they interfere destructively. If the etalon does not contain a dispersive material, then the Free Spectral Range (FSR) is determined by;

$$FSR = \Delta\nu_{FSR} = \frac{c}{2n(\lambda)l} \quad (3.12)$$

The effect of dispersion in the medium within a bulk FP interferometer formed between confocal mirrors, have been analysed by Vaughan et al [88]. The cavity contained a cell holding a vapour of calcium, which has a strong absorption at 423nm, figure (3.22).

Through the Kamers-Kronig relations, the strong absorption region will produce a dispersive effect whereby a large change of refractive index with wavelength, $\frac{dn}{d\lambda}$ will occur [88]. The condition for the on-axis resonance in transmission is given by;

$$p\lambda = 2l(\lambda)n(\lambda) \quad (3.13)$$

where p is the integer order of interference and l and n are functions of wavelength. This is simply a restatement of the fact that an integer multiple number of $\lambda/2$ must fit in the double pass cavity.

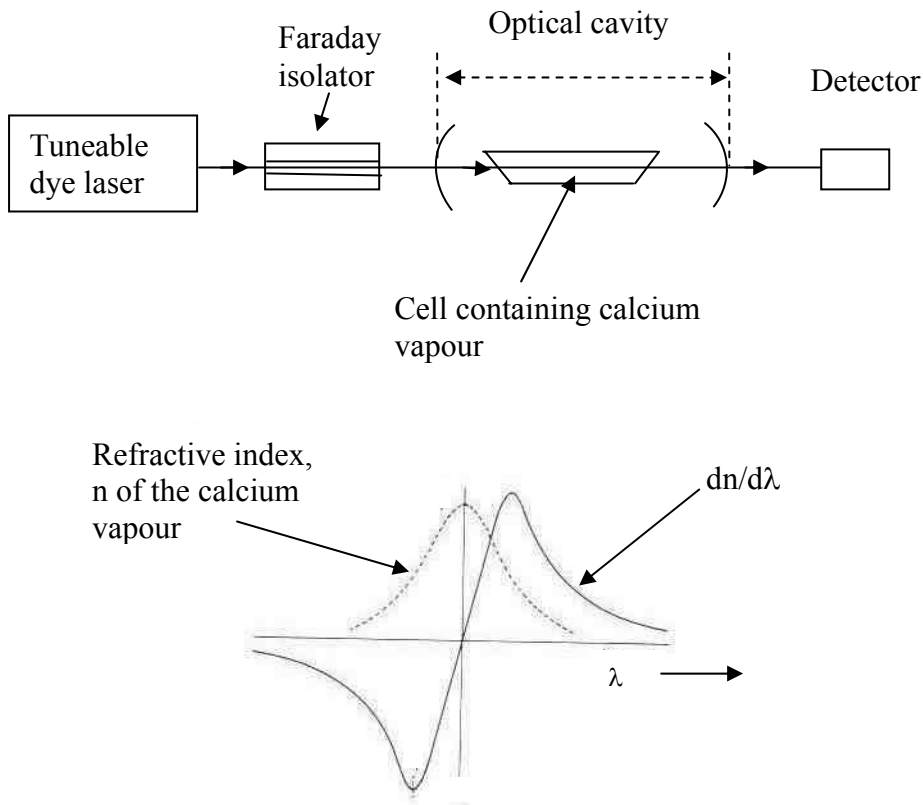


Figure 3.22, illustration of the experiment use to record the frequency response of a bulk FP containing a dispersive material. The inset shows the refractive index together with the index gradient with wavelength [88]

By considering the condition for the onset of next resonance, given that there is no change in length with wavelength (ie. no length dispersion), such that $\frac{dl}{d\lambda}$ is zero, a modification to the FSR by the 1st order of dispersion is given by[88];

$$\Delta\nu_{FSR} = \frac{\Delta\nu_0}{\left(1 - \frac{\lambda}{n} \frac{dn}{d\lambda}\right)} \quad (3.14)$$

where $\Delta\nu_0 = \frac{c}{2nl}$ is the standard definition of conventional FSR in optics, which is cavity length dependent. Away from the strong absorption line, where the dispersion is insignificant, equation (3.14) reduces to (3.12) where;

$$\Delta\nu_{FSR} = \Delta\nu_0.$$

In the region where there is strong absorption, dispersion, $\frac{dn}{d\lambda}$ is significant and the FSR of the dispersive cavity is modified according to equation (3.14). Experiment results have demonstrated that the FSR can change as much as 75% in value, figure (3.23).

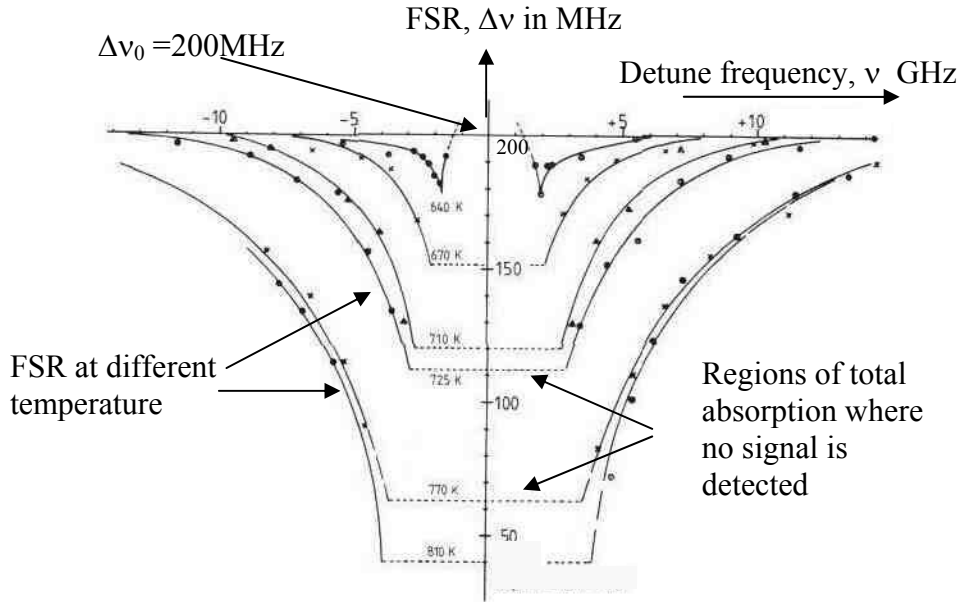


Figure 3.23, experimental measurement of the FSR of a FP cavity containing a dispersive medium. The FSR varied by 75%, depending on the temperature of the cavity [88]

For a dispersive FP with dispersion in refractive index, $\frac{dn}{d\lambda}$, the FSR or the spacing between cavity modes, depends on both n and $\frac{dn}{d\lambda}$, equation (3.14). Analysis of the resonance mode of the spontaneous emission emitted by a semiconductor sample ($\text{GaAs}_{1-x}\text{P}_x$) driven below threshold gives an indication of the FP resonance modes before the onset of a few or single mode operation when lasing. Using the same resonance mode analysis of the FP cavity with a dispersive element, equation (3.14) can be written in terms of wavelength [89];

$$\Delta\lambda_{FSR} = -\frac{\lambda^2}{2n_{eff}l} \quad (3.15)$$

where

$$n_{eff} = n(\lambda) - \lambda \frac{dn}{d\lambda}$$

The emission spectrum of this semiconductor is shown in figure (3.24).

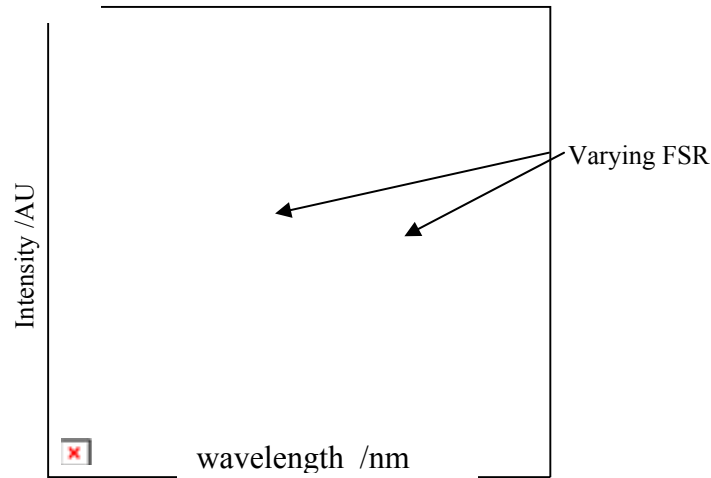


Figure 3.24, the spontaneous emission spectra from $\text{GaAs}_{1-x}\text{P}_x$ driven below threshold, showing varying FSR/resonance mode spacing [89]

The semiconductor has a length of 0.043cm with a refractive index of the material, $n=3.5$ giving the standard FP resonance mode spacing, from equation (3.12), $\text{FSR} = 0.14\text{nm}$. The effect of dispersion modified the FSR, with a measured $\text{FSR}=0.1053\text{nm}$ in the region 648.5-649nm and a larger value of $\text{FSR}=0.1175\text{nm}$ in the longer wavelength region 649.5-650.5nm, as shown in figure (3.24). Using equation (3.15), the effective refractive index of the semiconductor yields a value of $n_{\text{ef}} = 4.65$ and 4.18 respectively compared to the normal value of 3.5 for the material. For a dispersive material FP, the resonance mode spacing is not only determined by the cavity length, l and the refractive index, $n(\lambda)$ alone but the dispersion, $\frac{dn}{d\lambda}$ plays an important role in determining the FSR by modifying significantly the effective refractive index. If the material dispersion modifies the refractive index term in the FSR expression, then it would be expected that length dispersion relevant to the use of chirped gratings to form the cavity, should modify both the effective length of the cavity and the FSR.

To measure the dispersion of an optical fibre, the free space Mach-Zehnder interferometer, shown in figure (3.25) is used [90].

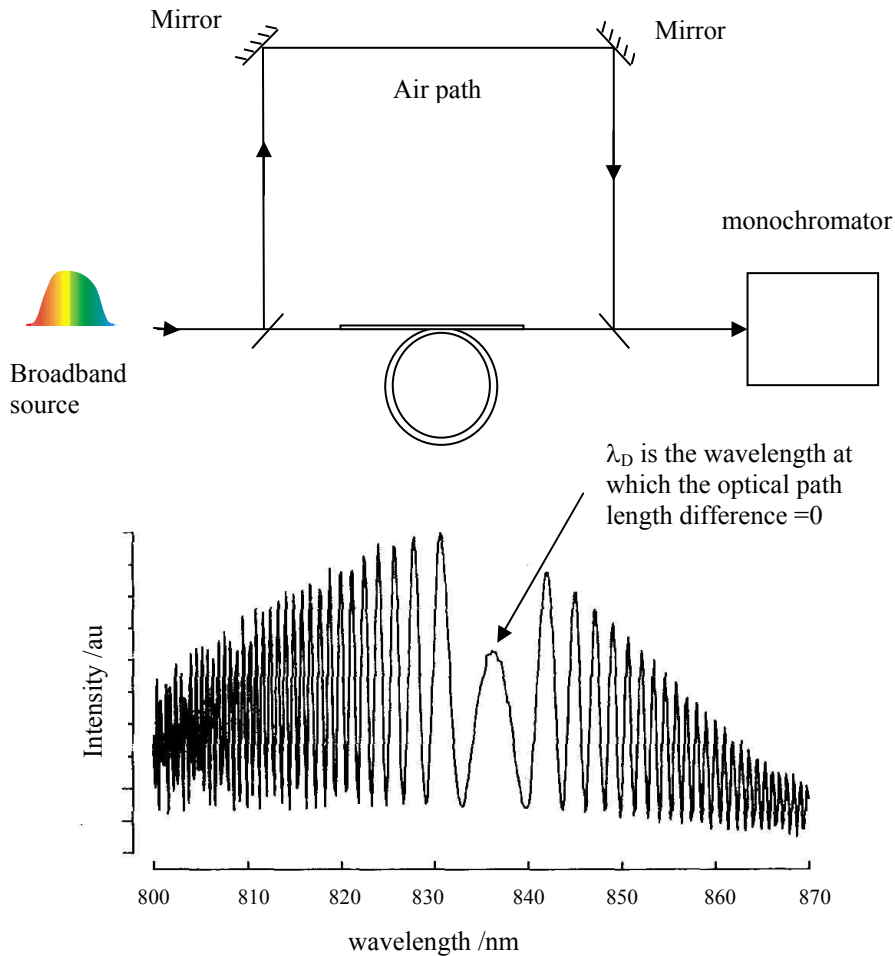


Figure 3.25, Mach-Zehnder interferometer to measure the dispersion of the optical fibre and the results of the wavelength response where there is a change of FSR [90].

The interferometer is illuminated by a broadband source. A length of optical fibre is placed in one path of the MZ and the other path is in free space. A wavelength is selected such that only the material dispersion is significant and the waveguide dispersion is small. At wavelength λ_D , as shown in figure (3.25), the optical length mismatch between the two paths is zero, such that the group delays between the two paths of the interferometer are equal. For all other wavelengths, the group delay will not be balanced and the wavelength response is cosinusoidal with a periodicity increasing on either side of λ_D [90].

3.7 Dispersive Optical delay line interferometer

Bulk optic gratings disperse different wavelength components into a range of angles. This effect may be exploited to shape laser pulses, by exploiting femtosecond Fourier transforms based on the optical delay line techniques[91]. A Rapid Scanning Optical Delay line (RSOD) consisting of a lens placed between a grating and a scanning mirror is shown in figure (3.26).

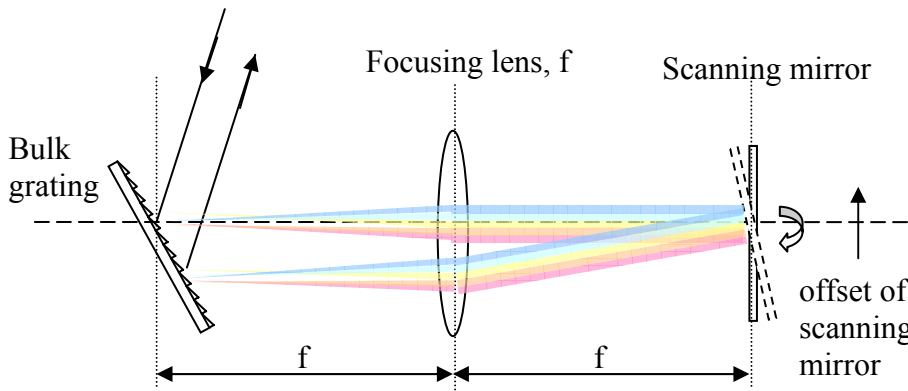


Figure 3.26, diagram of the rapid scanning optical delay line which consists of a bulk grating which transform the light in frequency domain. The lens focuses the dispersed light into the scanning mirror which impart a linear phase ramp to the frequency of the light[91].

Rotating the mirror imparts a time delay to every wavelength component of light which is equivalent to introducing a phase ramp in the frequency domain where, group delay is defined as; $\tau = \frac{d\theta}{d\omega}$. The result is a delay or advance in the time

domain. The wavelength dependent time delay is equivalent to an increase in distance. The RSOD has been used as a scanning element in low coherence interferometry [92,93]. The RSOD is generally used in an interferometric configuration, for example, incorporated in one arm of a Michelson interferometer as the interrogating interferometer. By matching the path length with a sensing interferometer, a large path length mismatch can be scanned in coherence interrogation. The scanning system separates the group and phase delay and allows the control of the carrier frequency (central frequency). When the scanning introduces no dispersion to the system, such as when all the components of the spectrum arrive at the same time, the output traces

out the autocorrelation of the source with a regular carrier frequency. The carrier frequency is determined by the offset of scanning mirror, figure (3.26). When dispersion is introduced, eg. by tilting the grating or moving the lens, the auto correlation traces a broadened spectrum and the carrier frequency varies across the spectrum as the wavelengths components arrive at different time as shown in figure (3.27).

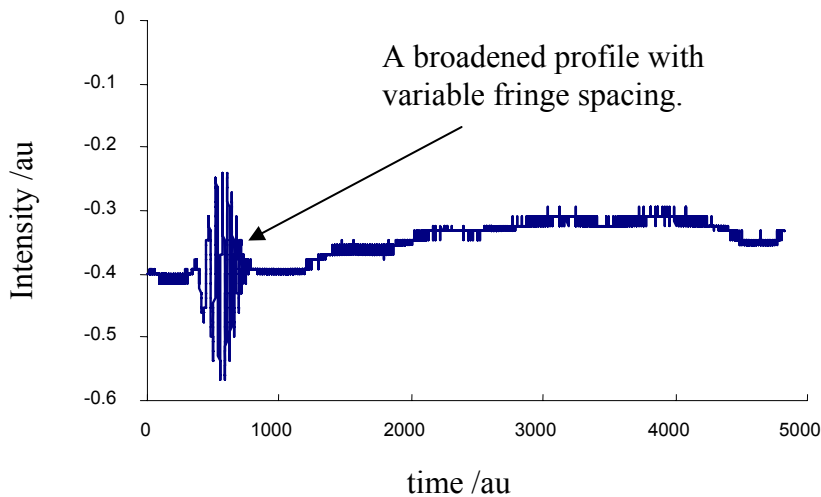


Figure 3.27, Coherent interrogation of a reflective surface using the optical delay line scanning technique. Dispersion causes the broadening of the auto-correlations of the source and also alters the carrier frequency inside the envelope (characterised in-house at Cranfield).

3.8 Chirped FBG Fabry-Perot and Michelson interferometer filter

Although narrow band uniform period FBG FP have been demonstrated, often, a response over a wide bandwidth, is required for dense WDM and wide bandwidth communications systems[94,97,98]. The limitation on the performance of a uniform FBG FP filter is the restriction placed on the operating bandwidth by the limited FWHM of the FBG~0.2nm. The use of chirped FBGs can extend the operating bandwidth much further. The structure of the filter is shown schematically in figure (3.28). The filter consists of two chirped FBGs written in series in an optical fibre, separated by a distance, l , forming a FP resonator. Each grating is linearly chirped in the same direction and acts as a broad band partial mirror. The response of the filter is determined by the strength and the bandwidth of the grating.

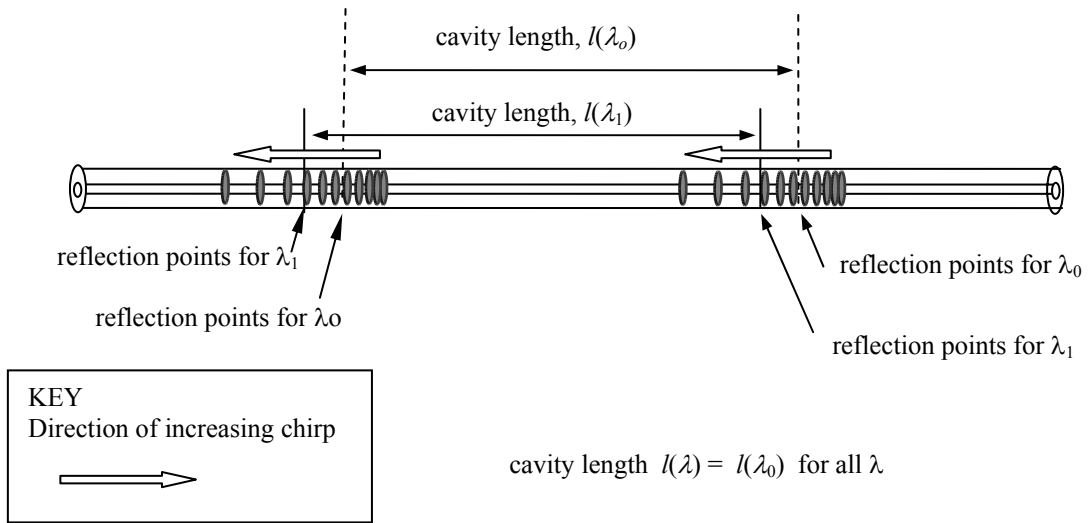


Figure 3.28, Chirped FBG FP filter with chirp oriented in the same direction, such that the cavity length, $l(\lambda)$ is the same for all wavelengths.

Using the FBG FP model developed using the TMM technique, a spectrum consists of the cavity resonance modes within the envelope of the chirped FBG reflection profile, as shown in figure (3.29).

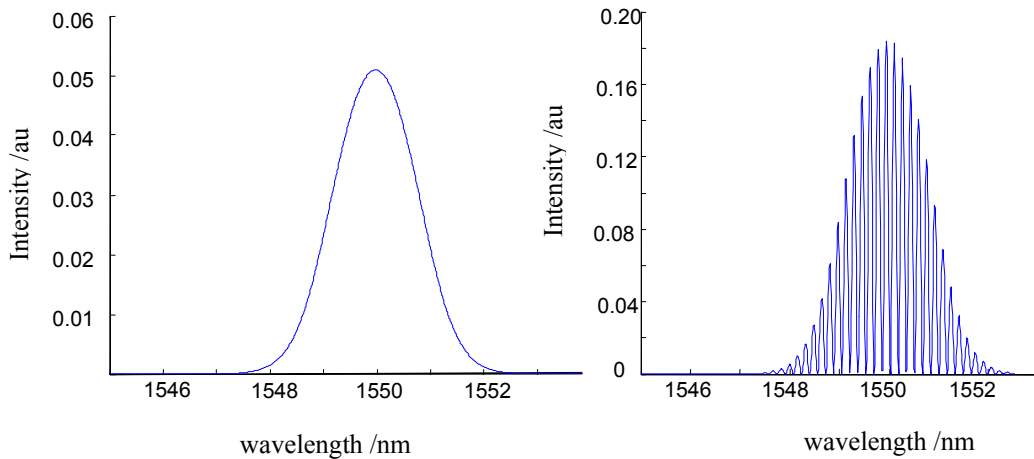


Figure 3.29, shows the reflection profile of the chirped FBG and the spectral response of the chirped FBG FP with the cavity resonance lies within the envelope of the chirped FBG reflection profile, giving a broad band response. The response was calculated using a TMM model of a pair of chirp FBGs (@1550nm, 2mm, 5nm) with a cavity length of 5mm, giving a FSR= 0.16nm.

Such devices have found applications as filters and sensors. A very broadband chirped FBG FP response has been demonstrated [94] and the spectral response is shown in figure (3.30). The filter comprises of two chirped FBGs centred @1550nm with the chirps of the two gratings oriented in the same direction having a grating length of

4mm and bandwidth of 150nm separated with a cavity length of 8mm between the grating centres. The experimental results indicate that a measured value of the FSR of 0.1nm correspond the cavity length of 8mm [94]. When the filter response was measured at wavelength, away from the centre of the chirped FBG reflection band, the spectral characteristics were identical to that at 1536nm with a measured FSR \sim 0.1nm.

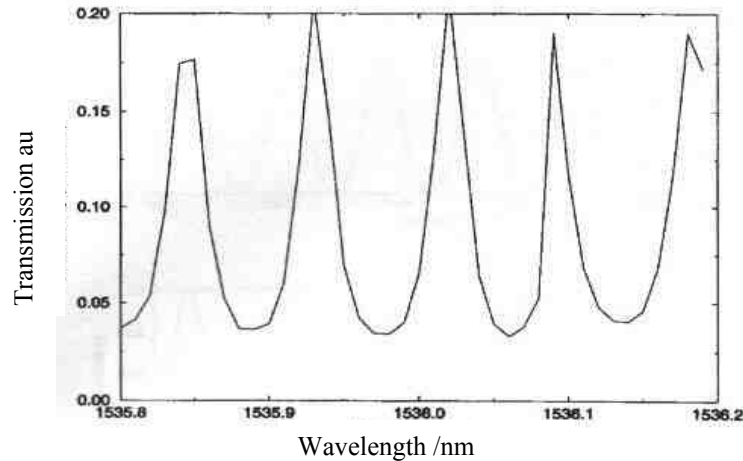


Figure 3.30, shows the measured transmission response of a chirped FBG FP filter with cavity length of 8 mm. The corresponding FSR = 0.1nm over a 0.4nm wavelength range around 1536nm is shown [94]

By arranging chirped FBG FPs in such a way that the chirps of the FBGs are oriented in the same direction, the complex reflectivity of the 1st chirped FBG is the conjugate of the 2nd so that the net dispersion inside the FP cavity will be zero [94]. The round trip phase shift (RTPS) is determined by the cavity length, which in turn is dependent on the location of the reflection points within the two gratings. The cavity length is equal for all wavelengths. Chirped FBG FP cavities formed with the chirp of the FBG oriented the same way behave like conventional FP interferometer where the FSR is given by the corresponding wavelength dependent cavity length.

The broadband/chirped FBGs FP have also been used to form tapped fibre optic transversal filters [95] with cavity length of 150.25mm (FSR=685MHz) and 28mm (FSR=3.7GHz). Making use of the dependence of FSR with cavity length, tuneable FSR cavities have been reported using the multiplexing of the broadband chirped FBG FP. Using 4 chirped FBGs with the first 3 chirped FBGs having bandwidths of

1nm occupying a different wavelength region and the 4th chirped FBG with a bandwidth of 8nm which covered all the wavelength region of the first 3. Using cavity lengths of 20mm, 28.7mm, 5.16mm, with their respective resonance spacing of 5.16GHz, 3.63GHz, and 1.78GHz, have been demonstrated in a single length of an optical fibre for application in microwave signal processing [96].

Theoretical analysis of the FBG FP response using numerical techniques such as the transfer matrix method (TMM) have been reported for the chirped FBG FP with the chirps of the FBG oriented in the same way [94,97]. The models demonstrated the dependence of the FSR on the cavity length. It can be shown that the cavities discussed above all obey the same bulk FSR dependence on the cavity length;

$$FSR = \Delta v_{FSR} = \frac{c}{2nl(\lambda)} \quad (3.16)$$

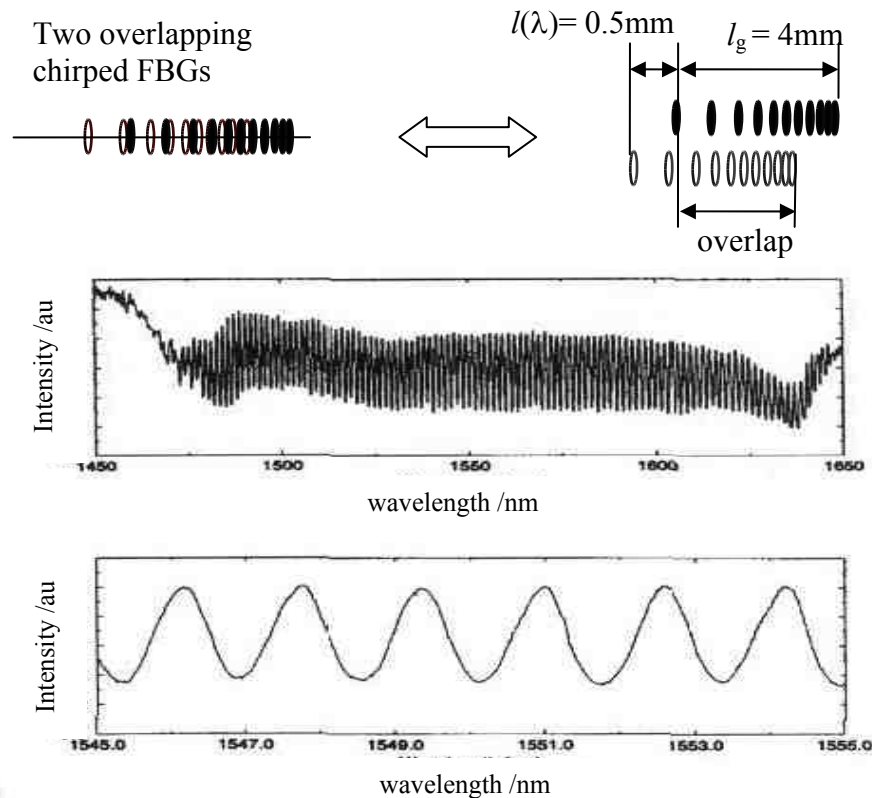


Figure 3.31, measured transmissivity of the chirped FBGs FP filter with the cavity length = 0.5mm. The top trace is for the entire spectrum where the bottom trace shows the same results over a reduced wavelength range. The measured FSR is 1.5nm [94]

To obtain a larger FSR, it is necessary to reduce the cavity length. In the extreme case it is possible to obtain a filter response when the two chirped FBGs overlap [94,98].

An overlapping chirped FBG FP using identically chirped FBGs in the same orientation with one grating displaced w.r.t. the other by 0.5mm has been reported[94]. Figure (3.31), illustrates the spectrum of a cavity formed between overlapping chirped FBGs, where a FSR of 1.5nm is achieved for a cavity length of 0.5mm. The overlapping chirped FBG FP with the chirped FBG oriented in the same way provides a uniform FSR response for all wavelengths, as the cavity length is the same for all wavelengths.

Michelson type filters consist of chirped FBGs with chirps oriented in the same direction have also been demonstrated and the results showed the same FSR response relationship with cavity length [99]. Figure (3.32) shows the configuration of a Michelson interferometer using chirped FBG as partial reflectors.

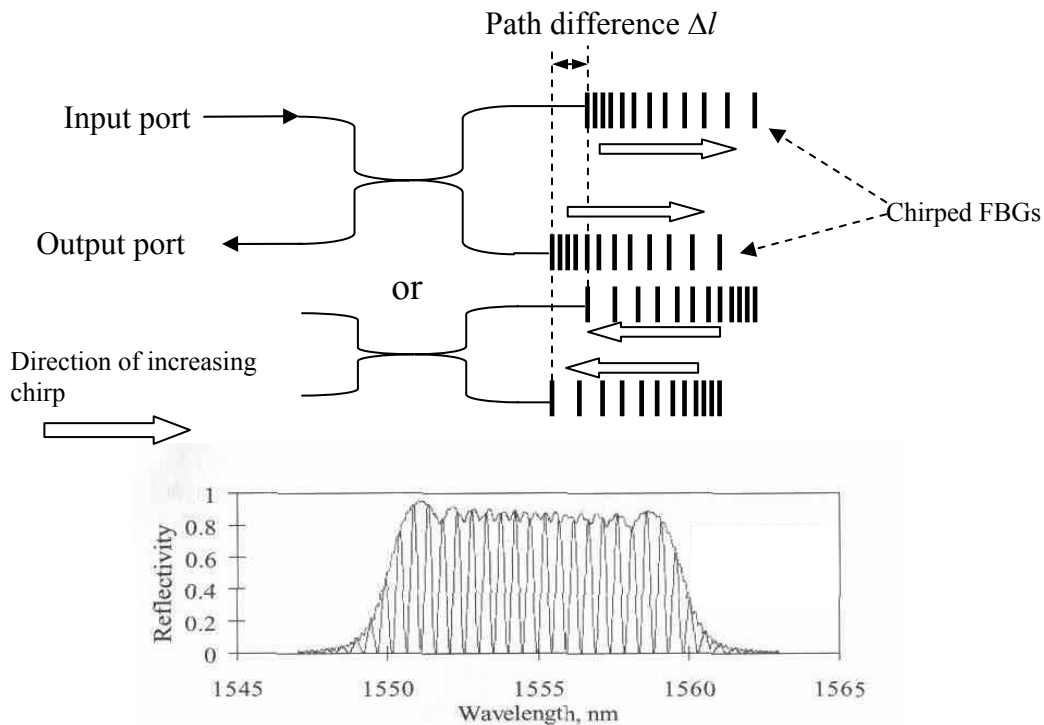


Figure 3.32, the spectral response of a Michelson filter consisting of 2 chirped FBGs (@1550nm, grating length of 5mm and bandwidth of 10nm) with length mismatch, $\Delta l = 1.724\text{mm}$ which corresponds to a measured FSR of $\sim 0.47\text{nm}$, from the graph[99]

The Michelson interferometer using chirped FBGs as partial reflectors with the chirps in the FBG orientated in the same way as shown with a path difference, Δl behaved like the overlapping chirped FBG FP with the chirps of the FBGs oriented in the same way. The cavity response, figure (3.32), shows that the FSR corresponds to the path difference, Δl and remains uniform with wavelength because this path difference/cavity length is the same for all wavelengths.

3.9 Dissimilar chirped FBG Fabry-Perot and Michelson interferometer filter

Chirped FBGs act as dispersive elements by introducing a different time delay to the reflected wavelength components. Cavities formed between similar chirped FBGs filters, as discussed in the section (3.8), have the chirps of the FBGs oriented in the same direction, and hence the individual dispersion of each chirped FBG is cancelled. However when the chirp of the two chirped FBGs is dissimilar, dispersion effects become significant.

Analogous to the response of the dispersive bulk FP in section (3.6), the effective refractive index term, n_{eff} in the conventional cavity response is modified by the material dispersion, $\frac{dn}{d\lambda}$, equation (3.15);

$$\Delta\lambda_{FSR} = -\frac{\lambda^2}{2n_{\text{eff}}l}$$

where the effective index is given by;

$$n_{\text{eff}} = n(\lambda) - \lambda \frac{dn}{d\lambda}$$

Thus in cavities formed by the dispersive chirped FBGs, where the dispersion is provided by the variation of the resonance position with wavelength, $\frac{dl}{d\lambda}$, the effective cavity length term in the FSR response should be modified by the factor, $\frac{dl}{d\lambda}$.

A theoretical study of the dispersive chirped FBG FPs, using the TMM, has shown a modification to the FSR response of the cavity through an effective cavity length, given by [100];

$$\Delta\lambda_{FSR} = \frac{\lambda^2}{2n(l_0 - l_g)} \quad (3.17)$$

where l_0 is the physical separation of the two grating centres and l_g is the grating length. Examination of equation (3.17), suggest that the FSR of a dispersive cavity is independent of the chirp rate, $\frac{dl}{d\lambda}$. The FP being modelled consisted of similar chirped FBGs oriented in the same direction where the dispersive effect of the FP should have been cancelled [94]. These cavities have been shown to behave with a conventional FP response.

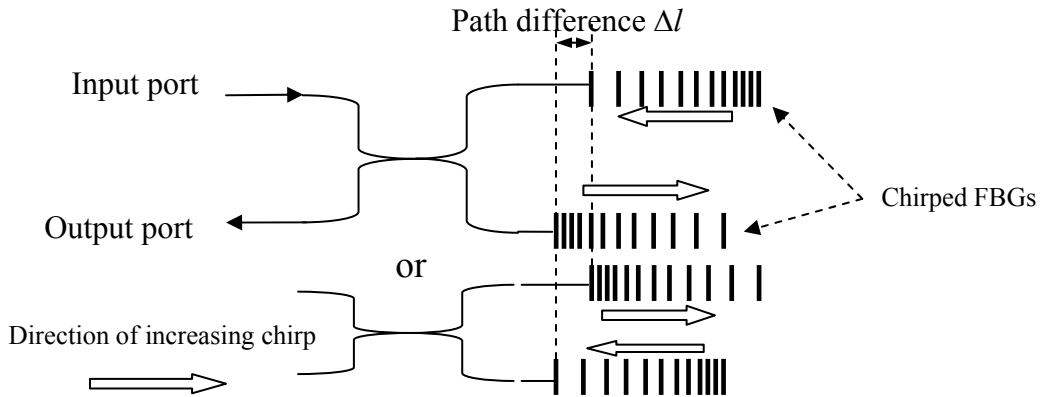


Figure 3.33, illustration of a Michelson filter consisting of 2 chirped FBGs with the chirps orientated in the opposite direction to each other [101].

An indication that the behaviour of cavities involving the use of chirped FBGs may behave differently to the conventional FP response, is provided by an equation describing the FSR of the chirped FBG asymmetric Michelson interferometer, figure (3.33), given in Kashyap [101] with a response;

$$\Delta\lambda_{FSR} = \frac{\lambda^2}{2n\Delta l + \Delta\phi(\lambda)} \quad (3.18)$$

where $\Delta\phi(\lambda)$ is given as the differential reflected phase change from the two chirped FBGs. The equation (3.18) bears similarity in form to the dispersive FP cavity, equation (3.15);

$$\Delta\lambda_{FSR} = -\frac{\lambda^2}{2l\left(n - \lambda \frac{dn}{d\lambda}\right)}$$

which suggest that there may be a modification to the FSR value for a dispersive Michelson interferometer when $\Delta\phi(\lambda)$, in equation (3.18) becomes significant in cavities made up of chirped FBGs with dissimilar properties, ie the chirps orientated in opposite direction. Examination of equation (3.18) reveals that there is an inconsistency in the units of dimension involved. Instead of the phase term in the denominator, there should be a term involving the dimension of optical path length.

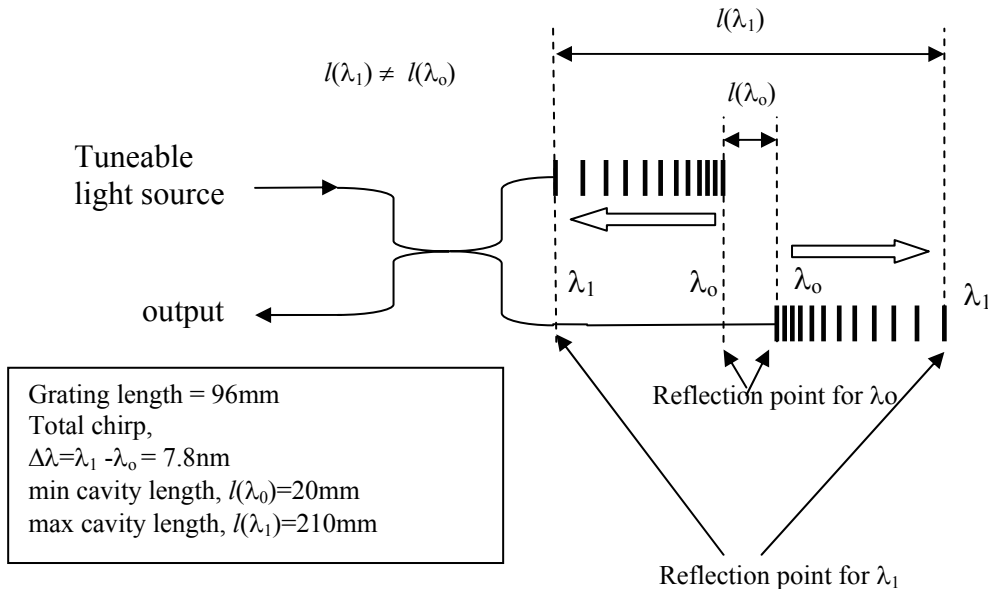


Figure 3.34, shows a Michelson interferometer filter consisting of 2 chirped FBGs centred @1541nm with chirp of 7.8nm and cavity length of 96mm with the minimum cavity length of 20mm and maximum cavity length of 210mm[102]

Dissimilar chirped FBGs have been used as reflectors in a Michelson interferometer as shown in figure (3.34) [102]. The dissimilar chirped FBG Michelson interferometric setup consists of two identical chirped FBGs configured so that the chirps are oriented in opposite directions as shown in figure (3.34).

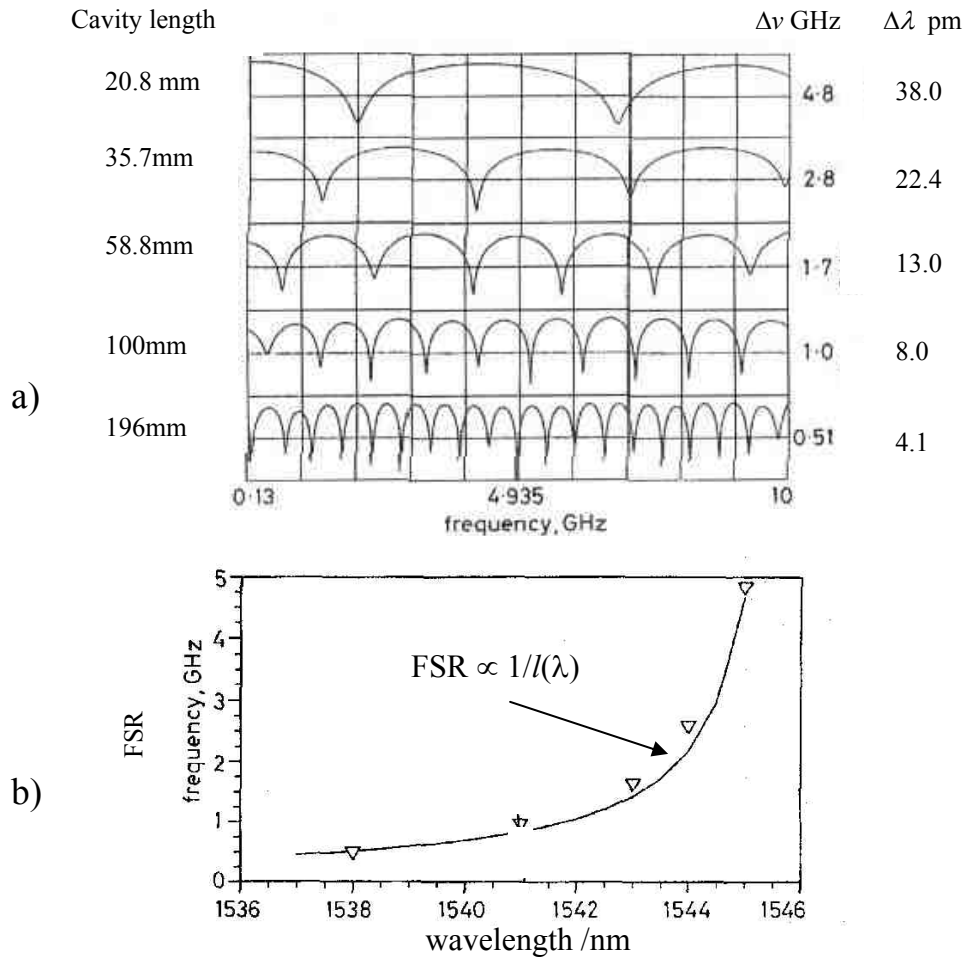


Figure 3.35, measured frequency response for the dissimilar chirped FBGs Michelson interferometer[102]. a) FSR of the various available cavities accessed by different wavelength and b) a plot of FSR with wavelength. Using the relationship of the detuned wavelength with position, the cavity length measured in terms of wavelength shows an inverse relationship with cavity length.

The light in the output port of the 3dB coupler experiences a decreasing chirp from the top grating and an increasing chirp in the bottom grating. Measuring the time delay experienced by a pulse reflected from their respective resonance positions reveals the separation of the reflecting points and thus the cavity length for the wavelength concerned. Since the chirp is linear, the separation is linearly related to wavelength. Figure (3.35a) shows the cavity response with a non dispersive characteristic, equation (3.16) where the FSR corresponds to the separation of the reflection points/cavity length. The cavity response demonstrates the tuneability of the device where a continuous range of FSR can be accessed by tuning across the bandwidth of the chirped FBG. Using the linear detuning relationship between wavelength and position of the reflection from the chirped FBG, the filter's response

can be reduced to the non-dispersive bulk FP response; $\Delta\nu_{FSR} = \frac{c}{2nl(\lambda)}$, where $l(\lambda)$ is the wavelength dependent cavity length and this is plotted in figure (3.35b) together with the experimental FSR values[102] and illustrates the inverse relationship with length, $l(\lambda)$. This relationship is contrary to what is expected of a dispersive cavity. Judging by the above results, where the FP cavities response is inversely proportional to the cavity length, $l(\lambda)$, reducing the cavity length will further increase the FSR value of the FP formed by dissimilar chirped FBGs. It is possible to have a situation where the cavity length is zero. The cavity length can be reduced by reducing the length mismatch of the two arms in the Michelson interferometer configuration [78] or writing the dissimilar chirped FBGs on top of one another to create an overlap cavity in the FP configuration [103] or in a loop mirror [104] configuration using just a single chirped FBG, as shown in figure (3.36).

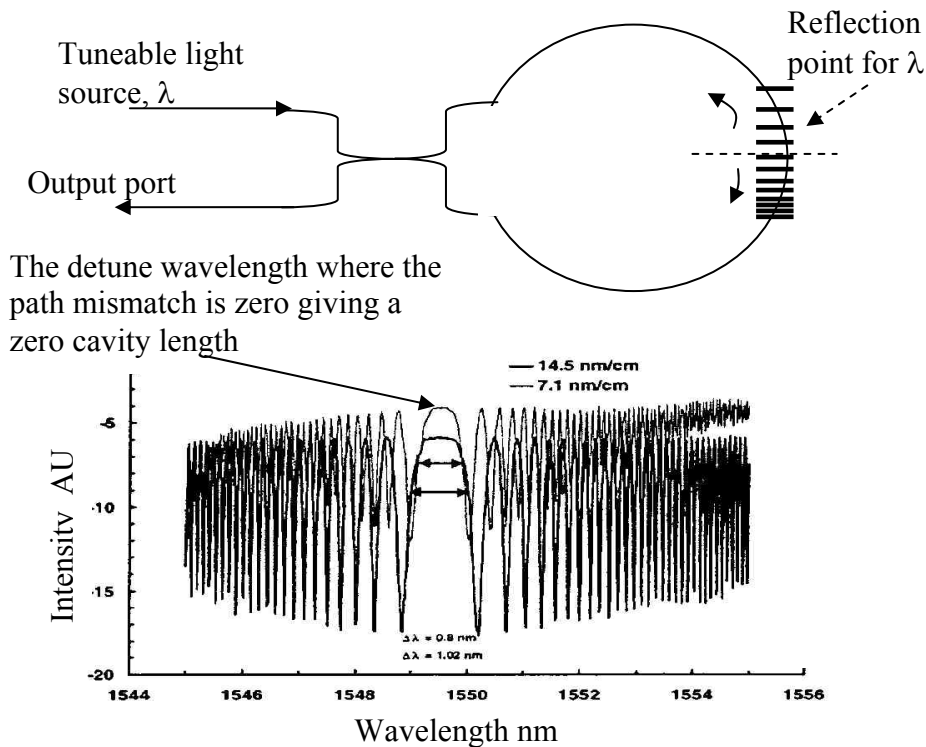


Figure 3.36, illustrates the loop mirror interferometer configuration, where the cavity length is given by the path difference of the two reflected waves. The filter response for 2 different chirped FBGs used is also shown [104].

The filter response for the loop mirror configuration incorporating a chirped FBG is given by [104];

$$\Delta\lambda_{FSR} = \frac{\lambda^2}{2n\left(\frac{dz}{d\lambda}\right)\delta\lambda} \quad (3.19)$$

where $\frac{dz}{d\lambda}$ is the inverse of the chirp rate and $\delta\lambda$ is the detuning. This equation can be rewritten in the standard non dispersive bulk FP response, since $\left(\frac{dz}{d\lambda}\right)\delta\lambda$ is the detuned distance and the variation in fringe space and FSR can be explain using the conventional FP response, $\Delta\lambda_{FSR} = -\frac{\lambda^2}{2nl(\lambda)}$. The temperature response of the loop mirror resonator showed that the whole spectrum shifted with temperature with a temperature response the same as that of the uniform FBGs [104].

3.10 Chirped FBG Michelson interferometric sensor

It can be seen that the FSR/cavity mode spacing of the FP or Michelson interferometer, formed by two dissimilar chirped FBGs depends on the length of the cavity created by the respective resonance position in the two chirped FBGs and that they are wavelength dependent. If the grating is not already chirped, chirp may be induced by applying a strain gradient or temperature gradient along the grating. The resonance position inside the chirped FBG can be interrogated using a Michelson interferometer configuration as shown in figure (3.37). If a broadband mirror, such as a cleaved end of a fibre is used to define one end of the Michelson interferometer, it may act as a reference reflection point for all wavelengths. The wavelength dependence of the resonance position in the chirped FBG will produce the fringe pattern. The filter response can provide an indication to the resonance position within the chirped FBG under examination. This is essentially what is involved in the phase based intragrating distributed strain sensing method [105,106]. From the filter response, every fringe is equivalent to 2π in the RTPS of the cavity. Unwrapping this phase information allows the cumulative phase to be determined. From the definition of the group delay, the gradient of which provides a measurement of length, in which case, it is the reflected position inside the chirped FBG, with respect to the mirror end, $l(\lambda)$;

$$\frac{d\theta}{d\lambda} = -\frac{4\pi n}{\lambda^2} l(\lambda) \quad (3.20)$$

where θ is the cumulative phase. Equation (3.20) is essentially the equation from what the FSR for a non dispersive FP cavity is derived. Figure (3.37) illustrates the intragrating distributed strain sensing method [105].

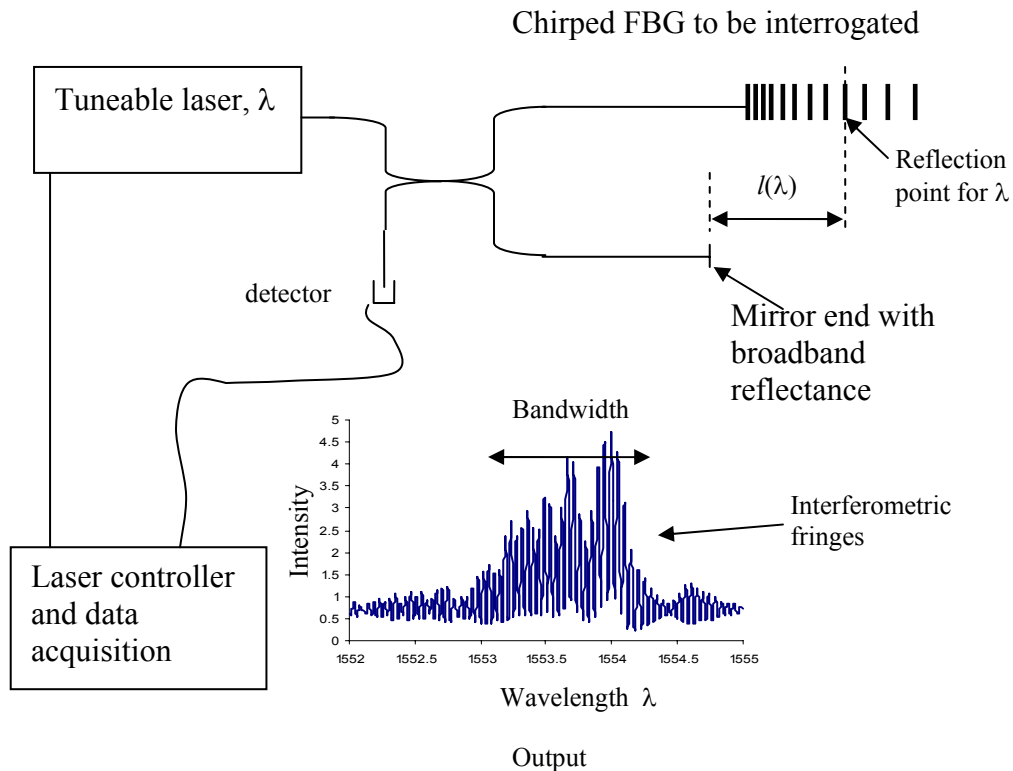


Figure 3.37, illustration of the phase based Bragg intragrating distributed strain measurement based on the dissimilar chirped FBG Michelson interferometer where one arm of the interferometer is terminated with a mirror with a broadband response[105].

From the Bragg condition; $\lambda = 2n\Lambda$, the reflected wavelength provides a measure of the period and refractive index, from which the local strain, ε , is estimated. The variation of strain along the length of a grating is encoded in the Bragg wavelength as a function of position so that the strain field can be mapped out across the chirped FBG. Problem arises when the strain profile is not monotonically increasing or decreasing when there are multi values of strain, which impose the same Bragg condition for many different points along the grating. This can cause complexity in resolving the resonance positions, which restrict the use of the technique as a practical device.

The problem of multiple resonance locations for a single wavelength in the distributed strain sensing scheme described above, can be overcome using a technique that has been used to measure the time delay and the reflectivity of chirped FBGs [107]. This technique has been adapted to determine the arbitrary strain profiles within FBGs [108]. The experimental setup is illustrated in figure (3.38). It consists of a balanced Michelson interferometer illuminated by a broadband source.

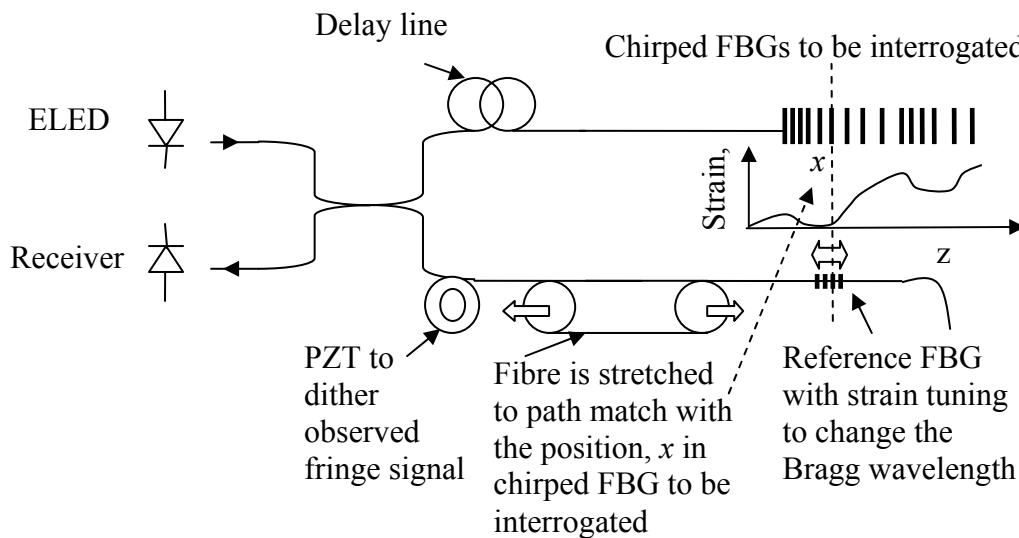


Figure 3.38, illustration of arbitrary strain profile measurement based on the dissimilar chirped FBGs Michelson interferometer where the path matching is determined by the amount of stretching and the wavelength is determined by the maximum return signal when matching wavelength [108].

In low coherence interferometry, interference fringes are observed when the path length mismatch of the arms of the Michelson interferometer is within the coherence length of the source. The maximum visibility occurs when the mismatch is zero. The reference arm containing the reference FBG is stretched to path match the distance, x , within the chirped FBG and a small dither signal of magnitude $\sim 2\mu\text{m}$, is applied via the PZT to scan over several interference fringes. The reference FBG is then strained tuned so that the wavelength of the reference FBG matches that of the local wavelength at x in the chirped FBG when the return signal is the maximum. The variation of strain along the length of the grating is encoded in the Bragg wavelength as a function of position and thus any arbitrary strain profile can be mapped out using the measured visibility. This is achieved irrespective of the fringe spacing/FSR values. Instead of strain tuning the reference FBG, a broadband mirror may be used in

the reference arm in conjunction with a wavelength selection device [109]. The accuracy of the method depends on the bandwidth of the reference FBGs in the former or the bandwidth of the wavelength selection device in the latter.

3.11 Strain enhancement of chirped FBG Michelson and large path-length scanning Fabry-Perot interferometer

When a chirped FBG is stretched, there is a redistribution of the period as well as a change in the mode index via the photo-elastic effect. The entire bandwidth of the grating shifts to a longer wavelength [61]. Along the changes to the period and mode index there is a concomitant change in the reflection point for a particular wavelength as illustrated in, figure (3.39).

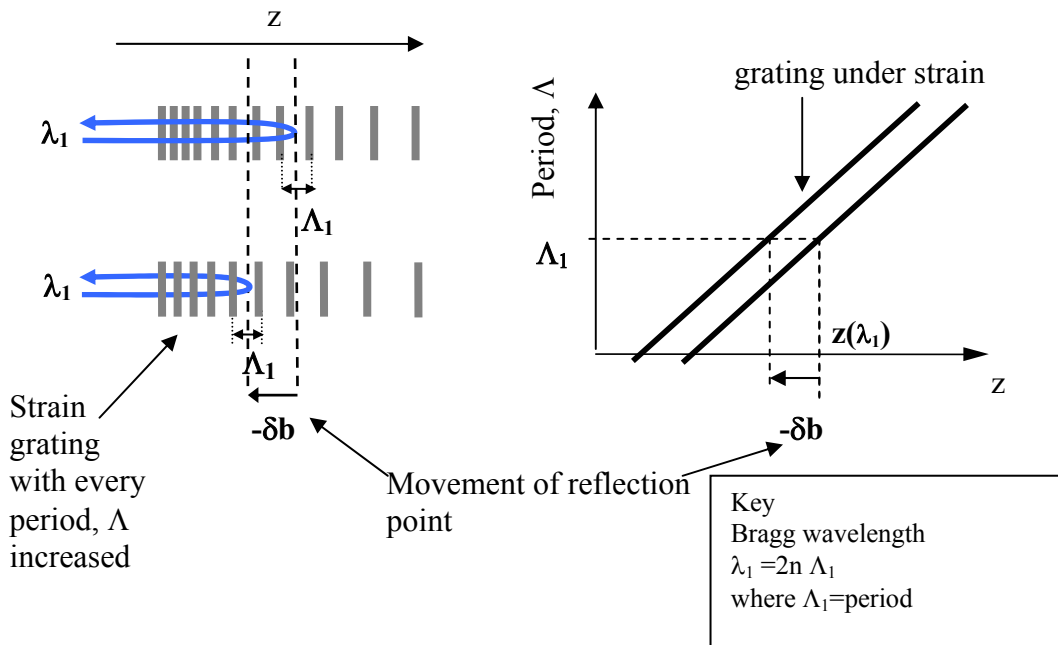


Figure 3.39, the effect of a perturbation upon a periodically chirped FBG showing the change in the resonance position.

From the wavelength detuning equation (3.3), $b(\lambda) = \frac{\lambda - \lambda_B}{\Delta\lambda_c} l_g$. Using the strain

response of an FBG, equation (3.2), $\xi = \frac{1}{\lambda_B} \frac{\delta\lambda}{\delta\varepsilon}$, the change of the resonance position

is given by [51];

$$\delta b = -\frac{\lambda}{\Delta\lambda_c} l_g \xi \delta\varepsilon \quad (3.21)$$

where l_g is the grating length, $\Delta\lambda_c$ is the total chirp and $\delta\varepsilon$ is the strain. Assuming that the strain responses of the FBG and of the optical fibre are the same, and comparing equation (3.21), with the strain response of the optical fibre, an effective length of the chirped grating, l_{eff} may be calculated [51];

$$l_{eff} = -\frac{\lambda}{\Delta\lambda_c} l_g$$

For a periodically chirped FBG, when it is subjected to axial strain, the location along the FBG from which light of a given wavelength is reflected changes, giving an effective extension enhancement of up to 3 orders of magnitude higher when compared to a bare fibre [51]. A fibre Michelson interferometer, with enhanced strain sensitivity, employing this idea has been demonstrated [51] and the setup is shown in figure (3.40).

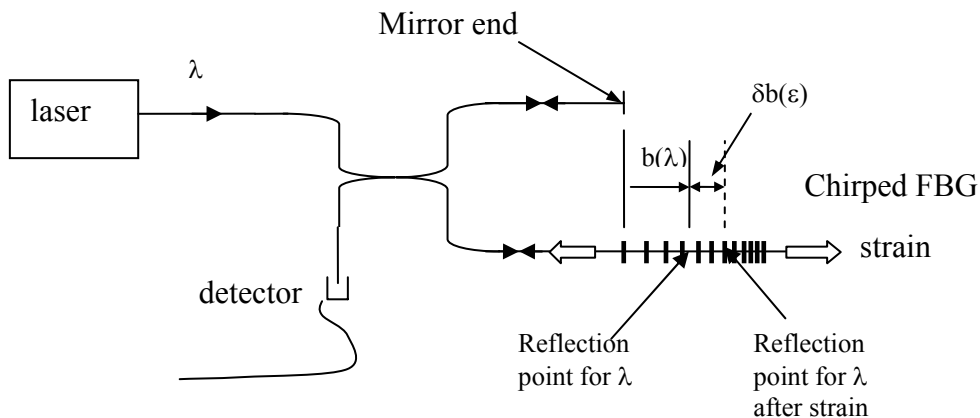


Figure 3.40, illustration of the Michelson interferometer used to demonstrate the strain magnification using a chirped FBG in one arm and a mirror end in the other[51].

The Michelson interferometer consisted of a chirped FBG ($\Delta\lambda=0.5\text{nm}$, grating length =1cm) in one arm and a mirror in the other, such that the dispersion in this interferometric setup were not cancelled. The chirped FBG is created by applying a temperature gradient across the uniform FBG (@1000nm, $\Delta\lambda=0.2\text{nm}$). The interferometer is illuminated by a tuneable laser source. The light is split at the coupler and one path is reflected off the mirror and the other path is reflected from the resonance point inside the chirped FBG and recombined to interfere on the detector.

The optical path difference between the two arms of the interferometer is dependent on the strain state of the chirped FBG. By modulating the laser frequency, a phase carrier is generated and the amplitude of the carrier frequency is directly proportional to the optical path length difference of the two arms. An axial strain of $500\mu\epsilon$ applied to a 1cm long grating (extension = $5\mu\text{m}$) produces an optical path length change of 1-3cm in the location of the resonance points [51], giving a 2000-5000 times of magnification, dependent on the chirp rate of grating used.

The large transduction of the movement of the reflection position that transpired to a large shift in phase measurement in the Michelson interferometer when the individual chirped FBG is strained have been translated to a large scanning range in path matched processing/reference chirped FBG FP interferometer for low coherence interferometry [110]. The concomitant change to the reflection point imparted to every component of the wavelength in the bandwidth of a chirped FBG when it is strained, translates to a large group delay and thus large optical path change. This effect has been utilised for strain magnification [51]. Interferometric configurations employing chirped FBGs can be used as a processing interferometer in low coherence interrogation [110], to scan the path length mismatch of the sensing interferometer. This is achieved by stretching the individual chirped FBG.

The effect of using the chirped FBG FP configuration as a processing/reference interferometer would depend on the dispersive effect of the cavity. A FP filter formed by a pair of identical chirped FBGs with chirps oriented in the same direction, will have a net dispersion equal zero [94] whereas using dissimilar chirped FBGs produces unwanted dispersion where the net dispersive effect is not cancelled. Figure (3.41a) shows the non dispersive chirped FBG FP configuration which consists of identical chirped FBG oriented in the same way and, figure (3.41b) and (3.41c) illustrate the dispersive FP cavities where some residual dispersive effect exists inside the cavity as the different wavelength components see different cavity lengths and thus on reflection inside the cavity, will incur different time delay.

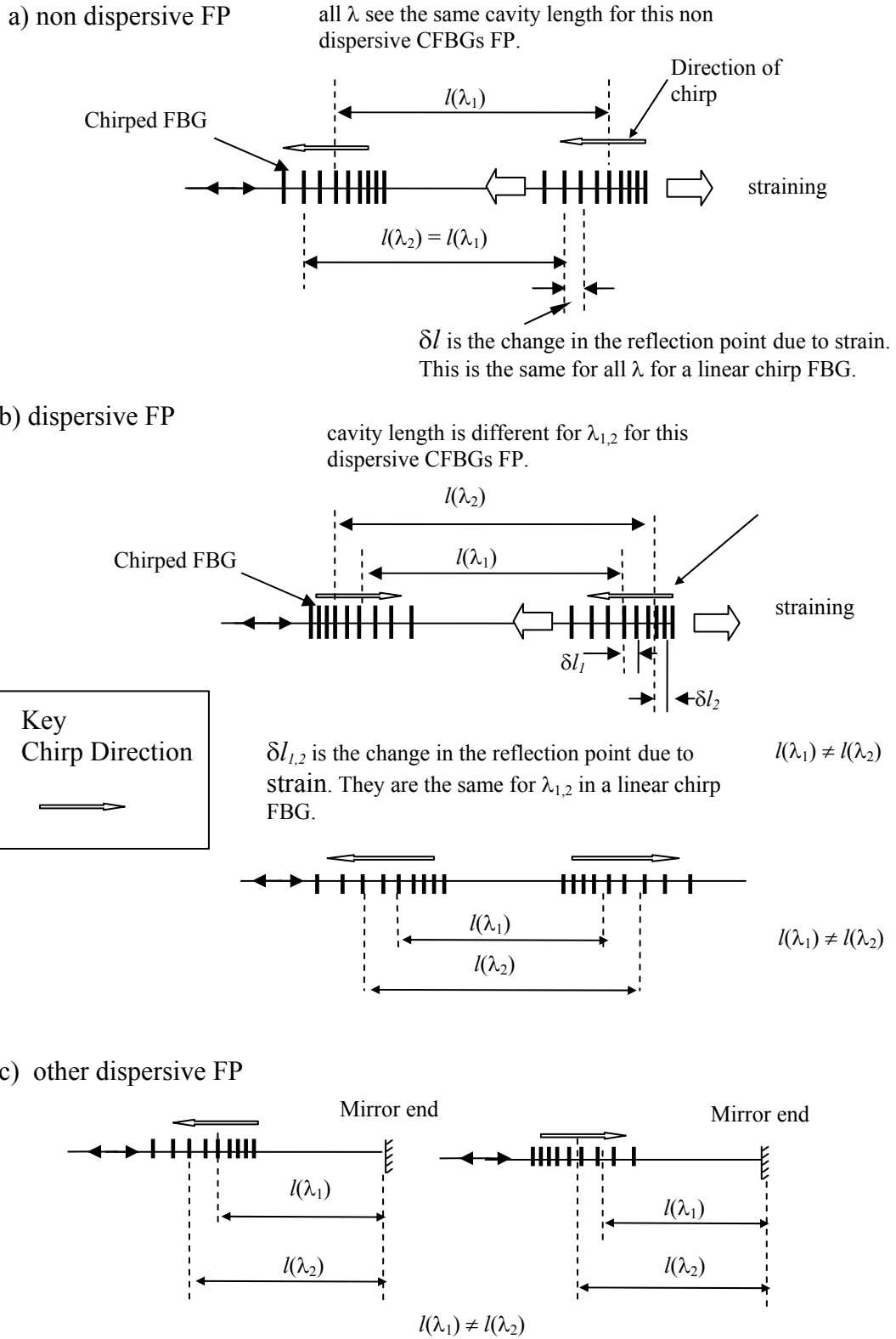


Figure 3.41, illustration of the dissimilar chirped FBG FP setup, a) non dispersive where the dispersion is cancelled, b) dispersion in the FP is not cancelled and there is the residual dispersive effect and c) other types of dispersive FP configurations.

This type of processing interferometer has been used in Optical Coherence Tomography (OCT) [111]. The processing interferometer consisted of a non dispersion chirped FBG FP, shown in figure (3.41a), where the orientation of the chirp is in the same direction. The OCT setup is shown in figure (3.42a). A chirped FBG with $\lambda_B @1300\text{nm}$, grating length of 1cm and a chirp bandwidth of $\Delta\lambda=20\text{nm}$, will give a theoretical strain amplification value, according to equation (3.21), of a factor of 75. An extension of $33\mu\text{m}$ applied to the 1cm grating produced a path scan of $3495\mu\text{m}$ [111], which corresponds to an amplification of a factor of 100 times. Figure (3.42b) shows the theoretical calculation of the autocorrelation function of the source with a bandwidth of 31nm, providing a coherence length, L_c of $52\mu\text{m}$. Figure (3.42c) shows the experimentally recorded autocorrelation of a much broader autocorrelation function with L_c of $317\mu\text{m}$. The broadening of the autocorrelation spectrum observed is due to the fact that some residual dispersion remained in the reference scanning interferometer. The two chirped FBGs used were ideally similar, however they are not exactly the same, which can introduce dispersion. The broadening of the autocorrelation was also observed from a dispersive fibre. When a section of dispersive fibres were placed in one arm of a free space Michelson interferometer and the optical path mismatch scanned using a mirror in the other arm, a broadened autocorrelation was produced as a result of this dispersion [112]. To ensure that there is no net dispersion inside the scanning reference processing interferometer, a single chirped FBG was used in a loop mirror configuration such that the net dispersion will be zero, figure (3.42d). The achieved experimental autocorrelation of the source produced a coherence length, L_c of $69\mu\text{m}$, which is still larger than the theoretical value with a possible reason being that the chirped FBG used is not linearly chirped but is non-linearly chirped which may introduce net dispersion.

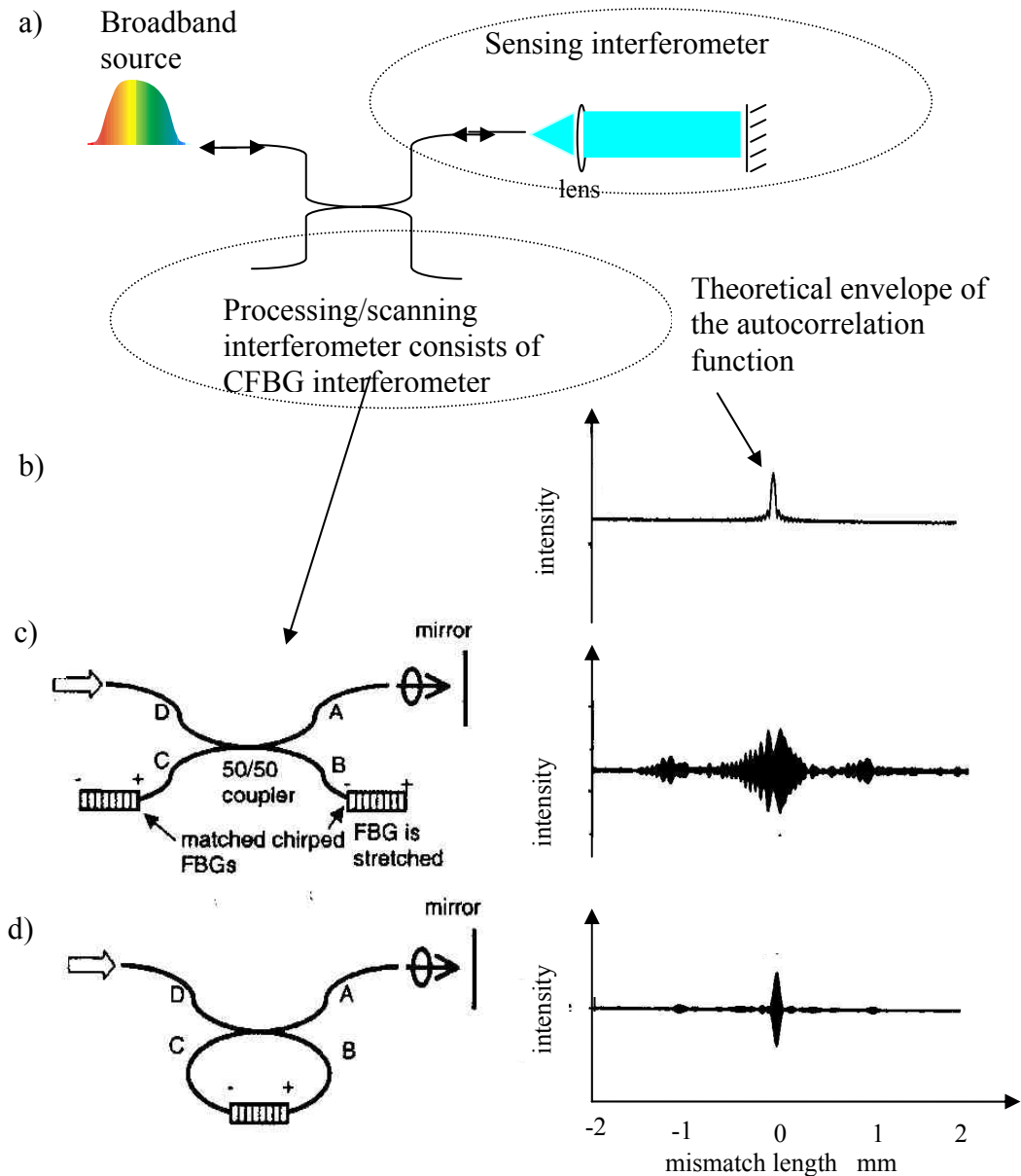


Figure 3.42a, illustrates the coherence interrogation configuration which consists of a reference interferometer and a sensing interferometer. b) the theoretical plot of the autocorrelation of the source, c) is the dispersion free configuration consists of 2 chirped FBGs but the scan revealed that there is still residual dispersion as the autocorrelation is broadened and d) 2nd interferometer configuration consisting of only a single chirped FBG and the scan produced a less broadened autocorrelation [111].

A high resolution FBG FP resonator strain sensing system using a synthetic heterodyne technique has been theoretically analysed and experimentally demonstrated [113]. The chirped FBG FP cavities consisting of broadband chirped FBGs. Once cavity is formed with chirped FBGs centred @1550nm with a bandwidth

of $\sim 27\text{nm}$ and a grating length of 0.504mm , separated by a cavity length of 60.504mm between the grating centres, and a shorter 2nd chirped FBG FP cavity formed with chirped FBGs centred @ 1548nm , bandwidth of 1.7nm and grating length of 0.2mm separated by a cavity length of 1.7mm . Figure (3.43) illustrates the setup of the experiment [113].

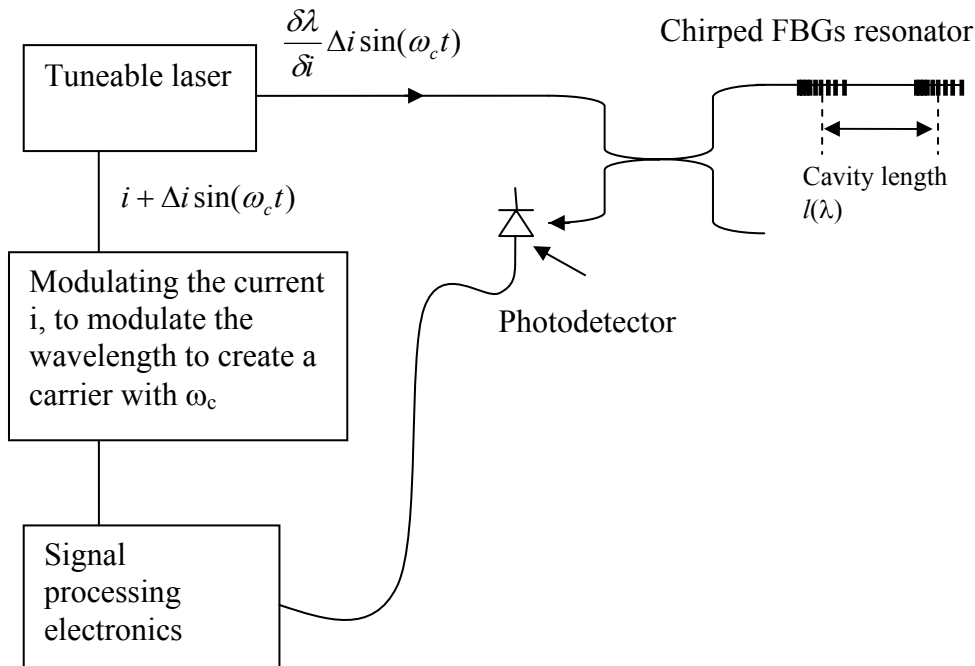


Figure 3.43, illustration of the heterodyne interrogation of a chirped FBG FP resonator. A carrier of frequency ω_c is created by ramping the injection current [113].

By ramping the injection current of the laser source, a carrier of frequency ω_c is created. This is converted to a phase modulation by the change in the RTSP of the cavity and synchronous detection is performed on the output of the cavity. The change of phase experienced by the cavity when axial strain is applied, is derived from the amplitude of the 1st and 2nd harmonics about the modulation frequency, ω_c . Experimental results demonstrated the phase sensitivity of $0.587 \text{ rad } \mu\epsilon^{-1}$ and $0.015 \text{ rad } \mu\epsilon^{-1}$ for the long (60.504mm) and short (1.7mm) cavities respectively. These phase responses are in keeping with the response calculated using the RTSP equation; $\theta = \frac{4\pi n l}{\lambda}$ with strain, which is determined by the length of the cavity. It appeared that using the dispersive chirped FBG as the partial reflectors to form the FP, only acted to

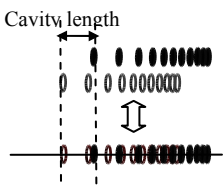
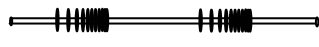
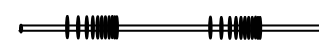
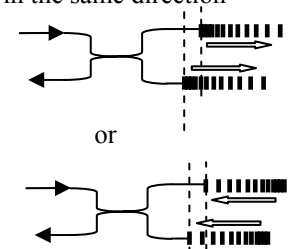
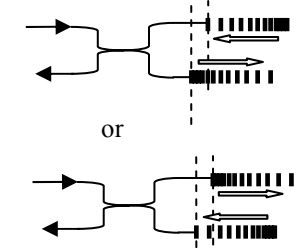
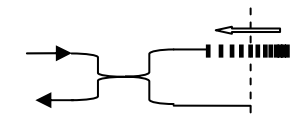
increase the dynamic range compared to uniform FBG and did not alter the strain sensitivity of these FPs. Though a theoretically determined FSR was quoted with a value of, $\Delta\lambda_{FSR} = 0.46\text{nm}$, which is much larger than would have been expect for a FP

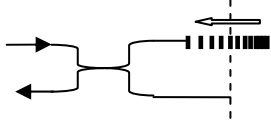
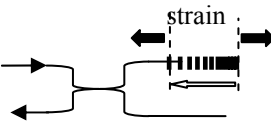
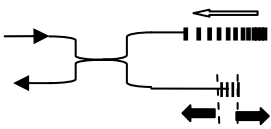
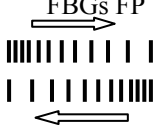
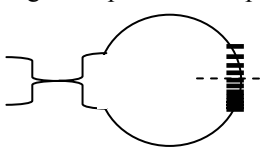
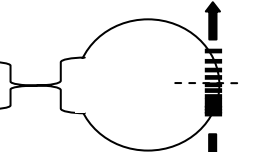
with a cavity length of 60.504mm using the standard FSR equation; $\Delta\lambda_{FSR} = -\frac{\lambda^2}{2nl}$.

The FSR value of 0.46nm corresponds to a FP with cavity length $\sim 16\text{mm}$. This theoretically determined decreased in wavelength sensitivity/increased FSR value was used in the estimation of temperature induced error in the experiment via the temperature response of the FBGs, equation (3.2). In the experiment, there was no mention of the orientation of the gratings chirping direction and though the simulation for strain result and the FSR response obeys the conventional FP response, the broadband chirped FBG only improved the dynamic range of the cavity.

3.12 Summary

Table 3.2 characteristics of interferometers involving the used of chirped FBGs				
configuration	characterised	sensing/filter	demonstrates distributed reflective nature	dispersive effect
Chirped FBG FP with chirps in FBG oriented in the same direction or 	broad band illumination, wavelength [94] theoretical TMM [94, 97]	filter filter	N/A all wavelengths sees the same cavity length N/A all wavelengths sees the same cavity length	no no
	broadband illumination straining single chirped FBG [111]	interrogating interferometer	N/A all wavelength sees the same cavity length	yes

configuration	characterised	sensing/filter	demonstrates distributed reflective nature	dispersive effect
<p>overlap cavity</p> 	<p>broad band illumination, wavelength [94,98] theoretical TMM [94,97]</p>	<p>filter</p>	<p>N/A all wavelengths sees the same cavity length</p>	<p>no</p>
<p>broadband FBGs, no mention of chirp orientation</p> 	<p>single wavelength, wavelength [95,96]</p>	<p>filter/ microwave signal processing</p>	<p>N/A</p>	<p>no</p>
<p>chirped FBGs FP no mention of chirps orientation</p> 	<p>sweeping wavelength to generate carrier [113] theoretical TMM [113]</p>	<p>strain</p>	<p>can not be distinguished</p>	<p>no</p>
<p>Chirped FBGs Michelson with chirps in FBG oriented in the same direction</p> 	<p>broadband illumination, wavelength [99]</p>	<p>filter</p>	<p>N/A all wavelengths sees the same cavity length</p>	<p>no</p>
<p>Chirped FBGs Michelson with dissimilar chirps</p> 	<p>broadband illumination, wavelength [101,102] analytical [101,102]</p>	<p>filter filter</p>	<p>yes yes</p>	<p>no no</p>
<p>chirped FBGs Michelson with an mirror end</p> 	<p>sweeping illuminating wavelength [105,106]</p>	<p>intra-grating strain sensor</p>	<p>yes</p>	<p>no</p>

configuration	characterised	sensing/filter	demonstrates distributed reflective nature	dispersive effect
chirped FBGs Michelson with an mirror end 	broadband source with wavelength selection device, wavelength [108]	arbitrary strain profile	yes	can not be distinguished
chirped FBGs Michelson with an mirror end 	sweeping wavelength to generate a carrier [51]	strain magnifications	no mention	yes
chirped FBG Michelson with another uniform FBG 	broadband source with FBG to select wavelength, wavelength [109]	arbitrary strain profile	yes	can not be distinguished
overlap dissimilar chirped FBGs FP 	broadband illumination, wavelength [103] strain [103]	filter/sensor	yes	no
single chirped FBG loop 	Broadband illumination wavelength [104] temperature [104] analytical [104]	filter/sensor	yes	no
single chirped FBG loop 	broadband illumination, straining the single chirped FBG [111]	Low coherence interrogating interferometer	N/A, broadband source	yes

A brief introduction to the FBG sensors and filters is presented. The effect of the action of the external measurands such as temperature and strain has on the coupling mechanism which influences the response characteristics is discussed and illustrated. How this simple FBG element is used as a sensor element is outlined. A brief review

of uniform periodic FBG and chirped FBG sensors and filters and their response characteristics with the different signal demodulation methods have been discussed. The interferometric type of sensors and filters, most notably the Fabry-Perot and Mach-Zehnder interferometer involving the use of uniform and chirped FBGs have been discussed and reviewed. Drawing on examples from the dispersive bulk Fabry-Perot interferometers, how the effect of dispersion has on the cavity response have been described. The effect of inherent dispersion such as with the dispersive optical fibre and in systems where dispersion can be introduced such as in the Optical Delay Line, can have on interferometers for processing/reference in Low Coherence interferometry have been described and the implication this will have on the use of dispersive chirped FBG interferometer was discussed.

There is no one comprehensive wavelength, strain and temperature response for the chirped FBG FP that gives a conclusive dispersive effect on the cavity response due to dispersion in the chirped FBG. Take for example the Sagnac configuration [104] involving the use of a single chirped FBG which gives a wavelength response similar to the physically overlapped chirped FBG FP [103], ie, the FSR/resonance mode is dependent on the wavelength detuned cavity length only and in which case, it is small which means large FSR (small wavelength sensitivity) but the same Sagnac configuration with the chirped FBG has been used as processing interferometer [111] to give a large scan of the path length mismatch ($\sim 3\text{mm}$), produced in the matched path length interferometer interrogation by straining. Now since strain scanning is similar to wavelength scanning in FBG FP interferometer [13], the consequence of the large path length scan (3mm) suggests a large phase excursion has occurred meaning a very high wavelength sensitivity for the interferometer. This is contrary to the former configured chirped FBG Sagnac interferometer response. This review suggests that there exist different interferometric response of interferometer consisting of chirped FBG.

References:

-
- 1 A. D. Kersey, M. A. Davis, H. J. Patrick, M. LeBlanc, K. P. Koo, C. G. Askins, M. A. Putnam and E. J. Friebele, 'Fiber Grating Sensors', *Journ. of Light. Tech.*, **15**, 1442-1463, 1997.

- 2 Y. J. Rao, P. J. Henderson, D. A. Jackson, L. Zhang and I. Bennion, 'Simultaneous strain, temperature and vibration measurement using a multiplexed in-fibre-Bragg-grating/fibre-Fabry-Perot sensor system', *Elect. Lett.*, **33**, 2063-2064, 1997.
- 3 W. Thongnum, N. Takahashi and S. Takahashi, 'Temperature stabilization of fiber Bragg grating vibration sensor', *15th OFS 2002*, **1**, 223-226.
- 4 A. D. Kersey, 'A Review of Recent Developments in Fiber Optic Sensor Technology', *Optical Fiber Tech.*, **2**, 291-317, 1996.
- 5 S. Barcelos, M. N. Zervas, R. I. Laming and D. N. Payne, 'Interferometric Fibre Grating Characterization', *IEE Colloquium (Digest)*, 017, 5/1-5/7, 1995.
- 6 K. T. V. Grattan and T. Sun, 'Fiber sensor technology: an overview', *Sensors and Actuators*, **82**, 40-61, 2000.
- 7 Y. J. Rao, 'In-fibre Bragg grating sensors', *Meas. Sci. Tech.*, **8**, 355-375, 1997.
- 8 Y. J. Rao, 'Recent progress in applications of in-fibre Bragg grating sensors', *Optics and Lasers in Engineering*, **31**, 297-324, 1999.
- 9 C. R. Giles, 'Lightwave Applications of Fiber Bragg Gratings', *Journ. of Light. Tech.*, **15**, 1391-1404, 1997.
- 10 K. O. Hill and G. Meltz, 'Fibre Bragg Grating Technology Fundamentals and Overview', *Journ. of Light. Tech.*, **15**, 1263-76, 1997.
- 11 R. Kashyap, 'Photosensitive Optical Fibers : Devices and Applications', *Optical Fiber Tech.*, **1**, 17-34, 1994.
- 12 I. Bennion, J. A. R. Williams, L. Zhang, K. Sugden and N. J. Doran, 'UV-written in-fibre Bragg gratings', *Optical and Quant. Elect.*, **28**, 93-135, 1996.
- 13 W. W. Morey, G. Meltz, and W. H. Glen, 'Fibre optic Bragg grating sensors', *Proc. of SPIE*, **1169**, 98-107, 1989.
- 14 W. W. Morey, 'Distributed fiber Grating Sensors', *OFS.7, Sydney Australia*, 285-287, 1990.
- 15 A. J. Roger, V. A. Handerek, S. E. Kanellopous and J. Zhang, 'New ideas in Nonlinear Distributed Optical-fibre Sensing', *Proc. of SPIE*, **2507**, 162-172, 1995.
- 16 Y. J. Rao, D. J. Webb, D. A. Jackson, L. Zhang and I. Bennion, 'High resolution wavelength division multiplexed in-fibre Bragg grating sensor system', *Elect. Lett.*, **32**, 924-926, 1996.

-
- 17 D. F. Murphy, D. A. Flavin, R. McBride and J. D. C. Jones, 'Interferometric Interrogation of In-Fiber Bragg Grating Sensors without Mechanical Path Length Scanning', *Journ. of Light. Tech.*, **19**, 1004-1009, 2001.
 - 18 A. D. Kersey, M. A. Davis, H. J. Patrick, M. LeBlanc, K. P. Koo, C.G. Askins, M. A. Putnam and E. J. Friebele, 'Fiber grating sensors', *Journ. of Light. Tech.*, **15**, 1442-1463, 1997.
 - 19 A.L.C Triques, C. L. Barbosa, L.C.G., Valente, A. M. B Braga, R. M. Cazo, J. L. S. Ferreira, R. C. Rabelo, 'Thermal treatment of fiber Bragg gratings for sensing and telecommunication applications', *Proceedings of the IMOC*, **2**, 883-886, 2003.
 - 20 A. D. Kersey, T. A. Berkoff and W.W. Morey, 'Fiber-grating based strain sensor with phase sensitive detection', *1st European Conf. on Smart Struct. and Materials*, Glasgow, 61-67, 1992.
 - 21 M. G. Xu, L. Reekie, Y. T. Chow and J. P. Dakin, 'Optical in-fibre grating high pressure sensor,' *Elect. Lett.*, **39**, 398-399, 1993.
 - 22 H. G. Limberger, P. Y. Fonjallaz and R. P. Salathe and F. Cochet, 'Compaction and photoelastic-induced index changes in fiber Bragg gratings', *Applied Phys Lett.*, **68**, 3069-3071, 1996.
 - 23 G. W. Yoffe, P. A. Krug, f. Ouellette and D. A. Thorncraft, 'Passive temperature-compensating package or optical fiber gratings', *Applied Optics* **34**, 6859-6861, 1995.
 - 24 M. O'Dwyer, S.W. James and R.P. Tatam, 'Thermal dependence of the strain response of optical fibre Bragg gratings', *Meas. Sci. and Tech.*, **15**, 1607-1613, 2004.
 - 25 G, Meltz, W.W. Morey, W. H. Glenn and J. D. Farina, 'In-fiber Bragg-grating temperature and strain sensors', *Proceedings of the ISAAerospace Instrumentation Symposium*, **34**, 239-242, 1988.
 - 26 M. G. Xu, J. L. Archambault, L. Reekie and J. P. Dakin, 'Discrimination between strain and temperature effects using dual-wavelength fibre grating sensors', *Elect. Lett.*, **30**, 1085-1087, 1994.
 - 27 A. D. Kersey, T. A. Berkoff, and W. W. Morey, 'Fibre optic Bragg grating strain sensor with drift compensated high resolution interferometric wavelength shift detection', *Opt. Lett.*, **18**, 72-74, 1993.
 - 28 Y. J. Rao, M. R. Cooper, D. A. Jackson, C. N. Pannell and L. Reekie, 'Simultaneous measurement of displacement and temperature using in fibre Bragg grating base ectrinsic Fizeau sensor', *Elect. Lett.*, **36**, 1610-1611, 2000.

-
- 29 Y. J. Rao, D. J. Webb, D. A. Jackson, L. Zhang and I. Bennion, 'High resolution, wavelength division multiplexed in fibre Bragg grating sensor system', *Elect. Lett.*, **32**, 924-925, 1996.
 - 30 R. M. Measures, S. Melle and K. Liu, 'Wavelength demodulated Bragg grating fiber optic sensing systems for addressing smart structure critical issues', *Smart. Mater. Struct.*, **1**, 36-44, 1992.
 - 31 S. M. Melle, A. T. Alavie, S. Karr, T. Coroy, K. Liu and R. M. Measures, 'A Bragg Grating-Tuned Fiber Laser Strain Sensor System', *IEEE Photon. Tech. Lett.*, **5**, 263-266, 1993.
 - 32 C. Y. Wei, S. W. James, C. C. Ye, R. P. Tatam and P. E. Irving, 'Application issues using fibre Bragg gratings as strain sensors in fibre composites', *Strain*, **36**, 143-150, 2000.
 - 33 A. D. Kersey, T. A. Berkoff and W.W. Morey, 'High-resolution fibre-grating based strain sensor with interferometrical wavelength-shift detection', *Elect. Lett.*, **28**, 236-238, 1992.
 - 34 S. W. James, R. P. Tatam, A. Twin, M. Morgan and P. Noonan, 'Strain response of fibre Bragg grating sensors at cryogenic temperatures', *Meas. Sci. and Tech.*, **13**, 1535-1539, 2002.
 - 35 A. D. Kersey and T. A. Berkoff, 'Fiber Optic Bragg Grating Differential-Temperature Sensor', *IEEE Photon. Tech. Lett.*, **4**, 1185-1183, 1992.
 - 36 W. Thongnum, N. Takahashi, S. Takahashi, 'Temperature stabilization of fiber Bragg grating vibration sensor' *OFS*, **1**, 223-226, 2002.
 - 37 S. Theriault, K. O. Hill, F. Bilodeau, D. C. Johnson and J. Albert, 'High-g Accelerater Based on an In-Fiber Bragg Grating Sensor', *Proc. OFS, Sapporo, Japan*, paper We 3-6, 196-199, 1996.
 - 38 B. Sorazu, G. Thursby, B. Culshaw, F. Dong, S. G. Pierce, Y. Yang and D. Betz, 'Optical Generation and Detection of Ultrasound', *Strain*, **39**, 111-114, 2003.
 - 39 S. F. O'Neill, M. W. Hathaway, N. E. Fisher, D. J. Webb, C. N. Pannell, D. A. Jackson, L. R. Gavrilov, J. W. Hand, L. Zhang and I. Bennion, 'High-frequency ultrasound detection using a fibre Bragg grating', *IEE Colloquium on Optical Fibre Gratings*, **23**, 79-84, 1999.
 - 40 A. D. Kersey and M. J. Marrone, 'Fiber Bragg Grating High-Magnetic-Field Probe', *Proc. of SPIE*, **2360**, 53-56, 1994.
 - 41 M. G. Xu, H. Geiger and J. P. Dakin, 'Fibre grating pressure sensor with enhanced sensitivity using a glass-bubble housing', *Elect. Lett.*, **32**, 128-129, 1996.

- 42 S.C. Tjin, J. Z. Hao and R. Malik, 'Fiber Optic Pressure Sensor using Fiber Bragg Grating', Proc. of SPIE, **3429**, 123-130, 1998.
- 43 S. P. Reilly, S. W. James and R. P. Tatam, 'Tuneable and switchable dual wavelength lasers using optical fibre Bragg grating external cavities', Elect. Lett., **38**, 1033-1034, 2002.
- 44 T. Blair and S. A. Cassidy, 'Wavelength Division multiplexed sensor Network using Bragg Fibre Reflection Gratings', Elect. Lett. **28**, 1734-1735, 1992.
- 45 C. R. Giles, 'Lightwave Applications of fiber Bragg Gratings', Journ. of Light. Tech., **15**, 1391-1404, 1997.
- 46 K. P Koo and A. D. Kersey, 'Bragg grating-based laser sensors systems with interferometric interrogation and wavelength division multiplexing', Journ. of Light. Tech., **13**, 1243-1249, 1995.
- 47 J. A. R. Willians, I. Bennion, K. Sugden and N. J. Doran, 'Fibre dispersion compensation using a chirped in-fibre Bragg grating', Elect. Lett., **30**, 985-987, 1994.
- 48 A. D. Kersey, T. A. Berkoff and W.W. Morey, 'High-resolution fibre-grating based strain sensor with interferometrical wavelength-shift detection', Elect. Lett., **28**, 236-238, 1992.
- 49 S. T. Winnall and A. C.Lindsay, 'DFB Semiconductor Diode Laser Frequency Stabilization Employing Electronic Feedback and Bragg Grating Fabry-Perot Interferometer', IEEE Photon. Tech. Lett., **11**, 1357-1359, 1999.
- 50 K. P. Koo and A. D. Kersey, 'Bragg grating base laser sensors system with interferometric interrogation and wavelength division multiplexing', Journ. of light. Tech., **13**, 1243-1249, 1995.
- 51 A. D. Kersey and M. A. Davis, 'Interferometric fiber sensor with a chirped Bragg grating sensing element', Proc. of SPIE, **2360**, 319-322, 1994.
- 52 H. Riedmatten, M.Weguller, H. Zbinden and N. Gisin, 'Group Delay Analysis of Chirped Fiber Bragg Gratings Using Photon Counting', IEEE Photon. Tech. Lett., **13**, 615-617, 1997.
- 53 S. Barcelos, M. N. Zervas, R. I. Laming and D. N. Payne, 'Interferometric fibre grating characterization', IEE Colloquium on 'Optical Fibre Gratings and Their Applications', 5/1-7, 1995.
- 54 R. Kashyap and M. L. Rocha, 'On the group delay characteristics of chirped fibre Bragg gratings', Optics Comm. **153**, 19-22, 1998.

-
- 55 A. A. Chtcherbakov and P. L. Swart, 'Chirped fibre optic Bragg grating strain sensor with sub-carrier phase detection', *Meas. Sci. Tech.*, **12**, 814-817, 2001.
- 56 A. Yariv, 'Optical Electronics', 4th ed. International Edition, HRW Saunders, 1991.
- 57 F. Ouellette, 'Dispersion cancellation using linearly chirped Bragg grating filters in optical waveguides', *Opt. Lett.*, **12**, 847-849, 1987.
- 58 J. A. R. Williams, I. Bennion, K. Sugden and N. J. Doran, 'Fibre dispersion compensation using a chirped in-fibre Bragg grating', *Elect. Lett.*, **30**, 985-989, 1994.
- 59 W. H. Loh, R. I. Laming, X. Gu, M. N. Zervas, M. J. Cole, T. Widdowson and A. D. Ellis, '10cm chirped fibre Bragg grating for dispersion compensation at 10 Gbit/s over 400km of non-dispersion shifted fibre', *Elect. Lett.*, **35**, 2203-2204, 1995.
- 60 A. Boskovic, J. R. Taylor and R. Kashyap, 'Forty times dispersive broadening of femtosecond pulses and complete recompression in a chirped fibre grating', *Optics Comm.* **119**, 51-55, 1995.
- 61 A. E. Willner, K. M. Feng, J. Cai, S. Lee, J. Peng and H. Sun, 'Tunable Compensation of Channel Degrading effects Using Nonlinearly Chirped Passive fiber Bragg Gratings', *Journ. of Selected Topics in Quant. Elect.*, **5**, 1298-1311, 1999.
- 62 R. W. Fallon, L. Zhang, A. Gloag and I. Bennion, 'Identical broadband chirped grating interrogation technique for temperature and strain sensing', *Elect. Lett.*, **33**, 705-707, 1997.
- 63 R. W. Fallon, L. Zhang, A. Gloag and I. Bennion, 'Multiplexed Identical broadband-chirped grating interrogation system for large strain sensing applications', *IEEE Photon. Tech. Lett.*, **9**, 1616-1618, 1997.
- 64 H. Kogelnik, 'Filtered Response of Nonuniform almost periodic structures', *The Bell system Technical Journal*, **55**, 109-126, 1975.
- 65 M. Yamada and K. Sakuda, 'Analysis of almost-periodic distributed feedback slab waveguides via a fundamental matrix approach', *Applied Optics*, **26**, 3474-3478, 1987.
- 66 S. Huang, M. M. Ohn and R. M. Measures, 'A novel Bragg grating distributed-strain sensor based on phase measurements', *Proc. of SPIE*, **2444**, 158-169, 1995.
- 67 M. LeBlanc, S. Y. Huang, M. Ohn and R. M. Measures, 'Bragg intragrating structural sensing', *Applied Optics*, **34**, 5003-5009, 1995.

-
- 68 C. C. Chang and S. T. Vohra, 'Spectral broadening due to non-uniform strain fields in fibre Bragg grating based transducers', *Elect. Lett.*, **34**, 1778-1779, 1998.
- 69 R. M. Measures, M. M. Ohn, S. Y. Huang, J. Bique and N. Y. Fan, 'Tunable laser demodulation of various fiber Bragg grating sensing modalities', *Smart Mater. Struct.*, **7**, 237-247, 1998.
- 70 M. G. Xu, L. Dong, L. Reekie, J. A. Tucknott and J. L. Cruz, 'Temperature-independent strain sensor using a chirped Bragg grating in a tapered optical fibre', *Elect. Lett.*, **31**, 823-824, 1995.
- 71 Y. Zhu, P. Shum, L. Chao, M. B. Lacquet, P. L. Swart, A. A. Chtcherbakov, and S. J. Spammer, 'Temperature insensitive measurement of static displacements using a fiber Bragg grating', *Optics Express*, **11**, 1918-1924, 2003.
- 72 S. C. Tjin, L. Mohanty and N.Q. Ngo, 'Pressure sensing with embedded chirped fiber grating', *Optics Comm.*, **216**, 115-118, 2003.
- 73 M. LeBlanc, S. Y. Huang, M. Ohn and R. M. Measures, 'Distributed strain measurement based on a fiber Bragg grating and its reflection spectrum analysis', *Optics Lett.*, **21**, 1405-1407, 1996.
- 74 M. Matsuhara, K. O. Hill and A. Watanabe, 'Optical-waveguide filters: Synthesis' *J. Opt. Soc. Am.*, **65**, 804-808, 1975.
- 75 S. Huang, M. M. Ohn, M. LeBlanc and R. M. Measures, 'Continuous arbitrary strain profile measurements with fiber Bragg gratings', *Smart Mater. Struct.* **7**, 248-256, 1998.
- 76 W.W. Morey, G. Meltz and W. H. Glen, 'Fiber Optic Bragg Sensors', *Proc. of SPIE*, **1169**, 89-107, 1990.
- 77 S. Legoubin, M. Douay, P. Bernage and P. Niay, 'Free Spectral range variations of grating-based Fabry-Perot filters photowritten in optical fibers', *J. Opt. Soc. Am. A*, **12**, 1687-1694, 1995.
- 78 R. Kashyap. *Fiber Bragg Gratings*, Academic Press, chapter 6, 243, 1999.
- 79 W.W. Morey, T. J. Bailey, W. H. Glenn and G. Meltz, 'Fiber Fabry-Perot interferometer using side exposed fiber Bragg Gratings', *Proc. of OFC, WA2*, 96, 1992.
- 80 W.W. Morey, G. A. Ball, and G. Meltz, 'Photoinduced Bragg Grating in Optical fibers', *OSA Optics & Photonics News*, 9-14, 1994.
- 81 X. Wan, 'Monitoring fiber Bragg Grating pair interferometer sensor with a modulated diode laser', *Optics Comm.*, **218**, 311-315, 2003.

-
- 82 N. Y. Fan, S. Huang and R. M. Measures, 'Localised long gage fiber optic strain sensors', *Smart Mater. Struct.*, **7**, 257-264, 1998.
- 83 Y. J. Rao, M. R. Cooper, D. A. Jackson, C. N. Pannell and L. Reekie, 'Absolute strain measurement using an in-fibre Bragg grating based Fabry-Perot sensor', *Elect. Lett.*, **36**, 708-709, 2000.
- 84 S. P. Christmas, D. A. Jackson, P. J. Henderson, L. Zhang, I. Bennion, T. Dalton, P. Butler, M. Whelan and R. Kenny, 'High-resolution vibration measurements using wavelength-demultiplexed fibre Fabry-Perot sensors', *Meas. Sci. Tech.* **12**, 901-905, 2001.
- 85 Y. J. Rao, P. J. Henderson, D. A. Jackson, L. Zhang and I. Bennion, 'Simultaneous strain, temperature and vibration measurement using a multiplexed in-fibre Bragg grating/fibre Fabry Perot sensor system', *Elect. Lett.*, **33**, 2063-2064, 1997.
- 86 M. G. Shlyagin, S. V. Miridonoc, D. Tentori, F. J. Mendieta and V. V. Spirin, 'Multiplexing of grating based fiber sensors using broadband spectral coding', *Proc. of SPIE*, **3541**, 271-278, 1998.
- 87 S. J. Petuchowski, T. G. Giallorenzi and S. K. Sheem, 'A Sensitive Fiber-Optic Fabry-Perot Interferometer', *Journ. of Quant. Elect.*, **17**, 2168-2170, 1981.
- 88 J.M. Vaughan, 'The Fabry-Perot Interferometer History Practice and Applications', IOP Publishing Ltd, Appendix 7, 478, 1989.
- 89 J. T. Verdeyen, 'Laser Electronics', 2nd edit, Prentice-Hall International Inc, 1989.
- 90 P. A. Merritt, R. P. Tatam and D. A. Jackson, 'Interferometric chromatic dispersion measurements on short lengths of monomode optical fiber', *Journ. of Light. Tech.*, **7**, 703-716, 1989.
- 91 K. F. Kwong, D. Yankelevich, K. C. Chu, J. P. Heritage and A. Diennes, '400Hz mechanical scanning optical delay line', *Optics Lett.*, **18**, 558-560, 1993.
- 92 A. M. Rollins, M. D. Kulkarni, S. Yazdanfar, R. Ung-arunyawee and J. A. Izatt, 'In Vivo video rate optical coherence tomography', *Optics Express*, **3**, 219-229, 1998.
- 93 A. V. Zvyagin, E. D. J. Smith and D. D. Sampson, 'Delay and dispersion characteristics of frequency-domain optical delay line for scanning interferometry', *Proc. OSA*, **20**, 333-341, 2003.
- 94 G. E. Town, K. Sugden, J. A.R. Williams, I. Bennion and S. B. Poole, 'Wide Band Fabry Perot like Filters in Optical Fiber', *IEEE Photon. Tech. Lett.*, **7**, 78-80, 1995.

- 95 D. B. Hunter and R. A. Minasian, 'Reflectively tapped fibre optic transversal filter using in-fibre Bragg Gratings', *Elect. Lett.*, **31**, 1010-1012, 1995.
- 96 W. Zhang, J. A. R. Williams, L. Zhang and I. Bennion, 'Optical fiber grating based Fabry-Perot resonator for microwave signal processing', *CLEO*, 330-331, 2000.
- 97 X. Peng and C. Roychoudhuri, 'Design of high finesse, wideband fabry-Perot filter based on chirped fiber Bragg grating', *Opt. Eng.*, **39**, 1858-1862, 2000.
- 98 S. Doucet, R. Slavik and S. LaRochelle, 'High finesse large band Fabry-Perot fibre filter with superimposed chirped Bragg gratings', *Elect. Lett.*, **38**, 402-403, 2002.
- 99 R. Kashyap, 'Fiber Bragg Gratings', Academic Press, chapter 6, 257, 1999.
- 100 S. H. Cho, I Yokota and M. Obara, 'Free Spectral Range Variation of a Broadband, High Finesse Multi Channel Fabry Perot filter using Chirped fiber Bragg Gratings', *Jpn. J. of Appl. Phys.*, **36**, 6383-6387, 1997.
- 101 R. Kashyap, 'Fiber Bragg Gratings', Academic Press, chapter 6, 256, 1999.
- 102 D. B. Hunter, R. A. Minasian and P. A. King, 'Tunable optical transversal filter based on chirped gratings', *Elect. Lett.*, **31**, 2205-2207, 1995.
- 103 K. P. Koo, M. LeBlanc, T. E. Tsai and S. T. Vohra, 'Fiber Chirped Grating Fabry-Perot Sensor with Multiple Wavelength Addressable Free Spectral Ranges', *IEEE Photon. Tech. Lett.*, **10**, 1006-1008, 1998.
- 104 A. K. Atieh and I. Golub, 'Scheme for measuring Dispersion of chirped FBG using Loop Mirror Configuration', *IEEE Photon. Tech. Lett.*, **13**, 1331-1333, 2001.
- 105 M. M. Ohn, S. Y. Huang, M. LeBlanc, R. M. Measures, S. Sandgren and R. Stubbe, 'Distributed strain sensing using long intracore fiber Bragg grating', *Proc. of SPIE*, **2838**, 66-75, 1996.
- 106 S. Huang, M. M. Ohn and R. M. Measures, 'Phase based Bragg strain sensor', *Applied Optics*, **35**, 1135-1142, 1996.
- 107 M. Volanthen, H. Geiger, M. J. Cole, R. I. Laming and J. P. Dakin, 'Low coherence technique to characterise reflectivity and time delay as a function of wavelength within a long fibre grating', *Elect. Lett.*, **32**, 757-758, 1996.
- 108 M. Volanthen, H. Geiger, M. J. Cole and J. P. Dakin, 'Measurement of arbitrary strain profiles within fibre gratings', *Elect. Lett.*, **32**, 1028-102, 1996.

- 109 M. Volanthen, H. Geiger and J. P. Dakin, 'Distributed Grating Sensors Using Low-Coherence Reflectometry', *Journ. of Light. Tech.*, **15**, 2076-2081, 1997.
- 110 Y. J. Rao and D. A. Jackson, 'Recent progress in fibre Optic low-coherence interferometry', *Meas. Sci. Tech.*, **7**, 981-999, 1996.
- 111 C. Yang, S. Yazdanfar and J. Izatt, 'Amplification of optical delay by use of matched linearly chirped fiber Bragg Gratings', *Optics Lett.*, **29**, 685-687, 2004.
- 112 W.N. MacPherson, R.R.J. Maier, J. S. Barton, J. D. C. Jones, A. Fernandez Fernandez, B. Brichard, F. Berghmans, J. C. Knight, P. StJ. Russell and L. Farr, 'Dispersion and refractive index measurement for Ge, B-Ge doped and photonic crystal fibre following irradiation at MGy levels', *Meas. Sci. and Tech.*, **15**, 1659-1664, 2004.
- 113 T. Allsop, K. Sugden and I. Bennion, 'A High Resolution Fiber Bragg Grating Resonator strain sensing system', *Fiber and Integrated Optics*, **21**, 205-217, 2002.

4 Theory of Fibre Optic Bragg Grating and Fabry-Perot Interferometers

4.1 Introduction

This chapter discusses the principles of operation of FBGs in detail, from an introduction to the propagation modes of optical fibres to the concept of the coupling between the forward and backward modes in the perturbed optical fibre system. Coupled mode theory is used to explain the interactions between the various modes, and the phase matching condition for a periodic perturbation of the fibre is presented. The dispersion inside the cavity affects the performance of the bulk FP interferometer. Chirped FBGs are dispersive element in their own rights and when they are used in the FP configuration, the effect of dispersion will change the characteristics of these cavities will be discussed.

4.2 Theory of light propagation in optical fibre

The advent of laser, coherent and monochromatic light as signal sources have made quartz-glass fibre as a transmission medium viable with measured losses below 20dB Km⁻¹. This opened up the prospect of using glass fibre to serve as the transmission media in optical communication systems.

4.2.1 Propagation modes in optical fibres

The propagation properties of the modes of optical fibres have been studied extensively [1]. The propagation of electromagnetic radiation such as light is governed by Maxwell's Equations, solution of which provides rich information on the propagation, dispersion and energy confinement of each mode [2]. The generalised solution for the electric field, E , from Maxwell's Equations consists of a travelling wave, in the form of [1];

$$E = \bar{E} e^{-i(\omega t \pm \beta z)} \quad (4.1)$$

where ω is angular velocity and β the propagation constant given by $\beta = k_0 n_{eff}$, where $k_0 = \frac{2\pi}{\lambda_0}$, λ_0 is the wavelength of the light and n_{eff} is the effective refractive index of the mode. The fibre geometry provides an insight into the light guiding properties of the fibre. For light which coupled into the core of the fibre will be confined and propagate indefinitely in the core region of the optical fibre. The behaviour of light travelling in the core can be described by considering the path of a zig-zag light ray in the core region as illustrated in figure (4.1).

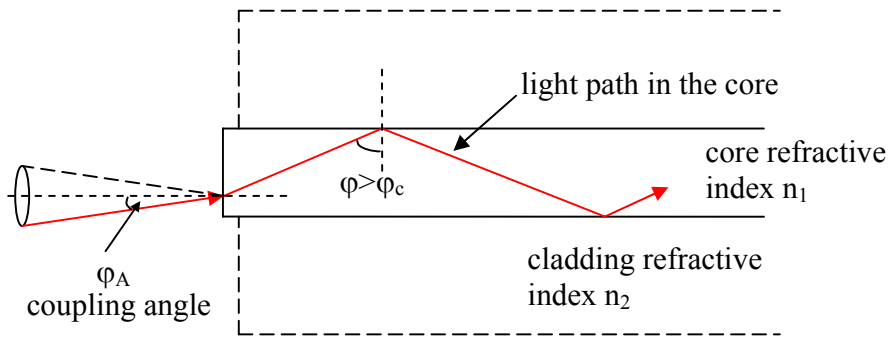


Figure 4.1, illustration of light in ray diagram undergoing internal reflection when the angle of incident to the core/cladding surface is greater than the critical angle ϕ_c

The rays undergo multiple reflections at the core/cladding interface. For rays which are incident upon the interface at angles greater than the critical angle, ϕ_c , total internal reflection occurs. Light propagating this way is thought of as being lossless in an ideal fibre with no absorption. This angle sets a limit on the coupling angle, ϕ_A , through the Fresnel reflection equation relationship at boundaries. The mode propagation constant β is bound by the limits set by the mode and cladding refractive index;

$$n_1 k_0 < \beta < n_2 k_0 \quad (4.2)$$

where the propagation constant, $\beta = \sin \phi$, is the horizontal component that travels down the fibre, n_1 and n_2 are the core and cladding refractive index respectively. Light radiation is a wave-like phenomenon and as well as a direction of travel, it also carries phase information. Taking into account the phase shift experienced on reflection at the boundary surfaces, constructive interference occur will promote a discrete set of angles, which gives rise to a discrete set of propagating constants, β . The extent of the fibre's ability to accept light into its bound modes is determined by the Numerical Aperture (NA). This value is the sine of the half angle of the cone of acceptance, given by [3];

$$NA = \sqrt{n_1^2 - n_2^2} = n_1 \sqrt{2\Delta n} \quad (4.3)$$

Single-mode fibres typically have an NA of ~ 0.1 whereas the NA of multimode fibres is in the range 0.2 to 0.3.

A summary to the guided modes solution to the Maxwell's equation in cylindrical coordinates is presented in Appendix A. Knowledge of the modal properties is fundamental for the understanding of the behaviour of light in a perturbed environment such as encountered with FBGs.

4.2.2 LP modes and cut off

The exact solution of the wave equation for a step index fibre is very complicated involving all six non-zero field components in the so called hybrid EH_{lm} and HE_{ml} modes [1]. A simplification to the solution can be arrived at using the approximation for the so called 'Weak guidance'[2] where the fractional refractive index difference is assumed to be small.

$$\Delta = \frac{(n_1 - n_2)}{n_1} = \frac{\Delta n}{n_1} \ll 1 \quad (4.4)$$

Using the Normalised Frequency, V , given by[2];

$$V^2 = (ah)^2 + (a\kappa)^2 \tag{4.5}$$

where $h^2 = n_1^2 k_0^2 - \beta^2$ and $\kappa^2 = \beta^2 - n_2^2 k_0^2$. The graph in figure (4.2) shows the dispersion of a selection of *LP* modes.

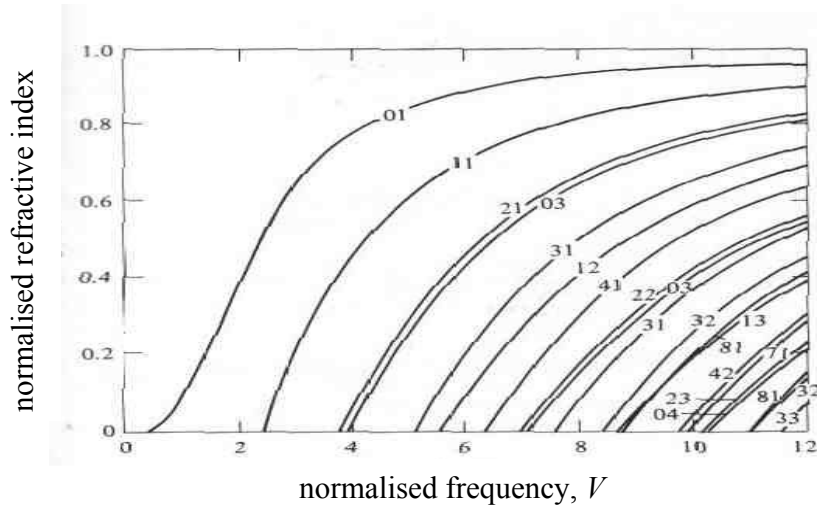


Figure 4.2, a plot of normalised refractive index against normalised frequency, *V* for the *LP* modes [2]

In the weakly guiding approximation, the lowest order *LP* mode, the *LP*₀₁, has no low-frequency cutoff. This mode is found to be identical to the exact *HE*₁₁ mode. The onset of the next *LP* mode, the *LP*₁₁, has a cutoff at *V* = 2.401. For some applications, fibres which support only a few modes or even just a single mode over a certain wavelength range are required. The condition for single-mode operation is when the normalised frequency *V* be less than < 2.405. The normalised frequency, *V* in equation (4.5), can be written as;

$$V = \frac{2\pi a}{\lambda} \sqrt{n_1^2 - n_2^2} \tag{4.6}$$

where *a* is the core radius and λ is the free space wavelength. The number of modes supported by an optical fibre is reduced as the fibre diameter is decreased, or when it is operated at a longer wavelength. Single mode fibres in the visible and infra-red part of the spectrum usually necessitate core diameters of only a few microns.

4.2.3 The effect of dispersion in light propagation

Light propagation can be considered as a superposition of many plane-wave solutions which satisfy Maxwell's equations. The electric field, E , in a Fourier representation, can be imagined to consist of a frequency bandwidth, $\Delta\omega$ centre at a frequency, ω_0 [3];

$$E(t) = \int_{\Delta\omega} \xi(\omega) \exp(i\omega t) d\omega \quad (4.7)$$

where $\xi(\omega)$ is the amplitude of the component of the plane wave, ω . After traveling a distance, z , the different components of the wave will have their phases changed by the amount $\beta(\omega)z$ where β can be expanded using the Taylor series around the central β_0 ;

$$\beta(\omega) = \beta_0 + \frac{d\beta}{d\omega} \Delta\omega + \frac{1}{2} \frac{d^2\beta}{d\omega^2} \Delta\omega^2 + \dots$$

where β_0 is the propagation constant at ω_0 . Substituting in equation (4.7),

$$E(z, t) = \int_{\Delta\omega} \xi(\omega) \exp i(\omega t - (\beta_0 + \frac{d\beta}{d\omega} \Delta\omega + \frac{1}{2} \frac{d^2\beta}{d\omega^2} \Delta\omega^2 + \dots)z) d\omega$$

which can be written as the propagation of a plane wave modulated by an envelope function whose phase velocity is given by; $(\beta/\omega)^{-1}$ and group velocity is given by; $(d\beta/d\omega)^{-1}$. The effect of dispersion (the relationship between ω and β) will cause the different components, ω to arrive at different times. The delay per unit length is given by [4];

$$\tau = \frac{1}{c} \frac{d\beta}{dk} = \frac{d\beta}{d\omega}$$

where c is the speed of light.

4.2.4 Phase matching and Bragg condition

Systems involving the exchange of energy can be represented by coupled mode equations with appropriate coupling constants. The coupled mode equation governing the forward and backward propagating modes in the FBGs can be written as [5];

$$\begin{aligned} \frac{dF}{dz} + i\delta F &= -ik_{ac}^* B \\ \frac{dB}{dz} - i\delta B &= +ik_{ac} F \end{aligned} \quad (4.8)$$

where F (Reference) represents the forward propagating mode, B (Signal) is the backward propagating mode and δ is the effective detuning given by;

$$\delta = k_{dc} + \frac{1}{2} \left(\Delta\beta - \frac{d\phi(z)}{dz} \right) \quad (4.9)$$

where $\Delta\beta = \beta_u + \beta_v - 2\pi N/\Lambda$, is the detuning, (4.10)

$$k_{dc} = n\omega\epsilon_o \iint \overline{\Delta n \xi_u \xi_u} dx dy \text{ is the dc coupling constant}$$

and

$$k_{ac} = n\omega\epsilon_o \iint \frac{\Delta n}{2} \xi_u \xi_v dx dy \text{ is the cross coupling constant.}$$

Since β_u and β_v are functions of wavelength, the $\Delta\beta$ has a strong spectral dependence. The strongest response is observed where, $\Delta\beta = 0$, resulting in a synchronous transfer of power between the two modes, (ie. when they are phase matched). The phase matched condition is given by[5];

$$\beta_u + \beta_v = \frac{2\pi}{\Lambda} \quad (4.11)$$

where, $\beta_u = \frac{2\pi n_{eff}^u}{\lambda}$ and $\beta_v = \frac{2\pi n_{eff}^v}{\lambda}$

where n_{eff}^u and n_{eff}^v are the mode index of the forward and backward propagating modes. Equation (4.11) can be written as;

$$\Lambda = \frac{\lambda}{n_{eff}^v + n_{eff}^u} \quad (4.12)$$

Consideration of the conservation of energy promotes the coupling of modes with the same optical frequency, ω . For identical forward and counter propagating modes, equation (4.12) produces the Bragg condition;

$$\lambda_B = 2n_{eff} \Lambda \quad (4.13)$$

where Λ is the period. The Bragg wavelength is reflected predominantly.

4.2.5 FBG parameters

The coupled mode equations for the forward and the backward propagating modes, when applied to a uniform period grating, can be solved using appropriate boundary conditions. Consider figure (4.3), where the grating has a length of L_g and the boundary conditions assume a forward propagating mode with $F(0) = 1$ and that the backward propagating mode, at the end of the grating, will be zero, $B(L_g) = 0$ as there are no perturbing beyond the end of the grating.

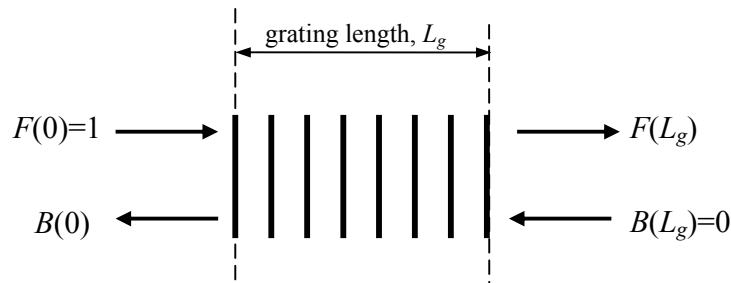


Figure 4.3, schematic of the grating with the boundary conditions as shown.

For uniform grating, $d\phi/dz = 0$, and at the phase matched condition, $\Delta\beta = 0$, It is possible to show that a closed form solution exists for the reflectivity, $R(0)$, which is given by[5];

$$R = \frac{|k_{ac}|^2 \sinh^2(\alpha L_g)}{|k_{ac}|^2 \cosh^2(\alpha L_g) - \delta^2} \quad (4.14)$$

for $|k_{ac}| < \delta$, where $\alpha = \sqrt{|k_{ac}|^2 - \delta^2}$

The reflectivity in equation (4.14) has a decay nature and drops off exponentially along the perturbation region as power is transferred from the forward to the backward propagating mode. The maximum reflectivity R_{max} is then obtained from equation (4.14) when $\delta = 0$, ie. at the phase matching condition, $\lambda_B = 2n_{eff}\Lambda$;

$$R_{max} = \tanh(k_{ac}L_g) \quad (4.15)$$

The first two zeros of equation (4.14) may be used to approximate the full Bragg grating bandwidth given by;

$$\Delta\lambda = \frac{\lambda^2}{2\pi n_{eff} L} \sqrt{(k_{ac}L_g)^2 + \pi^2} \quad (4.16)$$

The condition for weak grating corresponds to $k_{ac}L_g \ll \pi$, in which case the bandwidth is an inverse function of the grating length;

$$\Delta\lambda = \frac{\lambda^2}{2n_{eff} L_g} \quad (4.17)$$

This is length limited and while if the converse is true, $k_{ac}L_g \gg \pi$, ie. for a strong grating, (4.28) becomes;

$$\Delta\lambda = \frac{\lambda^2 k_{ac}}{2n_{eff}} \quad (4.18)$$

and the bandwidth depends on the coupling constant k_{ac} .

4.2.6 Chirped FBG and the grating phase shift

A variation of the grating period along the length of the FBG is termed chirp. Chirp can also be achieved by a variation of the mode refractive index. These different forms of chirp can both be represented by an additional phase function, $\phi(z)$, in the perturbed polarisation caused by the refractive index modulation given by[5];

$$P_{grating} = 2n\epsilon_0 \left[\bar{\Delta n} + \frac{\Delta n}{2} \left(e^{i((2\pi N/\Lambda)z + \phi(z))} + cc \right) \right] E$$

The chirp changes the effective detuning parameters, $\Delta\beta$ in equation (4.9);

$$\delta = k_{dc} + \frac{1}{2} \left(\Delta\beta - \frac{d\phi(z)}{dz} \right)$$

Period chirp is created by a change in phase of the refractive index modulations analogous to a phase modulated carrier. The index perturbation can be written as a sinusoidal function;

$$\cos(Kz + \phi(z))$$

which has constant spatial frequency, given by; $K = \frac{2\pi}{\Lambda}$ with an additional position dependent phase variation $\phi(z)$ to represent the change in periodicity. The chirp could be viewed as a perturbation with a varying spatial frequency [6];

$$\cos(K + \Delta K)(z)$$

The relationship between the period, Λ , and the spatial frequency can be written as;

$$dK = -\frac{2\pi}{\Lambda^2} d\Lambda \quad (4.19)$$

The rate of change of phase with distance along the grating, z , can be derived;

$$\frac{d\phi}{dz} = \Delta K \quad (4.20)$$

$$\frac{d\phi}{dz} = -\frac{2\pi}{\Lambda^2} d\Lambda \quad (4.21)$$

From the Bragg condition; $\lambda = 2n\Lambda$, equation (4.21) becomes[7]

$$\frac{d\phi}{dz} = -\frac{4\pi n}{\lambda^2} \frac{d\lambda}{dz} z \quad (4.22)$$

where $\frac{d\lambda}{dz}$ is the chirp rate of the FBG. Chirp in FBG can be represented by a variation of the periodicity or a variation of the mode refractive index along the grating length or a combination of the two or simply by an additional position dependent phase along the grating.

4.3 Theory of the Fabry-Perot interferometer

The bulk optic Fabry-Perot (FP) cavity, which consists of a pair of highly reflective optically flat surfaces arranged to form a resonance device is shown figure (4.4). When light enters into an FP etalon, it experiences multiple reflections between the highly reflective surfaces. When the multiple reflections are brought together by a focusing lens, they interfere coherently and narrow fringes are observed.

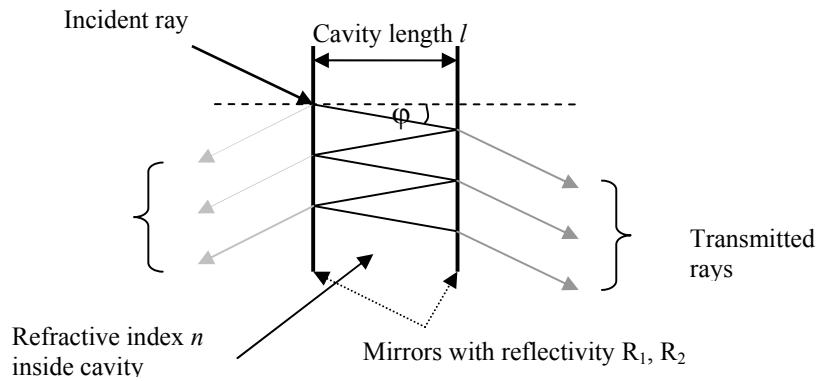


Figure 4.4, arrangement of the FP configuration.

FP can be constructed in many ways, a bulk optical FP is a free space optical device. A fibre type FP etalon has been demonstrated whereby one of the reflective surfaces is formed by the cleaved end of a fibre coated with a highly reflective material. The cavity is formed between the cleaved fibre end and a mirror, figure (4.5). In this configuration, alignment is critical for light to couple back into the fibre from the mirror, making this configuration inefficient.

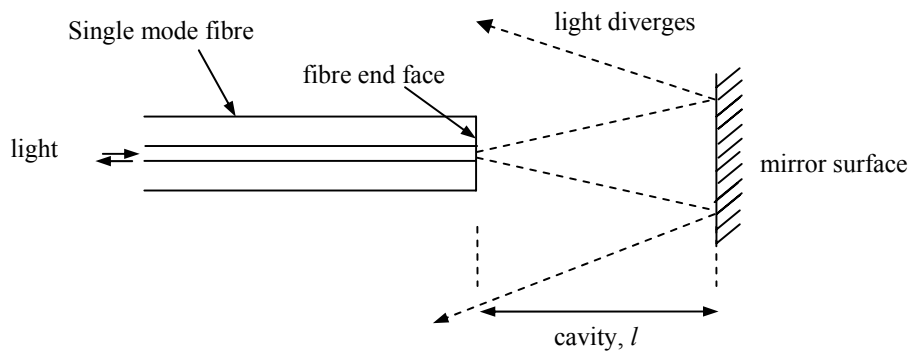


Figure 4.5, illustrates a FP cavity formed between a fibre end and a mirror.

An extension to this form of FP consists of the formation of an air cavity between two fibre ends, which requires supporting members to keep the two fibres in place, figure (4.6).

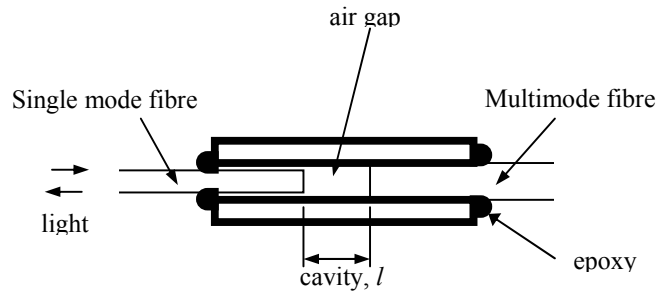


Figure 4.6, illustrates a FP cavity formed between 2 fibre ends with supporting members.

The alignment and strength of the device can be improved by creating mirrors within the fibre, by means of fusion splicing fibre ends together, figure (4.7). This creates mirrors within the fibre and offers all the merits of all fibre systems, but the integrity of the physical strength and the optical properties of the fibre can be compromised by the intrusion.

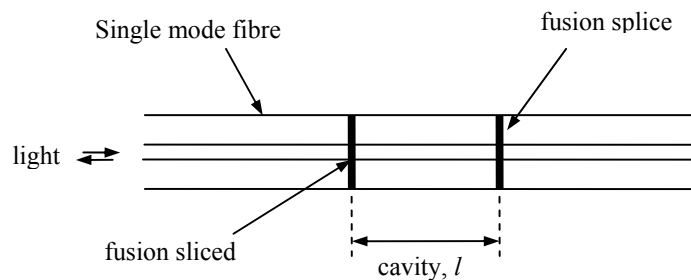


Figure 4.7, illustrates a FP cavity formed by fusion splicing piece of fibres together with a reflective surface to form reflective mirrors.

A way to overcome this problem is to inscribe a pair of identical FBGs within the fibre, with an appropriate physical separation. The FBGs act as the reflectors, creating cavity within the fibre core, with little intrusion to both the physical strength and the guiding properties of the fibre. The versatility of the inscribing technique allows a series of such FBG FP to be inscribed in the same fibre, with each occupying a different wavelength bandwidth, exploiting wavelength division multiplexing capability of FBGs.

4.3.1 The bulk Fabry-Perot Etalon

An FP Etalon, figure (4.4) is essentially an optical resonator. Consider normal incidence case, at which φ is zero. When the incident light enters the cavity, it will be reflected back and forth inside the cavity. The reflected waves at the two mirror surfaces will have a phase delay equivalent to twice the optical path length, nl . For a monochromatic wave of wavelength, λ , of a single polarisation, the round trip phase shift (RTPS) of the cavity is given by;

$$\theta = \frac{4\pi nl}{\lambda} \quad (4.23)$$

where n is the refractive index of the medium in the cavity. The collections of wavelets will interfere when brought together. When the phase delay is an integer multiple of 2π , the reflected waves interfere constructively and when they are of odd multiples of 2π , then they interfere destructively. Thus the cavity expresses a preference for fields with the right wavelength for which the RTSP is of multiples of 2π . Assuming a lossless cavity, the mathematical treatment of the transmitted intensity results in the expression [8];

$$I_T = I_o \frac{(1 - R_1)(1 - R_2)^2}{(1 - R_1)(1 - R_2) + 4\sqrt{R_1 R_2} \sin^2(\theta/2)} \quad (4.24)$$

where R_1 and R_2 are the reflectivities of the two mirrors. The FP cavity acts as a multiple beam interferometer, and narrow transmission fringes are seen in the output of the FP. Such devices may be used as filters by using a fixed cavity length, or as optical spectral analysers by tuning the cavity length for scanning spectral information in the signals.

From the equation (4.24), describing the transmission of the FP, the maximum intensity occurs when the RTPS, θ is an integer multiple of 2π radian. The condition can be achieved by changing the cavity length, l or via a change in the illuminating wavelength.

The change in the illuminating wavelength from one cavity resonant wavelength to the next which gives rise to a change in the RTSP of 2π radian, is termed the Free Spectral Range (FSR) and it is given by in terms of optical frequency, ν ;

$$FSR = \Delta\nu_{FSR} = \frac{c}{2nl} \quad (4.25)$$

The value of FSR is the measure of the device sensitivity. For highly reflective mirrors, the width of the resonant cavity mode is small and when the reflectance decreases, the width of the resonance cavity mode broadens. The full width half maximum of the resonant frequency is given by[8];

$$\Delta\nu_{1/2} = \Delta\nu \left(\frac{1 - (R_1 R_2)^2}{\pi(R_1 R_2)^{1/4}} \right) \quad (4.26)$$

and the Finesse (F_f) of the cavity is given by;

$$F_f = \frac{\Delta\nu_{FSR}}{\Delta\nu_{1/2}} = \frac{2\pi}{\Delta\delta_{1/2}} = \frac{\pi(R_1 R_2)^{1/4}}{1 - (R_1 R_2)^{1/2}} \quad (4.27)$$

The value of F_f is a measure of the device's resolution and it is related to the reflectivity, R as well as the losses incurred inside of the cavity. The wavelength resolution is given by the product of the FSR and the Finesse, F_f . Large FSR can only be obtained at the expense of a lower wavelength resolution and small FSR will give a higher sensitivity. A large FSR translates to large dynamic range.

The maximum and minimum transmissions are given by[8],

$$I_{\max} = \frac{(1 - R_1)(1 - R_2)}{(1 - \sqrt{R_1 R_2})^2} \quad (4.28)$$

and

$$I_{\min} = \frac{(1 - R_1)(1 - R_2)}{(1 + \sqrt{R_1 R_2})^2} \quad (4.29)$$

The visibility, V is a very important factor and it determines how well the spectral features can be resolved. The visibility is given by;

$$V = \frac{I_{\max} - I_{\min}}{I_{\max} + I_{\min}} \quad (4.30)$$

The visibility also depends on both the state of polarisation and the degree of coherence of the interfering light beams. When the reflectivity R is small, such as that encountered in the Fresnel reflection in air/glass interface in cleaved fibre ends, the spectrum becomes sinusoidal. Assuming $R_1 = R_2$, from (4.40-4.42), the visibility, V , in the transmission becomes very small. In reflected intensity is given as, $I_R = (1 - I_T)$ and assuming there is no loss in the cavity, then the visibility, V in reflection will have a value near to one, and the fringes can be resolved but at the cost of having reduced intensity, as illustrated in figure (4.8c).

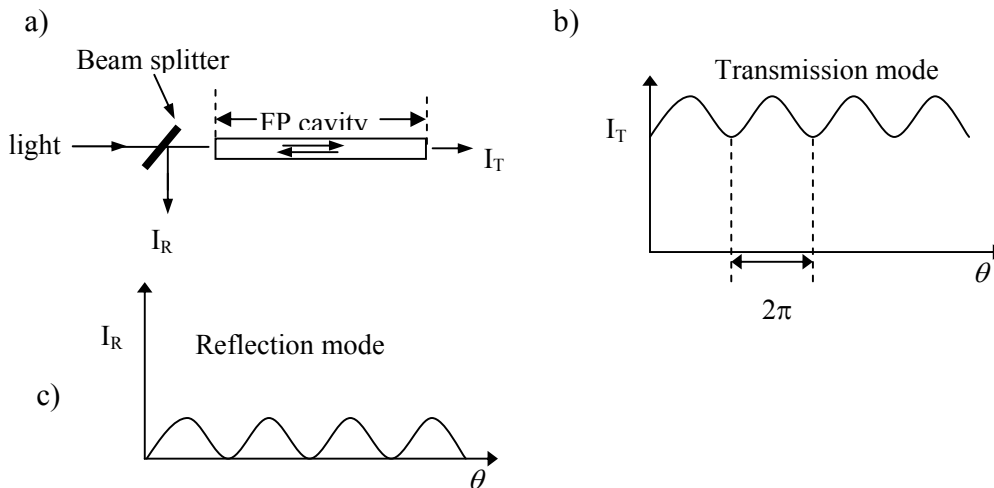


Figure 4.8a, schematic diagram showing a fibre FP cavity consisting of a section of an optical fibre forming a cavity with its' ends cleaved such that $R \sim 4\%$. b) showing the transmission response with a small visibility but high intensity throughput where as in c) the reflection response has a high visibility but a low intensity throughput.

In the low Finesse regime, which is encountered in fibre/air interface where the reflectivity is small, ($R \sim 4\%$), assuming that $R_1 = R_2$ and a lossless cavity, the reflectance according to equation (4.24) is [9];

$$I_r = \lim_{R \rightarrow 0} \left(I_o - I_o \frac{(1-R)^2}{(1-R)^2 + 4R \sin^2(\theta/2)} \right)$$

$$\lim_{R \rightarrow 0} I_r = I_o (1 + V \cos \theta) \quad (4.31)$$

where V is given by;

$$V = \frac{2R(1-R)^2}{R + R(1-R)^2} \quad (4.32)$$

The response indicated by equation (4.31) corresponds to the cosinusoidal transfer function of the two beam interferometer. This is most appropriate for sensing applications as many phase measurement techniques [10] have been developed over the years which could be used for demodulation of low Finesse FP sensors.

4.3.2 Dispersive Bulk Fabry-Perot

The cavities of interest in this thesis are based on chirped FBGs, which are dispersive elements in their own rights. Parallels can be drawn from the analysis on the dispersive cavity based on the bulk type FP. The effect of dispersion of the medium within an interferometer changes the Optical Path Length (OPL) as a function of wavelength, which in turn has an effect on the RTPS of the device. The change in the Optical Path Length, nl , with wavelength is given by [11];

$$\frac{\partial(nl)}{\partial \lambda} = n \frac{dl}{d\lambda} + l \frac{dn}{d\lambda} \quad (4.33)$$

Vaughan [12] presented a treatment for a bulk FP with a dispersive medium inside the cavity in which a large change in the FSR is observed. The absorption spectrum of the medium has a strong line in a wavelength region. The effect of absorption, through the Kamers-Kronig relations, causes dispersion in the material, whereby a large change of refractive index with wavelength occurs [12]. The condition for the on-axis cavity resonance in transmission for the type of device can be written as;

$$p\lambda=2l(\lambda)n(\lambda) \quad (4.34)$$

where p is an integer order of interference, and l and n are now functions of wavelength. Differentiating equation (4.34) gives;

$$\delta p\lambda + p\delta\lambda = 2\left(\frac{d(nl)}{d\lambda}\right)\delta\lambda \quad (4.35)$$

which may be rearranged to produce;

$$-\frac{c\delta\lambda}{\lambda^2} = \frac{c\delta p}{p\lambda} \frac{1}{\left(1 - \frac{2}{p} \frac{d(nl)}{d\lambda}\right)} \quad (4.36)$$

where c is the speed of light. For a unity change in the interference order, $\delta p = 1$, which is the definition of the FSR, using equation (4.34), equation (4.36) can be rewritten to describe the detuning of the FSR of a dispersive cavity, $\Delta\nu_{FSR}$;

$$\Delta\nu_{FSR} = \frac{\Delta\nu_0}{\left(1 - \frac{2\lambda}{2nl} \frac{d(nl)}{d\lambda}\right)} \quad (4.37)$$

where $\Delta\nu_0 = \frac{c}{2nl}$ is the conventional definition of the FSR. For a bulk FP etalon, the cavity length, l is fixed, and is independent of wavelength. The only dispersive effect available is within the material that constitutes the cavity. If the refractive index change

with wavelength is significant, then the change in optical path with wavelength, equation (4.33) can be reduced to; $\frac{d(nl)}{d\lambda} = l \frac{dn}{d\lambda}$ and substituting into equation (4.37);

$$\Delta\nu_{FSR} = \frac{\Delta\nu_0}{\left(1 - \frac{\lambda}{n} \frac{dn}{d\lambda}\right)} \quad (4.38)$$

If the material dispersion is very small, there is no noticeable change in FSR for the device, such that $\Delta\nu_{FSR} \sim \Delta\nu_0$. However if a material exhibits dispersion, there is a significant modification to the FSR value in equation (4.38). If a material whose dispersion can be controlled or tailor made with a specific wavelength response, is used in the FP cavity, the denominator in equation (4.38) can tend to zero, with the results that the $\Delta\nu_{FSR}$ can be infinite. The device then becomes insensitive to wavelength change. The condition for this to occur is;

$$\frac{n}{\lambda} = \frac{dn}{d\lambda} \quad (4.39)$$

This condition is independent of the cavity length, l . The condition holds if the ratio of the refractive index to wavelength is equal to the dispersion. If the condition in equation is not satisfied, as the wavelength is tuned away from this condition, the wavelength insensitive condition will no longer hold and the FSR will change. This observation depends on the functional form of the dispersion. Thus the wavelength response can be tuned by virtue of the illuminating wavelength and is not solely determined by the cavity length, l , as it would have been for the conventional FP response. Equation (4.38) can be written to allow comparison with the conventional cavity response[13];

$$\Delta\nu_{FSR} = \frac{c}{2\left(n - \lambda \frac{dn}{d\lambda}\right)l} = \frac{c}{2n_{eff}l} \quad (4.40)$$

where the effective refractive index term, n_{eff} in the conventional cavity response is modified by the material dispersion term, $\lambda \frac{dn}{d\lambda}$.

Chirped FBGs are dispersive elements and they offer a different dispersive effect, namely position detuning with wavelength, rather than refractive index dependence with wavelength. This distinction has a certain influence when they form FP interferometer.

4.3.3 Fibre Bragg Grating Fabry-Perot

Using FBGs as partial reflectors, FP can be created by writing 2 FBGs separated by a cavity length sharing the same wavelength bandwidth. Chirped FBG can be used the same way to provide the FP with a larger operating bandwidth.

4.3.3.1 Uniform Period Fibre Bragg Grating Fabry-Perot

The simplest type of fibre FBG FP consists of two uniform period FBGs separated by a cavity written in an optical fibre with the FBGs occupying the same wavelength [14,15,16]. Figure (4.9) shows the diagram of a FBG FP.

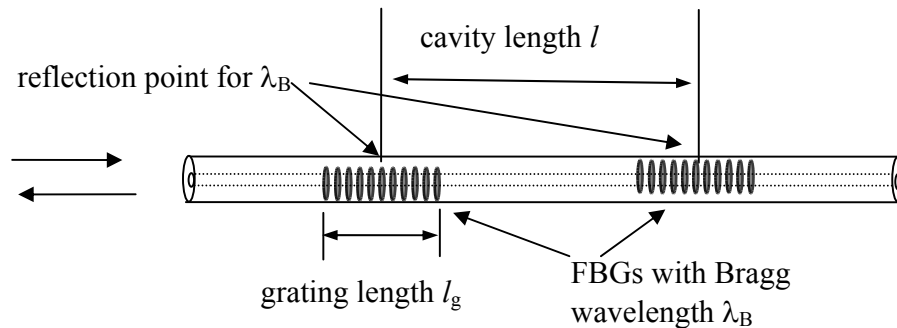


Figure 4.9, uniform FBG grating FP

The Bragg wavelength is given by equation (4.13) and the typical FBG bandwidth is given by equation (4.16-4.17) depending on the strength of the coupling between the backward and forward waves. At zero detuning, the peak reflectivity of the FP filter, R_{FP} , with FBGs of identical reflectivity, R , is given by [17];

$$R_{FP} = \frac{4R}{(1 + R)^2} \quad (4.41)$$

Increasing the cavity length, l between the two gratings enables multiple band-pass peaks to appear within the FBG stop band as shown in figure (4.10).

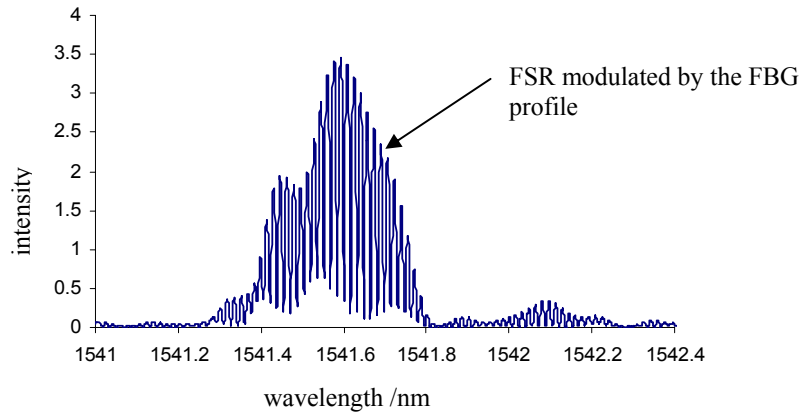


Figure 4.10, shows the FBG FP wavelength response shown the cavity resonance mode modulated by the FBG stopband.

These cavity resonance modes are given by the conventional *FP* response, FSR [17];

$$FSR = \Delta\nu = \frac{c}{2nl(\lambda)} \quad (4.42)$$

It has a bulk FP like characteristics and operates over a limited bandwidth, whose value depends on the overlap of the two FBGs' bandwidths. Analytical solutions to the uniform FBG FP have been developed by Legoubin et al [17] and the results indicate a variation in FSR of the order of 10% [17] for a uniform FBG FP. This variation is attributed to the distributed nature of FBGs as discussed in section (3.4).

4.3.3.2 Chirped Fibre Bragg Grating Fabry-Perot

Chirped FBGs can be fabricated by various methods, discussed in section (2.4.3). When the chirped FBG is illuminated by a broad band source, different wavelength components experience a different group delay resulting from the wavelength dependence of the resonance positions along the FBG. This dispersive effect has been used for pulse compression [18,19]. The chirped FBG FP offers a larger bandwidth [20,21,22]

compared to a uniform FBG FP provide a larger dynamic range. Figure (4.11) illustrates a chirped FBG FP which consists of two chirped FBGs separated by a cavity length.

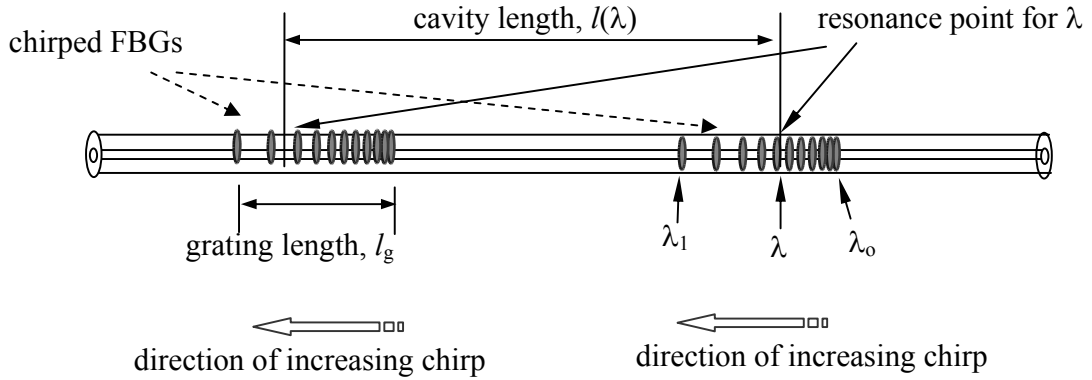


Figure 4.11, shows a chirped FBG FP, which consists of 2 chirped FBGs separated by cavity length, where $l(\lambda)$ is a wavelength dependent cavity length and the total chirps, $\Delta\lambda = \lambda_1 - \lambda_0$ where $\lambda_1 > \lambda_0$.

Consider the phase response of the chirped FBG FP cavity. Using the simple FP analysis in which the RTPS response is considered, equation (4.23), and differentiating with respect to wavelength gives [23];

$$\frac{d\theta}{d\lambda} = -\frac{4\pi nl}{\lambda^2} + \frac{4\pi}{\lambda} \left(\frac{\partial(nl)}{\partial\lambda} \right) \quad (4.43)$$

where $\frac{\partial(nl)}{\partial\lambda}$ is the change in OPL with wavelength. Equation (4.43) can be written as;

$$d\theta = \frac{4\pi}{\lambda} \left(\frac{d(nl)}{d\lambda} - \frac{nl(\lambda)}{\lambda} \right) d\lambda \quad (4.44)$$

The cavity response can be derived by considering the change of wavelength required to provide a 2π change in RTPS, equation (4.44). This is the definition of the FSR for the cavity, $\Delta\lambda_{FSR}$;

$$2\pi = \frac{4\pi}{\lambda} \left(\frac{d(nl)}{d\lambda} - \frac{nl(\lambda)}{\lambda} \right) \Delta\lambda_{FSR} \quad (4.45)$$

This can be simplified to provide a general expression for the FSR;

$$\Delta\lambda_{FSR} = \frac{\lambda}{2 \left(\frac{d(nl)}{d\lambda} - \frac{nl(\lambda)}{\lambda} \right)} \quad (4.46)$$

When there is no dispersion in the cavity, there is no change in the OPL with wavelength such that, $\frac{d(nl)}{d\lambda} = 0$. The FSR in equation (4.46) can then be reduced to the conventional non dispersive FP response;

$$\Delta\lambda_{FSR} = -\frac{\lambda^2}{2nl(\lambda)} \quad (4.47)$$

Equation (4.47) has the form of the standard FP response and has a standard FP behaviour where the FSR is determined by the length of the cavity. However the cavity length has a wavelength dependence, which may modify the FSR response. The effect of the wavelength dependent cavity length on the FSR variation is observed in the off-resonance wavelength region of the uniform period FBG FP response [17] where the penetration into the grating is greater giving rise to a longer cavity length than the on-resonance wavelength. It is also observed in the overlapping chirped FBG FP response [24, 25] as well as in the chirped FBGs Michelson interferometers [26] due to the distributed nature of the chirped FBG giving rise to different cavity length, $l(\lambda)$ for different wavelengths. An analytical equation for the FSR, equation (4.47), has been derived for such chirped FBGs cavities where the cavity length, $l(\lambda)$ is expanded about a reference wavelength using the Taylor expansion [26, 25, 27]. The response of such cavities can be explained using the conventional non dispersive cavity response, equation (4.47), though the chirped FBGs are dispersive elements.

As discussed in section (4.3.2) for cavities containing medium which are dispersive and in section (3.6) for cavities formed with dispersive fibre, the dispersion has an effect on the cavity where there is a change in the FSR response compared to the standard FP response to changes in the illuminating wavelength, equation (4.46). Chirped FBG provides a different means of dispersion, whereby a positional dependence of the reflection points of the different wavelengths inside the grating will also have an effect on the RTPS and thus the FSR of the chirped FBG FP cavities.

In a chirped FBG FP cavity, the wavelength dependent cavity length provides the means for dispersion, $\frac{dl}{d\lambda}$. Assuming that the modal and waveguide contributions to dispersion are small and can be neglected, ie $\frac{dn}{d\lambda} \sim 0$, the change in OPL, with wavelength;

$$\frac{d(nl)}{d\lambda} = n \frac{dl}{d\lambda} + l \frac{dn}{d\lambda}$$

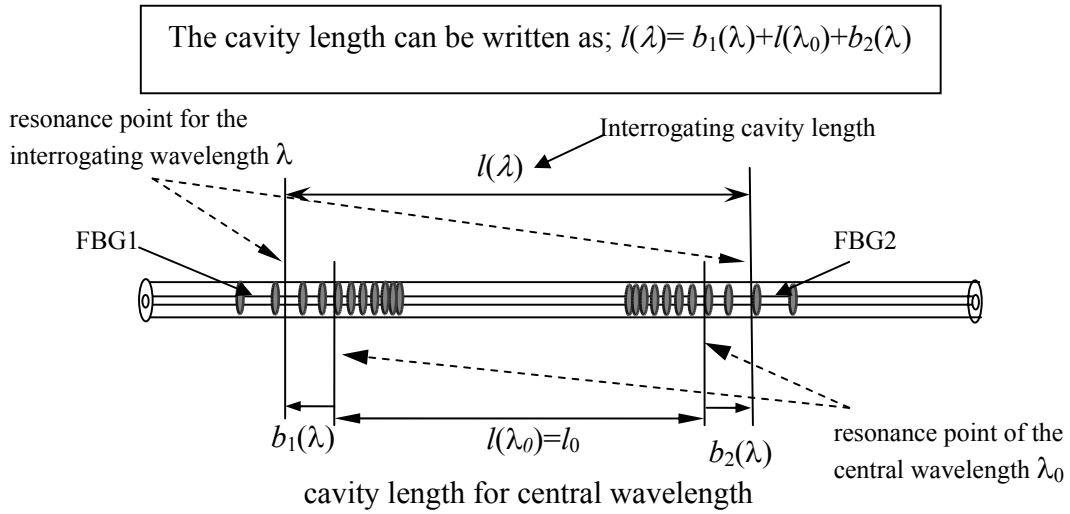
can be reduced to;

$$\frac{d(nl)}{d\lambda} = n \frac{dl}{d\lambda}$$

Substituting this back to the general expression for the FSR, equation (4.46), the general equation for the FSR of the chirped FBG FP can be written as;

$$\Delta\lambda_{FSR} = \frac{\lambda}{2 \left(n \frac{dl}{d\lambda} - \frac{nl(\lambda)}{\lambda} \right)} \quad (4.48)$$

Consider a chirped FBG FP configuration as shown in figure (4.12). The orientation of the chirp direction is arbitrary, but the FBGs have the same bandwidths.



where; b_1 , b_2 are detuned position about the central wavelength, λ_0 in FBG1 and FBG2 respectively.

Figure 4.12, illustration of the chirped FBG FP cavity with FBG having the same central wavelength, λ_0 , where the cavity length for the, λ_0 , is the distance between the grating centres, $l(\lambda_0) = l_0$. The cavity length, $l(\lambda)$, changes with different illumination wavelength.

Assuming that the reflection position of the central wavelength, λ_0 , is located at the grating centres, FBG1 and FBG2, the cavity length for the centre wavelength is given by the distance between the grating centres; $l(\lambda_0) = l_0$. When the cavity is illuminated by a wavelength, λ , the wavelength will see a cavity length measured from the respective reflection position inside the two gratings which can be written as;

$$l(\lambda) = b_1(\lambda) + l(\lambda_0) + b_2(\lambda)$$

where b_1 and b_2 are the detuned reflection positions for the wavelength λ about the centre wavelength, λ_0 . The rate of change of the cavity length with wavelength is given by;

$$\frac{dl(\lambda)}{d\lambda} = \frac{db_1(\lambda)}{d\lambda} + \frac{db_2(\lambda)}{d\lambda} \quad (4.49)$$

where, $l(\lambda_0)=l_0$ is constant for all wavelength. Substituting into the general equation (4.48) gives;

$$\Delta\lambda_{FSR} = \frac{\lambda}{2\left(n\left(\frac{d(b_1)}{d\lambda} + \frac{d(b_2)}{d\lambda}\right) - \frac{nl(\lambda)}{\lambda}\right)} \quad (4.50)$$

Two factors affect the change in the FSR response. The first is the detuned position, $l(\lambda)$, and the second which changes the OPL with wavelength;

$$\frac{dl}{d\lambda} = \frac{db_1}{d\lambda} + \frac{db_2}{d\lambda}$$

a factor which causes different wavelengths to experience different OPL. The magnitude and direction of the rate of position detuning with wavelength depends on the orientation and the parameters of the chirped FBGs. Consider a cavity comprising of 2 chirped FBGs with arbitrary orientation as shown in figure (4.13).

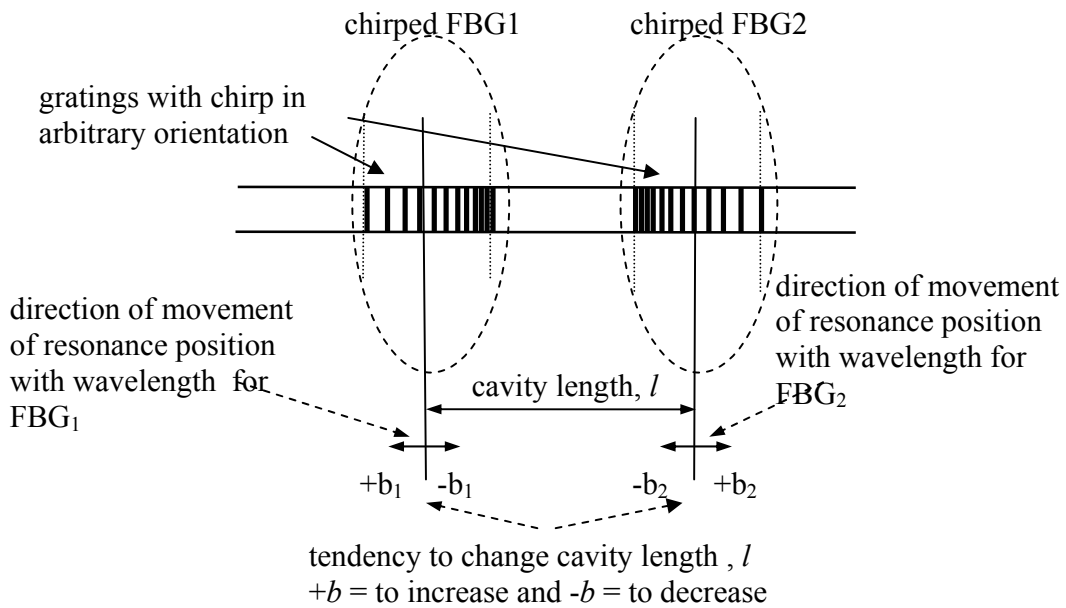


Figure 4.13, diagram showing the tendency to change the cavity length, l by the effect of movement of the resonance points within the grating, $+b$ to increase the cavity length and $-b$ to decrease the cavity length.

The tendency to change the cavity length, l by the direction of movement of the reflection points inside the two gratings is illustrated in figure (4.13). Depending on the orientation of the chirped FBGs, the movement of the reflection point with detuned wavelength will either to increase/increase the cavity length of the illuminating wavelength. The reflection position moves in the direction of the increasing chirp of the FBG with increasing wavelength. From figure (4.13), the tendency for the movement of the reflection point to increase the cavity length is associated with it a positive wavelength detuned position, $+b$ whereas the opposite effect will have a negative wavelength detuned position, $-b$ for the gratings. The changes in the cavity length with wavelength have an effect on the RTSP and thus the FSR of these dispersive chirped FBG cavities.

4.3.3.3 Co-propagating chirped FBG Fabry-Perot cavity

The co-propagating cavities are chirped FBG FP cavities which consist of 2 identical chirped FBG separated by a distance and that the orientation of the increasing chirp of the FBGs are aligned in the same directions as shown in figure (4.14). Changing the illumination wavelength changes the resonance position inside the chirped FBGs and thus alters the length of the cavity. The movement of the reflection points with wavelength in a chirped FBG is to move in the direction of the increasing chirp. Consider the co-propagating chirped FBG FP cavity in figure (4.14a). In FBG1, the tendency for the movement of the reflection point with wavelength is to reduce the cavity length whereas in FBG2, the movement of the reflection point with wavelength is to increase the cavity length. If FBG1 and FBG2 are identical, then the movement of the distance between the reflections points inside the 2 chirped FBG remains unchanged thus the cavity length remains constant. The same argument applies to the co-propagating chirped FBG FP with the direction of the increasing chirp oriented in the same direction, figure (4.14b) but opposite to the cavity in figure (4.14a).

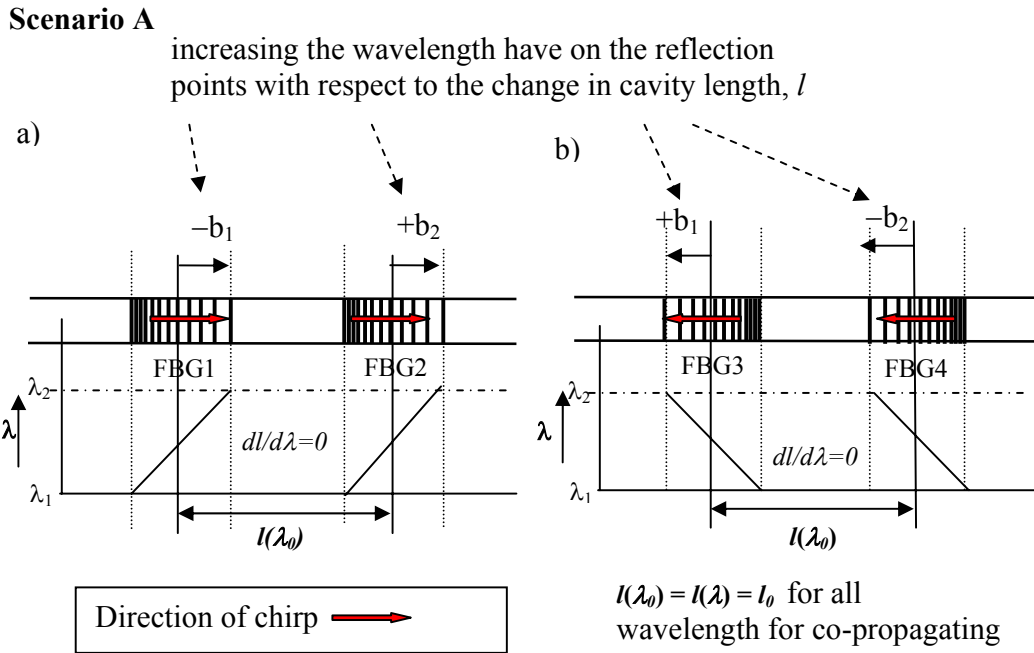


Figure 4.14, shows the co-propagating cavities of chirped FBG FP with chirps of the FBG oriented in the same direction as shown in a) and in the b) but in the opposite sense. When the wavelength is increased, the movement of the reflection point moves in the direction of the increasing chirp. The net effect in the 2 chirped FBGs cancels out each other such that there is no change in the cavity length.

For identically chirped FBGs, the magnitude of movement of the reflection point with wavelength;

$$\left| \frac{db_1}{d\lambda} \right| = \left| \frac{db_2}{d\lambda} \right| = \left| \frac{db}{d\lambda} \right|$$

are the same and that they act against each other as shown in figure (4.14). Equation (4.49) becomes; $\frac{dl}{d\lambda} = 0$ and substituting this result into the general FSR equation (4.48)

gives;

$$\Delta\lambda_{FSR} = -\frac{\lambda^2}{2nl_0} \quad (4.51)$$

The wavelength response of chirped FBG FP with the chirps of the FBG oriented in the same direction is similar to the conventional FP response [10,28] where the FSR is given by the corresponding cavity length between the gratings centres, equation (4.51).

4.3.3.4 Contra-propagating chirped FBG FP: The reduced Configuration

The contra-propagating cavities which consist of the chirped FBG FP, comprises of 2 identically chirped FBG separated by a distance with the direction of the increasing chirp oriented not in the same direction. The reduced configuration is of the contra-propagating chirped FBG FP cavity configuration where the direction of the increasing chirp of the FBG is oriented away from the centre of the cavity as shown in, figure (4.15). This configuration is designed to have a reduced sensitivity to wavelength.

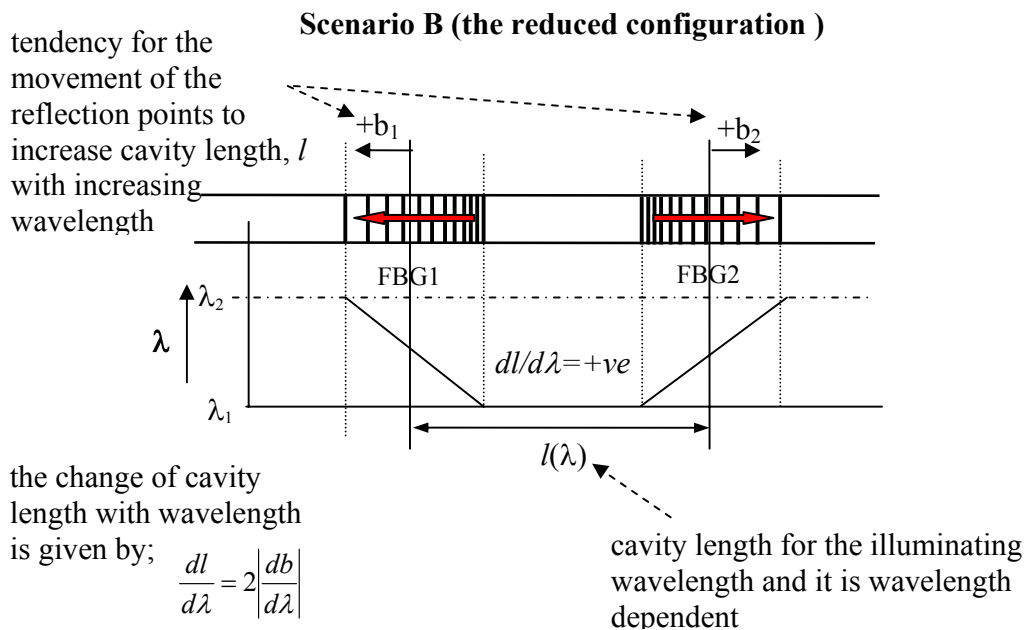


Figure 4.15, shows the reduced configuration of the contra-propagating chirped FBG cavity which consists of 2 identical chirped FBGs separated by a distance with the direction of the increasing chirped oriented away from the centre of the cavity. Increasing the wavelength will have a corresponding increase in the cavity length.

When the cavity is illuminated by a wavelength, λ , due to the positional dependence of the reflection position with wavelength in the 2 chirped FBG, the light will see a cavity

length, $l(\lambda)$, and this is wavelength dependent, figure (4.15). As the wavelength increases, the movement of the resonance position, b_1 in FBG1, moves in the direction of the increasing chirp such that there is a tendency for the cavity length to increase with wavelength. The same argument applies to FBG2 which can be seen in figure (4.15). The increase in the reflection positions with wavelength in the 2 FBGs are given by; $\frac{db_1}{d\lambda}$ and $\frac{db_2}{d\lambda}$ for FBG1 and FBG2 respectively. There is a tendency for the cavity length, l to increase with wavelength so that $\frac{dl}{d\lambda} = +ve$. From the dependence of the RTSP upon the illuminating wavelength for the general cavity, equation (4.43);

$$\frac{d\theta}{d\lambda} = -\frac{4\pi l}{\lambda^2} + \frac{4\pi}{\lambda} \left(\frac{\partial(nl)}{\partial\lambda} \right),$$

an increase in the cavity length, dl , provides a positive phase shift (2nd term RHS) which counteracts the negative phase shift (1st term RHS) induced by the optical wavelength change in the cavity [29]. The overall effect of the two counteracting responses to wavelength changes in the cavity will provide a reduced phase response. Therefore, this configuration has a reduced sensitivity to wavelength than is exhibited by a conventional FP cavity. The sensitivity depends on how the two phase shifts are balanced out. The change in cavity length is related to the chirp rate for a reduced configuration. Given that $\frac{dl}{d\lambda} = +ve$, equation (4.48) can be written as;

$$\Delta\lambda_{FSR} = \frac{\lambda}{2n \left(\frac{dl}{d\lambda} - \frac{l(\lambda)}{\lambda} \right)} \quad (4.52)$$

For the identical chirped FBGs, the values of $\left| \frac{db_1}{d\lambda} \right| = \left| \frac{db_2}{d\lambda} \right| = \left| \frac{db}{d\lambda} \right|$, such that the change of cavity length with wavelength can be written as $\frac{dl}{d\lambda} = 2 \left| \frac{db_2}{d\lambda} \right| = 2 \left| \frac{db}{d\lambda} \right|$. From the grating

response, the movement of resonance position with wavelength can be represented by[30];

$$\frac{db}{d\lambda} = \frac{l_g}{\Delta\lambda_c} = \frac{1}{C} \quad (4.53)$$

where l_g is the grating length, $\Delta\lambda_c$ is the total chirp and C is the chirp rate nm/mm. Substituting into Equation (4.52);

$$\Delta\lambda_{FSR} = \frac{\lambda}{2n \left(2\frac{1}{C} - \frac{l(\lambda)}{\lambda} \right)}$$

$$\Delta\lambda_{FSR} = \frac{\Delta\lambda_0}{\frac{1}{l_0} \left(l(\lambda) - 2\frac{\lambda}{C} \right)} \quad (4.54)$$

where $\Delta\lambda_0 = -\frac{\lambda^2}{2nl_0}$ is the conventional FSR for a FP with the cavity of length l_0 .

Analogous to the dispersive bulk FP, where the FSR is modified by the material dispersion, the dispersive chirped FBG cavity response is modified by the chirp rate, which is a length dependent term. When the denominator of equation (4.54) becomes zero, the FSR for the reduced cavity becomes infinite; $\Delta\lambda_{FSR} \rightarrow \infty$. At this point the reduced cavity becomes a cavity which is insensitive to wavelength. This condition occurs on the loci of the curve;

$$l(\lambda) = 2\frac{\lambda}{C} \quad (4.55)$$

Figure (4.16) shows the plot of this wavelength insensitive cavity length for the 3 wavelengths, 1550nm, 1300nm and 800nm.

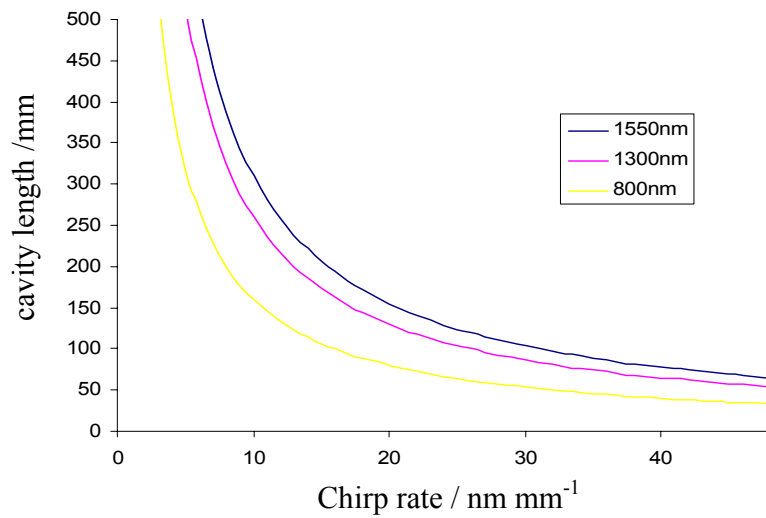


Figure 4.16, a plot of the equation (4.55) for 3 wavelengths, 1550nm, 1300nm and 800nm.

Table (4.1), below provides some figures of merit to compare the cavity lengths required to construct a wavelength insensitive cavity for 3 different interrogating wavelengths, for a range of chirp rates;

Table 4.1

Table indicating the insensitive length required for the wavelength for 800nm, 1300nm and 1500nm from equation (4.55).			
Wavelength	Chirp rate 10nm/mm	Chirp rate 20nm/mm	Chirp rate 25nm/mm
800nm	160mm	80mm	64mm
1300nm	260mm	130mm	104mm
1500nm	300mm	150mm	120mm

As can be seen from table (4), the cavity length is inversely proportional to the chirped rate. If the cavity were formed between a single chirped FBG and a reflective fibre end, the cavity length for wavelength insensitive would be halved, such that $l = \frac{\lambda}{C}$. At the design wavelength, the rate of change of phase with wavelength is zero. Such a device

could be useful to reduce frequency jitter noise for wavelength stabilisation of external cavity lasers but such configuration usually requires a large cavity length which will suffer from polarisation fading effect if the FBG is fabricated in single mode fibre.

As the wavelength is tuned away from the design wavelength, the condition for zero sensitivity no longer holds. By expanding the cavity length, $l(\lambda)$ about the central wavelength cavity length, l_0 to a 1st order approximation;

$$l(\lambda) = l(\lambda_0) + \frac{dl(\lambda)}{d\lambda} \delta\lambda,$$

equation (4.54) can be written about the detuned wave $\delta\lambda$;

$$(\Delta\lambda_{FSR})_{\delta\lambda} = \frac{\lambda}{2n \left(2\frac{1}{C} - \frac{1}{\lambda} \left(l(\lambda_0) + 2\frac{1}{C} \delta\lambda \right) \right)}$$

This can be simplified to;

$$(\Delta\lambda_{FSR})_{\delta\lambda} = -\frac{\lambda^2}{2n \left(2\frac{1}{C} \delta\lambda \right)} = -\frac{\lambda^2}{2n \left(2\frac{dz}{d\lambda} \delta\lambda \right)} \quad (4.56)$$

where $\frac{dz}{d\lambda}$ is the inverse of the chirp rate C^{-1} , expressed here as a positional detuning factor.

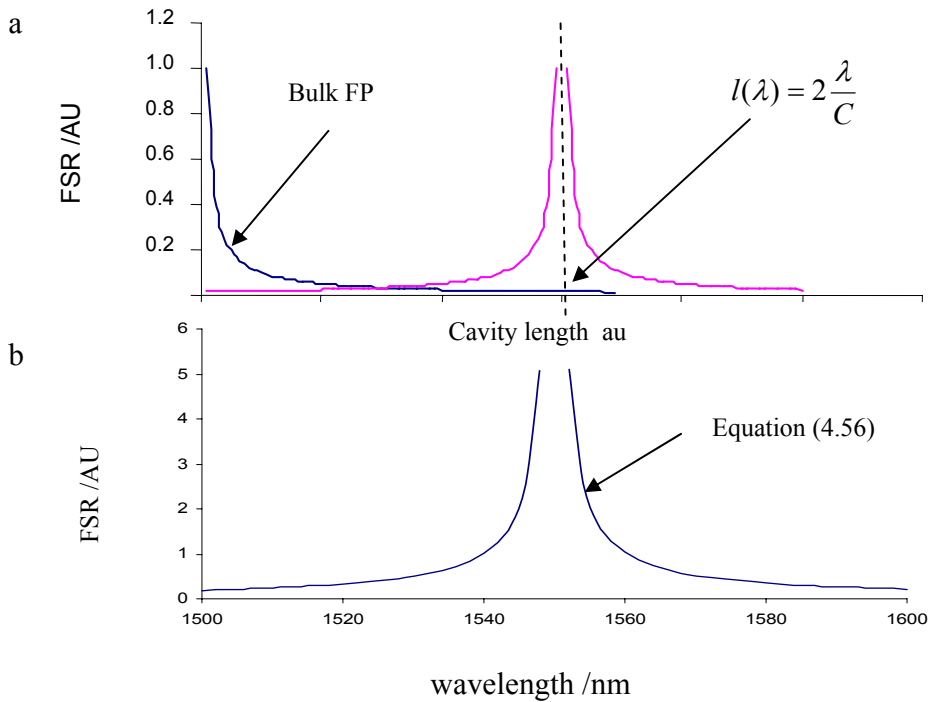


Figure 4.17a) the FSR variation of the insensitve cavity configuration compared to the Bulk FP response and b) using the relationship of the positional dependence of wavelength, the equivalent FSR with wavelength is plotted using equation (4.56).

The equation (4.56) has the same functional form as the expression describing the conventional FSR, except that it is offset by the insensitve cavity length, $l(\lambda) = 2\frac{\lambda}{C}$, which is shown in figure (4.17a). By careful design of the chirped FBG cavity, the bulk equivalent FSR, $\Delta\lambda_{FSR} = -\frac{\lambda^2}{2nl}$ can be offset by an effective length such that there is a physical length, $l(\lambda) \neq 0$ for which $\Delta\lambda_{FSR} = \infty$. The FSR can then be tuned by changing the wavelength as shown in figure (4.17b). As the device has a wavelength dependent cavity length, this is equivalent to having access to a Bulk Fabry-Perot with many cavity lengths. The FSR variation depends on the chirp parameters of the FBGs.

The response of the dispersive chirped FBG FP cavity is analogous to the dispersive bulk FP in section (4.3.2). Using the treatment carried out by Vaughan [12] on the analysis of

the dispersive bulk Fabry-Perot interferometer using the on axis resonance condition for a cavity, equation (4.34);

$$\lambda p = 2n(\lambda)l(\lambda)$$

Differentiating the equation and consider the condition of onset of the next cavity resonance provides a general cavity response in terms of the optical frequency which is given in equation (4.37);

$$\Delta v_{FSR} = \frac{\Delta v_0}{\left(1 - \frac{2\lambda}{2nl} \frac{d(nl)}{d\lambda}\right)}$$

Treating the chirped FBG FP in a similar fashion, the change in OPL for the chirped FBG FP is related to the change in the cavity length;

$$\frac{d(nl)}{d\lambda} = n \frac{dl}{d\lambda}$$

Since from equation (4.53);

$$\frac{dl}{d\lambda} = 2 \frac{1}{C}$$

the equation (4.37) becomes;

$$\Delta v_{FSR} = \frac{\Delta v_0}{\left(1 - \frac{2\lambda}{Cl}\right)} \quad (4.57)$$

When the denominator becomes zero, the condition for wavelength insensitive cavity becomes;

$$l = 2 \frac{\lambda}{C}$$

which is the same condition for a wavelength insensitive cavity derived using the RTSP consideration, equation (4.55). This demonstrates the consistency in using the two methods to derive the insensitive cavity length. The analogy between using the two different types of dispersive elements is very close. The condition for the insensitive bulk type FP occurs when the functional form; $\frac{n}{\lambda} = \frac{dn}{d\lambda}$ is satisfied (which is length

independent) and the condition for the insensitive chirped FBG FB occurs when $\frac{l}{\lambda} = \frac{dl}{d\lambda}$ is satisfied (which is independent of the refractive index). One advantage of using chirped FBGs is that the dispersion can be controlled by means of chirping parameters. Different FBGs with different chirp rates can be fabricated which can form FP cavities with a wide range of sensitivities for all wavelengths and not being limited by material properties.

4.3.3.5 Contra-propagating chirped FBG FP: The enhanced Configuration

The enhanced configuration comprises of 2 identical chirped FBGs separated by a cavity length to form a FP with the increasing chirp of the FBGs oriented towards the centre of the cavity as show in figure (4.18). When the cavity is illuminated by a wavelength, λ , the light will experience a cavity length, $l(\lambda)$ because of the positional dependence of the reflected wavelength in the 2 chirped FBGs. As the reflection position of the wavelength moves in the direction of the increasing chirp with increasing wavelength, there is a tendency for the movement of the reflection point, b_1 in FBG1 to reduce the cavity distance and the same argument is applied to the movement of the reflection point, b_2 in FBG2, figure (4.18). Increasing the wavelength has a tendency to reduce the cavity length the wavelength experiences in this cavity and hence, $\frac{dl}{d\lambda} = -ve$. Consider the RTSP with wavelength for a general cavity, equation (4.43);

$$\frac{d\theta}{d\lambda} = -\frac{4\pi nl}{\lambda^2} + \frac{4\pi}{\lambda} \left(\frac{\partial(nl)}{\partial\lambda} \right).$$

The reduction in the cavity length, dl provides a negative phase shift (2nd term in the RHS) but there is also the normal wavelength response of the cavity with a further negative the phase shift (1st term in the RHS).

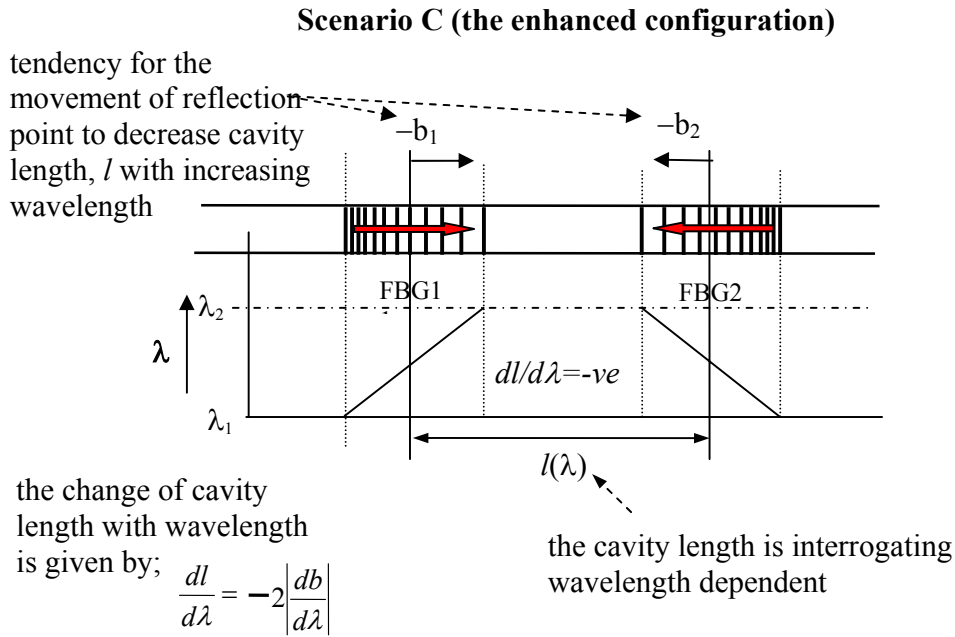


Figure 4.18, shows the enhanced configuration of the contra-propagating chirped FBG cavity where there is a decreased in the cavity length, l with wavelength.

The overall effect of the two responses of the cavity enhances the negative shift in phase as the wavelength is tuned, therefore giving an enhanced wavelength sensitivity cavity compared to a standard FP with the same cavity length. Assuming identical chirped FBGs, the change of cavity length can be expressed in terms of the chirp rate [30];

$$\frac{\partial l(\lambda)}{\partial \lambda} = -2 \left| \frac{db}{d\lambda} \right| = -2 \frac{B}{\Delta \lambda_c} = -2 \frac{1}{C} \quad (4.58)$$

where C is the chirp rate. Substituting into the FSR equation for a general chirped FBG FP cavity; equation (4.52) becomes;

$$\Delta \lambda_{FSR} = \frac{\lambda}{2n \left(-2 \frac{1}{C} - \frac{l(\lambda)}{\lambda} \right)} \quad (4.59)$$

Under the condition of the wavelength insensitive cavity, equation (4.55);

$$l(\lambda) = 2 \frac{\lambda}{C}$$

the equation can be rearranged to give;

$$\frac{C}{2} = 2 \frac{\lambda}{l(\lambda)}$$

Substituting back into equation (4.59), the wavelength sensitivity of the cavity is given by;

$$\begin{aligned} \Delta\lambda_{FSR} &= \frac{\lambda}{2n \left(-2 \frac{l(\lambda)}{\lambda} \right)} \\ \Delta\lambda_{FSR} &= -\frac{\lambda^2}{2n(2l(\lambda))} \end{aligned} \quad (4.60)$$

This has the form of a conventional FP response, however the apparent cavity length is 2 times the actual length or the cavity has become twice as sensitive. The enhanced configuration under the wavelength insensitive condition for the reduced configuration with a cavity length, $l(\lambda)$, will become twice as sensitive to wavelength, equation (4.60). The effect of detuning the wavelength is small, and the FSR is almost constant. By using chirped FBG FP in the enhancing configuration, the sensitivity of the cavity can be increased without the need for a large cavity length FP, making small device with high sensitivity possible. A small cavity length device with high wavelength sensitive has implications in low coherence interferometry. It can be used as a processing interferometer where the small length of the cavity will be less stringent on the coherence of the signal source and at the same time providing a high wavelength sensitivity readout.

4.3.3.6 Phase response of the insensitive chirped FBG FP

The general RTSP equation for the dispersive chirped FBG FP is given by equation (4.44);

$$d\theta = \frac{4\pi n}{\lambda} \left(\frac{dl}{d\lambda} - \frac{l(\lambda)}{\lambda} \right) d\lambda$$

In the reduced configuration, section (4.3.3.4), the change of cavity length with wavelength is positive and is given in terms of C ;

$$\frac{\partial l(\lambda)}{\partial \lambda} = 2 \frac{1}{C}$$

Using the Taylor expansion, the cavity length, $l(\lambda)$ can be written about the cavity length of the central wavelength, λ_0 of the chirped FBG, using the 1st order approximation and substituting back into equation (4.44) gives;

$$d\theta = \frac{4\pi m}{\lambda} \left[\frac{2}{C} - \frac{1}{\lambda} \left(l(\lambda_0) + \frac{dl(\lambda)}{d\lambda} \Delta\lambda \right) \right] d\lambda$$

$$d\theta = \frac{4\pi m}{\lambda} \left[\frac{2}{C} - \frac{1}{\lambda} \left(l(\lambda_0) + \frac{2}{C} \Delta\lambda \right) \right] d\lambda \quad (4.61)$$

For a wavelength insensitive cavity designed for the central wavelength, λ_0 , equation (4.55) can be written as;

$$\frac{2}{C} = \frac{l(\lambda_0)}{\lambda}$$

Substituting back into equation (4.61) gives;

$$d\theta = -\frac{4\pi m}{\lambda} \left(\frac{1}{\lambda} 2 \frac{\Delta\lambda}{C} \right) d\lambda$$

$$d\theta = -\frac{8\pi m}{C} \left(\frac{\Delta\lambda}{\lambda^2} \right) d\lambda \quad (4.62)$$

Integrating from λ_0 to the detuned wavelength, $\lambda_0 + \Delta\lambda$, the phase change incurred will be;

$$\int d\theta = -\frac{8\pi m}{C} \int_{\lambda_0}^{\lambda_0 + \Delta\lambda} \frac{\Delta\lambda}{\lambda^2} d\lambda$$

which gives (details of which can be found in Appendix B);

$$\theta = -\frac{8\pi n}{C} \left[\ln \lambda + \lambda_0 \frac{1}{\lambda} \right]_{\lambda_0}^{\lambda_0 + \Delta\lambda}$$

This can be simplified to;

$$\theta = -\frac{4\pi n}{C} \left(\frac{\Delta\lambda}{\lambda_0} \right)^2 \quad (4.63)$$

A plot of equation (4.63) is shown in figure (4.19) assuming $n=1.5$, and a chirp rate of 25nm mm^{-1} . The graph demonstrates that the cavity has a quadratic phase response.

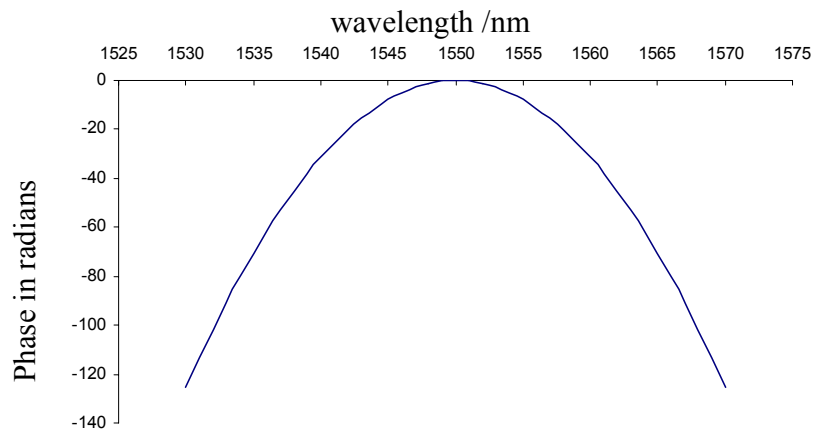


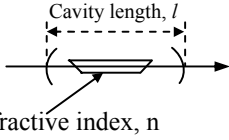
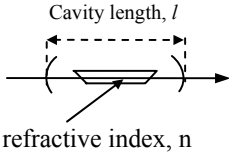
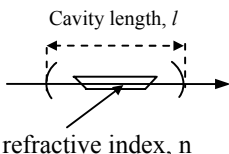
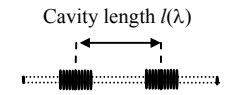
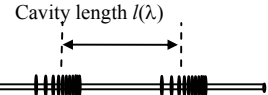
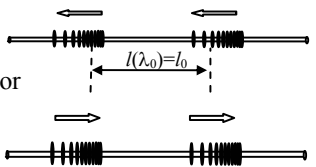
Figure 4.19, a plot of equation (4.63) with λ_0 of 1550 nm and chirp rate of 25nm mm^{-1} .

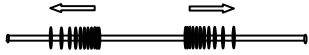
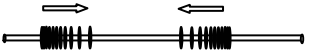
The phase response of the wavelength insensitive cavity is quadratic about the central wavelength. When this is used in the FP response equation (4.31);

$$I = I_0(1 + V \cos \theta)$$

The nature of the cavity response with wavelength, produces a variation of the FSR, symmetrical about the insensitivity wavelength. The sensitivity increases with increasing detuning about this wavelength.

The dispersion present in these cavities changes the wavelength response, and, dependent on the chirp parameters of the grating, different wavelength sensitivities can be achieved. These different wavelength sensitivities may have implications to the strain and temperature sensitivities for the cavities.

Table 4.2, FP response of interferometers involving the used of chirped FBGs		
configuration	FP response	Equation
general bulk FP cavity 	$\Delta\nu_{FSR} = \frac{\Delta\nu_0}{\left(1 - \frac{\lambda}{n} \frac{dn}{d\lambda}\right)}$	equation (4.38)[12]
bulk FP cavity 	$\Delta\nu_0 = \frac{c}{2n(\lambda)l}$	equation (4.25) corresponding wavelength dependent refractive index
dispersive bulk FP cavity 	$\Delta\nu_{FSR} = \frac{c}{2\left(n - \lambda \frac{dn}{d\lambda}\right)l} = \frac{c}{2n_{eff}l}$	equation (4.40)[13] corresponding dispersion modified effective refractive index response
uniform FBG FP 	$\Delta\nu_{FSR} = \frac{c}{2nl(\lambda)}$	equation (4.42)[17] corresponding wavelength dependent cavity length
general chirped FBG FP with arbitrary chirps 	$\Delta\lambda_{FSR} = \frac{\lambda}{2\left(n \frac{dl}{d\lambda} - \frac{nl(\lambda)}{\lambda}\right)}$	equation (4.48)
Chirped FBG FP with chirps in FBG oriented in the same direction [20, 21,22] 	$\Delta\lambda_{FSR} = -\frac{\lambda^2}{2nl_0}$	equation (4.51) corresponding wavelength dependent cavity length but all wavelengths have the same cavity length

configuration	FP response	Equation
<p>general reduced configuration</p>  <p>wavelength insensitive cavity condition, equation (4.67)</p> $l(\lambda) = 2 \frac{\lambda}{C}$ <p>phase response about the design wavelength</p>	$\Delta\lambda_{FSR} = \frac{\lambda}{2n \left(\frac{dl}{d\lambda} - \frac{l(\lambda)}{\lambda} \right)}$ $\Delta\lambda_{FSR} = \frac{\Delta\lambda_0}{\frac{1}{l_0} \left(l(\lambda) - 2 \frac{\lambda}{C} \right)}$ $\Delta\nu_{FSR} = \frac{\Delta\nu_0}{\left(1 - \frac{2\lambda}{Cl} \right)}$ $(\Delta\lambda_{FSR})_{\delta\lambda} = - \frac{\lambda^2}{2n \left(2 \frac{1}{C} \delta\lambda \right)}$ $(\Delta\lambda_{FSR})_{\delta\lambda} = - \frac{\lambda^2}{2n \left(2 \frac{dz}{d\lambda} \delta\lambda \right)}$ $\theta = - \frac{4\pi n}{C} \left(\frac{\Delta\lambda}{\lambda_0} \right)^2$	<p>equation (4.52), corresponding dispersion modified effective cavity length response</p> <p>equation (4.54) corresponding dispersion modified effective cavity length response</p> <p>equation (4.57) corresponding dispersion modified effective cavity length response</p> <p>equation (4.56)</p> <p>equation (4.56)</p> <p>equation (4.63)</p>
<p>enhanced configuration</p>  <p>at condition equation (4.67)</p> $l(\lambda) = 2 \frac{\lambda}{C}$	$\Delta\lambda_{FSR} = \frac{\lambda}{2n \left(-2 \frac{1}{C} - \frac{l(\lambda)}{\lambda} \right)}$ $\Delta\lambda_{FSR} = - \frac{\lambda^2}{2n(2l(\lambda))}$	<p>equation (4.59) corresponding dispersion modified effective cavity length response</p> <p>equation (4.60)</p>

4.4 Summary

The principles of operation of FBGs have been discussed using the coupled mode theory to explain the interactions between the forward and backward propagating mode due to the periodic perturbation of refractive index modulation. The dispersion inside the cavity affects the performance of the bulk FP interferometer such that the cavity characteristics are changed by dispersion. Analysis using the RTPS for FP cavities has been performed on the chirped FBGs FP and the performance of these dispersive cavities is analogous to the dispersive bulk FP. The summary of the FP configuration and FP responses have been tabulated. Depending on the chirped FBG FP configurations, the sensitivity could be altered by the chirp parameters of the FBG and different sensitivity device with different gauge length can be configured.

From the analysis of the wavelength response of the chirped FBG FP, the effect of scanning the wavelength changes the reflection point in the two FBGs which can have an enhance/reduce effect on the normal wavelength response of the cavity. Using the relationship between strain and wavelength scanning [15] in the FBG FP, by suitable design of the chirp parameter in the chirped FBG FP, the cavity can be made such that the effect of changing wavelength in the chirped FBG will encounter act the effect of the cavity and hence a reduced or zero strain sensitivity chirped FBG FP can be configured.

References:

-
- 1 E. Snitzer, 'Cylindrical Dielectric Waveguide Modes', OSA, **51**, 491, 1961.
 - 2 D. Gloge, 'Weakly Guiding fibers', Applied Optics, **10**, 2252-2258, 1971.
 - 3 L. B. Jeunhomme, 'Single-mode fibre optics: principles and applications' New York, Marcel Dekker, chapter 1, 6, 1990.
 - 4 D. Gloge, 'Dispersion in Weakly Guiding Fibers', Applied Optics, **10**, 2442-2445, 1971.
 - 5 R. Kashyap, 'Fiber Bragg Gratings', Academic Press, chapter 4, 144, 1999.
 - 6 H. Kogelnik, 'Filter Response of Nonuniform Almost-Periodic Structures', The

- Bell System Technical Journal, **55**, 109-125, 1979.
- 7 T. Erdogan, 'Fiber Grating Spectra', Journ. of Light. Tech., **15**, 1277-1294, 1997.
 - 8 J. T. Verdeyen, 'Laser Electronics', 2nd edit, Prentice-Hall International Inc., chapter 6, 131, 1989.
 - 9 S. R. Kidd, P. G. Sinha, J. S. Barton and J. D. C. Jones, 'Fibre optic Fabry-Perot sensors for high speed heat transfer measurements', Proc. of SPIE, **1504**, 180-190, 1991.
 - 10 T. G. Giallorenzi, J. A. Bucaro, A. Dandridge, G. H. Siegel Jr. J. H. Cole, S. C. Rashleigh and R. G. Priest, 'Optical fiber Sensor Technology', IEEE Journ. of Quant. Elect., **18**, 625-665, 1982.
 - 11 S. J. Petuchowski, T. G. Giallorenzi and S. K. Sheem, 'A Sensitive Fiber-Optic Fabry-Perot Interferometer', IEEE Journ. of Quan. Elect., **17**, 2168-2170, 1981.
 - 12 J. M. Vaughan, 'The Fabry-Perot interferometer', IOP publishing, Appendix 7, 478, 1989.
 - 13 J. T. Verdeyen, 'Laser Electronics', 2nd edit, Prentice-Hall International Inc., chapter 9, 288, 1989.
 - 14 W. W. Morey, G. Meltz and W. H. Glenn, 'Fiber Optic Bragg Sensors', Proc. of SPIE, **1169**, 98-107, 1990.
 - 15 W. W. Morey, T. J. Bailey, W. H. Glenn and G Meltz, 'Fiber Fabry-Perot interferometer using side exposed fiber Bragg Gratings', Proc. of OFC, 96, 1992.
 - 16 S. LaRochelle, V. Mizrahi, K. D Simmons and G. I. Stegeman, 'Photosensitive optical fibers used as vibration sensors', Optics letters, **15**, 399-401, 1990.
 - 17 S. Legoubin, M. Douay, P. Bernage and P. Niay, 'Free Spectral range variations of grating-based Fabry-Perot filters photowritten in optical fibers', J. Opt. Soc. Am. A, **12**, 1687-1694, 1995.
 - 18 K. O. Hill, S. Theriault, B. Malo, F. Bilodeau, T. Kitagawa, D.C. Johnson, J. Albert, K. Takiguchi, T. Kataoka and K. Hagimoto, 'Chirped in-fibre Bragg grating dispersion compensators: Linearisation of dispersion characteristic and demonstration of dispersion compensation in 100km, 10Gbit/s optical fibre link', Elect. Lett., **30**, 1755-1756, 1994.
 - 19 R. Kashyap, S.V. Chernikov, P. F. McKee and J. R. Taylor, '30ps chromatic dispersion compensation of 400fs pulses at 100Gbits/s in optical fibres using an all fibre photoinduced chirped reflection grating, Electron. Lett., **30**, 1994, 1078-1079.

- 20 E. Town, K. Sugden, J. A. R. Williams, I. Benion and S. B. Poole, 'wide-Band Fabry-Perot-Like in Optical Fiber', *IEEE Photon. Tech. Lett.*, **7**, 78-80, 1995.
- 21 S. Doucet, R. Slavik and S. LaRochelle, 'High finesse large band Fabry-Perot fibre filter with superimposed chirped Bragg gratings', *Elect. Lett.*, **38**(9), 402-403, 2002.
- 22 X. Peng and C. Roychoudhuri, 'Design of high finesse, wideband fabry-Perot filter based on chirped fiber Bragg grating,' *Opt. Eng.*, **39**, 1858-1862, 2000.
- 23 S. J. Petuchowski, T. G. Giallorenzi and S. K. Sheem, 'A Sensitive Fiber-Optic Fabry-Perot Interferometer', *IEEE Journ. of Quant. Elect.*, **17**, 2168-2170, 1981.
- 24 D. B. Hunter, R. A. Minasian and P. A. King, 'Tunable optical transversal filter based on chirped gratings', *Elect. Lett.*, **31**, 2205-2207, 1995.
- 25 K. P. Koo, M. LeBlanc, T. E. Tsai and S. T. Vohra, 'Fiber Chirped Grating Fabry-Perot Sensor with Multiple Wavelength Addressable Free Spectral Ranges', *IEEE Photon. Tech. Lett.*, **10**, 1006-1008, 1998.
- 26 R. Kashyap, 'Fiber Bragg Gratings', Academic Press, chapter 6, 246, 1999.
- 27 D. B. Hunter, R. A. Minasian and P. A. King, 'Tunable optical transversal filter based on chirped gratings', *Elect. Lett.*, **31**, 2205-2207, 1995.
- 28 S. Doucet, R. Slavik and S. LaRochelle, 'High-finesse large band Fabry-Perot fibre filter with superimposed chirped Bragg gratings', *Elect. Lett.*, **38**, 402-403, 2002.
- 29 D. A. Jackson, 'Monomode optical fibre interferometers for precision measurement', *J. Phys. E: Sci. Instrum.*, **18**, 981-1000, 1985
- 30 A. D. Kersey and M. A. Davis, 'Interferometric fiber sensor with a chirped Bragg grating sensing element', *Proc. of SPIE*, **2360**, 319-322, 1994.

5 Variable Strain and Temperature sensitive chirped FBG FP cavity

5.1 Introduction

The strain sensitivity of the uniform period FBG FP cavity corresponds to the cavity length, l of the device. To ensure good spectral overlap between the two FBGs and to extend operational range, broadband chirped FBGs may be used as the partial reflectors [1]. Not only does a chirped FBG provide a broadband response, it is also a dispersive element which imparts a wavelength dependent delay to the reflected signal. In section (4.4.3), the analysis showed that the presence of a dispersive element within the interferometric cavity has led to significant modification to the cavity response with wavelength. This implies that the presence of the dispersive element will also influence the strain and temperature sensitivities of the cavity.

When a chirped FBG is subjected to axial strain, the location along the FBG from which light of a given wavelength is reflected changes, giving an effective extension enhancement of up to 3 orders of magnitude when compared to a bare fibre [2]. An enhanced strain sensitised fibre Michelson interferometer, employing this idea has been demonstrated [2]. By appropriately configuring chirped FBGs in a FP cavity, the strain sensitivity can be enhanced or reduced depending on the parameters of the FBGs. The ability to alter the strain sensitivity via the parameters of the chirped FBG pairs, instead of using the length of the cavity, gives an added dimension and capability to fibre FP sensors. A reduced sensitivity to strain increases the unambiguous measurement range of the sensor whereas enhanced strain sensitivity would allow high-resolution measurements with smaller gauge lengths.

5.2 Strain sensitivity of chirped FBG Fabry-Perot

Consider a chirped FBG FP with two identical chirped FBGs separated by a cavity length with the increasing chirp of the FBGs directed away from the centre of the cavity as shown in figure (5.1). Let the two chirped FBGs be of equal but opposite chirp around the central wavelength, λ_0 .

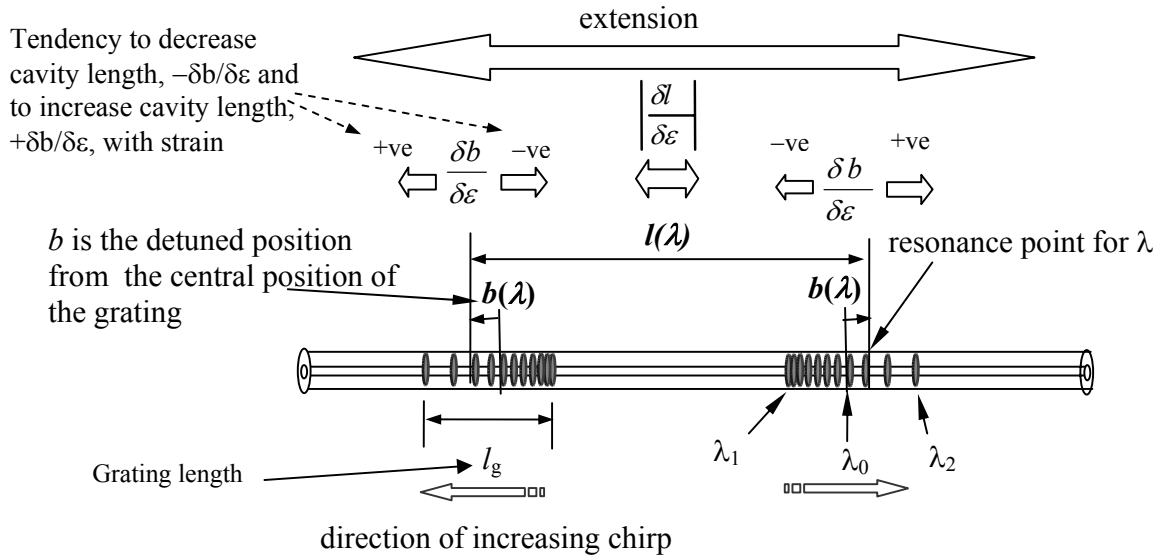


Figure 5.1, illustrates a chirped FBG FP cavity configured to have reduced sensitivity to strain. The cavity consists of 2 chirped FBGs with the direction of increasing chirp oriented away from the centre of the cavity λ_0 . The cavity is interrogated with a wavelength, λ and has a cavity length, $l(\lambda)$, measured between the resonance positions. The total chirp, $\Delta\lambda = \lambda_2 - \lambda_1$ where $\lambda_2 > \lambda_1$.

When illuminated by a laser operating at wavelength, λ , the length of the cavity, $l(\lambda)$ is the distance between the corresponding reflection position within the two FBGs, as indicated figure (5.1). When the cavity is subjected to strain, 2 counteracting effects occur. There is the tendency for the reflection point in the chirped FBGs to move against the direction of the chirp, thus reducing the cavity length. There is also the physical elongation of the cavity. Consider an optical fibre with length, l , subjected to axial strain, $\delta\varepsilon$, the change in the optical length with strain is given by[2];

$$\frac{\delta(l)}{\delta\varepsilon} = \xi l \quad (5.1)$$

where l is the equivalent optical length of the fibre and ξ is the strain responsivity determined by the photoelastic properties of the fibre with a typical value of; $\xi = 0.75 \varepsilon^{-1}$ [3].

To determine the parameters of the chirped FBGs required to counteract the strain induced change in fibre length, the effect of strain upon the chirped FBGs must be considered. The

resonance position of an interrogating wavelength, λ , measured relative to the reflection point of the central wavelength, λ_0 , within a chirped FBG of length l_g and total chirp $\Delta\lambda_c$, can be written as[2]:

$$b(\lambda) = \frac{\lambda - \lambda_0}{\Delta\lambda_c} \alpha l_g \quad (5.2)$$

where α is a multiplying factor <1 [2], which determines how deep into the grating the illuminating wavelength can penetrate. The value of α is dependent on the fibre material constants, the strength and the extent of the chirp of the grating. The normalised shift in central wavelength of the FBG in response to strain is given by [2]:

$$\frac{1}{\lambda} \frac{\delta\lambda}{\delta\varepsilon} = \xi \quad (5.3)$$

Applying strain to a chirped FBG causes a movement of the resonance location at the interrogating wavelength. This can be determined by differentiating equation (5.2) with respect to strain and combining the result with equation (5.3) [2]:

$$\frac{\delta(b(\lambda))}{\delta\varepsilon} = \alpha \frac{\lambda}{C} \xi \quad (5.4)$$

where C is the chirp rate given by $\Delta\lambda_c/l_g$. The value of α is assumed to be 0.80 [2], where the chirped FBG under investigation is subjected to strain under similar condition.

In the chirped FBG FP cavity, the movements of the resonance positions in the chirped FBGs under the application of strain, will have the tendency to either increase or decrease the cavity length, which is dependent on the orientation of the grating in the FP. When they are used in the enhanced configuration, section (4.3.3.5), the movement of the reflection points in the chirped FBGs are fashioned such that the cavity length has a tendency to increase, coupled with the action of strain has on stretching the physical cavity, will further enhance the strain response of the cavity.

In a reduced configuration shown in figure (5.1), the relative movement of the resonance points in the two oppositely oriented chirped FBGs can counteract the increase in the length of the cavity in response to tensile strain, so that there is no net change to the cavity length. For this to happen, the RHS of both equation (5.1) and equation (5.4) (given that there are 2 chirped FBGs in the FP cavity) must be balanced. For the cavity to be strain insensitive, the following relationship between the cavity length, illuminating wavelength, grating strength and chirp must be satisfied;

$$l(\lambda) = 2\alpha \frac{\lambda}{C} \quad (5.5)$$

This strain insensitive cavity length is similar to the wavelength insensitive cavity length derived in section (4.3.3.4) except for the grating strength factor, $\alpha = 0.8$ [2]. The analytical solution given in equation (5.5) is plotted in figure (5.2).

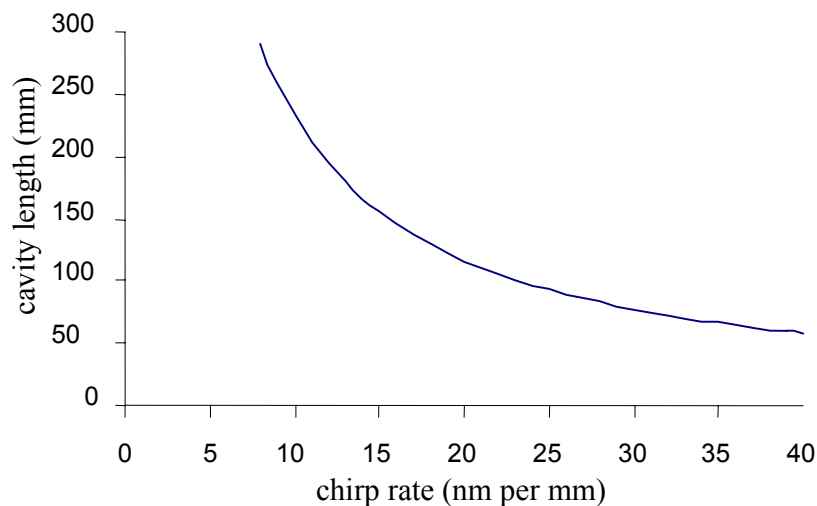


Figure 5.2, a plot of the cavity length vs chirp rate required to construct a chirped FBG FP cavity that is insensitive to strain. The line is calculated using equation (5.5), assuming that, $\alpha=0.80$ and $\lambda = 1550\text{nm}$.

From equation (5.4), it can be seen that the smaller the chirp rate C , the larger the movement of the resonance points, which allows the strain acting on a large cavity length to be counteracted.

It is useful to consider the effect of operating away from this design wavelength, for example, at wavelength, $(\lambda+\delta\lambda)$, upon the response of the cavity. In this case, using equation (5.2), the increase in cavity length is given by;

$$l(\lambda + \delta\lambda) = l(\lambda) + 2 \frac{1}{C} \delta\lambda. \quad (5.6)$$

from which

$$\delta l = 2 \frac{1}{C} \delta\lambda \quad (5.7)$$

where δl is the change in the cavity length caused by the change in the illuminating wavelength, $\delta\lambda$. Since the FBGs are considered to have a linear chirp (ie C is a constant), when the cavity is subjected to strain the movement of the resonance position at the wavelength $(\lambda + \delta\lambda)$ can only compensate for the extension of a cavity of length $l(\lambda)$. Thus it is only the affect of strain on the additional length, δl , that gives rise to a change in the overall cavity length and thus in the phase of the output. The change in RTPS in response to strain is given by[4];

$$\delta\theta = \frac{4\pi}{\lambda} \xi \delta l \delta\varepsilon \quad (5.8)$$

where δl (from equation (5.7)) is the detuned length which contributes to the phase shift. Using equation (5.7), equation (5.8) becomes;

$$\delta\theta = \frac{8\pi m}{\lambda} \xi \frac{1}{C} \delta\lambda \delta\varepsilon \quad (5.9)$$

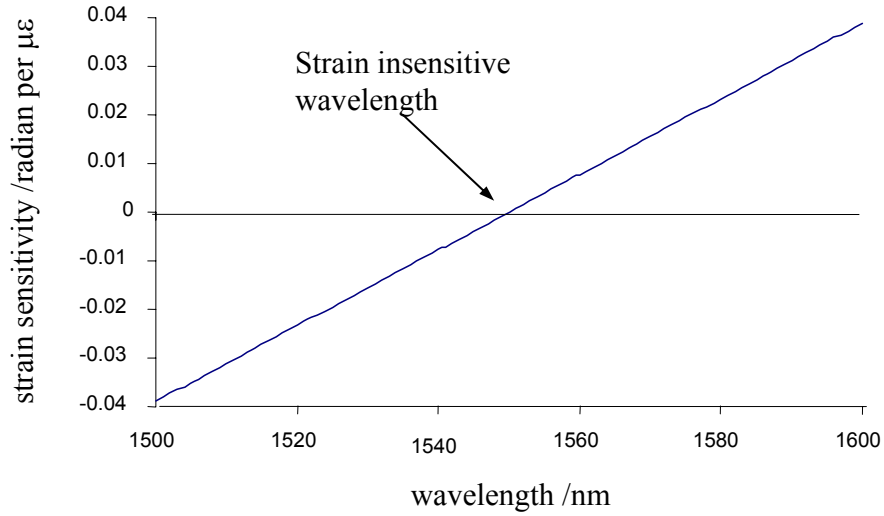


Figure 5.3, a plot of the strain sensitivity of equation (5.9) as a function of wavelength.

Detuning the illuminating wavelength from the design wavelength allows a degree of tuning of the strain sensitivity of the cavity. A plot of the strain sensitivity determined using equation (5.9) is shown in figure (5.3). The strain sensitivity is plotted as a function of illuminating wavelength determined using the parameters; $n=1.458$, $\xi=0.8\pm.1$ [3] and $C=25\text{nm mm}^{-1}$ for a cavity with the design wavelength of 1550nm.

5.3 The phase response of the chirped FBG FP to strain

Consider a general chirped FBG FP. The RTSP of this general FP cavity with an OPL of nl is given by; $\theta = \frac{4\pi nl}{\lambda}$. By differentiating the RTPS with strain, the change in the RTSP of the cavity under the influence of an applied strain can be written as[4];

$$\frac{d\theta}{d\varepsilon} = \frac{4\pi}{\lambda} \frac{\partial(nl)}{\partial\varepsilon} = \frac{4\pi}{\lambda} \left(l \frac{dn}{d\varepsilon} + n \frac{dl}{d\varepsilon} \right) \quad (5.10)$$

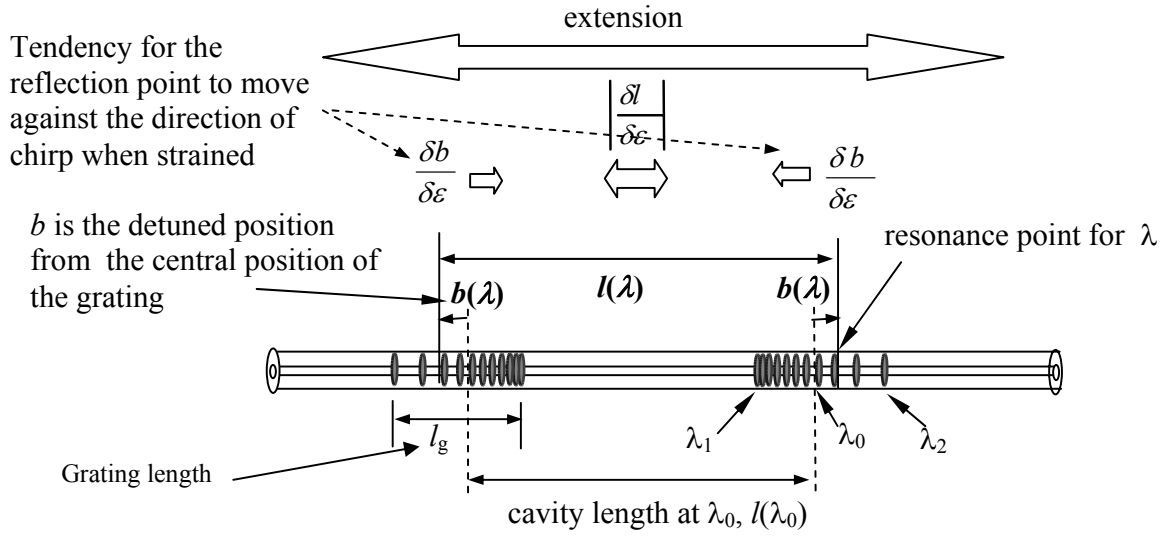


Figure 5.4, illustrating a chirped FBG FP cavity that consists of 2 chirped FBGs with arbitrary chirp, with a central Bragg wavelength, λ_0 . The cavity is interrogated at a wavelength, λ , with a corresponding the cavity length, $l(\lambda)$, measured between the appropriate resonance positions. The total chirp, $\Delta\lambda = \lambda_2 - \lambda_1$ where $\lambda_2 > \lambda_1$.

Consider chirped FBG FP cavity that is made up of 2 identical chirped FBG configured in an arbitrary orientation, as shown in figure (5.4). When the cavity is interrogated at a wavelength, λ , the cavity length, $l(\lambda)$ can be written in terms of the cavity length from the central Bragg wavelength, $l(\lambda_0)$ and the wavelength detuned position, b ;

$$l(\lambda) = l(\lambda_0) + 2b(\lambda)$$

Differentiating the expression with respect to strain;

$$\frac{dl}{d\epsilon} = \frac{dl(\lambda_0)}{d\epsilon} + 2\frac{db}{d\epsilon} \quad (5.11)$$

From equation (5.4); $\frac{db}{d\epsilon} = \alpha \frac{\lambda}{C} \xi_g$, where ξ_g is the strain response of the FBG, equation (5.11) can be written as;

$$\frac{dl}{d\varepsilon} = \frac{dl(\lambda_0)}{d\varepsilon} + 2 \frac{db}{d\varepsilon} \quad (5.12)$$

Assuming that the length of the cavity at the interrogating wavelength is the same as the length of the cavity of the central wavelength; $l \approx l_0$ and substituting equation (5.12) into the expression, equation (5.10), describing the change in the RTSP under the influence of an applied strain;

$$\frac{d\theta}{d\varepsilon} \approx \frac{4\pi}{\lambda} \left(nl \left(1 + \frac{1}{n} \frac{dn}{d\varepsilon} \right) + 2\alpha n \xi_g \frac{\lambda}{C} \right) \quad (5.13)$$

where $\left(1 + \frac{1}{n} \frac{dn}{d\varepsilon} \right) = \xi_f$ and ξ_g are strain responses of the fibre and FBG respectively. Assuming the value for the strain responses for fibre and FBG are the same, as they are determined by the same values in the elasto-optic and strain coefficients[2], Equation (5.13) can be reduced to;

$$\frac{d\theta}{d\varepsilon} = \frac{4\pi n \xi}{\lambda} \left(l + 2\alpha \frac{\lambda}{C} \right) \quad (5.14)$$

From equation (5.14), the phase response with strain of the chirp FBG FP cavities is dependent on the cavity length, l as well as the direction and magnitude of the movement of the resonance position. By using different value of C with different orientations of chirps, the strain sensitivity of the cavity can be changed for a given length of cavity in the chirped FBG FP.

In a chirped FBG FP which consists of 2 identical chirped separated by a distance forming a cavity with the direction of the increasing chirps oriented away from the centre of the cavity, figure (5.4), the cavity is fashioned such that the movement of the reflection positions of the illuminating wavelength in the chirped FBG have a tendency to decrease the cavity length to the application of strain. Thus $\frac{db}{d\varepsilon}$ is negative and equation (5.15) becomes;

$$\frac{d\theta}{d\varepsilon} = \frac{4\pi n \xi}{\lambda} \left(l - 2\alpha \frac{\lambda}{C} \right) \quad (5.15)$$

The phase of the cavity is strain insensitive when the cavity length satisfies the condition;

$$l = 2\alpha \frac{\lambda}{C}$$

For a given illuminating wavelength, a chirped FBG FP configured as shown in figure (5.4), with the chirped FBG having a given chirp rate, C , there exists a cavity length that the cavity becomes insensitive to strain. This same condition is derived from considering the balancing the movements of resonance position as the cavity is subjected to strain, equation (5.5).

When operating wavelength is detuned away from the wavelength at which the cavity is designed to be insensitive to strain, the cavity length can be expanded as a Taylor series about the designed 'strain insensitive cavity length', $l(\lambda_0)$;

$$l(\lambda) = l(\lambda_0) + 2 \frac{1}{C} \Delta\lambda$$

and equation (5.15) can be written as;

$$\left(\frac{d\theta}{d\varepsilon} \right)_{\lambda+\Delta\lambda} = \frac{4\pi m \xi}{\lambda} \left(l(\lambda_0) + 2 \frac{1}{C} \Delta\lambda - 2\alpha \frac{\lambda}{C} \right) \quad (5.16)$$

Since the cavity is designed such that; $l(\lambda_0) = 2\alpha \frac{\lambda}{C}$, the above equation becomes;

$$\left(\frac{d\theta}{d\varepsilon} \right)_{\lambda+\Delta\lambda} = \frac{4\pi m \xi}{\lambda} \left(2 \frac{1}{C} \Delta\lambda \right) \quad (5.17)$$

which is the same as equation (5.9) in the previous section, derived from considering the balancing of the movement of the resonance position as the cavity is subjected to strain.

5.4 The phase response of the chirped FBG FP to temperature

The resonance position of an interrogating wavelength, λ , measured relative to the reflection point of the central wavelength, λ_0 , within a linearly chirped FBG of length, l_g and total chirp $\Delta\lambda_c$, is written as;

$$b(\lambda) = \frac{\lambda - \lambda_0}{\Delta\lambda_c} \alpha_T l_g \quad (5.18)$$

where α_T now is a temperature factor to reflect the fact that movement of the resonance position is temperature driven. This factor determines how deep into the grating the illuminating wavelength can penetrate into the grating with temperature. Together with the wavelength response of the FBGs[3];

$$\frac{1}{\lambda} \frac{\delta\lambda}{\delta T} = \zeta_g \quad (5.19)$$

where ζ_g is the temperature response of FBGs. Differentiating equation (5.18) with respect to temperature and combining the result with equation (5.19) gives the rate of change of the resonance point with temperature;

$$\frac{\delta(b(\lambda))}{\delta T} = \alpha_T \frac{\lambda}{C} \zeta_g \quad (5.20)$$

Following a similar argument to that prescribed in section (5.3) for the strain response, the temperature sensitivity of the chirped FBG FP cavity may be derived and it is written as;

$$\frac{d\theta}{dT} = \frac{4\pi}{\lambda} \left(nl\zeta_f + 2n\alpha_T \zeta_g \frac{\lambda}{C} \right) \quad (5.21)$$

where ζ_f and ζ_g are the fibre and FBG temperature responses respectively. If the temperature response; $\zeta_f = \zeta_g = \zeta$ which is a reasonable assumption to make for the same fibre material, then the equation becomes;

$$\frac{d\theta}{dT} = \frac{4\pi n \zeta}{\lambda} \left(l - 2\alpha_T \frac{\lambda}{C} \right) \quad (5.22)$$

The cavity exhibits temperature insensitivity at the wavelength λ which satisfies the condition;

$$l = 2\alpha_T \frac{\lambda}{C} \quad (5.23)$$

From the analyses for the wavelength insensitive cavity presented in, section (4.3.3.4) and for strain insensitive cavity, section (5.3), the insensitive cavity length for wavelength, temperature and strain of this reduced configuration are given by $l_\lambda = 2\frac{\lambda}{C}$, $l_\varepsilon = 2\alpha \frac{\lambda}{C}$ and $l_T = 2\alpha_T \frac{\lambda}{C}$ respectively. For a given wavelength, the insensitive cavity length for wavelength, strain and temperature occur at different cavity lengths, dependent on the value of α and α_T . This is because the phase change in response to a change of wavelength is different to the phase response to strain tuning or temperature tuning. For example, the strain response of FBG is given by;

$$\frac{1}{\lambda_B} \frac{\delta\lambda}{\delta\varepsilon} = \xi$$

and the definition of strain is given by;

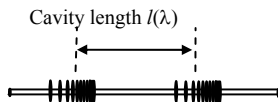
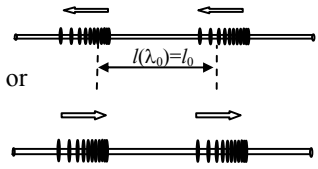
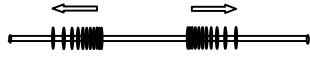
$$d\varepsilon = \frac{\delta l}{l}$$

substitute into the strain response gives;

$$\frac{d\lambda}{\lambda} = \xi \frac{dl}{l}$$

where ξ has a value $\sim 0.75 \varepsilon^{-1}$ [3]. This means that the strain tuning of the wavelength is only about 75% efficient which is near to the value of $\alpha \sim 0.8$. The value of $\alpha \sim 0.8$ is the average penetration depth over the bandwidth of the chirped FBG due to strain which reflects the FBG strain responsivity, $\xi \sim 0.75$.

5.5 Summary

Table 5.1, strain response of FP interferometers involving the used of chirped FBGs		
configuration	FP strain response	equation
general chirped FBG FP with arbitrary chirps 	$\frac{d\theta}{d\varepsilon} = \frac{4\pi n \xi}{\lambda} \left(l + 2\alpha \frac{\lambda}{C} \right)$	equation (5.14)
Chirped FBG FP with chirps in FBG oriented in the same direction 	$\frac{d\theta}{d\varepsilon} = \frac{4\pi n l}{\lambda} \xi$	corresponding wavelength dependent cavity length but all wavelength the same
general reduced configuration 	$\frac{d\theta}{d\varepsilon} = \frac{4\pi n \xi}{\lambda} \left(l - 2\alpha \frac{\lambda}{C} \right)$	equation (5.15)
strain insensitive cavity condition, equation (5.5)	$l(\lambda) = 2\alpha \frac{\lambda}{C}$	equation (5.5)
under the strain insensitive cavity condition;	$\left(\frac{d\theta}{d\varepsilon} \right)_{\lambda+\Delta\lambda} = \frac{4\pi n \xi}{\lambda} \left(2 \frac{1}{C} \Delta\lambda \right)$	equation (5.17)
phase response about the design wavelength in term of the detuned length	$\delta\theta = \frac{4\pi}{\lambda} \xi \delta l \delta\varepsilon$	equation (5.8)
phase response about the design wavelength in term of the detuned wavelength	$\delta\theta = \frac{8\pi n}{\lambda} \xi \frac{1}{C} \delta\lambda \delta\varepsilon$	equation (5.9)
temperature response about the design wavelength	$\frac{d\theta}{dT} = \frac{4\pi n \zeta}{\lambda} \left(l - 2\alpha_T \frac{\lambda}{C} \right)$	equation (5.22)
temperature insensitive cavity	$l = 2\alpha_T \frac{\lambda}{C}$	equation (5.23)

The strain sensitivity of the chirped FBG FP has been discussed. The dispersive element of the chirped FBG modifies the FSR of the cavity response and because of the relationship between the wavelength detuning with strain in FBG, the strain sensitivity is also related to the wavelength sensitivity of the dispersive chirped FBG FP. The reduce strain sensitive chirped FBG FP was analysed using the movement of the reflection of the illuminating wavelength with strain and from the phase response of the cavity with strain for which the relationship between the chirp rate and the length of the cavity required to configured a strain insensitive cavity has been presented.

The analytical results for the chirped FBG FP presented in section 4 and 5 give indications of the performance of the FP cavity to wavelength and strain. Using Numerical techniques to solve the coupled mode equations of the FBG will provide solutions with phase information which is lacking in the analytical techniques. At present there are no literatures with numerical results to suggest the effect of dispersion in the chirped FBG on the interferometric response of the chirped FBG FP and the solution using numerical techniques will compliment and support of the theory put forward so far.

References:

-
- 1 T. Allsop, K. Sugden and I. Bennion, 'A High Resolution Fiber Bragg Grating Resonator strain sensing system', *Fiber and Integrated Optics*, **21**, 205-217, 2002.
 - 2 A. D. Kersey and M. A. Davis, 'Interferometric fiber sensor with a chirped Bragg grating sensing element', *Proc. of SPIE*, **2360**, 319-322, 1994.
 - 3 Y. J. Rao, 'Recent progress in applications of in-fibre Bragg grating sensors', *Optics and Lasers in Engineering*, **31**, 297-324, 1999.
 - 4 C. D. Butter and G. B. Hocker, 'Fiber optics strain gauge', *Appl. Opt.*, **17**, 2867-2869 1978.

6 FBG and FBG FP Simulation

6.1 Introduction

Periodic structures pervade many areas of science and technology. Many works have been published detailing the interactions of waves with periodically modulated refractive index structures [1,2]. The perturbation created by the periodic structure, such as that comprise a FBG, to the uniformity of the material provides the means for a coupling mechanism. Recent advances in fabrication methods have allowed the writing of uniform period and non-uniform period FBGs [3]. The use of a non-uniform FBG provides extra degrees of freedom over those offered by uniform FBGs. A variety of analytical formalisms have been derived for the spectral response [4,5,6,7] and results have provided information on the performance of FBG structures, such as dispersion, the appearance of side lobes and the coupling strength. Numerical techniques [8,9] have been applied to solve the coupled mode equations, equation (4.8), that describe the interaction of the guided light with FBGs. Analytical solutions exist in closed form for FBGs with uniform period [10], but solutions for FBGs with varying FBG parameters require the use of numerical techniques such as the Runge-Kutta method [11]. As well as providing solutions to the coupled modes equation for non-uniform FBG parameters, numerical techniques provide solutions with phase information which is lacking in the analytical techniques. From the studies of periodic structure filters, matrix method [12] has been developed for grating analysis. This class of method was developed to model the performance of optical thin films and integrated optical devices, and includes the effective-index method [12], the transfer matrix method [13] and the effective medium method [8,9]. These techniques have all been applied to the study of FBGs.

The effective index method [12] involves the division of the grating into its periodic sections. The propagation constant, β , for each section is computed from the standard, three-layer guide dispersion relations. Using the Maxwell equations the component of the magnetic field can be written in terms of the perpendicular components of the electric field. Using the boundary

condition that requires that the electric and magnetic fields are continuous across the interface and that the fields in each section are impedance matched to those of its preceding section, yielding a matrix relationship between the fields at the left and right side of each section can be determined. The overall structure is characterised by a global matrix obtained by multiplying the individual matrices together. Rouard's method [14] was developed for thin film design. It is a recursive method where the reflectivity of the each layer is determined by summation of the multi-beam reflection from a single layer, with a phase value dependent on the separation distance between the layers. The function has an Airy shape similar to the FP response. The reflectivity of one layer is used progressively to calculate the reflectivity of the following layer in a recursive manner until the whole grating is represented.

The effective medium method uses the coupled mode equation (4.8) and reduces it to a propagating wave equation, where the principle root, or the effective index of the equation is related to the detuning and the coupling coefficients of the FBG. The principal root provides information on the reduced wave propagation constants. The sign of the root and its analysis provides physical interpretation to the wave guiding characteristics [6,8] within the wavelength band of the grating. If the wavelength is close to the Bragg wavelength of the grating, it is strongly reflected through constructive interference of the reflected wavelets. This reflection band is associated with the opening of a photonic band gap, which is related to the Bragg wavelength of the grating. In the photonic band gap (reflection band) regions, light will not propagate and thus termed evanescent, whereas light whose wavelength lies outside the reflection band is defined as propagating wave. This analysis technique can be adapted to the non-uniform period case where this photonic bandgap has a positional dependence. For a non-uniform period FBG, each position along the grating has a associated local Bragg wavelength and a local photonic band gap. The solution to the reduced propagating equation comes from Quantum Mechanics where the phase integral technique is employed. The Wentzel-Kramers-Brillouin(WKB) method [8], is a technique that applies a second-order approximation to the non-uniform FBG equation with a slowly varying envelope function. A general solution exists and is matched across the boundary of the photonic bandgap by considering it as a boundary layer problem where a 2x2 transfer matrix is derived. A semi-analytical approximation is then obtained for the reflectance spectrum of the non-uniform period FBG.

The TMM method [13] involves the division of the length of the grating into many sections, where the length of each section is much larger than the period of the index modulation corrugation. Each section assumed to have a uniform grating response with constant parameters such as period, coupling coefficient and refractive index modulation, for which an analytical solution to the coupled mode equation exists. These solutions can be written as a 2x2 transfer matrix for the forward and backward waves for each section. The solution to each section of grating is used as the input field to the following section of the grating, which may have a different functional dependence of its grating parameters. The process is repeated until the whole of the grating section is transformed under the constraint of appropriate boundary conditions. The overall structure is characterised by a global matrix obtained as the product of the individual matrices. This approach is simply a numerical method for solving the coupled-mode equations for non-uniform FBGs[12].

6.2 The Transfer Matrix Method

The solution to the coupled mode equation (4.8) has a closed form solutions only for Bragg gratings with uniform periodicity and uniform refractive index modulation. To represent a real FBG, parameters such as variation in period along the grating length (chirp) and variation in the amplitude of the refractive index modulation (apodisation) need to be included in the model. The refractive index modulation induced in the fibre generally has a certain spatial profile, eg Gaussian, as, in general, the UV laser used in FBG fabrication systems has a Gaussian intensity profile which could present a physical effect. It is desirable to design FBG devices with controlled transfer characteristics for specific applications and requirements. The modelling of FBGs with non-uniform characteristics requires the use of numerical solutions such as the Runge-Kutta method, which is very time consuming, or with other techniques, which can be more complex to implement. The transfer matrix method (TMM) is the most appropriate technique for FBG modelling, as a result of its simplicity, accuracy and speed with which it allows simulation of FBGs with arbitrary parameters [15].

The technique involves the division of the grating length, l_g into a large number, N , of sections each of length δl . One section of the grating is shown in figure (6.1). Parameters such as index change, grating period and coupling coefficient are taken to be constant within each section, allowing the closed form solution to be used. The coupled mode equations (4.8) are used to calculate the output fields of each short section δl_i . Each section may possess a unique and independent function for which a closed form solution exists. For such a grating section with an integral number of periods, the analytical solution for the amplitude reflectivity, transmission and phase may be determined. These quantities are then used as the input parameters for the proceeding section, which may have a different functional dependence for the grating parameters.

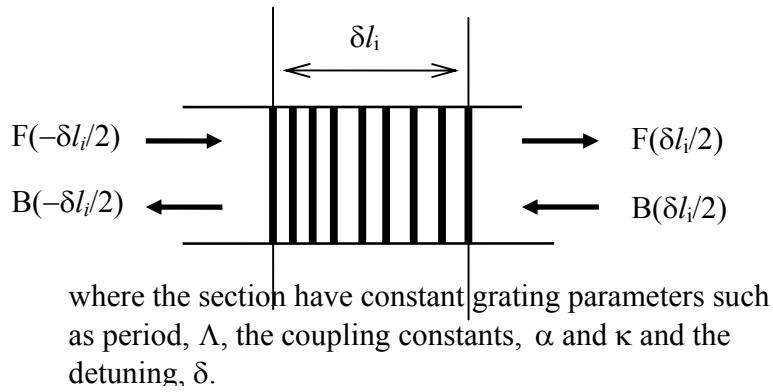


Figure 6.1, schematic diagram showing the input and output fields at the start and the end of the section.

The input and output fields for a single grating section are shown in figure (6.1). The grating may be considered to be a four-port device with input fields of $F(-\delta(l_i/2))$ and $B(-\delta(l_i/2))$ and output fields of $F(\delta(l_i/2))$ and $B(\delta(l_i/2))$. For a short uniform grating, the two fields on the RHS of the following equation are transformed by the matrix into the field on the LHS;

$$\begin{bmatrix} F(-\frac{\delta l_i}{2}) \\ B(-\frac{\delta l_i}{2}) \end{bmatrix} = [T_i] \begin{bmatrix} F(\frac{\delta l_i}{2}) \\ B(\frac{\delta l_i}{2}) \end{bmatrix} \quad (6.1)$$

From the solution of the coupled-mode equation for the uniform grating, the transfer matrix, T_i , connecting the input and output fields is given by [13];

$$T_i = \begin{bmatrix} [\cosh(\alpha_i \delta l_i) + \frac{i \delta_i \sinh(\alpha_i \delta l_i)}{\alpha_i}] e^{i \beta_i \delta l_i} & -\frac{i k_{aci} \sinh(\alpha_i \delta l_i)}{\alpha_i} e^{i(\beta_i \delta l_i + \theta_i)} \\ \frac{i k_{aci} \sinh(\alpha_i \delta l_i)}{\alpha_i} e^{-i(\beta_i \delta l_i + \theta_i)} & [\cosh(\alpha_i \delta l_i) + \frac{i \delta_i \sinh(\alpha_i \delta l_i)}{\alpha_i}] e^{-i \beta_i \delta l_i} \end{bmatrix} \quad (6.2)$$

The whole grating matrix transformation is constrained by the boundary conditions $F(0) = 1$ and $B(L_g) = 0$. Working from left to right, the field at the output of each section are calculated in turn and used as the input of the preceding section, figure (6.2).

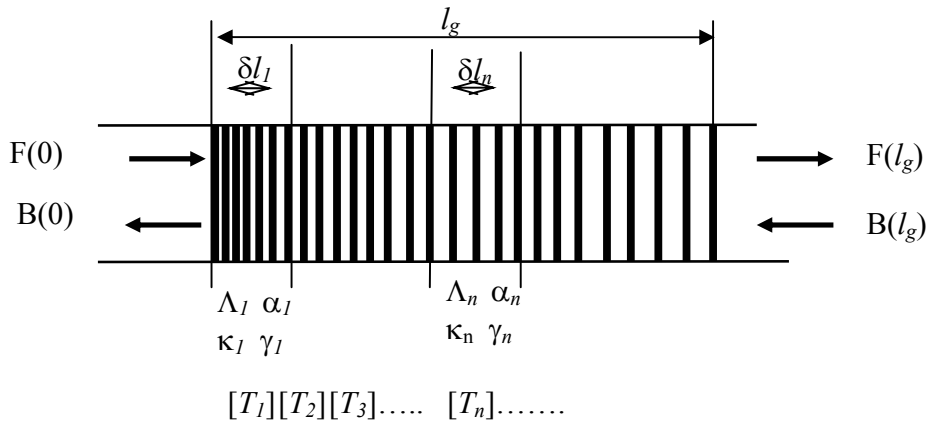


Figure 6.2, the division of a FBG into section to facilitate the use of the TMM. Each section has constant FBG parameters to form a composite grating of varying period, to model a stepped chirped grating.

The process continues until all of the matrices representing the individual element have been calculated to give;

$$\begin{bmatrix} F(0) = 1 \\ B(0) \end{bmatrix} = [T] \begin{bmatrix} F(l_g) \\ B(l_g) = 0 \end{bmatrix} \quad (6.3)$$

where

$$[T] = \prod_{i=1}^N [T_i] = \begin{bmatrix} t_{11} & t_{12} \\ t_{21} & t_{22} \end{bmatrix}$$

The transmittivity, Γ and the reflectivity, R_ρ are given by;

$$\Gamma = \frac{1}{t_{11}} \quad (6.4)$$

$$R_\rho = \frac{t_{21}}{t_{11}}$$

The accuracy of grating simulation by this technique is strongly dependent on the choice of N , the number of grating sections. It is important to make N sufficiently large otherwise the coupled mode theory collapses.

6.3 Penetration and transmission depth

There is a growing interest in the exploitation of the dispersive properties of FBGs for applications such as dispersion compensation and pulse shaping in all fibre optical systems. The basis upon which the group delay dispersion can be determined is from the phase response of the known complex reflectivity of the grating spectra. The group delay, which is the time difference between the arrival of the wavelength components, is related the distance travelled and this can be determined from the relative phase of the individual component of the grating response [16].

Light reflected or transmitted from a FBG contains both phase and amplitude information. From equation (6.4), the complex reflectivity, R_ρ and complex transmittivity, Γ can be rewritten as;

$$R_\rho(\lambda) = \frac{|B(0)|}{|F(0)|} e^{-i\psi_\rho(\lambda)} \quad (6.5)$$

$$\Gamma(\lambda) = \frac{|F(L_g)|}{|F(0)|} e^{-i\psi_\Gamma(\lambda)}$$

where B is the reflected wave, F is the incident wave, and $\psi_\rho(\lambda)$ and $\psi_\Gamma(\lambda)$ are the relative phases of the two waves for reflection and transmission respectively. Figure (6.3) shows the typical phase response of a linearly chirped grating.

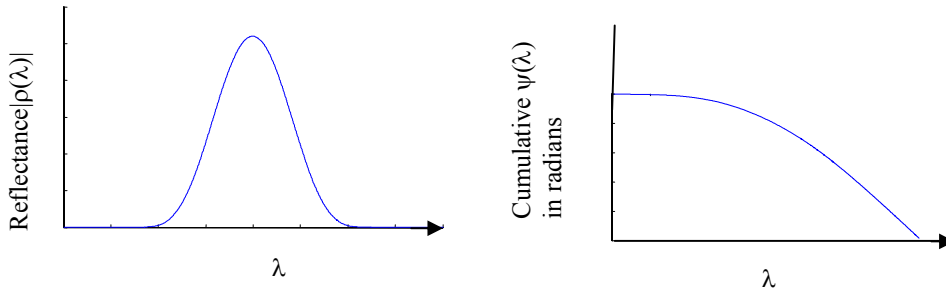


Figure 6.3, the intensity and the phase response of a chirped FBG

The group delay of the reflected light can be determined from the phase $\psi(\lambda)$ of the amplitude reflection coefficient, $R_r(\lambda)$, by using equation (6.5). The first derivative provides an indication of the time delay τ , and is given by [17];

$$\tau = -\frac{d\psi}{d\omega} = -\frac{\lambda^2}{2\pi c} \frac{d\psi}{d\lambda} \quad (6.6)$$

where ω is the angular frequency and c is the velocity of light. Thus an optical wave travelling through a medium of length L and refractive index n will undergo a phase change;

$$\psi = \frac{2\pi nL}{\lambda} \quad (6.7)$$

where λ is the wavelength. The derivative of the phase with respect to wavelength is an indication of the delay experienced by the wavelength component of the reflected light;

$$\frac{d\psi}{d\lambda} = -\frac{2\pi nL}{\lambda^2} \quad (6.8)$$

The time delay, equation (6.6) imparted to an incident light is related to the change in phase with wavelength which in turn is related to the distance travelled, equation (6.8). For the reflected light, it is the distance to its resonance position inside the FBG at which the Bragg resonance condition (2.1) is satisfied. Therefore, each wavelength can be associated with a reflection point along the length of the FBG and a concomitant wavelength dependent penetration depth into the

FBG. The time delay also provides information regarding the optical path traversed for the transmitted wave. To determine the magnitude of the penetration depth and path traversed, FBGs have been modelled and the phase response analysed to determine the penetration depth for reflected wave and distance traversed for the transmitted wave.

6.4 TMM simulation of FBGs

The tangent of the phase of the reflected and transmitted waves is taken to be the ratios of the imaginary to the real part of the complex reflectivity or transmittivity in equation (6.5). The gradient of the phase with wavelength can reveal the time delay and thus the positional dependent of the reflection point of the wavelength.

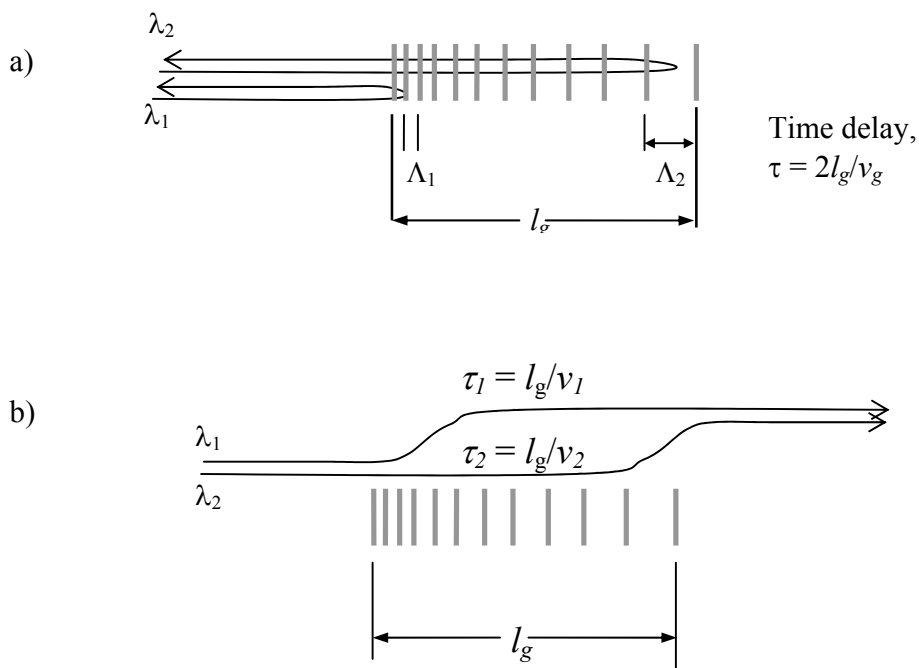


Figure 6.4, illustration of the time delay for the reflected and transmitted beam in a FBG through, a) positional dependent reflection point and b) through a difference in the group velocity

Consider the waves in reflection and transmission, where the incident light comes from the left and impinges on the grating structure as shown in figure (6.4). In transmission, the wave proceeds to the right whereas under reflection, the wave will coupled to the backward

propagation wave at the point where it is phase matched and satisfies the resonance condition. The reflected wave will travel in the backward direction to the left as shown. The delay τ is related to the wavelength gradient of the accumulated phase according to equation (6.6-6.8). The delay and thus the length associated with reflection or transmission is derived from the phase.

6.4.1 Uniform FBG

In a uniform FBG, figure (6.5), the Bragg wavelength is strongly reflected whereas the off resonance wavelength is reflected less strongly. The time delay for the different components of the wavelength as they are reflected from different portions of the grating can be distinguished from the phase information of the grating.

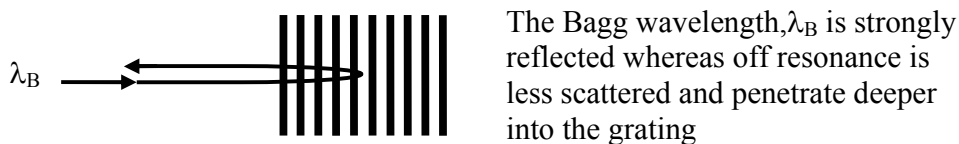


Figure 6.5, illustrates a uniform FBG where the Bragg wavelength, λ_B is strongly reflected and the off resonance wavelength is less so allowed a deeper penetration into the grating.

Figure (6.6) demonstrates the reflection spectrum and the phase response of a uniform FBG with a grating length of 4mm, with a central wavelength of 1550nm and FWHM~0.3nm. From the penetration depth of the wavelength components determined from equation (6.8) are shown in figure (6.6). The discontinuities in the phase response, figure (6.6b) correspond to the band-edges of the FBG, arising from of the grating boundary causing a FP effect[17], where the wave is trapped by cavity effects and undergoes multiple reflections, resulting in an increased time delay, indicated by the sharp peaks in the penetration depth, figure (6.6c). Off resonance, the penetration into the grating is greater than on-resonance, leading to a larger penetrating depth.

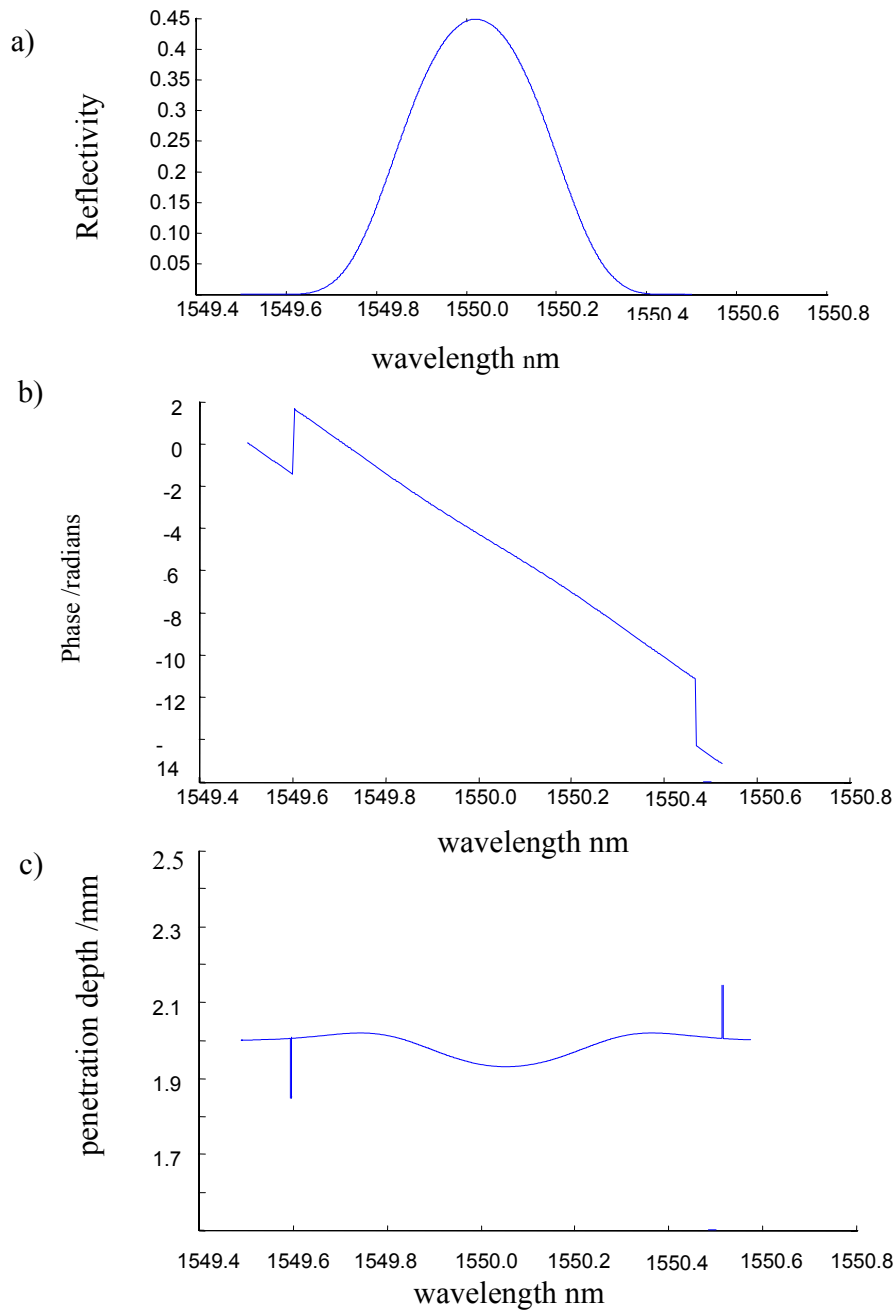


Figure 6.6, illustrates the reflection spectrum of a uniform FBG centred at wavelength of 1550nm having length of 4mm. (a) reflectivity, (b) phase and (c) the penetration depth.

From the analysis, the cavity response of a FP formed between uniform period FBGs is modified by the different penetration depth. In the conventional FSR equation, the cavity length becomes a function of wavelength [10];

$$FSR = \frac{c}{2nl(\lambda)} \quad (6.9)$$

where, $l(\lambda)$ is the wavelength dependent cavity length of the FBG FP.

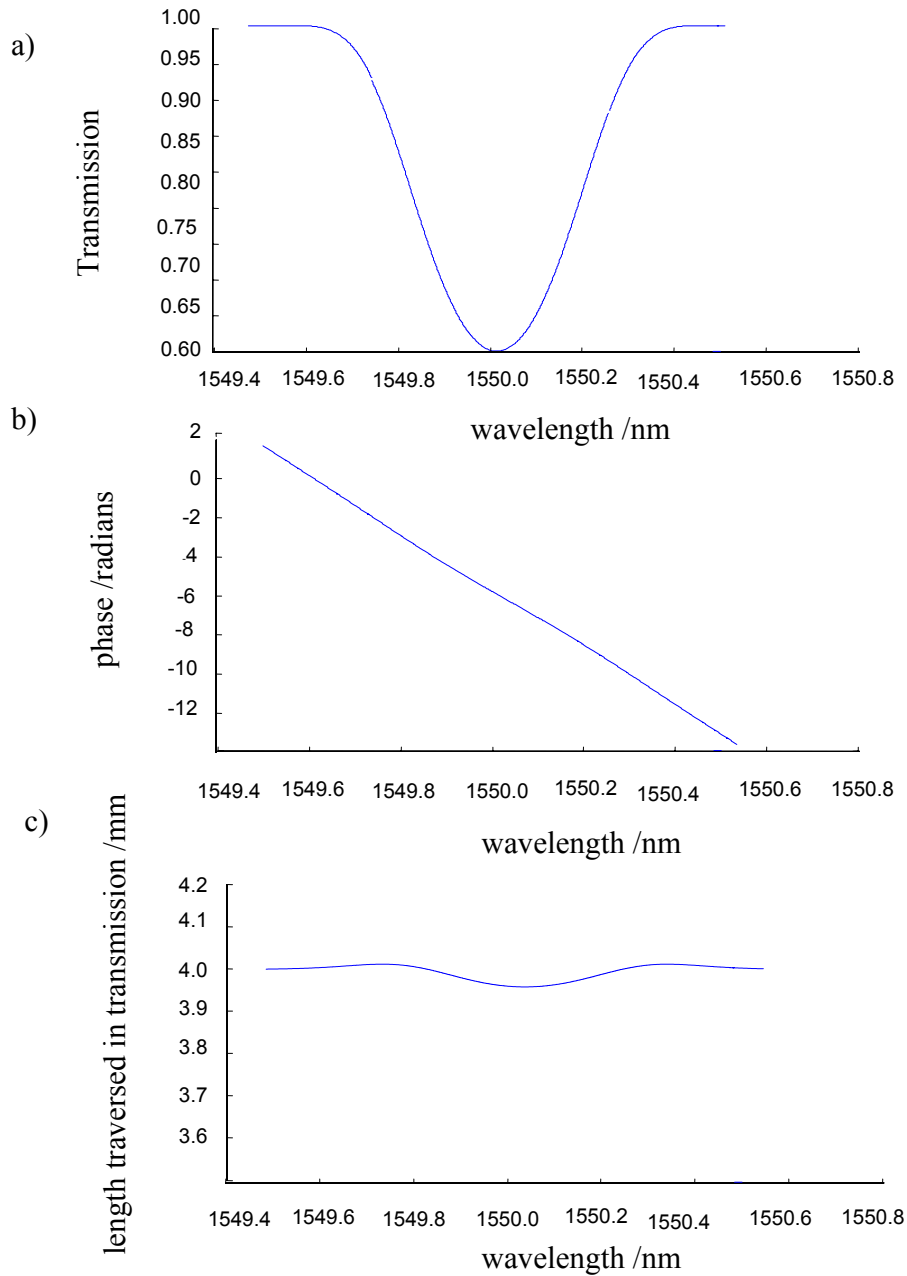


Figure 6.7, shows the transmission profile for a uniform FBG having length of 4mm. (a) the transmittivity, (b) the phase response and (c) the path traversed.

The equation gives a larger FSR at the edges of the FP bandwidth than the on resonance wavelength. Figure (6.7) shows the transmission response of a uniform FBG, the phase response and the path length travelled, calculated assuming the parameters detailed previously. There is a small variation of the path length travelled by the different wavelength components, figure (6.7c). The on-resonance wavelength sees a much shorter path than the off-resonance wavelength.

6.4.2 Positively chirped FBG

In a chirped FBG, the positional dependence of the resonance condition gives rise to a broadened spectrum. As well as the broadened spectrum, different wavelength experience different delays as they are reflected from different positions along the FBG. Figure (6.8) shows light incident from the left and reflected from a positively chirped FBG, where the longer wavelengths are reflected from position further into the grating.

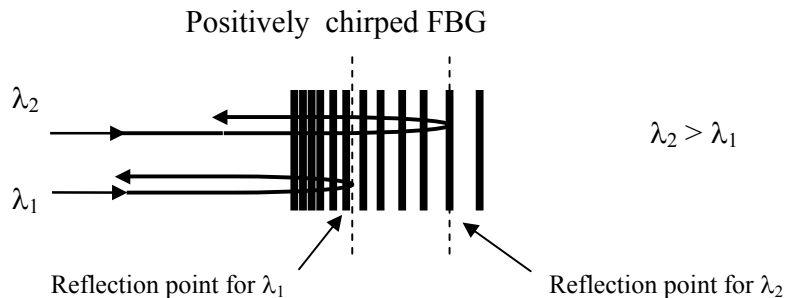


Figure 6.8, illustrates a positively chirped FBG where the light is incident from the left. The longer wavelength, λ_2 is reflected from a position in the FBG further to the right (positive in the right direction) compared to the shorter wavelength, λ_1 in a Cartesian coordinate system.

Figure (6.9) shows the simulated reflection, phase response and penetration depth for a 4mm long chirped FBG with a total chirp of +10nm, central wavelength of 1550nm. It can be seen that the longer wavelength penetrates deeper into the grating. The higher the chirp, the more linear the slope of the wavelength dependence of the penetration depth becomes.

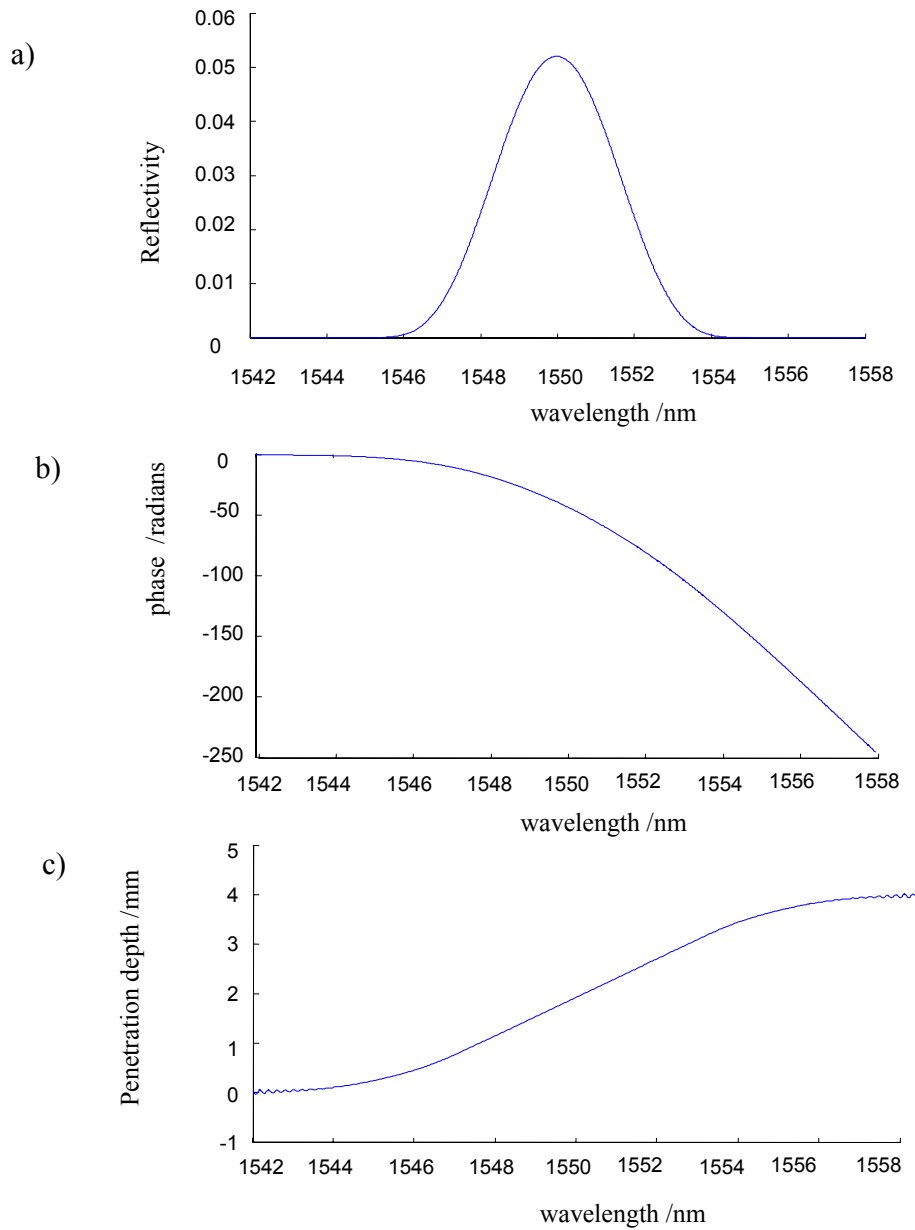


Figure 6.9, illustrates the reflection response for a chirped FBG having length of 4mm with a chirp of +10nm. (a) the reflectivity, (b) the phase response and (c) the penetration depth.

Figure (6.10), shows the transmission profile, phase and path travelled for a FBG with a central wavelength of 1550nm, grating length of 4mm and a total chirp of +10nm. As was the case for the transmission response of the uniform FBG in figure (6.7), there is a small variation of the grating length with wavelength in traversing the grating, is seen for the positively chirped FBG.

Again there is the FP effect, where the wavelength at the band-edge remains trapped in the structure to produce a longer delay and hence a longer length response. In transmission, all the wavelengths see the same grating length of 4mm, except for the small variation near the central wavelength regions of 1550nm, shown in figure (6.10c).

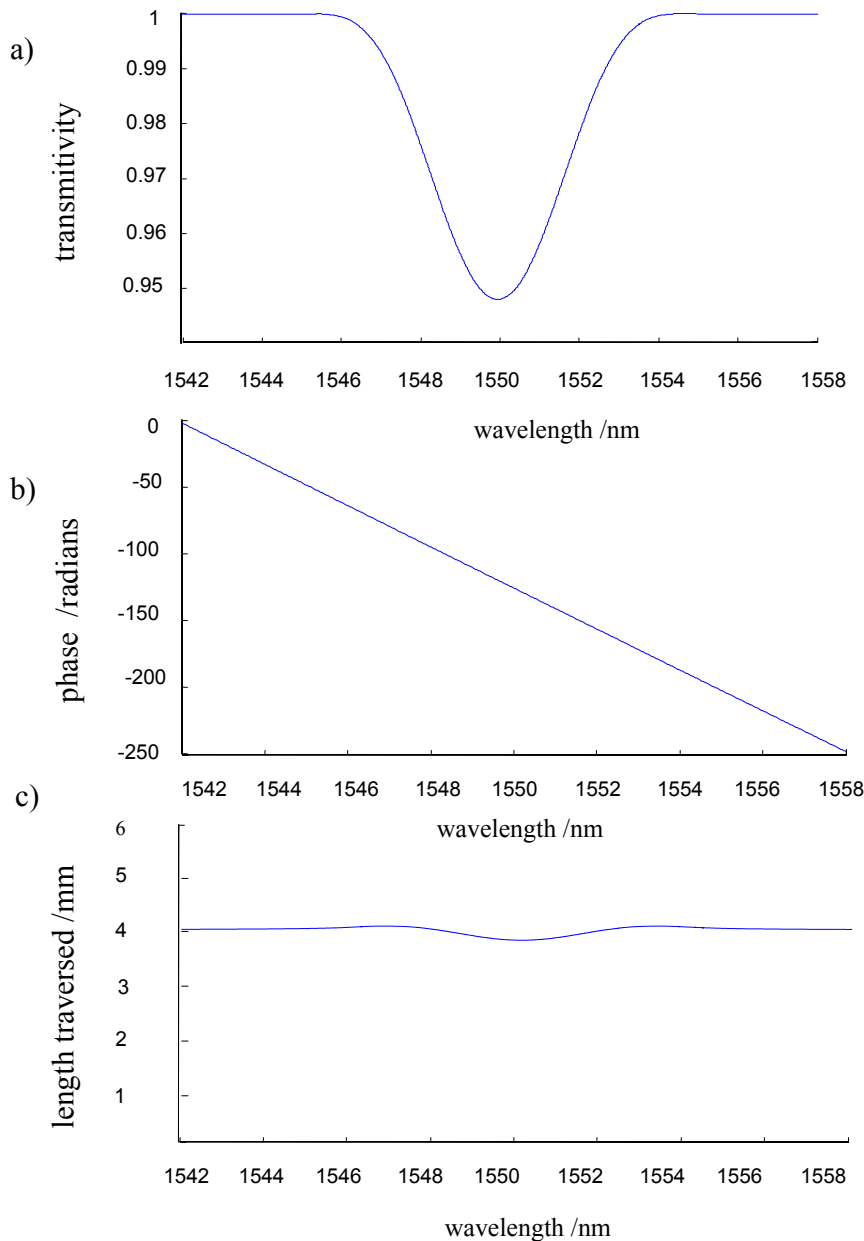


Figure 6.10, illustrates the transmission response for a chirped FBG having a length of 4mm and a total chirp of +10nm. (a) the transmission (b) the phase response and (c) the path traversed which is the grating length .

6.4.3 Negatively chirped FBG

For a negatively chirped FBG, the positional dependence of the resonance condition is opposite to that of the positively chirped FBG, such that the longer wavelength component is reflected from a position near to the left hand side of the FBG, as shown in figure (6.11).

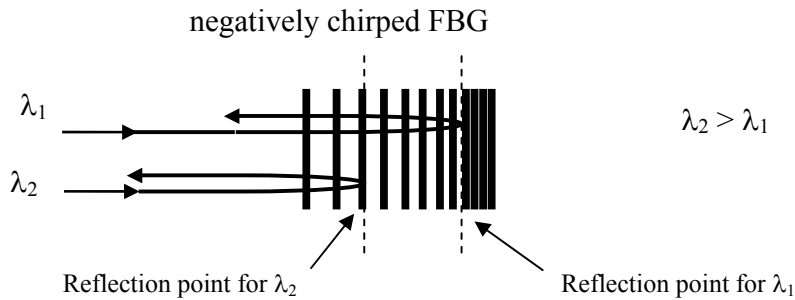


Figure 6.11, illustrates a negatively chirped FBG where light is incident on the grating from the left. The longer wavelength, λ_2 is reflected from a point near on the left hand side of the FBG (more negative towards the left) compared to the shorter wavelength, λ_1 in a Cartesian coordinate system.

Figure (6.12) shows the simulated reflection response, phase and penetration depth of a FBG of 4mm length with a total chirp of -10nm with central wavelength at 1550nm. Notice that the phase response for the negatively chirped FBG, figure (6.12b) is inflected the other way compared to phase response of the positively chirped FBG, figure (6.9b). This time, the shorter wavelength penetrates deeper into the grating, figure (6.12c) and the penetration depth trend reverses compared to the positive chirped FBG, figure (6.9c). The chirped FBG has a grating length of 4mm with a central wavelength of 1550nm and a total chirp of -10nm. The simulated transmission response for the negatively chirped FBG is shown in figure (6.13). The transmission response for the negatively chirped FBG is very similar to that of the positively chirped FBG in figure (6.10).

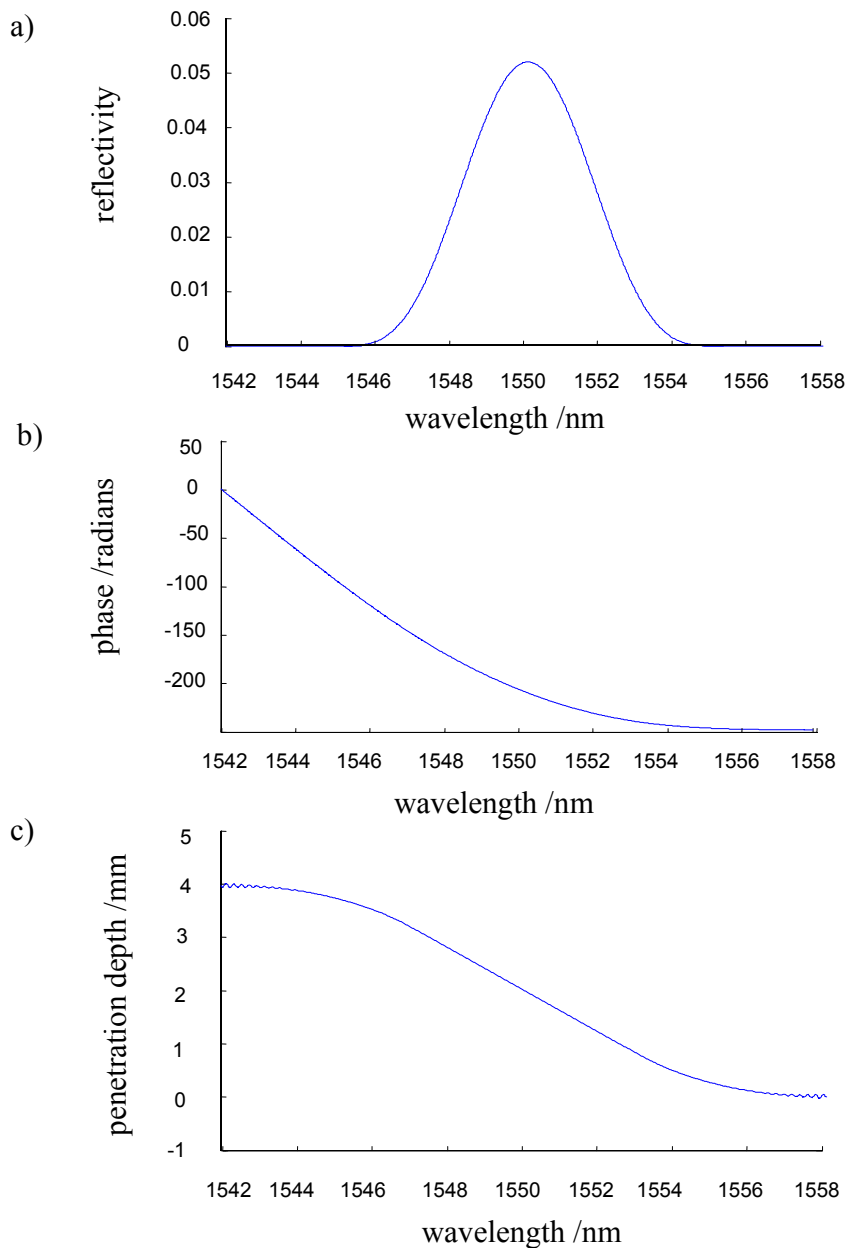


Figure 6.12, illustration of the reflection response for a negatively chirped FBG having a length of 4mm and total chirp of -10nm. (a) the reflectivity, (b) the phase response and (c) the penetration depth.

There is the same cavity effect due to the boundary of the grating edge where the wavelength in the bandedge is trapped in the structure giving a longer time delay. The variation of the grating length with wavelength in travelling through the negatively chirped FBG is small and all the wavelengths see a grating length of ~ 4 mm as shown in figure (6.13c).

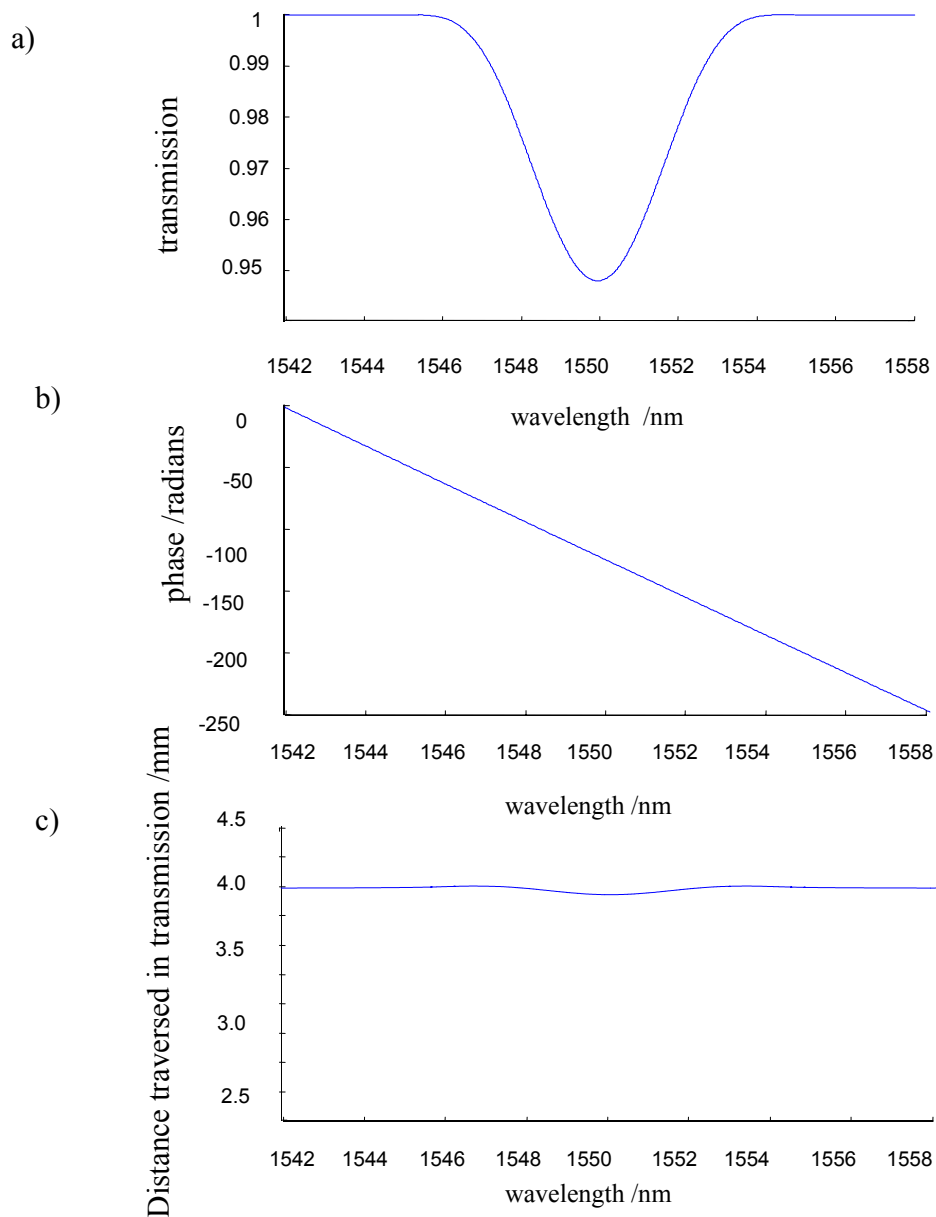


Figure 6.13, illustrates the transmission response for a negatively chirped FBG of 1550nm central wavelength, having a grating length of 4mm and a total chirp of -10nm. (a) the transmission profile, (b) the phase response and (c) the distance travelled across the grating.

6.5 Modelling the strain effect on the chirped FBG

The change in penetration depth in reflection and the distance traversed in transmission in response to an applied axial strain for chirped FBG is investigated using the TMM model. Under the influence of strain, the FBG will experience a physical elongation of the grating period, Λ and a change of refractive index, n due to the elasto-optic effect. Both of these effects influence the Bragg condition, equation (2.1). The refractive index of the optical fibre is dependent on the strain experienced according to [18];

$$n(d\varepsilon) = n_0 - \frac{n_0^3}{2} [p_{12} - \nu(p_{11} + p_{12})] d\varepsilon \quad (6.10)$$

where n_0 = the initial refractive index,
 ν = Poisson ratio
 p_{11} and p_{12} = Pockels coefficients

Using the TMM method, the change in the penetration depth in reflection and the change in the distance traversed in transmission in response to an applied strain is investigated for a chirped FBG with a central wavelength of 1550nm. FBGs with a range of grating lengths and total chirp are simulated and the phase information of the reflected and transmitted waves, derived from the complex reflectivity, R_ρ and transmittivity, T , equation (6.5), is analysed to determine the penetration depth and distance traversed. The changes in these distances when the FBGs are subjected to the axial strain, is investigated for the illuminating central wavelength at 1550nm. This response to strain is considered in the context of the FBG FP configuration and is dependent on the orientation of the chirped FBGs. The strain response of the FBG will affect the strain sensitivity of the FP cavity.

6.5.1 The change in the penetration depth of the chirped FBG with strain

The effect of strain on FBG will shift the whole reflection profile according to the strain responsivity of the FBG. Incorporating the strain parameters into the model, a grating centred at a wavelength of 1550nm with grating length of 4mm and a total chirp of +10nm is used. The strain dependent wavelength shift of the central wavelength is simulated and the predictions are plotted in figure (6.14).

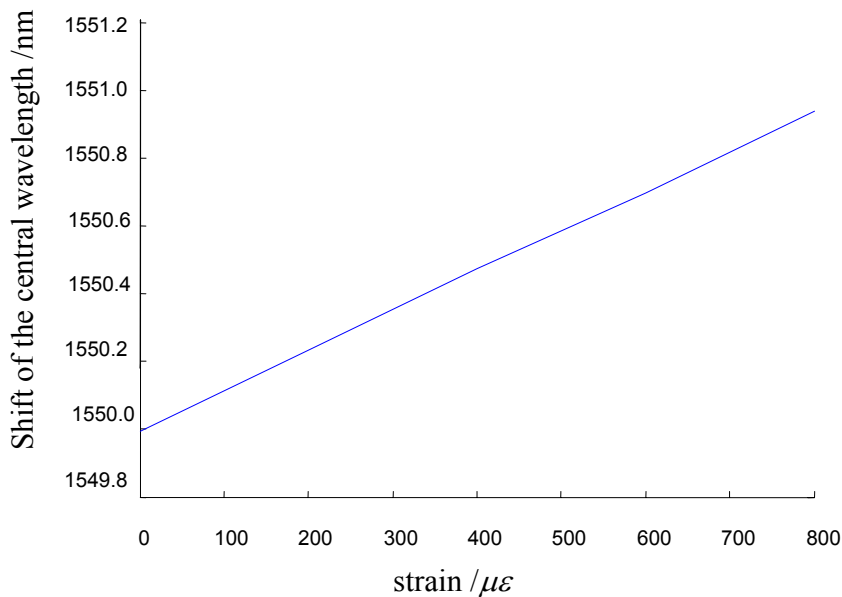


Figure 6.14 showing the movement of the central wavelength with strain for a 4mm FBG with a total chirp of +10nm.

From figure (6.14), the shift of the central wavelength with strain gives a linear response and a value of $\frac{d\lambda}{d\epsilon} = 1.1812 \text{ pm } \mu\epsilon^{-1}$ is determined, compared to the accepted value of $1.2 \text{ pm } \mu\epsilon^{-1}$ [19]. The value of the strain sensitivity of the FBG determined by the model serves as an indicator for the validity of the approximation of the strain parameters used.

The shift of the grating reflection profile is due to the redistribution of the reflection positions for different wavelengths in the presence of a uniform strain. In a positively chirped FBG as shown in figure (6.15), interrogated with a wavelength, λ , the increasing period of the FBG is directed towards the positive direction in the Cartesian system. Under the influence of an axial strain, the reflection point for an arbitrary wavelength λ will move in the direction against the increasing

chirp, as shown in figure (6.15). This has the effect of reducing the penetration depth in a positively chirped FBG.

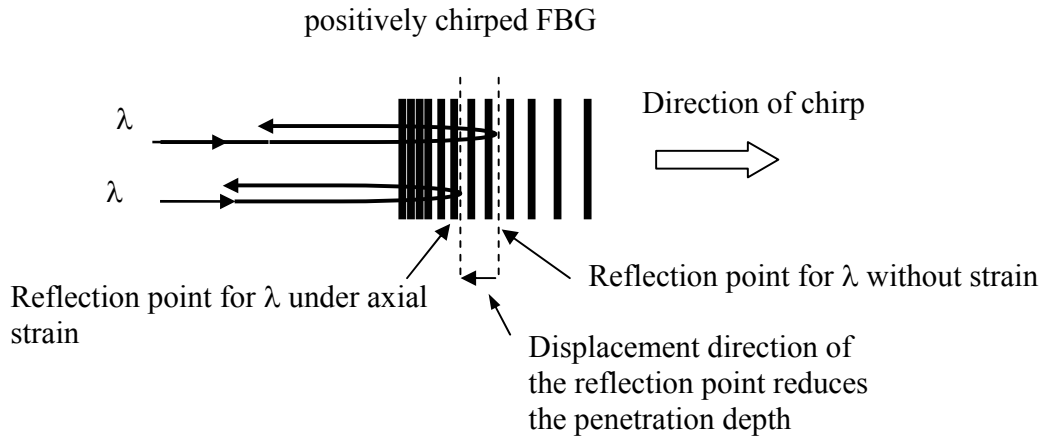


Figure 6.15, illustrates a positively chirped FBG experiencing axial strain and being interrogated at wavelength, λ . The displacement of the reflection point goes against the direction of chirp and hence reduces the penetration depth in this positively chirped FBG.

The effect of strain on the penetration depth profile for a positively chirped FBG is shown in figure (6.16). As the strain increases in the FBG, the whole reflection profile is shifted towards the increasing wavelength region thus the movement of the whole penetration profile is shifted to the right.

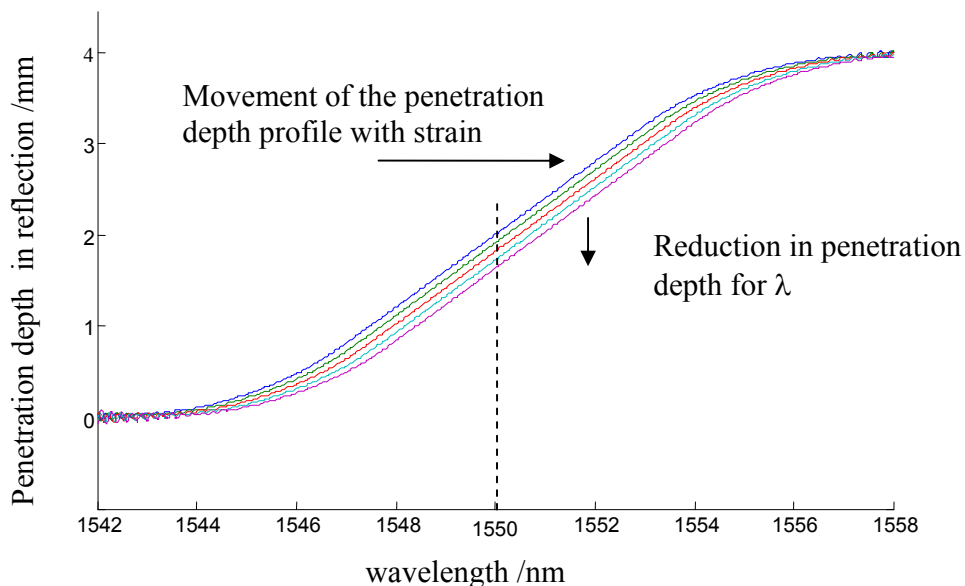


Figure 6.16, showing what the increasing strain has on the penetration depth of the reflected wave in the positive chirped 4mm FBG.

For a given wavelength, this has the effect of reducing the distance of the reflection point from the edge of the grating, thus reducing the penetration depth of the light at that wavelength.

Assuming that the grating is illuminated with the wavelength of the central wavelength, of 1550nm, the variation of the penetration depth for the illuminating wavelength with strain is simulated for the same positive chirped FBG and is shown in figure (6.17).

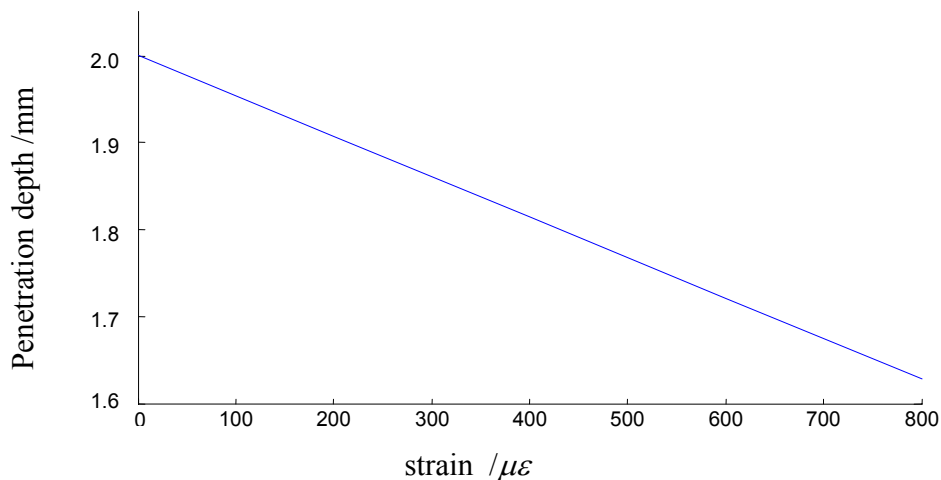


Figure 6.17, shows the variation of the penetration depth as a function of axial strain for a FBG of length 4mm with total chirp of +10nm illuminated at the central wavelength.

From figure (6.17), the change of the penetration depth with strain at the wavelength of 1550nm gives a value of $\frac{db}{d\epsilon} = -464.66 \times 10^{-6} \text{ mm } \mu\epsilon^{-1}$ which compares well with a value of $-460 \times 10^{-6} \text{ mm } \mu\epsilon^{-1}$ using equation (5.4) with a strain response of $\xi = 0.742 \times 10^{-6} \mu\epsilon^{-1}$ [19]. This change in the wavelength detuned distance, b with strain serves as a validation of the strain simulation.

The change in the penetration/reflection position of the chirped FBG with the application of axial strain is investigated using the reflection response of the FBG. FBGs with a central wavelength of 1550nm and grating lengths, l_g in the range of (0.5-5mm) and with different total chirps in the range of (3-30nm) is used in the simulations. The change in penetration depth with strain of the central wavelength of 1550nm is evaluated for different grating length, l_g and different total

chirp, $\Delta\lambda_c$. The movement of the reflection point for 1550nm with strain, $\frac{db}{d\varepsilon}$ is plotted as a function of grating length, l_g for different total chirp, $\Delta\lambda_c$ as shown in figure (6.18).

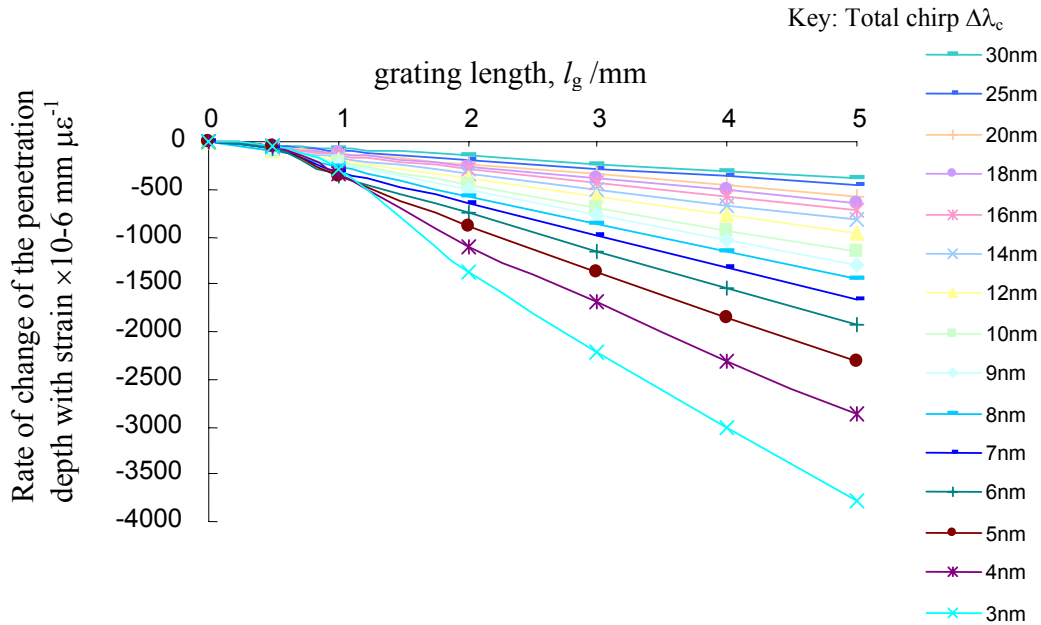


Figure 6.18, showing the rate of change of reflection point w.r.t strain as a function of grating length, l_g for different total chirp in the FBGs at the central wavelength of 1550nm

Figure (6.18), shows a plot of the rate of change of reflection point of the central wavelength at 1550nm for a chirped FBG subject to an axial strain as a function of the grating length. As a figure of merit, the application of a strain of $1\mu\varepsilon$ on a piece of 1mm of bare fibre will produce an extension of; $\frac{dx}{d\varepsilon} = 1 \times 10^{-6} \text{mm } \mu\varepsilon^{-1}$ ($\sim 0.8 \times 10^{-6} \text{mm } \mu\varepsilon^{-1}$ in terms of optical path). Thus for a 5mm long FBG, with a total chirp of 3nm, the rate of change of the reflection point with strain, determined from figure (6.18) is $-4000 \times 10^{-6} \text{mm } \mu\varepsilon^{-1}$ which is equivalent to applying a strain of $1\mu\varepsilon$ to 4m length of optical fibre. In a FP configuration employing a dispersive element such as a chirped FBG as a compensating partially reflective mirror, the large movement of the reflection point in response to the applied strain would compensate for the optical path length increase in a cavity of length of 4m. This is simply a restatement of equation (5.4); $\frac{db}{d\varepsilon} = \frac{\lambda}{\Delta\lambda_c} l_g \xi$. For a given total chirp $\Delta\lambda_c$, the rate of change of reflection point with strain is proportional to grating length.

The larger the grating length, l_g or smaller the total chirp $\Delta\lambda_c$, the larger the movement of the reflection point.

A similar conclusion can be drawn in the case of a cavity employing chirped FBGs oriented in such a direction that the movement of the reflection point with strain will have an enhancing effect on strain sensitivity of the cavity. From this analysis, a highly strain sensitive cavity could be configured by just employing FBGs with small chirp rate and long grating length in a short FP cavity.

6.5.2 The change in length of the chirped FBG with strain

The change in the length of the chirped FBG with the application of axial strain is investigated using the transmission response of the FBG. FBGs with different grating lengths in the range of (0.5-5mm) and total chirps in the range of (3-30nm), were modelled and the change in the length of the grating for the illumination wavelength of 1550nm, under the application of strain is evaluated from the phase information of the complex transmission, Γ . The values for the change in the length of the grating with strain experienced by the central wavelength of 1550nm, is plotted in figure (6.19).

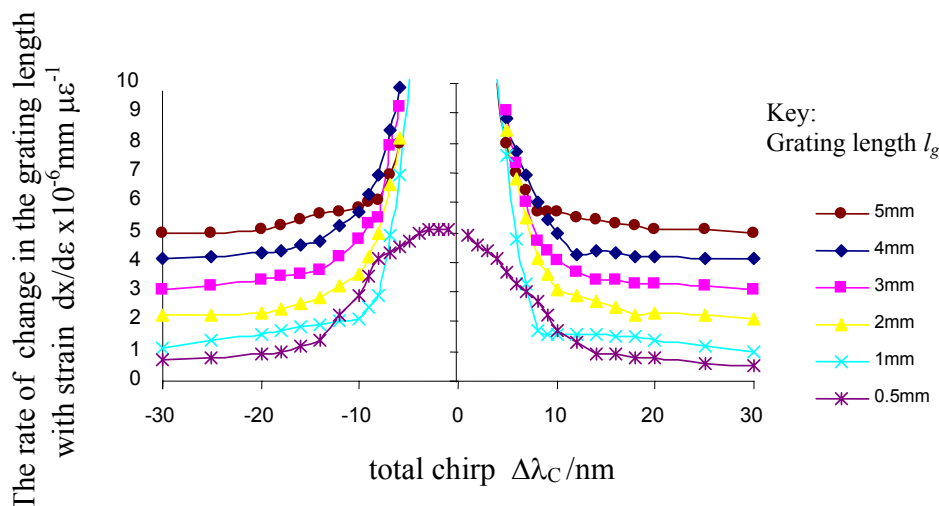


Figure 6.19, showing the rate of change of the grating length with strain for the FBG as a function of the total chirp, $\Delta\lambda_c$ for different grating length for the central wavelength.

The graph in figure (6.19) is a plot of the change in the length of the grating with strain as a function of total chirp for different grating lengths, experienced by the central wavelength of 1550nm. It can be seen that the smaller the magnitude of the total chirp, the larger the change in the length of the grating with strain experienced by the central wavelength. As the magnitude of the total chirp, $\Delta\lambda_c$ increases, the change in the grating length with strain converges to a value which is equivalent to straining the grating length, l_g in question. This is expected of straining a length of a grating. The effect is the same for both the negatively and positively chirped FBG, figure (6.19). The change in the grating length with strain in transmission is consequential in the FP cavity which comprises of the chirped FBG where the light is required to travel through the grating where the difference in the path length travelled between the 2 lights needs to be considered for the cavity response with strain, figure (6.20).

6.5.3 Strain response of the chirped FBG FP: A semi TMM approach

Consider the chirped FBG FP, figure (6.20) which consists of two chirped FBGs separated by a cavity length, L measured from the inner grating edges between the two. The FBGs are identical with the chirp orientated in an arbitrary direction. The two rays with wavelength, λ , are incident on the cavity from the left. One is reflected from the first grating and the second one traverses the 1st grating, as well the cavity length, L , before it undergoes reflection from the 2nd grating. The strain sensitivity of this FP cavity is characterised by the change of distances experienced by the 2 rays and it is dependent on the orientation of the chirp of the two FBGs. The change in distances experienced by the 2 rays under the application of strain is considered and the aggregate effect of the changes in the reflection position and changes in the grating length is evaluated together with the changes in the cavity length, L is considered. The strain sensitivity of the chirped FBGs cavity is determined.

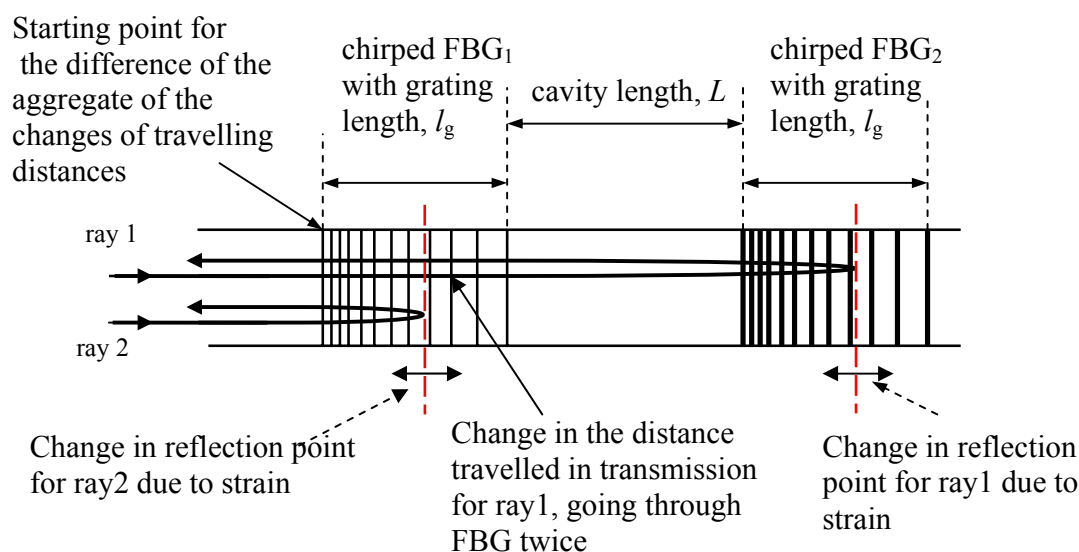


Figure 6.20, illustration of an arbitrary chirped FBG FP cavity demonstrating the aggregate changes in the reflection position and the length traversed in the grating which determines the strain sensitivity of the cavity.

6.5.4 Strain insensitive chirped FBG FP cavity

Consider the chirped FBG FP cavity which consists of 2 identical chirped FBG with a central wavelength of 1550nm and, with the increasing chirp of the FBGs oriented away from the centre of the cavity as shown in figure (6.21). Excluding the cavity length, L , the path travelled by ray 1 on a single round trip of the cavity consists of the transmission through FBG1, reflection from FBG2 then another transmission through FBG1. On its second pass through FBG1, the chirp has an opposite sense. Ray 2, experiences one reflection from FBG1. Under the application of strain, the reflection points of ray 1 and ray 2 move in the direction against the increasing chirp in the respective FBGs, which has a tendency to reduce the length of the cavity L , figure (6.21). In contrast, the transmitted ray 1 will experience an increased in the length of the grating FBG1 under the application of strain.

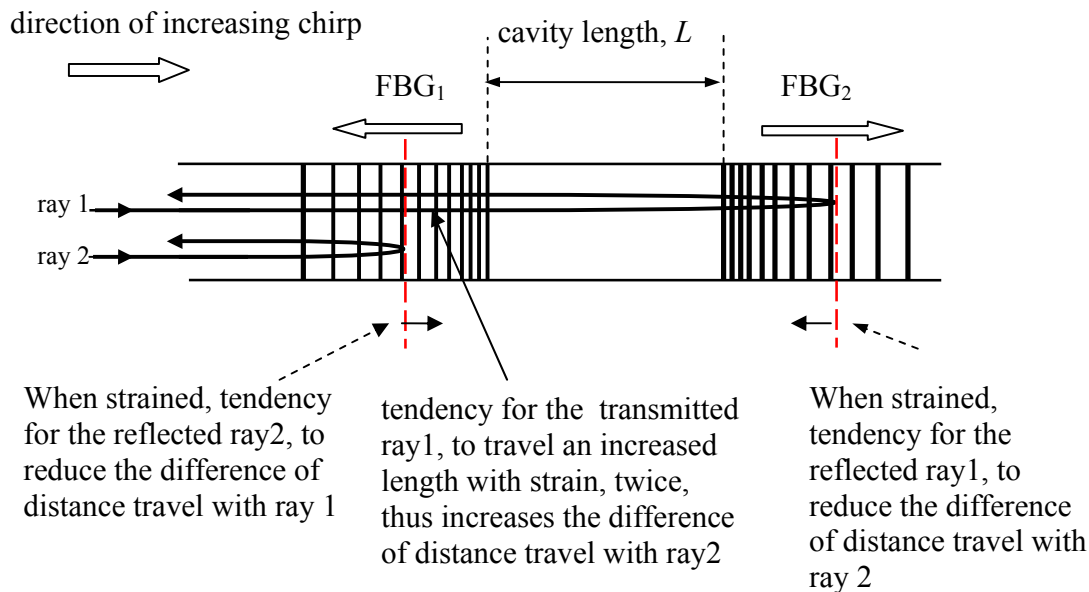


Figure 6.21, illustration of an arbitrary chirped FBG FP cavity demonstrating the aggregate changes in the reflection position and the length traversed in the grating which determines the strain sensitivity of the cavity.

Using the data from sections (6.5.1) and (6.5.2) for the changes in penetration depth in reflection and the changes to the grating length in transmission experienced by the central wavelength at 1550nm under the application of strain. The accumulated changes of the distances experienced for the 2 rays are determined for different total chirps and different grating lengths. For a cavity to be strain insensitive, the aggregate of the accumulated change in distances for the 2 rays experienced in their travel through the cavity must equal to zero. The cavity length, L , required to create a strain insensitive cavity is plotted, against the grating length, l_g for different total chirp $\Delta\lambda_c$ in figure (6.22).

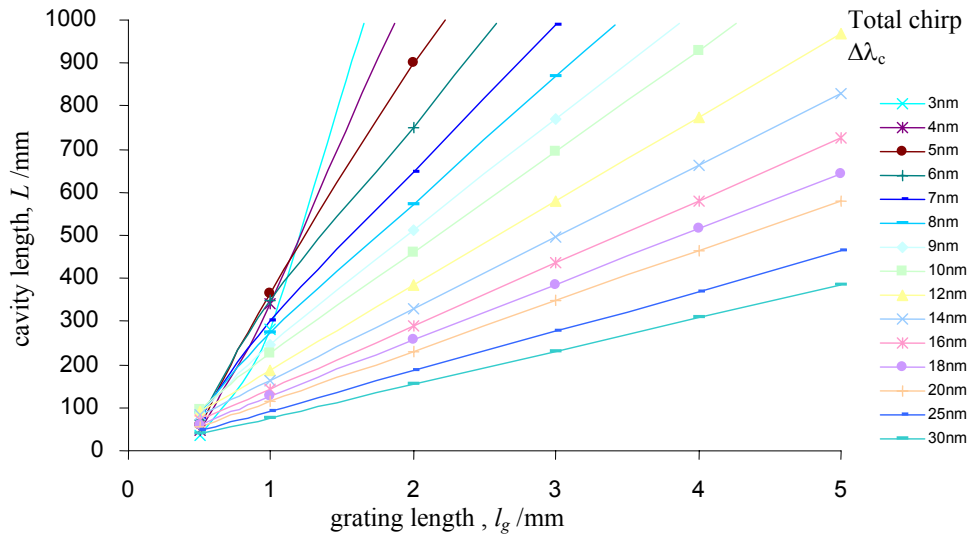


Figure 6.22, shows the cavity length required for a strain insensitive chirped FBG FP cavity employing two identically chirped FBGs in the reduced configuration shown in figure (6.21).

From figure (6.22), for a given total chirp, $\Delta\lambda_c$, the smaller the grating length, l_g the shorter the strain insensitive cavity length, L will be and for a given grating length, the higher the total chirp, the smaller the cavity length, L will be for a strain insensitive chirped FBG FP cavity.

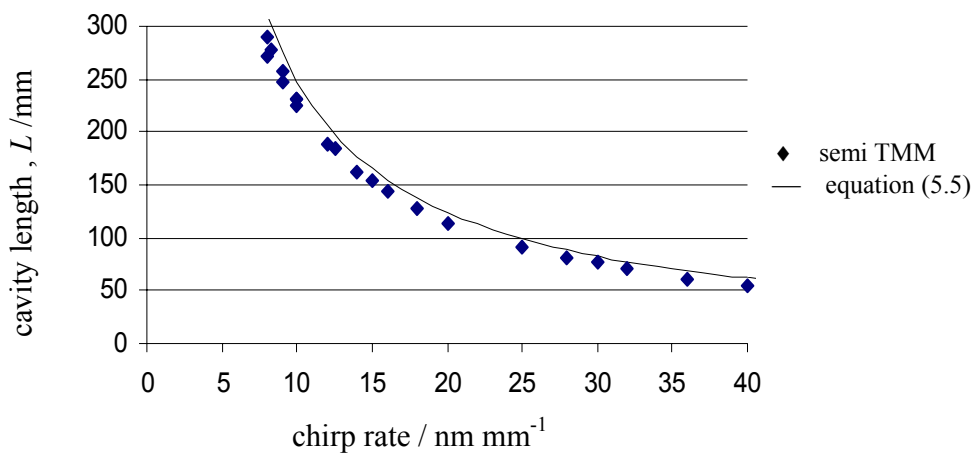


Figure 6.23, using the results in figure (6.22), a plot of cavity length required to achieve a strain insensitive cavity against chirp rate for the central wavelength @1550nm, using the Semi-TMM approach together with equation (5.5), using $\xi = 0.8 \text{ } \epsilon^{-1}$.

Plotting the strain insensitive cavity length, L , against chirp rate (nm/mm), figure (6.23), shows that the cavity length required to achieve a strain insensitive FP cavity has an inverse relationship with the FBG chirp rate. The result of the analysis for the strain insensitive configuration using this semi TMM is compared to the strain insensitivity length derived analytically in section (5.4) for the chirped FBG FP and the two results demonstrates the same trend except for a multiplying factor which depends on the elasto-optic parameters used in the semi TMM simulation. By careful design of the chirped FBG FP, the strain sensitivity can be reduced or enhanced depending on the orientation and the size of chirp rate, C in the FBGs.

6.6 Summary

The different modelling techniques that have been applied to the FBG have been discussed and outlined. A brief introduction to TMM method have been presented and the coding of the TMM using Matlab has been developed to model the FBGs. Using the relationship between the phase response with wavelength, the group delay has been determined from which, the penetration depth for reflection and distance traversed for transmission have been presented for the FBGs. Using the idea of penetration depth and distance traversed for the FBG, a semi TMM approach to the strain response of the chirped FBG FP has been presented and the condition for the strain insensitivity chirped FBG FP has been derived which is consistent with the treatment using the RTPS of the chirped FBG FP cavity considered in chapter 5. For a given gauge length of the chirped FBG FP, the chirp rate required to configured a strain insensitivity cavity can be determined using figure (6.23) or using equation (5.5) in section 5.

References:

-
- 1 P. Yeh, 'Optical Waves in Layered Media', Wiley, 1991.
 - 2 A. Yariv, 'Optical Electronics', 4th Edition, Saunders, chapter 13, 493, 1991.
 - 3 I. Bennion, J. A. R. Williams, L. Zhang, K. Sugden and N. J. Doran, 'UV-written in fibre Bragg gratings', *Optical and Quant. Elect.*, **28**, 93-135, 1997.
 - 4 M. Matsuhara, K. O. Hill and A. Watanabe, 'Optical-waveguide filters: Synthesis', *Journ. of OSA*, **65**, 804-808, 1975.

-
- 5 H. Kogelink, 'Filter Response of Nonuniform Almost-Periodic Structures', *The Bell System Technical Journal*, **55**, 109-126, 1976.
 - 6 G. I. Stegeman and D. G. Hall, 'Modulated index structures', *J. Opt. Soc. Am. A*, **7**, 1387-1398, 1990.
 - 7 K. Hinton, 'Ramped, Unchirped fiber Gratings for Dispersion Compensation', *Journ. of Light. Tech.* **15**, 1411-1418, 1997.
 - 8 J. Sipe, L. Poladian and C. Martijin de Sterke, 'Propagation through nonuniform grating structures', *J. Opt. Soc. Amer. A*, **11**, 1307-1320, 1994.
 - 9 L. Poladian, 'Graphical and WKB analysis of nonuniform Bragg gratings', *Phys. Rev. E*, **48**, 4758-4767, 1993.
 - 10 S. Legoubin, M. Douay, P. Bernage and P. Niay, 'Free Spectral range variations of grating-based Fabry-Perot filters photowritten in optical fibers', *J. Opt. Soc. Am. A*, **12**, 1687-1694, 1995.
 - 11 W. E. Boyce and R. C. DiPrima, 'Elementary Differential Equations and boundary value problems', 6th edit., John Wiley & Sons. Inc., 1997.
 - 12 K. A. Winick, 'Effective-index method and coupled-mode theory for almost-periodic waveguide gratings: a comparison', *Applied Optics*, **31**, 757-764, 1992.
 - 13 M. Yamada and K. Sakuda, 'Analysis of almost-periodic distributed feedback slab waveguides via a fundamental matrix approach', *Applied Optics*, **26**, 3473-3478, 1987.
 - 14 L. A. Weller-Brophy and D. G. Hall, 'Analysis of waveguide gratings: application of Rouard's method', *J. Opt. Soc. Am. A*, **2**, 863-871, 1985.
 - 15 R. Kashap, 'Fiber Bragg Gratings', Chap. 4, Academic Press, chap. 4, 180, 1999.
 - 16 T. Erdogan, 'Fiber Grating Spectra', *Journ. of Light. Tech.*, **15**, 1277-1249, 1997.
 - 17 V. Mizrahi and J. E. Sipe, 'Optical Properties of photosensitive fiber phase gratings', *Journ. of Light. Tech.*, **11**, 1513-1517, 1993.
 - 18 A. Henriksson, S. Sandgren and A. Asseh, 'Temperature insensitivity of a fiber optic Bragg grating sensor', *Proc. of SPIE*, **2839**, 20-33, 1996.
 - 19 A. D. Kersey, M. A. Davis, H. J. Patrick, M. LeBlanc, K. P. Koo, C. G. Askins, M. A. Putnam and E. J. Friebele, 'Fiber Grating Sensors', *Journ. of Light. Tech.*, **15**, 1442-1463, 1997.

7 Details and specifications of devices used in the design of experiment

7.1 Introduction

This chapter aims to detail the experimental setup used in the characterisation of the FBG FP sensitivity to wavelength, strain and temperature. A discussion of the operation and performance of the devices used will be presented and the implementation of the monitoring systems and their calibration will be discussed.

7.2 Experimental set up

The experimental characterisation of a FP formed between two chirped FBGs has been undertaken using the set-up shown in figure (7.1). The characterisation has been performed by comparing the spectral response of two cavities. One cavity (1st cavity) is formed between 2 chirped FBGs (details of the gratings used are provided in chapter 8) with their chirps oriented such that a reduced sensitivity to strain or a variable FSR is expected, while the other cavity (reference 2nd cavity) has been formed between two chirped FBGs with the same orientation, such that the response would mimic that of a bulk cavity or of a FP cavity formed between two uniform period FBGs. The advantage of the use of chirp FBGs to form the reference cavity is that the operational bandwidth will be similar to that of the 1st cavity. These FP cavities formed between chirped FBGs with their chirps oriented the same way have been experimentally to have the conventional FP response to wavelength [1] and for strain [2].

The two cavities are mounted on a strain rig, where they are subjected to the same level of strain and interrogated simultaneously. One end of each cavity is fixed to a V-groove using an adhesive (Cyanocrylate) whilst the other ends are attached a second V-groove mounted on a translation stage. A known extension, and thus strain, can be applied to the FP cavity by adjusting the separation of the 2 V-grooves. The output from a tuneable source (Photonetics Tuneable external cavity laser or Ti/sapphire), is coupled into the fibre and it is split by a 3 dB fibre coupler (FC1) into two paths. One path is directed to a second 3 dB coupler (FC2), to interrogate a reference

(2nd) cavity, while the other path is split once more by a 3 dB coupler (FC3) to interrogate the chirped FBG FP cavity (1st cavity).

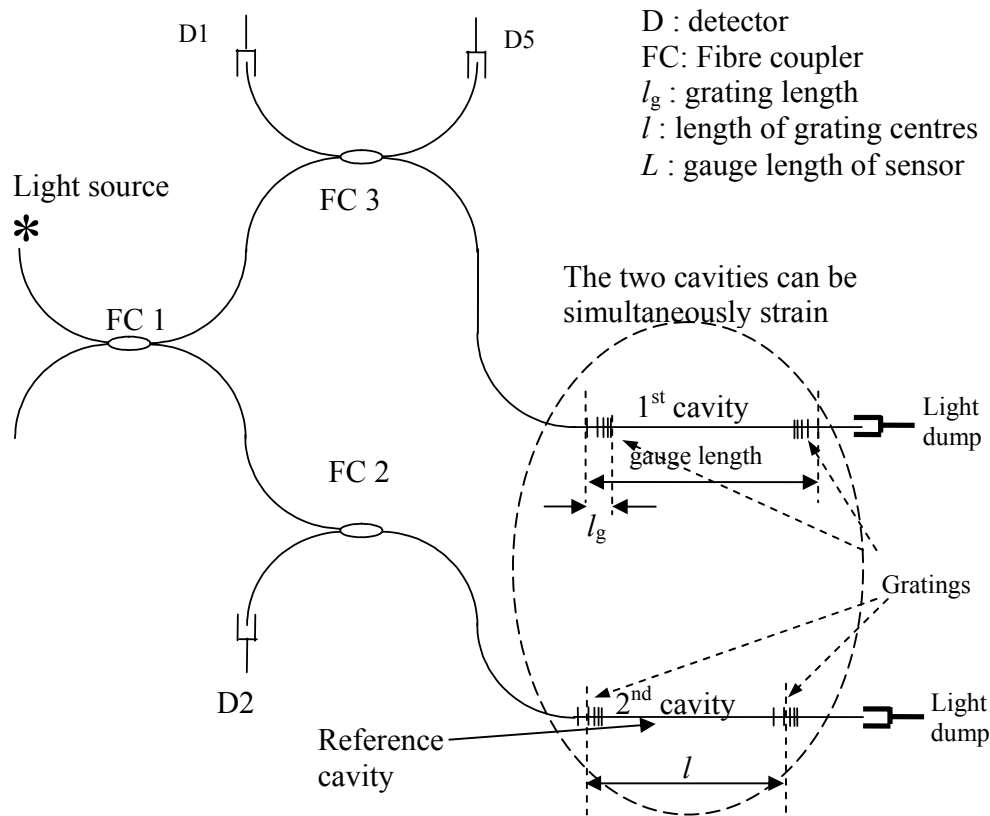


Figure 7.1, shows the experimental setup which uses 3dB fibre couplers to split and direct light to interrogate cavities simultaneous or individually with wavelength scanning or with a calibrated strain.

Detector (D1) is used to monitor the reflected signal from the 1st cavity (reference) and detector (D2) is used to monitor the reflected signal from the 2nd cavity. Detector (D5) is used to monitor intensity fluctuations of the input light source, which may be used to correct the corresponding signals from the other detectors in the network.

The fibre network is designed to allow the characterisation of the cavities with wavelength and strain sensitivities individually. The FBG FP cavities can easily be removed and re-spliced back into the fibre network. The strain rig shown in figure (7.2) can be calibrated by monitoring the extension of a bulk FP, illuminated with a known wavelength such as a HeNe source, where one

of the reflectors is mounted on the translation stage. The separation of the blocks on the translation stage where the FP cavity is to be mounted can be altered by means of a travelling vernier and the extension is applied by a piezo-actuator.

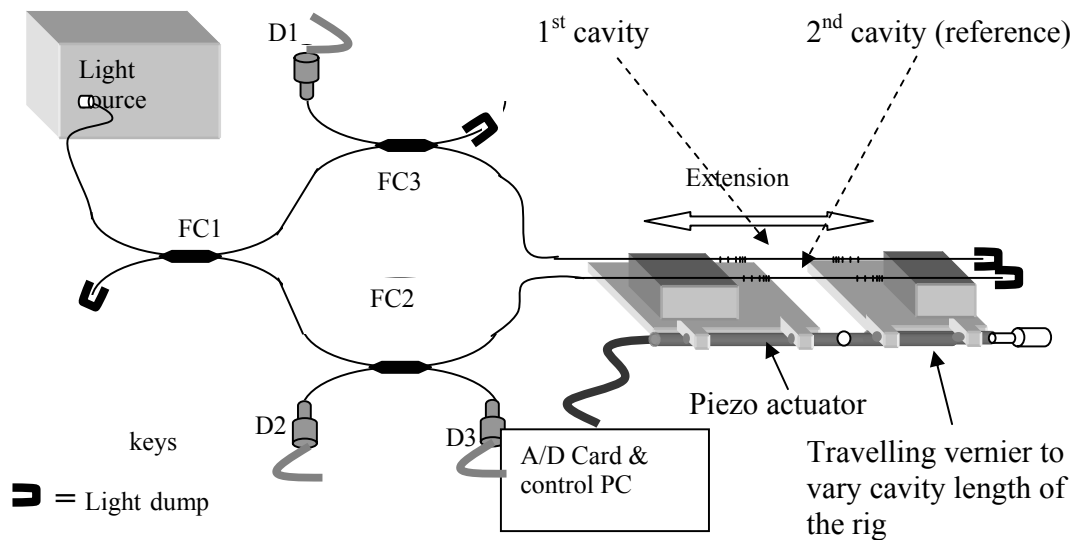


Figure 7.2, the implementation of the strain rig with travelling stages where the width between the two travelling stages forming a cavity can be varied by means of a travelling vernier and a piezo-actuator to apply the extension to the cavity.

7.3 The light source

Two light sources have been used in the investigations described in this chapter. The first is a Ti:Sapphire tuneable laser produced by Schwartz Electro-Optics, Inc. The broad gain bandwidth of the Ti:Sapphire medium allows operation in the infra-red wavelength region when pumped by the all lines output of an argon ion laser. It is of a stable confocal cavity design which makes the adjustment of mirrors for alignment of the cavity and optimisation of the laser much easier.

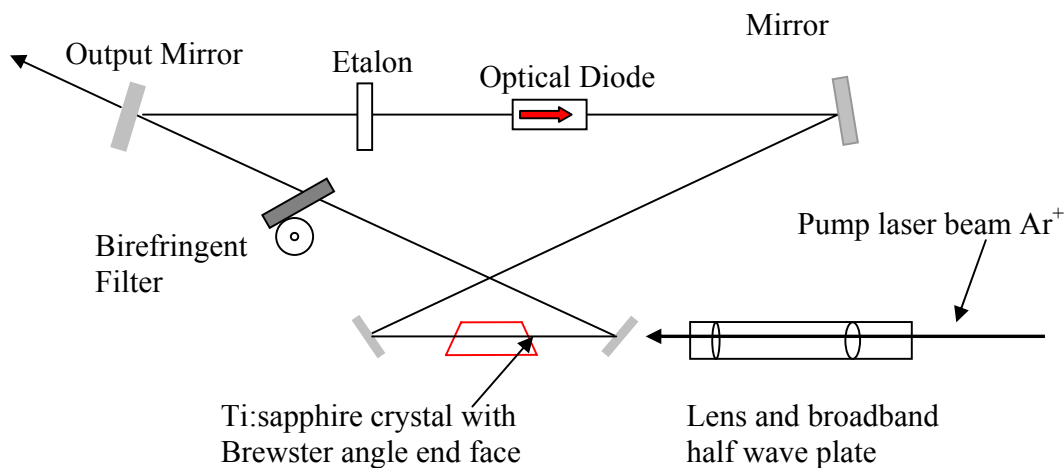


Figure 7.3, A diagram illustrating the ring cavity configuration of the tuneable Ti:sapphire laser configured in the figure of 8.

Figure (7.3), shows a schematic diagram of the tuneable Ti:Sapphire laser. It is a solid state laser, which consist of the Titanium doped Sapphire crystal with a very broad emission spectrum ranging from around 700nm to 1100nm. The crystal is pumped by a high powered argon ion laser. The surface of the crystal is polished at Brewster's angle so that a single polarisation can lase. The laser is configured as a ring cavity. The incorporation of the optical diode permits the light to circulate around the cavity in one direction only. Single mode operation is ensured by the addition of the Etalon filter with a very small cavity length which makes its' FSR large enough to sample the linewidth of the crystal only once. Tuning of the laser emission wavelength is facilitated by a birefringent filter. As a result of the large bandwidth of the gain spectrum, different set of wavelength dependent reflective mirrors are provided corresponds to specific wavelength range in the bandwidth. To match the characteristics of the FBGs, the mirror set used had the laser operating in the 780nm to 860nm region.

The specifications of the SEO TITAN-CW Series, Ti:sapphire Tuneable Laser [3] are detailed in Appendix C.

The 2nd light source used, is a Photonics Tuneable External Cavity Laser (Tunics Plus CL-band) which operates in the wavelength range 1500nm-1640nm. Figure (7.4) illustrates the operation of the external cavity laser.

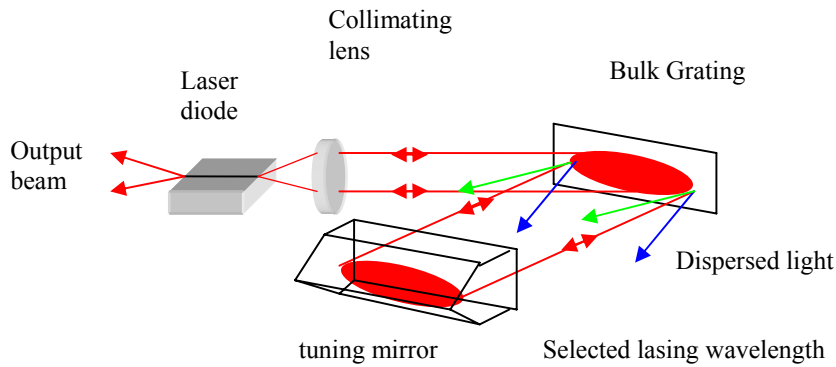


Figure 7.4, diagram illustrating the design of the external cavity tuneable laser.

The external cavity is of the modified Littman-Metcalf configuration which is comprised of the end face of the laser diode and the retro-reflective mirror surface with a dispersive, bulk grating in between. The mirror is placed such that it retro-reflects the 1st order diffraction from the grating. The grating disperses the light and the first order diffracted beam travels to the tuning mirror and is reflected back the way it came into the laser diode as an optical feedback for linewidth narrowing of the laser. The lasing frequencies are determined by the co-incidence of the resonance frequencies of the cavity with the wavelength selective elements of the bulk grating. Tuning of the laser wavelength is achieved by varying the angle of the mirror, which changes the wavelength selection for the optical feedback. Due to the detrimental effect of spurious reflections and feedback sources, the laser has an optical isolator and angled-polished output fibre connector. The laser provides mode hop free operation with resolution of 1 *pm* and output power of up to 20mW. The wavelength jitter is < 3 *pm* [4] and its linewidth is better than 150kHz. The laser may be continuously scanned across the wavelength range, or stepped scanned with step size as little as 1pm with time interval of 0.1 to 25 sec. per step.

7.4 Calibration of the piezo-actuator

The application of axial strain to the cavity was achieved using the configuration illustrated in figure (7.5). The strain rig consists of two stages, where one of the stages is fixed and the other is held with a linear piezoelectric actuator (Newport 17PAS 013). The actuator is driven by a 0-10 V DC function generator, which produces a linear voltage ramp of amplitude 65V, producing an extension of 100 μm . The spacing between the two stages can be varied by a manual travel as shown.

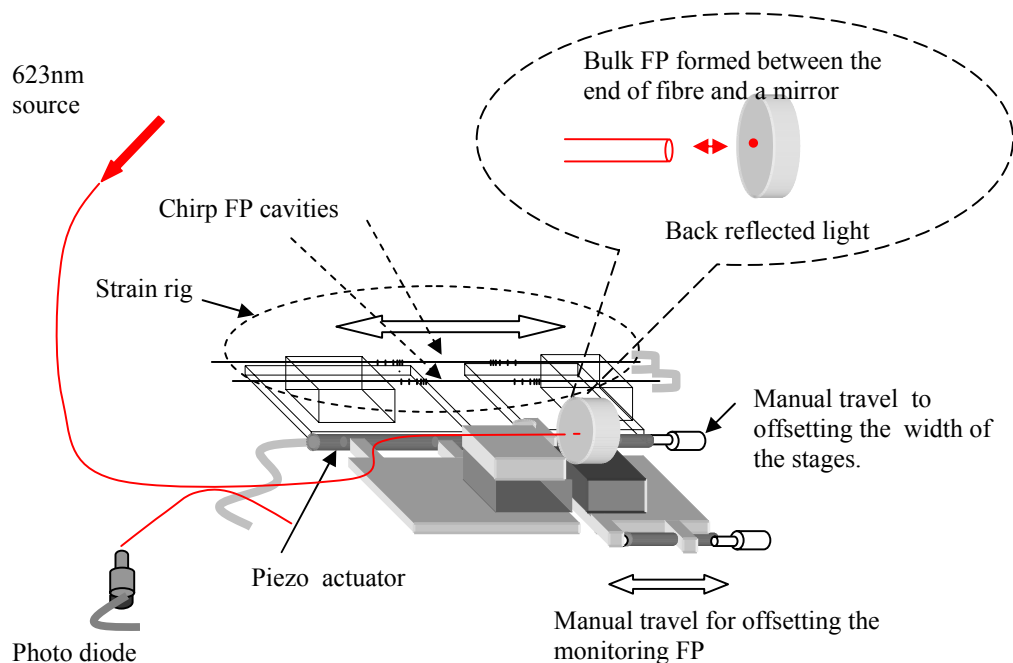


Figure 7.5, illustrates how a bulk optics FP is used to monitor the extension of the straining rig. The cavity is formed between a cleaved fibre end and the mirror surface. It is attached onto an adjacent moving stage, which shared the moving mechanism.

The extension of the cavity is monitored by a bulk FP formed between a cleaved fibre end attached to a moveable travelling stage, and a mirror surface mounted on to a fixed travelling stage as shown in figure (7.5). The moveable part of the travelling stage at which the fibre end is placed, is attached to the moving stage of the strain rig. A HeNe laser is used as the light source. This monitoring FP experiences the same extension as the travelling stages of the strain rig, as shown in figure (7.5). From the knowledge of the extension and the spacing of the travelling

stages, the strain can be determined. The extension produced by the actuator is calibrated against the known wavelength of the HeNe source. The low reflectivity of the fibre end (4%) coupled with the inefficiency associated with coupling the reflection from the mirror into the fibre results in the FP having a low finesse, and therefore a $(1+\cos\theta)$ response. A sawtooth modulation voltage (5 VPP, offset 2.44VDC at 30mHz) is applied to the actuator driver which produces a corresponding voltage (0-65V) at the input of the piezo-actuator. This voltage (0-65V) at the input of the piezo-actuator is stepped down to an acceptable value for the DAQ card ($< \pm 12$ V) which is used to monitor the driving voltage of the piezo-actuator. A 2nd analogue input channel of the DAQ is used to capture the output of the FP response with applied voltage, monitored by a photodiode. A typical scan of the monitoring FP cavity by the application of a ramp of amplitude 65V and of frequency 30mHz to the piezo-actuator is shown in figure (7.6).

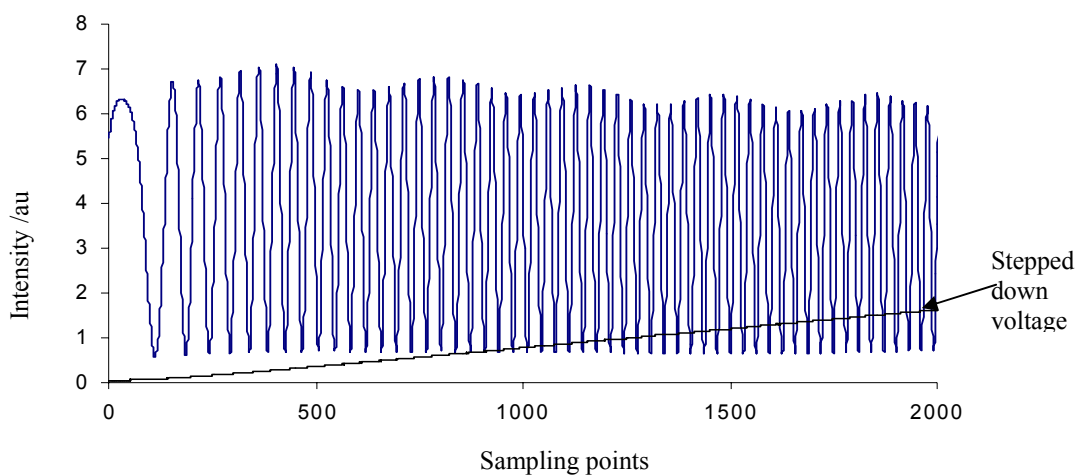


Figure 7.6, illustrates the monitoring FP response with the applied voltage showing the sinusoidal response.

For an extension of the cavity length of $\lambda/2$, there is change in phase of 2π radians in the FP response. A visual interpretation of the output phase can resolve a $1/4$ of a fringe and this is equivalent to an $1/8$ of the HeNe wavelength. Using the number of fringes measured and thus extension, a graph of the applied voltage against extension can be determined. The calibration is repeated for the downward ramp of applied voltage. The result of the calibration is shown in figure (7.7).

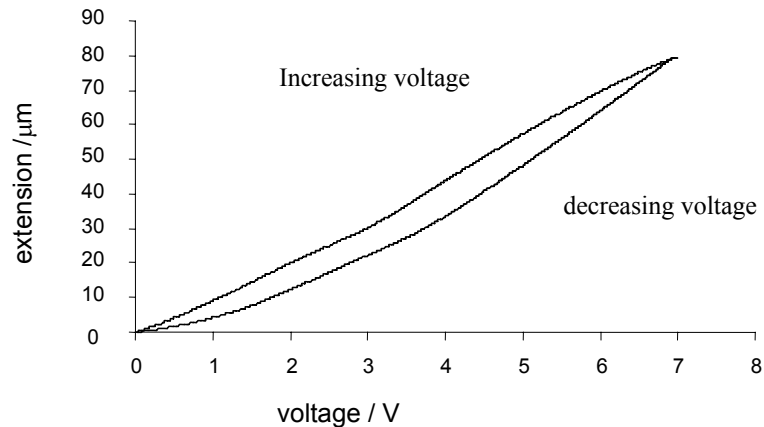


Figure 7.7, shows the variation of the extension as a function of applied voltage produced by the piezo-actuator. The graph demonstrates the expansion and contraction of the piezo-actuator in response to a sawtooth signal, driven at 30mHz. The hysteresis can be seen clearly.

The maximum measured extension was $79.58 \pm 0.08\mu\text{m}$, compared with the manufacturer quoted value of $100\mu\text{m}$. The discrepancy is probably due to wear and age of the device. Figure (7.7) demonstrate the typical hysteresis of the piezo-actuator. The hysteresis information allows the calibration of the extension with the applied voltage so that the strain can be determined.

7.5 Wavelength monitoring for the 800nm source

A scanning FP Interferometer (TecOptics, FPI-25) is used to monitor the spectral stability of the lasers used. It consists of a pair of highly reflective mirrors with a variable cavity length which allows the FSR to be adjusted and thus provides measurements with different sensitivity to be performed. The mirrors have a 96% reflectivity at 780nm giving it a maximum Finesse of 77. A fraction of the collimated output of the tuneable Ti/Sapphire laser is diverted into the aperture of the scanning FP, entering the cavity formed by a pair of flat mirrors. One of the mirrors is scanned by the movement of a piezo-stack in the orders of a wavelength in movement which sweeps across a FSR of the cavity. The output of the scanning FP is monitored in transmission. The sensitivity of the measurements are defined by the FSR, which is controlled by the virtue of the cavity length. Figure (7.8), illustrates a scan of the Ti/Sapphire laser where the FSR is given by the separations of the two peaks.

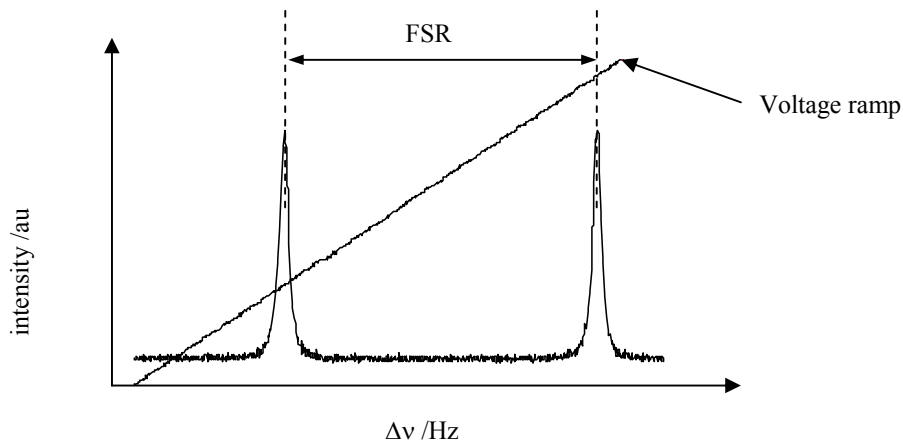


Figure 7.8, shows a scan of the FP where the separation of the two peaks provides the value of the FSR together with the voltage ramp to scan the mirror with.

7.6 Temperature measurement

The cylindrical tube furnace, supplied by Carbolite Furnaces Ltd., was 180mm long with an internal diameter of 15mm. The furnace had a temperature range of 900°C with an accuracy of $\pm 1^\circ\text{C}$. The furnace used a PID circuit to maintain the desired temperature with a stability of $\pm 1^\circ\text{C}$. The furnace had a uniform temperature zone of length 40mm in the middle of its ceramic inner tube. A photograph of the tube furnace is shown in figure (7.9). The large volume inside the furnace will create a large temperature fluctuation. To overcome this, a narrow piece of copper tubing is inserted and suspended in the furnace cavity. The temperature within the tubing was determined by using a K-type thermocouple positioned near the centre of the furnace.

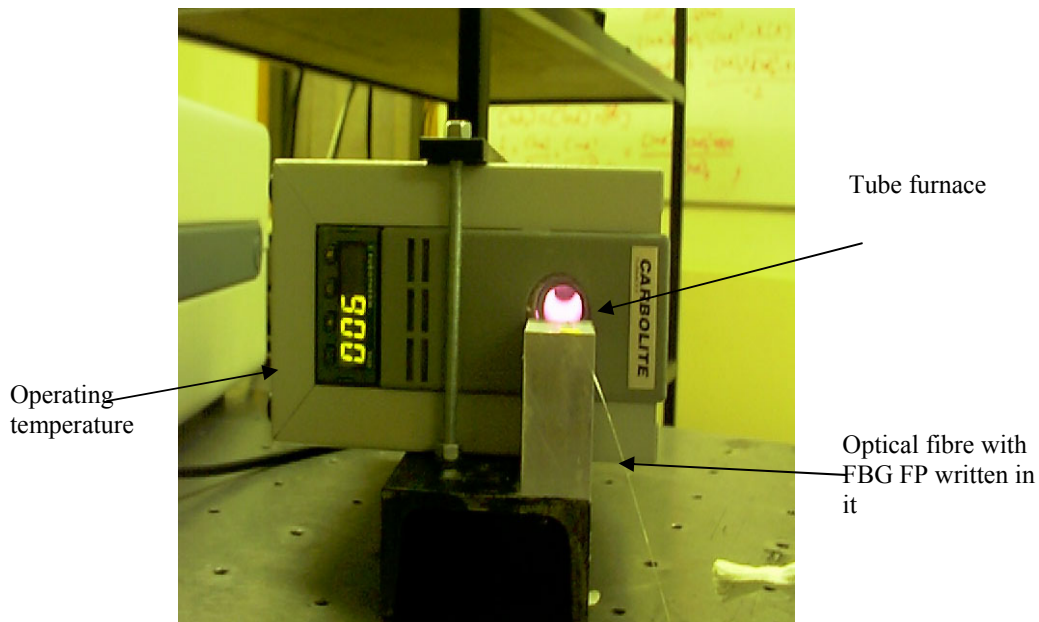


Figure 7.9, shows a photograph of the tube furnace.

7.7 Summary

The experimental setup for the characterisation of the FBG FP has been outlined in detail. A brief discussion of the operation and performance of the devices used have been presented and details of the implementation and calibration of the strain monitoring systems have been reviewed.

References:

- 1 G. E. Town, K. Sugden, J. A.R. Williams , I. Bennion and S. B. Poole, 'Wide Band Fabry Perot like Filters in Optical Fiber', *IEEE Photon. Tech. Lett.*, **7**, 78-80, 1995.
- 2 T. Allsop, K. Sugden and I. Bennion, 'A High Resolution Fiber Bragg Grating Resonator strain sensing system', *Fiber and Integrated Optics*, **21**, 205-217, 2002.
- 3 Schwartz Electro-Optics, Inc. Operator's manual.
- 4 Photonetics manufacturer's information.

8 Calibrations of chirped FBG Fabry-Perots

8.1 Introduction

In chapter 4 and 5, an analysis of the dependence of the resonance point in a chirped FBG upon wavelength and applied strain indicated the ability to create interferometers with variable sensitivity to strain, and the possibility of fabricating FP etalons with variable free spectral range. FP cavities were formed between chirped FBGs, fabricated via a range of techniques. The properties of the cavities are investigated using a variety of methods including the application of axial strain, scanning the wavelength of the illuminating source and varying the temperature.

(I am very grateful to my colleague, Dr. C-C. Ye for taking his precious time to write these chirped FBGs, in-house at Cranfield, unless stated otherwise)

8.2 Observation of reduced strain sensitivity in a chirped FBG FP illuminated at 800nm

A chirped FBG FP is configured such that the direction of the increasing chirp of each FBG is oriented in opposite sense, aligned away from the centre of the FP, as shown in figure (8.1). The chirped FBGs are fabricated by exposing a bent optical fibre to uniformly spaced UV interference fringes, section (2.4.3)[1] which creates a chirp of $\sim 20\text{nm}$ centred at 810nm . The chirped FBGs are written with a distance of 132mm apart to create a FP cavity.

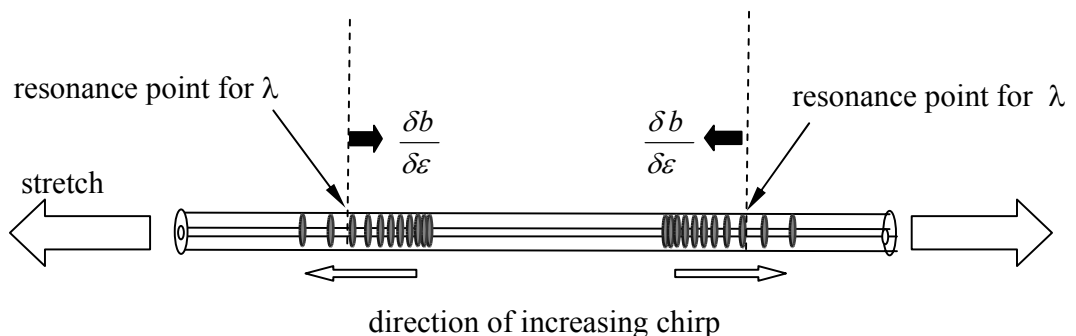


Figure 8.1, schematic of a reduced strain sensitivity chirped FBG FP cavity where the movement of the resonance positions, $\frac{\delta b}{\delta \epsilon}$ opposes the increase in cavity length caused by application of axial strain.

When the cavity is illuminated by a wavelength, λ , the length of the cavity is measured between the reflection positions in the respective FBGs. In this configuration, the movement of the reflection point with strain moves in the direction against the increasing chirp, which counteracts the increasing in cavity length associated with axial strain, so that this cavity will be less sensitive to strain.

Attempts are made to compare the strain sensitivity of the chirped FBG FP with a uniform period FBG FP. The second FP, used for comparison, is formed between a pair of uniform period FBGs, and is arranged to have the same cavity length as the chirped FBG FP. The parameters of the two FPs are indicated in table (8.1).

Table 8.1

Uniform FBG cavity		Chirped FBG cavity	
Central Wavelength	812.3nm	Central wavelength	815nm
Bandwidth	0.1nm	total chirp	20nm
Grating Length	2.2mm	Grating Length	2.6mm
Reflectivity	7%	Reflectivity	5%
Cavity Length	132mm	Cavity Length	132mm

The profiles of the chirped FBGs are shown in figure (8.2). The profile of the two FBGs are very closely matched. The discrepancy between the reflection spectrum are probably due variation in the configuration of the UV writing beam between the sequential exposure of the fibre to form the 2 FBGs. The low reflectivity of the FBGs results in the FP cavity response with a cosinusoidal transfer function[2].

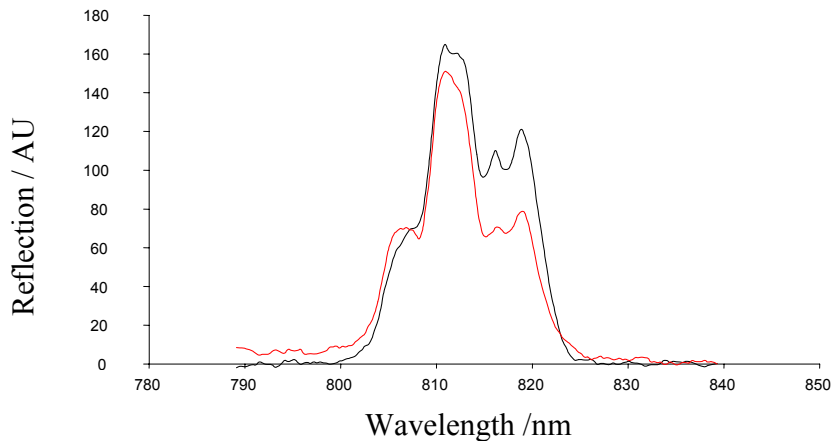


Figure 8.2 the reflection profile of the two chirped FBGs used to form the FP cavity (parameters detailed in table (8.1))

The cavities are mounted on the rig shown in figure (8.3), so that both cavities will experience the same axial strain. The cavities are interrogated using a Ti/Sapphire laser, operating in the 800nm wavelength range and the reflected signals from D1 and D2 are captured using a digital storage oscilloscope. The application of strain to the cavities has to be done manually, as the strain tuning by the piezo-actuator or the strain monitoring by use of the bulk FP with a HeNe source had not been implemented at the time.

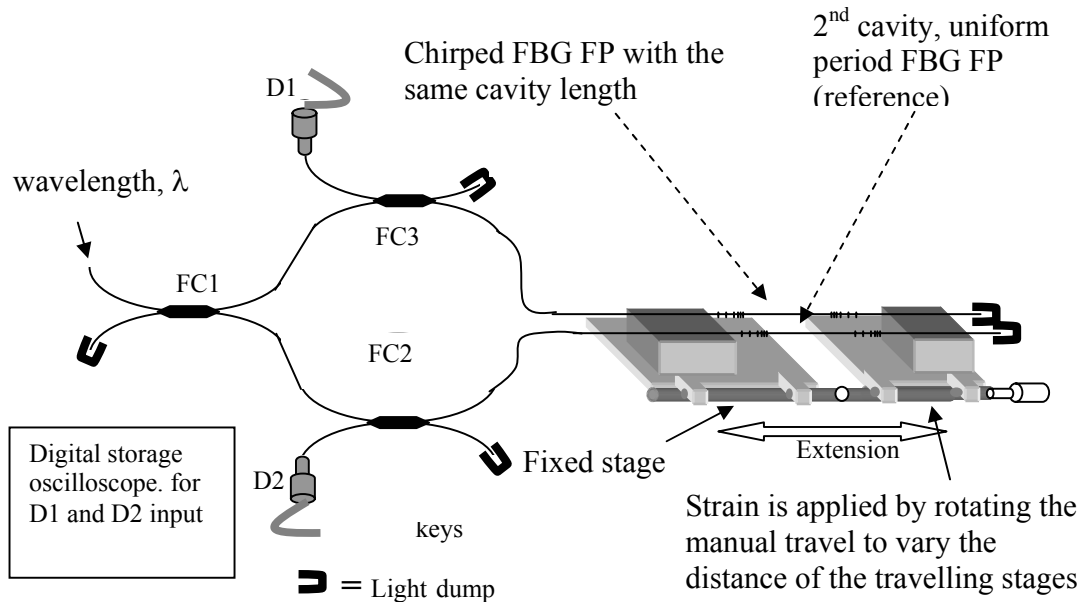


Figure 8.3, the implementation of the strain rig with a manual travel to impart strain on both of the cavities in question. The lead screw is twisted back and forth to create the extension and the signal from D1 and D2 are captured simultaneously.

Strain is applied to the cavities by rotating the lead screw of the stage. The extension to the FP cavities and the reflected signals of the two cavities were captured simultaneously. A typical result is shown in figure (8.4).

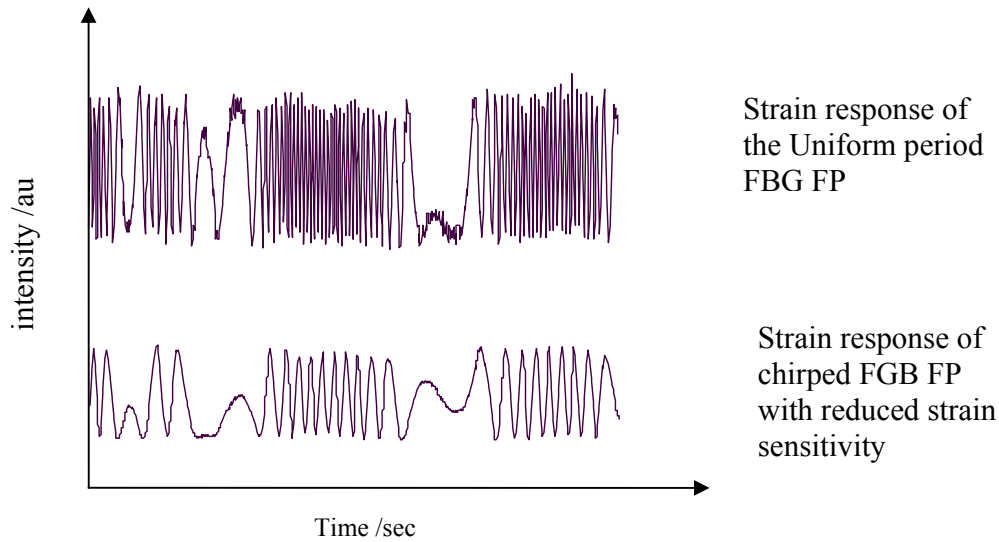


Figure 8.4, the strain response of the two cavities is simultaneously captured using a storage oscilloscope. The chirped FBG FP, shows a reduced strain sensitivity, as compared with the FP formed between the uniform period FBG FP

In figure (8.4), the phase response of the two cavities is shown. The phase response is different for the two cavities even though they have the same cavity length. This demonstrates that the strain sensitivity of the chirped FBG FP cavity does not depend on the cavity length alone but it is modified by the dispersive effect introduced by the chirped FBG. The phase noise (ratio of noise to magnitude of the modulation) in the chirped FBG FP cavity is less than that exhibited by the uniform period FBG FP, because of the reduced effective cavity length of a dispersive cavity, described by equation (4.57), for the reduced strain sensitivity chirped FBG FP configuration, section (4.4.3.4).

The ratio of phase response of the uniform period FBG FP to the chirped FBG FP, determined from figure (8.4) is approximately 3:1. Using the expression for the RTSP of a non dispersive

FP; $\theta = \frac{4\pi ml}{\lambda}$, the change in the RTSP to an applied strain is [3];

$$\frac{d\theta}{d\varepsilon} = \frac{4\pi n \xi}{\lambda} l \quad (8.1)$$

where l is the cavity length and ξ is the strain response of the fibre. For a dispersive chirped FBG FP cavity configured to have the strain sensitivity reduced, section (4.4.3.4), the phase response to applied strain is derived by differentiating the RTPS, taking into account the movement of the reflection point with strain in the chirped FBG (dispersive effect), Thus for a chirped FBG FP, the dependence of the phase upon strain is given by equation (5.15);

$$\frac{d\theta}{d\varepsilon} = \frac{4\pi n \xi}{\lambda} \left(l - 2 \frac{\lambda}{C} \right)$$

Assuming that the FBG's strain responsivity, ξ , is the same as the fibre strain responsivity, the ratio of the phase response for the uniform FBG FP to the reduced configuration chirped FBG FP can be written as the ratios of equation (8.1) to (5.15);

$$\frac{l}{\left(l - 2 \frac{\lambda}{C} \right)} \quad (8.2).$$

From the FP parameters given in table (8.1), a ratio of the phase response is estimated to be ~2:1 which compares well with the experimental value of 3:1. The discrepancy may arise from the estimation of the experimental data used in the calculation.

From equation (5.4), the change of resonance position is inversely proportional to the chirp rate, C . There is a large movement for the resonance position of a wavelength with strain in a FBG with small chirp rate which means a larger cavity length needs to be configured to realise a reduced strain sensitivity configuration chirped FBG FP. Attempts were made to realise a further reduction in strain sensitivity of the chirped FBG FP. A cavity length of ~ 10cm will be of use for practical systems, be less susceptible to frequency jitter noise and be easier to isolate from the environment than a longer cavity.

8.3 Chirped FBG FP with chirp rate of 25nm mm⁻¹ and cavity length of 97mm

The Ti:Sapphire laser was used only for initial studies of FP cavities. During the course of the work, the power output for the Ar⁺ laser used as a pump fell below the threshold. In addition, issues arising from vibrations produced by the flow of cooling water through the Ar⁺ laser induced frequency jitter and the lack of control in wavelength tuning in the 800nm Ti:Sapphire laser. It was decided to change to the wavelength region of the newly acquired 1550nm Photonetics tuneable laser source.

From equation (5.5), the formation of a strain insensitive cavity with length of around ~10cm requires the use of chirped FBGs with a chirp rate of ~25nm/mm. Chirped FBGs with high chirp rate may be fabricated using the interference of UV beams with dissimilar wavefronts [4]. By introducing a cylindrical lens in one arm of the holographic arrangement when writing gratings, the wavefront will be distorted with a different curvature to the other beam. Using geometry considerations, the variation in period along the grating can be written as [5];

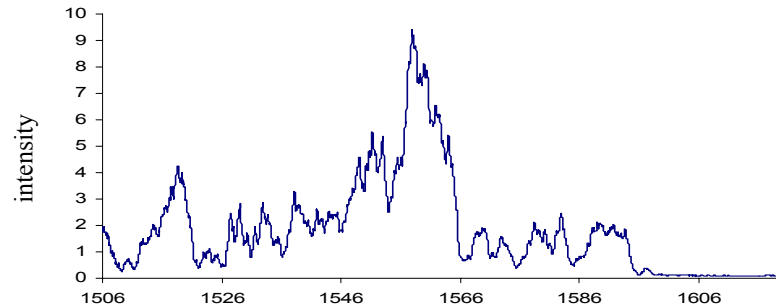
$$\Lambda(\lambda) = \frac{\lambda_{UV}}{\frac{D_1 \cos \phi_1 + z}{(D_1^2 + 2D_1 z \cos \phi_1 + z^2)^{1/2}} + \frac{D_2 \cos \phi_2 + z}{(D_2^2 + 2D_2 z \cos \phi_2 + z^2)^{1/2}}} \quad (8.3)$$

where ϕ_1 and ϕ_2 are the angles of two interfering beams with respect to the fibre, D_1 and D_2 , are the distances between the lens and the fibre, z is the position along the fibre and λ_{UV} is the UV writing wavelength. Using a single lens in one path of the holographic arrangement with a distance D of ~10cm [5], an FBG with the total chirp of ~100nm in a grating length of ~4mm has been written with this method. Cavities with length ~93mm comprising of chirped FBGs oriented in different directions have been created.

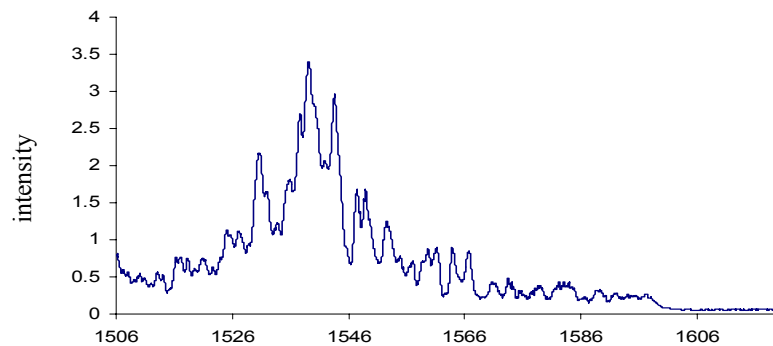
Using the Photonetics tuneable laser source and sweeping the wavelength from 1506nm up to 1610nm in steps of 0.05nm, the reflected intensity is recorded and compared to the reflection off a fibre end. The reflectivity for all the gratings is less than 4%. Figure (8.5) shows the profile of

some of the gratings that have been used in the experiments. More details of the grating profiles can be found in Appendix D.

a) the grating profile of FBG no.2



b) the grating profile of FBG no.3



c) the grating profile of FBG no.5

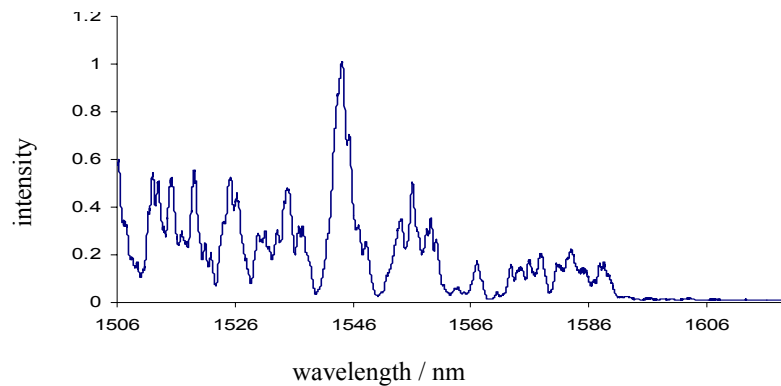


Figure 8.5, shows the grating profiles used in the experiment where the reflectivity for all gratings used $<4\%$. The scan is achieved by sweeping the scanning wavelength of the Photonetics laser from 1506 to 1610nm in steps of 0.05nm.

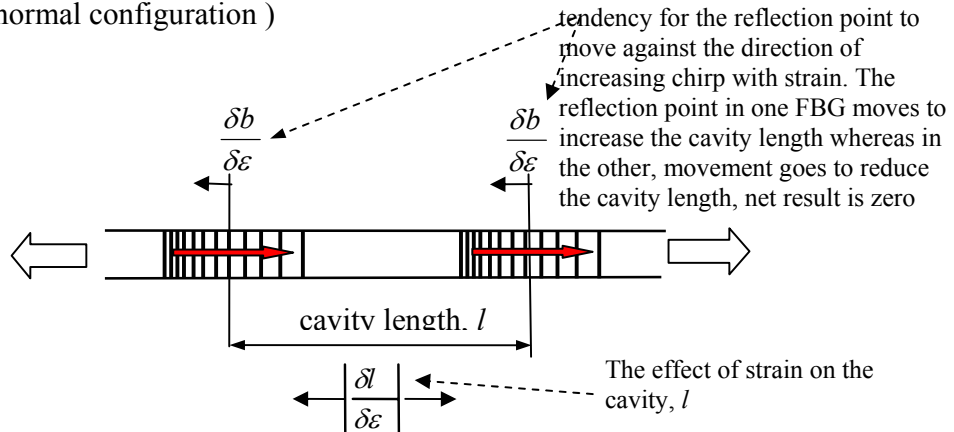
The jagged appearance of the reflection profile of the gratings is probably due to FP effect by the grating edges as well as the quality of the 2 interfering UV beam profiles, in general, where the mismatch in intensity across the beam causes different fringe visibility within the grating profile. The appearance of FBG profile will not affect the performance of the chirped FBG FP, aspect from the visibility of the return signal. However, if the variation in the profile is caused by the

effective concatenation of individual FBGs, each occupying a different bandwidth, then the reflection points of the wavelength will become non-unique. As a result, it might be expected that there would not be any movement of the reflection points in response to applied strain and that the performance of the FP would be equivalent to that of a conventional FP. The strain, temperature and wavelength responses of chirped FBG FP cavities employing these FBGs in different orientations were investigated.

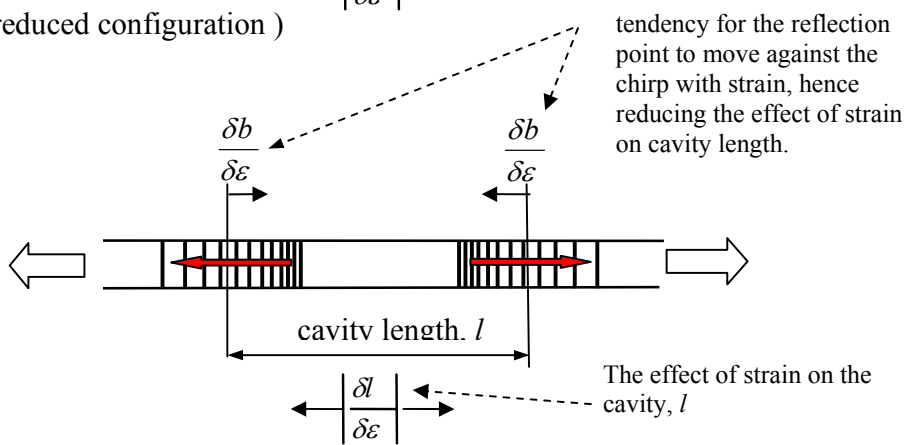
8.3.1 The strain response

FP cavities were constructed using a pair of chirped FBGs separated by a cavity length of ~ 97 mm. Figure (8.6) illustrates the 3 types of chirped FBG FP configurations. These cavities are configured such that the direction of increasing chirp for each FBG is aligned in the same direction, figure (8.6.a) (normal configuration), figure (8.6b) where the direction of increasing chirp for the FBG are aligned in opposite directions, away from the centre of the FP (reduced sensitivity configuration) and figure (8.6c) where the direction of the increasing chirp for the FBGs are aligned in opposite directions but towards the centre of the FP (enhanced sensitivity configuration). From the analysis presented in chapter (5), the response of each of these cavities to an applied axial strain should produce a response which depends on the orientation of the chirped FBG. For the normal configuration, figure (8.6a), the phase response with strain should correspond to the conventional FP response with a cavity length of 97mm. The reduced strain sensitivity configuration should demonstrate a much reduced phase response to applied strain, whereas the enhanced sensitivity configuration should demonstrate a phase response to strain that is around twice the phase response of the normal configuration. Figure (8.7) illustrates the experimental setup where a chirped FBG FP cavity is mounted on the strain rig (previously described in figure (7.4)). The application of strain, the monitor of strain and the monitoring of the reflected signal from detector, D1 is controlled by the PC.

a) Scenario A (normal configuration)



b) Scenario B (reduced configuration)



c) Scenario C (enhanced configuration)

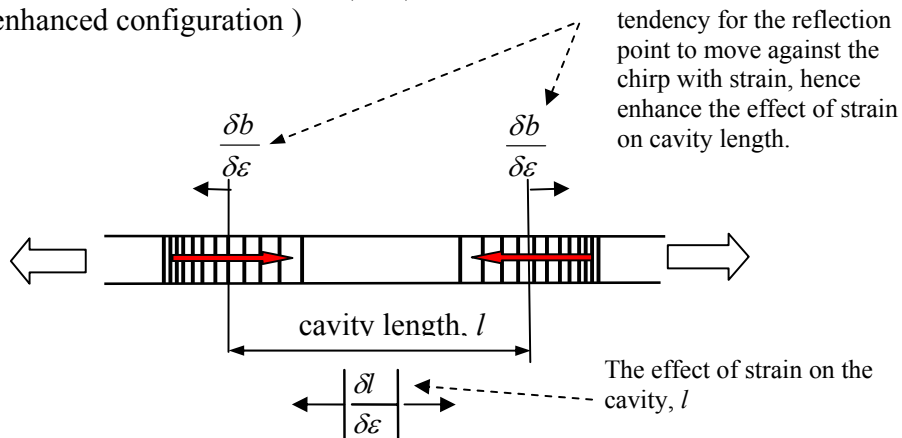


Figure 8.6, illustrating the effect that strain has on chirped FBG FP cavities in a) the normal configuration where the movement of the reflection points in one grating acts to increase, in the other, act to decrease the cavity length, hence effect is nulled and the FP response will be that of the cavity length response to strain, b) the reduced configuration where the movement of the reflection points with strain reduces the effect strain has on the cavity and c) the enhanced configuration when the movement of the reflection point with strain in the grating enhances the effect of strain has on the cavity length.

The cavity is illuminated at wavelength, λ , and it is strain tuned by applying a modulation voltage across a piezo-actuator with a frequency of 30mHz. The strain is monitored by the HeNe laser and bulk FP and the reflected signal from D1 is recorded. The whole process is controlled by a PC and the data is captured using a DAQ card with software written in Labview™.

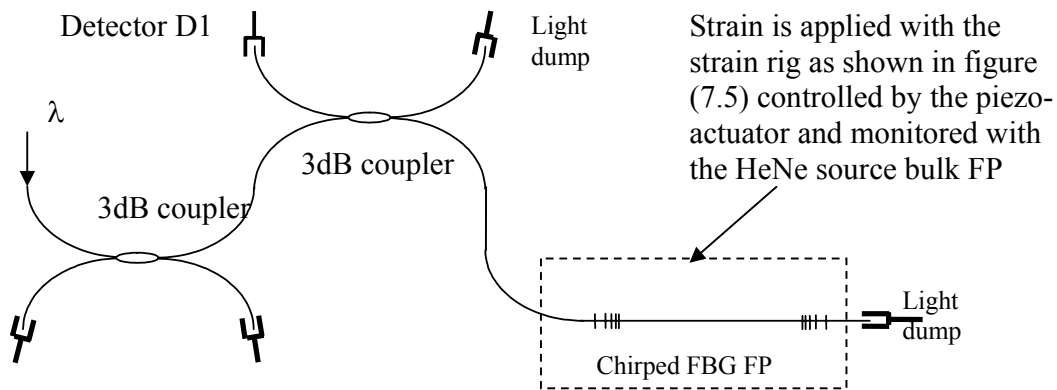


Figure 8.7, the experiment configuration which involved the use of fibre couplers so that the cavities can be interrogated and monitored with a computer controlled software. The signal is captured in detector D1.

Figure (8.8a) shows the applied voltage from the input of the piezo-actuator used to apply strain to the cavity, figure (8.8b) shows the response of the bulk FP illuminated at 633nm, used to calibrate the extension and figure (8.8c) shows the strain response of the normal configuration chirped FBG FP cavity at 1510nm. The experiment is repeated for a range of different illuminating wavelengths within the bandwidth of the chirped FBG FP. The strain response for the normally configured chirped FBG FP cavity, figure (8.8c), for different illumination wavelengths can be found in Appendix E.

The experiment is repeated for the 2 other chirped FBG FP cavities (reduced and enhanced sensitive configurations). The strain sensitivity of the 3 cavities are calculated and plotted against the inverse of wavelength, as shown in figure (8.9). The predicted strain sensitivity for the reduced configuration will be near zero, equation (5.15) and the enhance configuration will give twice the value of the normal configuration, equation (5.14) at a cavity length of a cavity length of $l=97\text{mm}$ with $\alpha=0.8$.

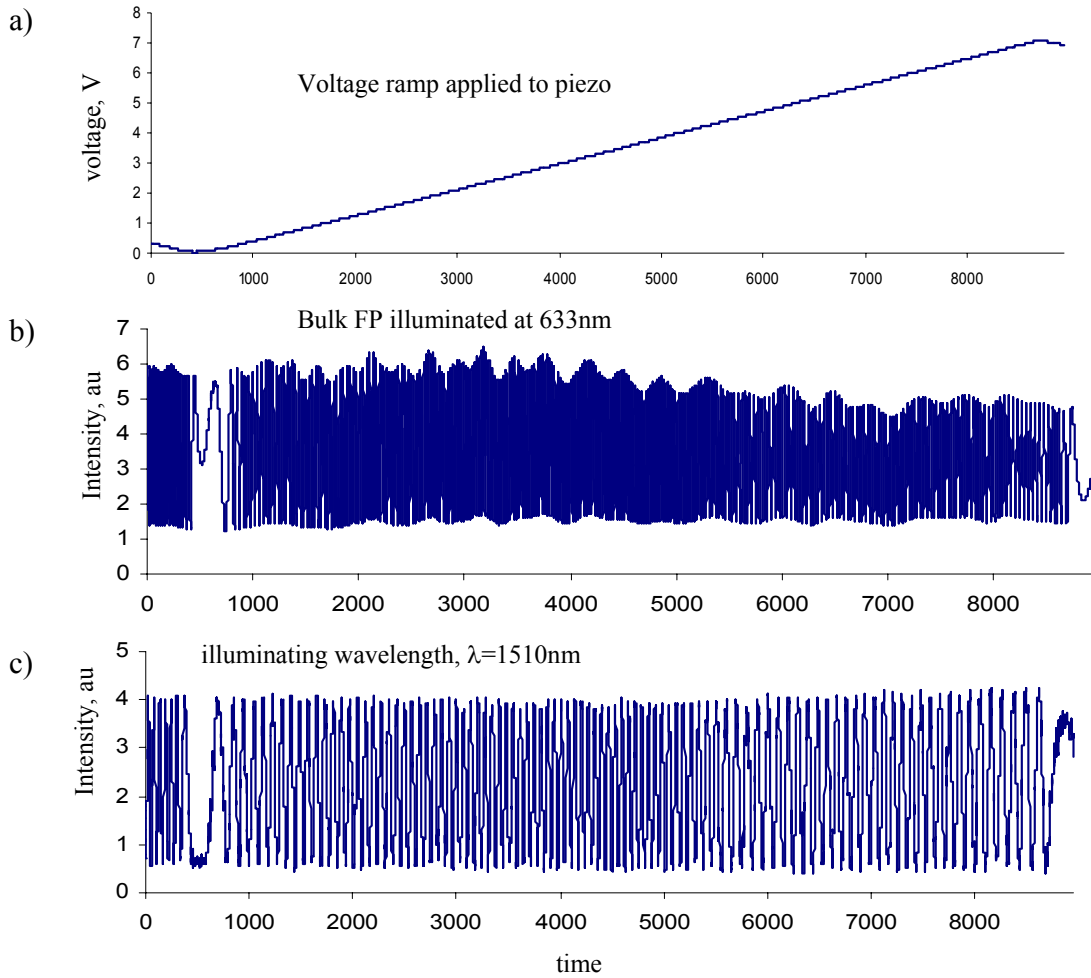


Figure 8.8, Strain response of the chirped FBG FP in the normal configuration. a) the driving voltage of the piezo, b) the intensity output from the monitoring bulk FP used in strain calibration and c) the strain response of the chirped FBG FP in the normal configuration interrogated at 1510nm. The calibrated strain level is $\sim 730\mu\epsilon$ giving ~ 100 fringe cycles.

Far from showing different strain sensitivities, the chirped FBG FP cavities all demonstrate a strain sensitivity akin to the conventional FP response where the strain sensitivity is proportional to the cavity length, equation (8.1).

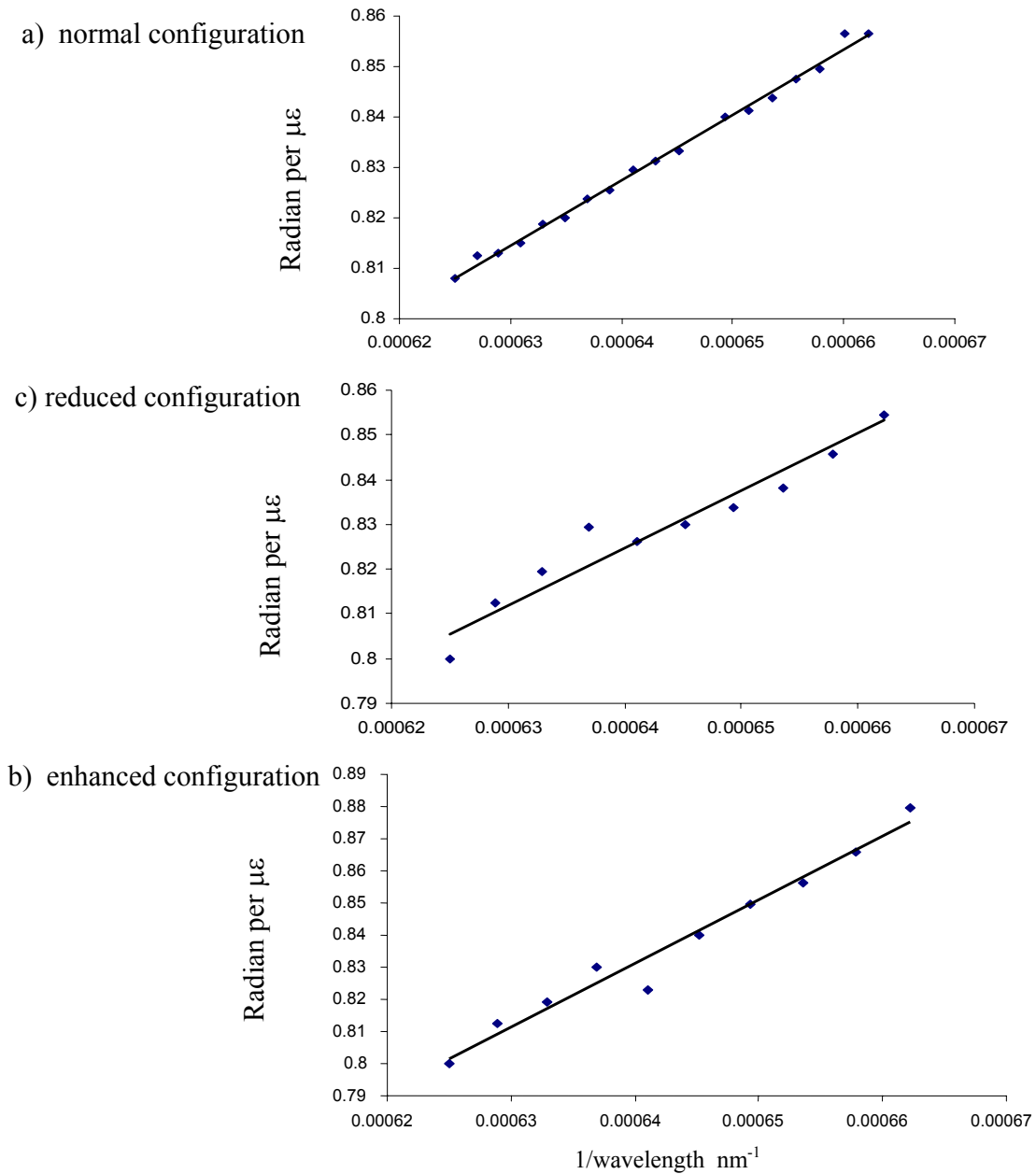


Figure 8.9, shows the plot of the strain sensitivity as a function of the inverse of the illuminating wavelength a) for normal, b) reduced strain sensitivity and c) enhanced strain sensitivity configurations. The linear relationships demonstrate that the strain sensitivity is proportional to the cavity length only and is not dependent upon the orientation of the chirp of the FBGs in the FP formations

From the data presented in figure (8.9a), the strain sensitivity for the chirped FBG FP configured with the chirps oriented the same way, has an average strain of 0.83 radian $\mu\epsilon^{-1}$. This compares well with an experimentally demonstrated strain sensitivity of 0.83 radian $\mu\epsilon^{-1}$, for a uniform FBG FP measured at a wavelength of 1562nm. Equation (5.14) which describes the strain sensitivity of chirped FBG FP cavities, can be modified by ignoring the movement of the reflection points in response to strain. The equation is reduced to the standard FP strain response, equation (8.1);

$$\frac{d\theta}{d\epsilon} = \frac{4\pi n \xi}{\lambda} l.$$

A plot of $\frac{d\theta}{d\epsilon}$ against $\frac{1}{\lambda}$ should then give a linear relationship. Figure (8.9) demonstrates this linearity, where the cavity length, remains constant at ~97mm for all cases. The cavity length is not effectively reduced/increased, as predicted for a dispersive FP. From the slope of the graph in figure (8.9), the values for the strain responsivity, ξ are 0.70, 0.71 and $0.71 \pm 0.01 \epsilon^{-1}$ determined for the 3 chirped FBG FP cavities respectively, assuming $n = 1.5$ and $l = 97\text{mm}$. The theoretical value of the strain sensitivity using equation (8.1), assuming the strain responsivity of the fibre, ξ is $0.78 \epsilon^{-1}$ [6] and that the refractive index, $n = 1.5$, gives a strain sensitivity of ~ 0.88 radian $\mu\epsilon^{-1}$ at a wavelength of 1550nm, which is similar to the average strain sensitivity exhibited by the 3 chirped FBG FP cavities.

From the strain characterisation of the chirped FBG FP, the results indicate that these cavities behaved like a non-dispersive conventional fibre FP cavity. No significant enhancement or reduction in strain sensitivity is observed. The strain response of the cavity appeared to be decoupled from expected influence of the dispersive chirped FBG. This could happen if the chirp is not continuous in the grating, as in the case of stepped chirp or concatenated FBGs, where the gross total chirp is still significant but the period change with position is created in discreet steps. In this case, as the cavity is subjected to an axial strain, there is no movement of the reflection points inside the chirped FBGs. The strain response is then equivalent to that of a cavity of length measured between the respective reflection points inside the chirped FBGs. The appearance of the chirped grating profiles, figure (8.5) is similar to the sum of many short

uniform period FBGs. The individual peaks may be interpreted as the spectra of broadband uniform FBGs with very small lengths with some wavelength overlaps with neighbouring FBGs.

8.3.2 Temperature response

The chirped FBG FP configured to have a reduced sensitivity to strain, figure (8.6b) with the increasing chirp oriented in opposite directions, away from the centre of the FP, is used in this experiment to investigate the temperature sensitivity of the cavity. This FP cavity was placed in the modified tube furnace with a narrow conducting copper tubing inside, to redistribute the heat more evenly inside the furnace and to reduce convection, which may cause temperature fluctuations.

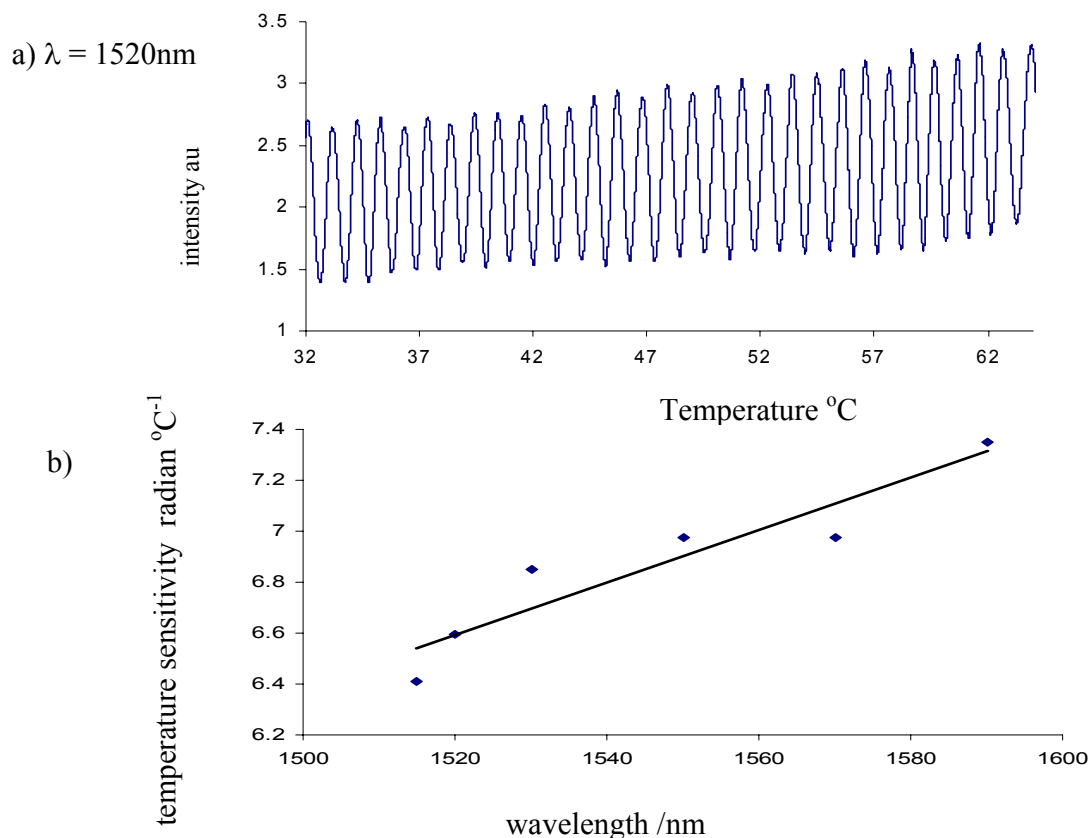


Figure 8.10, shows the temperature response of the chirped FBG FP arranged in the reduced strain sensitivity configuration with the FBGs having a chirp rate of ~ 25 nm/mm and cavity length of 97mm, a) the temperature response at an illuminating wavelength of 1520nm and b) the temperature sensitivity at different illuminating wavelengths.

The experimental arrangement is shown in figure (8.7), with the heating furnace in place of the strain rig. The FP cavity was interrogated with a single wavelength and the temperature of the furnace was increased gradually. The temperature and the reflected signal were captured using a DAQ card and data acquisition software written in Labview™. The experiment was repeated for a range of different illuminating wavelengths. Figure (8.10) shows the temperature response of this reduced configured chirped FBG FP with chirp rate of 25nm/mm with a cavity length of 97mm. By differentiating the RTSP with respect to temperature, the temperature sensitivity of the fibre FP can be written as;

$$\frac{d\theta}{dT} = \frac{4\pi n \zeta}{\lambda} l \quad (8.4)$$

This equation can be arrived at by using equation (5.21) and ignoring the movement of reflection points in the chirped FBG in response to temperature. Using equation (8.4), with a temperature response value of $\zeta = 6.67 \times 10^{-6} \text{ }^\circ\text{C}^{-1}$ [6] and $8.39 \times 10^{-6} \text{ }^\circ\text{C}^{-1}$ [7], $n = 1.5$ and $l = 97\text{mm}$, the temperature sensitivity is predicted to be in the region of 7-10 radian $^\circ\text{C}^{-1}$. When compared to the measured temperature sensitivity of the chirped FBG FP, 6.86 radian $^\circ\text{C}^{-1}$. The experimental and theoretical predictions are of the same order of magnitude. The small difference in the theoretical and experimental sensitivity values is probably due to the fibre type and the presence of a temperature gradient along the length of the oven and that this temperature gradient increases with increasing temperature. This chirped FBG FP cavity has a standard fibre FP response to temperature without significant reduction in the sensitivity as predicted for the reduced configuration. From equation (8.4) a plot of $\frac{d\theta}{dT}$ against λ should record a $1/\lambda$ relationship.

Instead, the graph demonstrates a positive gradient, figure (8.10b). Using the average temperature sensitivity of 6.86 radian $^\circ\text{C}^{-1}$ in equation (8.4), a temperature response of the fibre is predicted to be $\zeta = 5.6 \times 10^{-6} \text{ }^\circ\text{C}^{-1}$, compared to accepted value of $\zeta = 8.39 \times 10^{-6} \text{ }^\circ\text{C}^{-1}$. This temperature experiment will not yield accurate temperature response measurement because of the long cavity length of this FBG FP $\sim 10\text{cm}$, and it is difficult to establish a constant temperature throughout the cavity length which is reflected in the differences in the theoretically predicted and experimental value for the temperature sensitivity.

8.3.3 The wavelength response

The wavelength response of the chirped FBG FP is investigated, using the same experimental setup used for the strain characterisation, figure (8.7). When scanning the wavelength of the external cavity laser in the 1550nm region, the reflected intensity is recorded. The chirped FBG FP cavity used is of the reduced configuration as shown in figure (8.6b). The cavity has a length of 97mm between the grating centres with each grating having a chirp rate of $\sim 25\text{nm/mm}$. From the analysis performed in section (4.4.3.4), the wavelength response of this cavity will have a much reduced phase response to wavelength. Figure (8.11) shows the configuration of the chirped FBG FP, with the alignment of the increasing chirp opposite to each other and away from the centre of the FP.

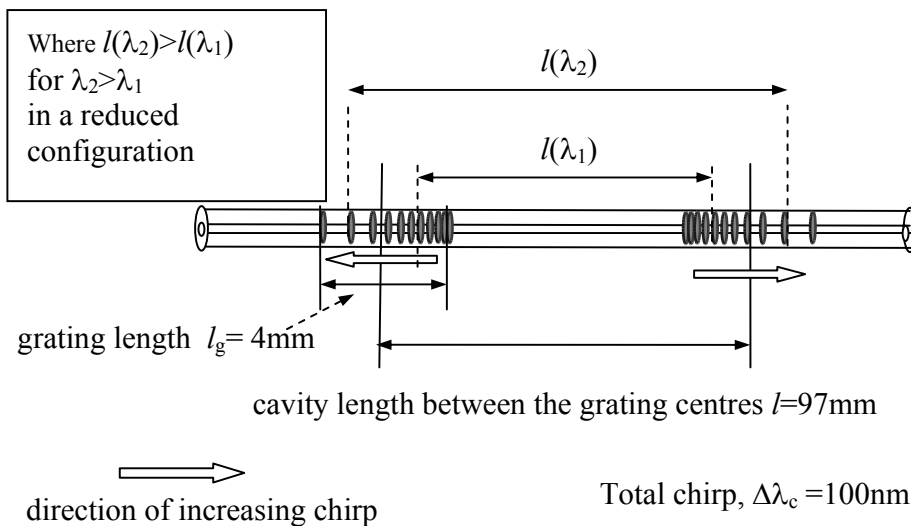


Figure 8.11, illustration of the reduced configuration of the chirped FBG FP cavity which consist of 2 chirped FBG with grating length $\sim 4\text{mm}$, total chirp, $\Delta\lambda_c \sim 100\text{nm}$ with the orientation of chirp going away from each other and having a cavity length between the grating centre $\sim 97\text{mm}$

The wavelength response is shown in figure (8.12a) in the wavelength range of 1510nm to 1565nm. No reduction or enhancement in the wavelength sensitivity is observed. The figure shows the varying visibility for the FSR across the bandwidth due to the mismatch of the reflectivity of the 2 gratings. The FSR can be seen more clearly in a smaller wavelength region of, figure (8.12b), where a FSR $\sim 0.008\text{nm}$ can be resolved.

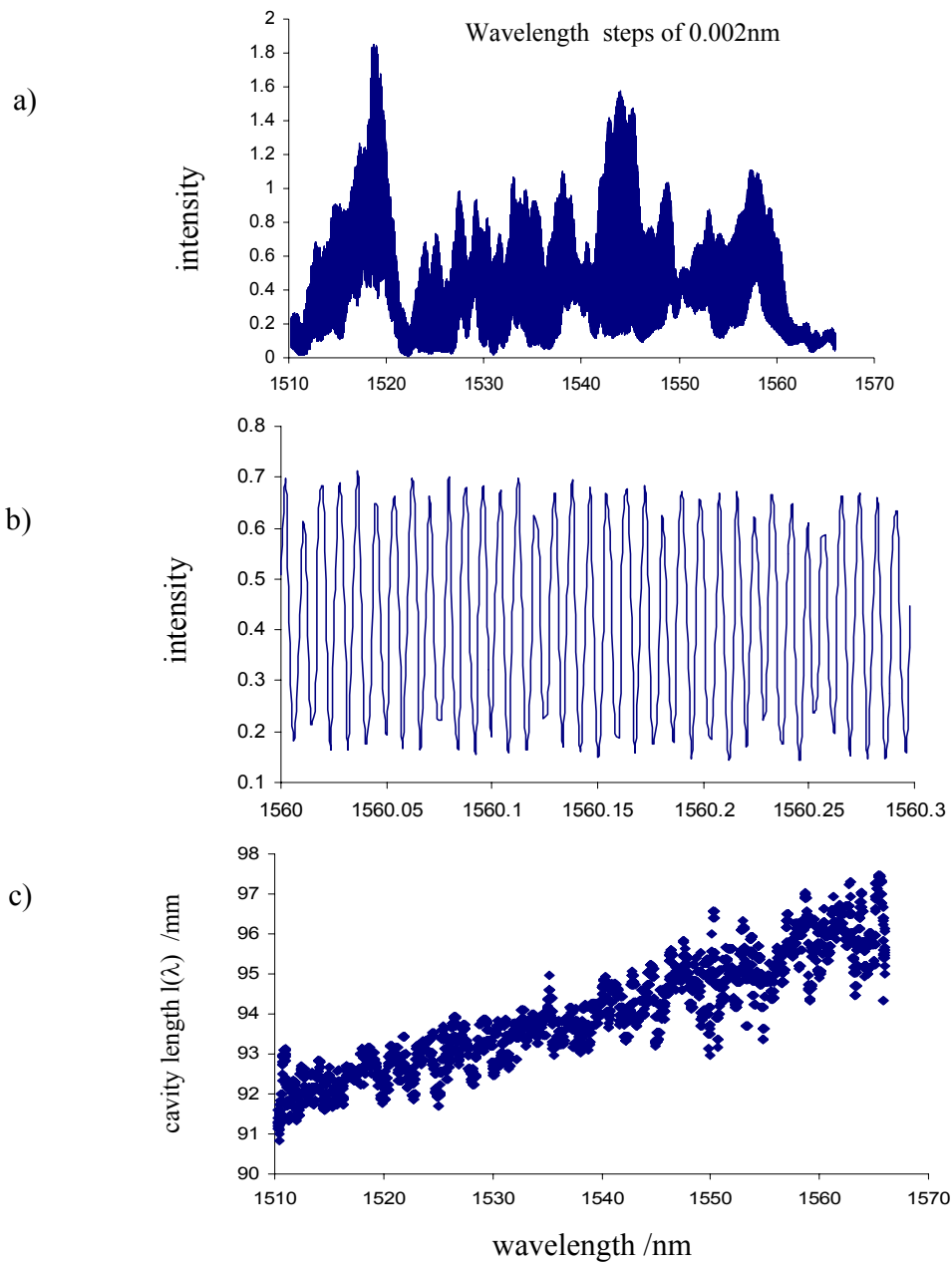


Figure 8.12, the wavelength response of the chirped FBG FP in the reduced configuration with no reduction of the sensitivity observed, b) a FSR $\sim 0.008\text{nm}$ is shown in the wavelength region of 1560nm and this cavity has a uniform wavelength response across the bandwidth and c) using the non dispersive chirped FP FSR response, equation (4.59), the detuned cavity length, $l(\lambda)$ can be determined using the FSR values. The detuned cavity length can be distinguished with $l(\lambda_2) > l(\lambda_1)$ for $\lambda_2 > \lambda_1$ which is consistent with the chirped FBGs arranged in the reduced configuration, figure (8.11).

The results in figure (8.12a) do not indicate an alteration to the wavelength response, which is contrary to what is expected of this chirped FBG FP cavity. The behaviour of this cavity can be explained using the conventional non dispersive FSR equation (4.47);

$$\Delta\lambda_{FSR} = -\frac{\lambda^2}{2nl(\lambda)}$$

which retains the wavelength detuned cavity length, $l(\lambda)$, of the chirped FBG FP. This FP response can be derived if the dispersive element is ignored in the general FSR equation that describes a dispersive FP, equation (4.48). From figure (8.12.a) and (8.12b), a measured FSR value of $\sim 0.008\text{nm}$, correspond to a cavity length $\sim 10\text{cm}$ using equation (4.47). The wavelength response of this chirped FBG FP cavity is very much uniform throughout the bandwidth but on closer examination of FSR in figure (8.12a), there is a small variation of the FSR due to the wavelength detuned cavity length, $l(\lambda)$, figure (8.12c). This wavelength detuned cavity length can be determined using equation (4.47) together with the measured FSR values, $\Delta\lambda_{FSR}$. The calculated detuned cavity length, $l(\lambda)$ is shown in figure (8.12c) and the smaller wavelength sees a shorter cavity length than the longer wavelength. This is consistent with the arrangement of the 2 chirped FBG in this reduced configuration, figure (8.11) where the smaller cavity length appearing in shorter wavelength region.

The experiment is repeated using the other cavities. All of the cavities have the same length $\sim 97\text{mm}$. The measured FSR for all cavities was in the region of $\sim 0.008\text{nm}$, irrespective of the configuration of the cavity used. The wavelength response and behaviour of these cavities adhere to the conventional non dispersive FP response, equation (4.47), where FSR is modified by the variation in the wavelength detuned cavity length, $l(\lambda)$ accordingly. This variation of the FSR, $\Delta\lambda_{FSR}$ can be clearly seen when the chirped FBG FP has a small cavity length.

In the wavelength response of the chirped FBG FP, there is no observation of a reduced/increase in the effective cavity length by the effect of dispersion in the chirped FBG. The possible reason being that there is no continuity in the period of the chirped FBG as discussed in the strain

response section (8.3.1) where the chirped FBG behaved like the stepped chirped FBG or the concatenations of many uniform period FBGs.

8.4 Dissimilar chirped FBG FP formed between a chirped FBG with chirp rate of 25nm/mm and a cleaved end of an optical fibre

The discussion to date has focussed in the formation of an FP cavity between two chirped FBGs with identical parameters but differing orientation with the aim of modifying the phase response to strain and wavelength. It is possible to achieved similar performance by employing chirped FBGs in the cavity that have differing parameters such as length, chirped rate etc. In section (4.3.3), which provides an analysis of the wavelength response of chirped FBG FP, the analysis assumed that the cavity consists of chirped FBG with similar parameters, differing only in the orientation. The cavities will be dispersive unless the chirps of the FBGs are oriented in the same directions such that, the dispersive effect cancels. Dissimilarly chirped FBG FPs formed with FBGs of different chirp parameters will always be dispersive as discussed in, sections (3.9) and (3.11). From the analysis of the chirped FBG FP presented in section (4.3.3.2), the general equation describing the wavelength sensitivity of the chirped FBG FP provided by equation (4.48);

$$\Delta\lambda_{FSR} = \frac{\lambda}{2 \left(n \frac{dl}{d\lambda} - \frac{nl(\lambda)}{\lambda} \right)}$$

For 2 differently chirped FBGs, the dispersive term, describing the change in cavity length with wavelength, is given by equation (4.49);

$$\frac{dl(\lambda)}{d\lambda} = \frac{db_1(\lambda)}{d\lambda} + \frac{db_2(\lambda)}{d\lambda}$$

An extreme example of the dissimilar chirped FBG FP would be the FP formed using a chirped FBG to form one reflector and using a mirror or cleaved fibre end to form the other reflector. In this case, one of the terms on the RHS of equation (4.49) will be zero and the change of the

cavity length with wavelength will be determined by the rate of the wavelength detuned resonance position for the single chirped FBG.

The behaviour of the dissimilar chirped FBG FP is demonstrated by cleaving the chirped FBG FP in half and using the cleaved end of the fibre as a broad band reflective surface as shown in figure (8.13). The cleaved fibre end provides a reflectivity of $\sim 4\%$ at all wavelengths.

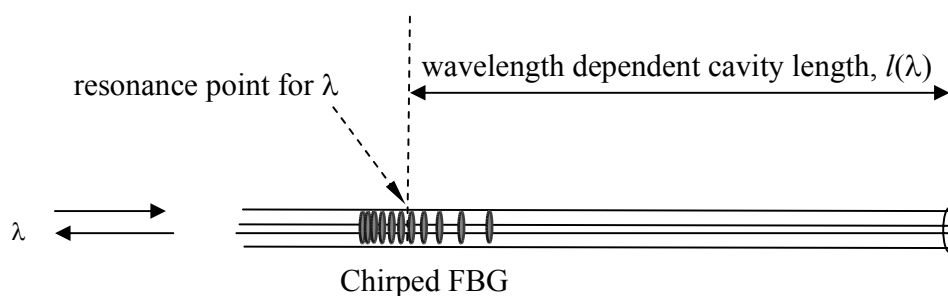


Figure 8.13, Schematic diagram of a dissimilar chirped FBG FP configuration employing a chirped FBG as one reflector and a cleaved fibre end as the other with a wavelength dependent cavity length, $l(\lambda)$.

8.4.1 Wavelength response of the dissimilar chirped FBG FP

As the dissimilar chirped FBG FP is considered dispersive, the wavelength response, ie the FSR of the cavity is modified by the inclusion of the dispersive element and will be significantly different to the conventional FP wavelength response, equation (4.48). In a similar way to the identical chirped FBG FP, they can be configured to show reduced or enhanced wavelength response, section (4.3.3). Following similar argument for the chirped FBG FP configured to provide a reduced wavelength sensitivity as discussed in section (4.3.3.4), the chirped FBG FP consists of a single chirped FBG and a cleaved fibre end will show a reduced wavelength sensitivity if the orientation of the increasing chirp of the FBG is aligned away from the centre of the cavity as shown in figure (8.14).

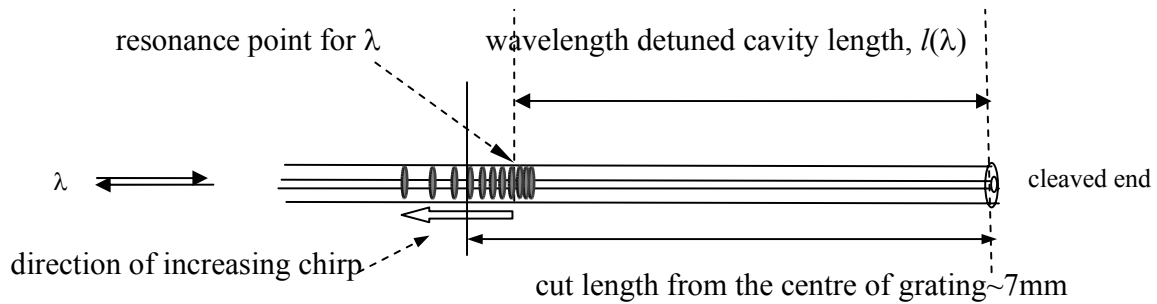


Figure 8.14, shows the reduced wavelength sensitive dissimilar chirped FBG FP configuration, where the direction of the increasing chirp is aligned away from the centre of the cavity.

In this experiment, a dissimilar chirped FBG FP cavity is formed in which the reflectors are a chirped FBG, with a chirp rate of $\sim 25\text{nm/mm}$, and the other reflector consists of a fibre cleaved end, as shown in figure (8.14). The cavity length, measured from the centre of the grating to the end of the fibre is $\sim 7\text{mm}$. The change in the reflected intensity is observed when the wavelength of the laser used to illuminate the cavity is scanned from 1513nm to 1600nm . The results are shown in figure (8.15). The varying visibility of the FSR is due to the difference between the reflectivity of the chirped FBG with that of the cleaved fibre end, figure (8.15a). The measured FSR has an average value of $\sim 0.12\text{nm}$. Using equation (4.47);

$$\Delta\lambda_{FSR} = -\frac{\lambda^2}{2nl(\lambda)}$$

This FSR corresponds to a cavity length of $\sim 6.7\text{mm}$, which is similar to the estimated length of $\sim 7\text{mm}$ from the centre of the grating to the fibre end. The observed average FSR of 0.12nm is akin to a non-dispersive FP response and again there is no significant reduction in the wavelength sensitivity in this dispersive cavity.

The measured FSR is plotted against wavelength in figure (8.15b) and, using the standard non dispersive FSR equation (4.47), the wavelength detuned cavity length, $l(\lambda)$ is calculated from the FSR values, assuming that the refractive index, $n = 1.5$, The calculated wavelength detuned cavity length, $l(\lambda)$ is plotted as a function of wavelength in figure (8.15c).

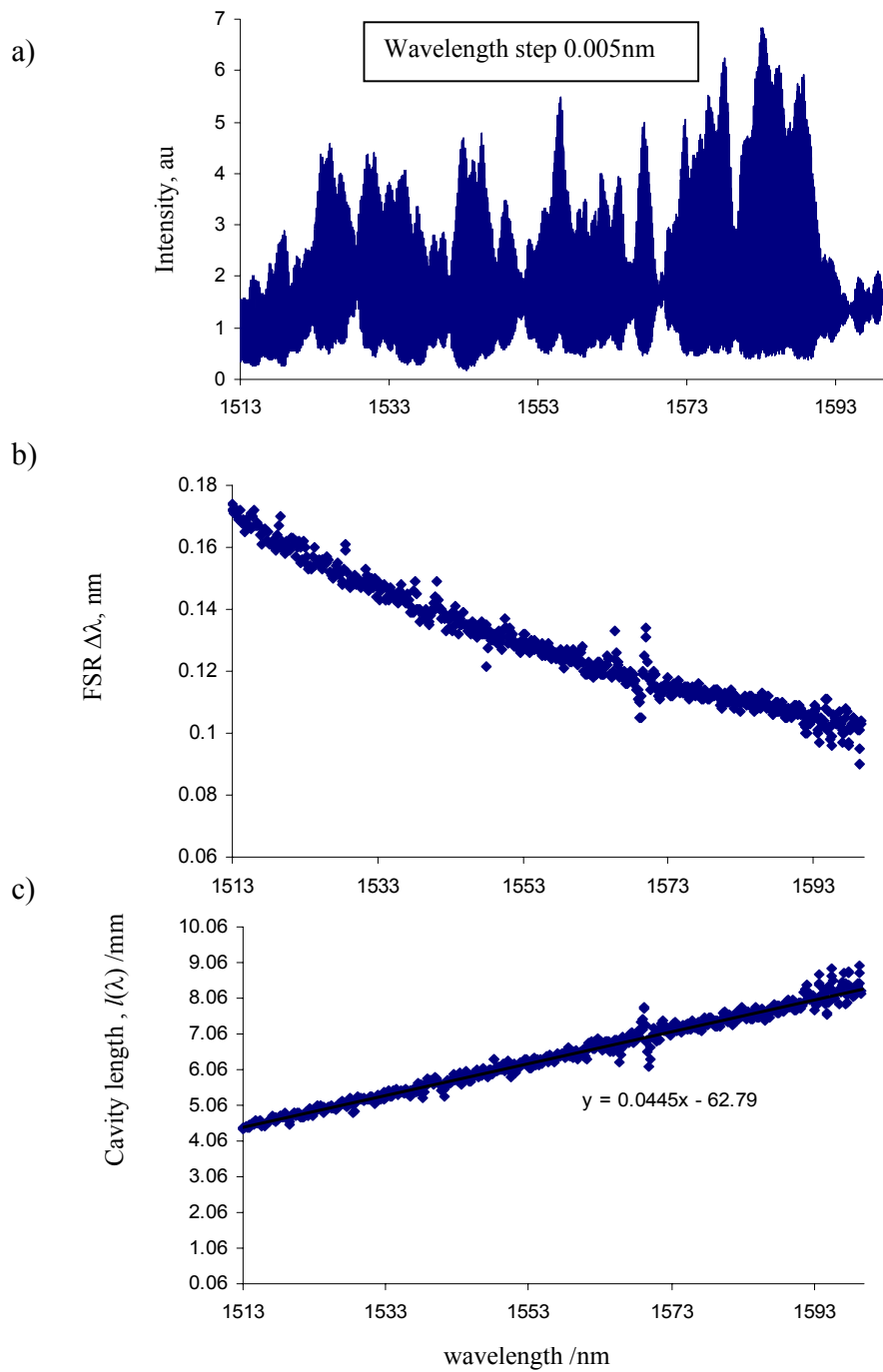


Figure 8.15a shows the wavelength response of the dissimilar chirped FBG FP which consists of a chirped FBG and a cleaved end of the fibre forming a cavity with the length of ~ 7 mm, measured from the centre of the FBG to the fibre end. b) a plot of the variation of the FSR with wavelength and c) a plot of wavelength detuned cavity length, $l(\lambda)$ as a function of wavelength defined from equation (4.47).

In figure (8.15c), the dependence of the cavity length upon the illuminating wavelength demonstrates the effect of the variation in reflection position of the chirped FBG. The chirped FBG was configured such that the shorter wavelength was reflected from position nearer to the cleaved end of the fibre, figure (8.14). A linear regression fit to the data reveals a gradient of 0.0445 mm/nm. The inverse, 23nm/mm should match the chirp rate of the chirped FBG, which was fabricated to be 25nm/mm.

When the orientation of the chirped FBG is reversed, such that the orientation of the increasing chirp is towards the centre of the cavity, figure (8.16). Following a similar argument to that put forward in section (4.3.3.5), the arrangement of the chirped FBG in the cavity is akin to the enhanced wavelength sensitivity configuration of the chirped FBG FP.

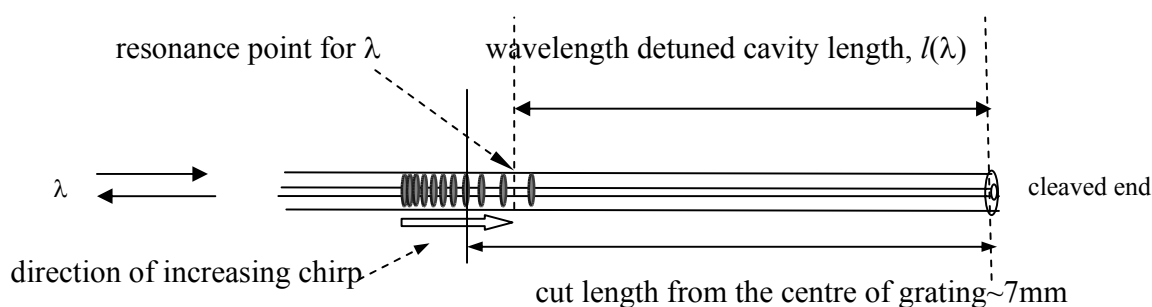


Figure 8.16, shows the enhanced wavelength sensitive dissimilar chirped FBG FP configuration, where the direction of the increasing chirp is aligned towards the centre of the cavity.

The wavelength of the illuminating external cavity laser is scanned from 1513nm to 1594nm in steps of 0.002nm. The reflected signal from the cavity is shown in figure (8.17). In figure (8.17a), the reflected spectrum is very different to when the chirped FBG is reversed in the cavity, figure (8.15a), though the appearances of the peaks in the reflection profile bear similarities. The varying visibility of the FSR is due to the difference between the reflectivity of the chirped FBG with that of the cleaved fibre end, figure (8.17a).

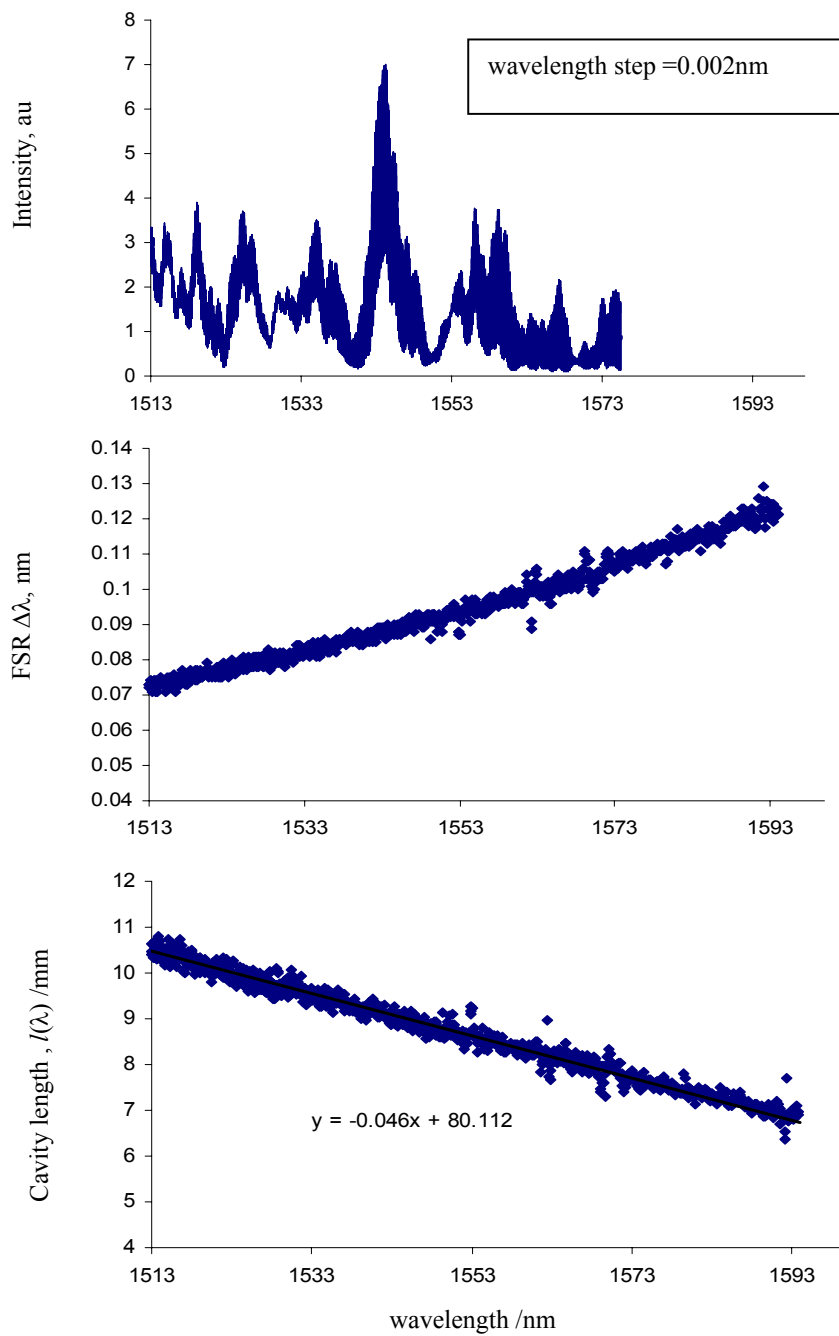


Figure 8.17a shows the wavelength response of the dissimilar chirped FBG FP which consists of a chirped FBG and a cleaved end of the fibre. The cavity length is ~ 7 mm, measured from the centre of the FBG to the fibre end. b) a plot of the variation of the FSR with wavelength and c) a plot of cavity length as a function of wavelength defined from equation (4.47).

The measured FSR from figure (8.17a) has an average value of 0.1nm. Using the non-dispersive FP response equation (4.47), a cavity length of $\sim 8\text{mm}$ is derived, which again is similar to the estimated length of $\sim 7\text{mm}$. The observed average FSR of 0.1nm is what is expected from a non-dispersive FP response using equation (4.47) and there is no significant enhancement in the observed sensitivity from the measured FSR value, figure (8.17b). Using the standard non dispersive FSR equation (4.47), the wavelength detuned cavity length, $l(\lambda)$ is calculated from the measured FSR values, assuming that the refractive index, $n = 1.5$. The calculated wavelength detuned cavity length is plotted as a function of wavelength in figure (8.17c). The chirped FBG was configured such that the longer wavelength was reflected from a position nearer to the cleaved end of the fibre, figure (8.16). A linear regression fit to the data produced a gradient of 0.046 mm/nm and the inverse, 22nm/mm matches the designed chirp rate of 25nm/mm of the grating used.

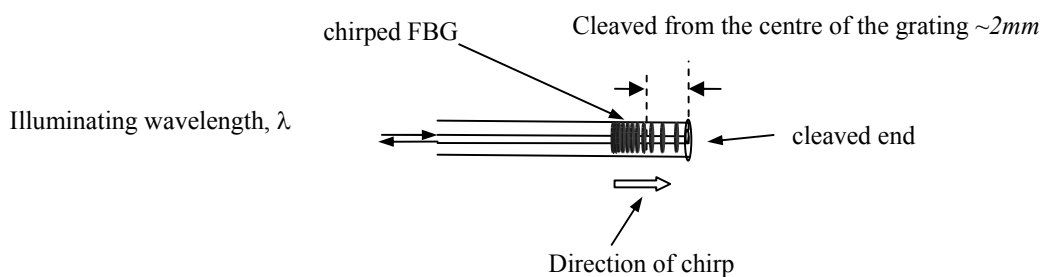


Figure 8.18, showing the dissimilar chirped FBG FP with a very short cavity length with the chirped FBG having a chirp rate of $\sim 25\text{nm/mm}$ and cavity length $\sim 2\text{mm}$ measured from the centre of the grating to the cleaved end

If the cavity length of this dissimilar chirped FBG FP is reduced further, to within sub-millimetres in length, the cavity should still be dispersive and the FSR/wavelength response will be modified by the inclusion of the dispersive factor, equation (4.48). The FP response of this cavity should not adhere to a conventional FP response. The dissimilar chirped FBG FP is shown in figure (8.18) with the chirped FBG oriented such that the increasing chirp is directed towards the centre of the FP. The cleaved end of the fibre is located at $\sim 2\text{mm}$ away from the centre of the grating forming a cavity as shown in figure (8.18). The wavelength response of the cavity is shown in figure (8.19).

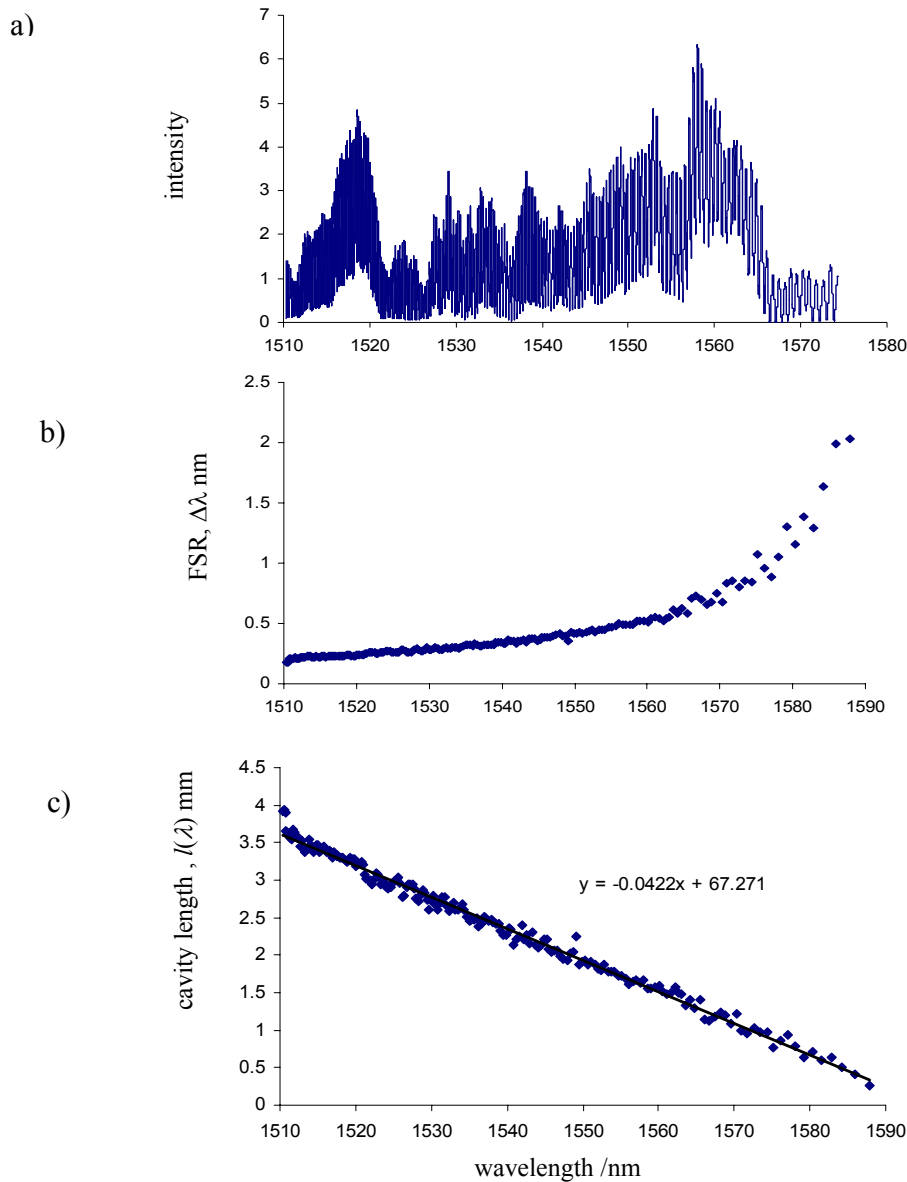


Figure 8.19a shows the wavelength response of the dissimilar chirped FBG FP which consists of a chirped FBG and a cleaved end of the fibre forming a cavity with the length of ~ 2 mm, measured from the centre of the FBG to the fibre end. b) a plot of the variation of the FSR with wavelength and c) a plot of cavity length as a function of wavelength defined from equation (4.47).

The wavelength response shown in figure (8.19a) demonstrates a large variation of FSR, as much as 500% across the spectrum of the grating, figure (8.19b). This large variation of the FSR can be explained by the non dispersive FP response, equation (4.47). The derivative of the FSR with respect to cavity length, l is inversely proportionally to the square of the cavity length. For small

cavity length, the rate of change in the FSR with cavity length is large, figure (8.19b). Using the standard non dispersive FSR equation (4.47), the wavelength detuned cavity length is calculated from the measured FSR, with the assumption that the refractive index, $n = 1.5$. The calculated wavelength detuned cavity length is plotted as a function of wavelength in figure (8.19c). The calculated wavelength detuned cavity length, $l(\lambda)$ in figure (8.19c) shows the longer wavelength is reflected from the position in the chirped FBG nearer to the cleaved fibre end and that the central wavelength is reflected near the centre of the grating with a cavity length of $\sim 2\text{mm}$ which agreed with the estimated distance measured from the grating centre to the fibre end. The linear fit to the wavelength detuned cavity length, figure (8.19c) predicts a chirp rate of 24nm/mm .

There is no significant change to the observed FSR of the above dispersive dissimilar chirped FBG FP cavity. The responses of these cavities obeyed the conventional non dispersive FSR equation (4.47) and there is nothing to suggest that the wavelength responses of these dissimilar chirped FBG FP cavities are dispersive. Other than the wavelength detuned cavity length, $l(\lambda)$, there is no significant change to the value of the FSR value of these cavities.

8.4.2 Straining the dissimilar chirped FBG FP

When an axial strain is applied to a chirped FBG, the location inside the FBG from which light of a given wavelength is reflected changes. The concomitant change in the reflection point imparted to every wavelength component within the bandwidth of the chirped FBG translates to a large group delay and thus a large optical path change, and a concomitant change in the RTSP in an interferometric configuration. This effect has been utilised in a Michelson interferometer with enhanced strain sensitivity [8] and in chirped FBG FP configuration used as a path length matching processing interferometer in low coherence interferometry [9]. The chirped FBG Michelson interferometer configuration used in the stain magnification experiment [8] is similar in that of the low finesse chirped FBG FP formed by a chirped FBG and a cleaved fibre end with low reflectivity.

Attempts were made to repeat the strain sensitivity enhancement observed by Kersey et al [10] in a FP arrangement. The chirped FBG FP consists of a chirped FBG and a fibre cleaved end, as shown in figure (8.20). Instead of measuring the modulation of the carrier frequency created by ramping the wavelength of the illuminating laser, a direct measurement of the shift in the RTSP of the reflected signal is used. The large displacement of the reflection point in response to applied strain should translate to a larger shift in RTSP. The chirp is fabricated in the wavelength region of 1550nm by the method of fibre bending technique [1]. The FBG has a total chirp of $\sim 12\text{nm}$ over a length of $\sim 4\text{mm}$. The distance between the translation stages of the strain rig is set with the width equal to the grating length of chirped FBG. The chirped FBG FP is mounted on the strain rig such that the fibre cleaved end is held free and the length of the grating is stretched over the width of the space between the two travelling stages of equal length and secured by the application of glue so that when the stages are stretched, strain is applied across the grating and not anywhere else, figure (8.20). The extent of the strain is monitoring using the bulk FP with a HeNe source.

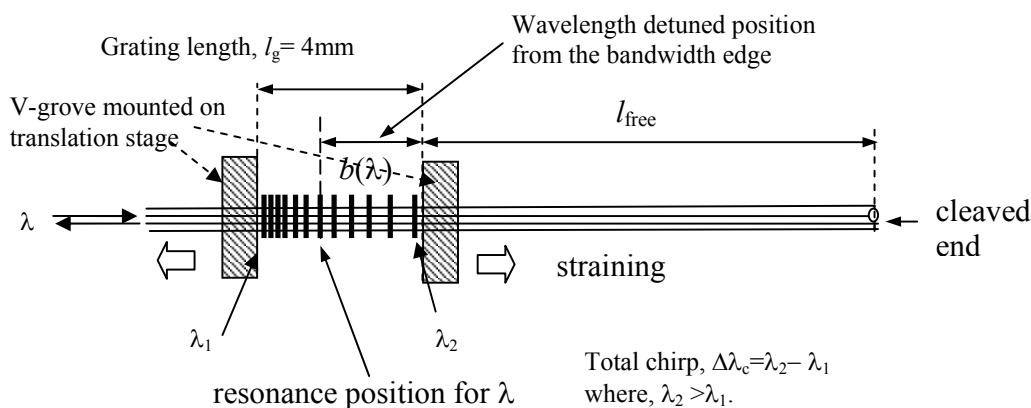
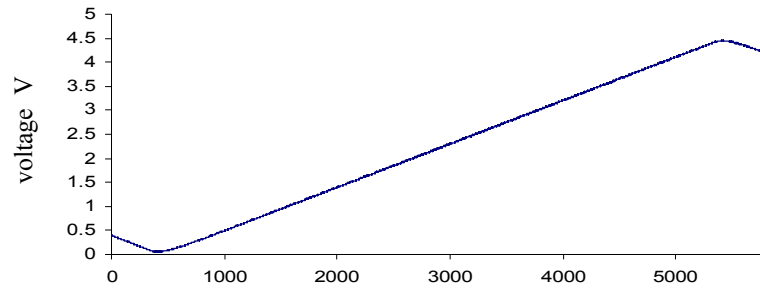


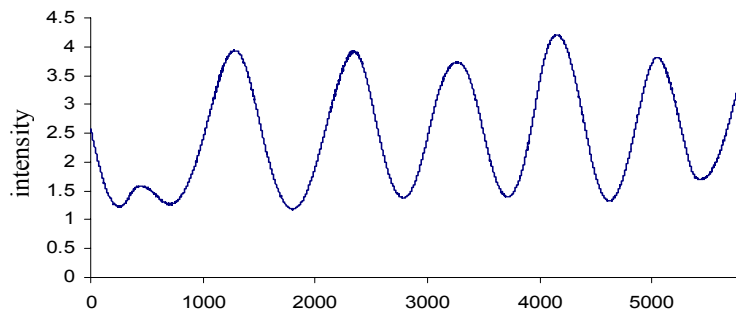
Figure 8.20, experimental arrangement to strain only the grating of the chirped FBG FP. The shift in the RTSP with the application of strain is monitored.

The cavity is illuminated by the output from the tuneable laser and an axial strain is applied to the FBG. The extension of the strain rig is monitored using the bulk FP illuminated by the HeNe source. The reflected signal from the chirped FBG FP is detected by a photodiode which is monitored and captured using a DAQ card. The experiment is repeated for the illuminating wavelength in the range of 1565nm to 1575nm in steps of 2nm. The results are shown in figure (8.21).

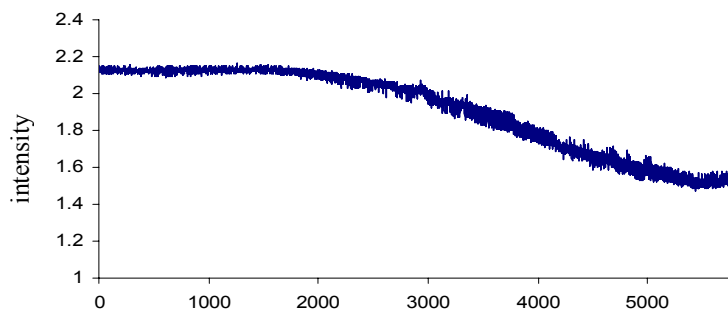
a) voltage ramp



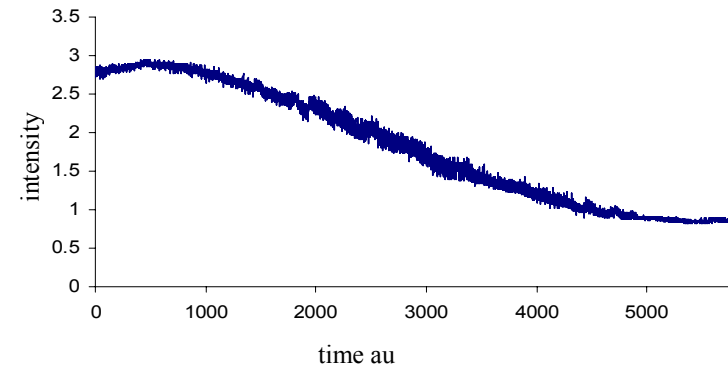
b) HeNe wavelength for monitoring the extension



c) $\lambda = 1565$ nm



d) $\lambda = 1569$ nm



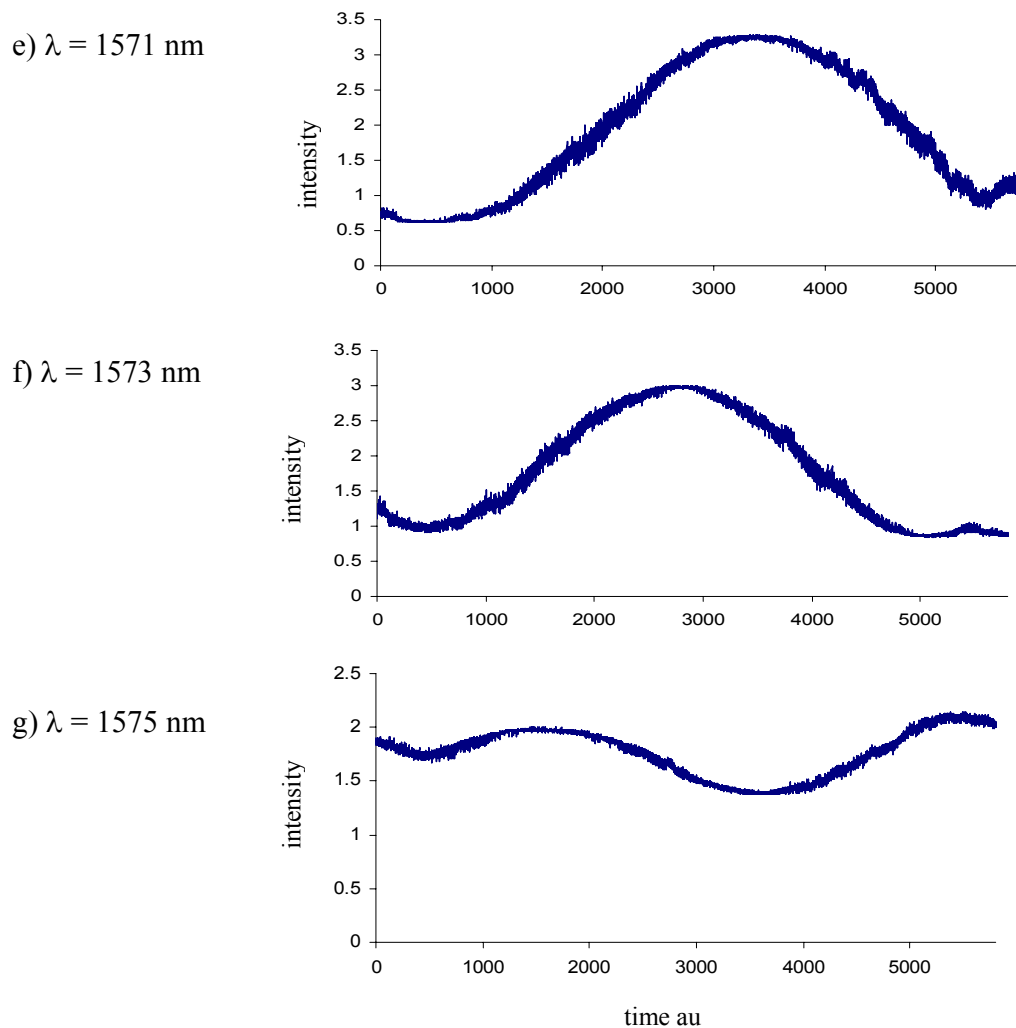


Figure 8.21a) the voltage ramp, b) the calibrating HeNe wavelength at which ~ 5 fringes appeared giving an extension of $\sim 1.5\mu\text{m}$ in a grating of $\sim 4\text{mm}$ which corresponds to an applied strain of $\sim 375\mu\epsilon$. A progressing increasing strain sensitivity with increasing illuminating wavelength can be seen from c) to g) with wavelength in the range of 1565nm to 1575nm in steps of 2nm . The maximum observed phase change $\sim 2\pi$ radian @ 1575nm .

Figure (8.21a) shows the applied voltage from the input of the piezo-actuator used to apply strain to the FBG. Figure (8.21b) shows the response of the bulk FP illuminated at 633nm , used to calibrate the extension. The observed ~ 5 fringes of the calibrating HeNe wavelength, corresponds to an extension of $\sim 1.5\mu\text{m}$. Given that the length of the grating is 4mm , this translates to a strain of $\sim 375\mu\epsilon$.

The strain response of this cavity can be explained using the conventional FP response to strain. From the RTSP of a FP cavity;

$$\theta = \frac{4\pi n l}{\lambda}$$

the cavity length l can be written as;

$$l = b + l_{free}$$

The strain sensitivity of this cavity can be rewritten as;

$$\frac{d\theta}{d\varepsilon} = \frac{4\pi n}{\lambda} \frac{d(n(b + l_{free}))}{d\varepsilon}$$

When there is no movement of the reflection point of the wavelength with applied strain inside the FBG, the equation can be simplified to;

$$\frac{d\theta}{d\varepsilon} = \frac{4\pi n}{\lambda} b(\lambda) \xi \quad (8.5)$$

where $b(\lambda)$ is the distance measured from the resonance position inside the FBG to edge of the grating near to the centre of the FP, as shown in figure (8.20). From equation (8.5), the strain sensitivity is proportional to the wavelength detuned length $b(\lambda)$. As the length of the grating is the only portion of the cavity experiencing the strain, the contribution to the change in the RTSP comes only from the response of the FBG. The maximum value b can take is that of the grating length. An applied strain of $\sim 375\mu\varepsilon$ is predicted to induce a maximum of $\sim 4\pi$ radian (2 fringes). From the observed strain response of the cavity, figure (8.21c)-(8.21g) for the 5 increasing illuminating wavelengths, the strain sensitivity increases with increasing wavelength. This indicates that the wavelength detuned length b is shorter for shorter wavelength than for longer wavelength which gives an indication of the orientation of the chirp in the FBG. From figure (8.21g), the observed maximum phase excursion with applied strain is $< 4\pi$ radian. So the strain response of this cavity is proportional to the wavelength detuned length, b and when the reflection position of the wavelength is near the bandage of the grating, λ_2 or near where b is small, the strain sensitivity will be a minimum.

The strain response in figure (8.21) shows no observable large phase change due to the movement of the reflection position with strain. Chirped FBG fabricated by the technique of interference of different wavefront [11] have also been used in this experiment but they also yielded a conventional FP response with applied strain.

The strain response of the chirped FBG FP in response to straining only the chirped FBG shows no indication of strain enhancement or magnification, but the strain response does illustrate the positional dependent of the reflection position of the wavelengths of the chirped FBG.

8.4.3 Wavelength response of dissimilar chirped FBG FP with the chirp in the FBG created by applying a strain gradient along the length of FBG

Using a different method of generating chirp in the FBG, a chirped FBG FP is formed between a FBG and a cleaved end of the fibre to see if the dispersive effect of chirped FBG will have any observable changes to the wavelength response of the cavity

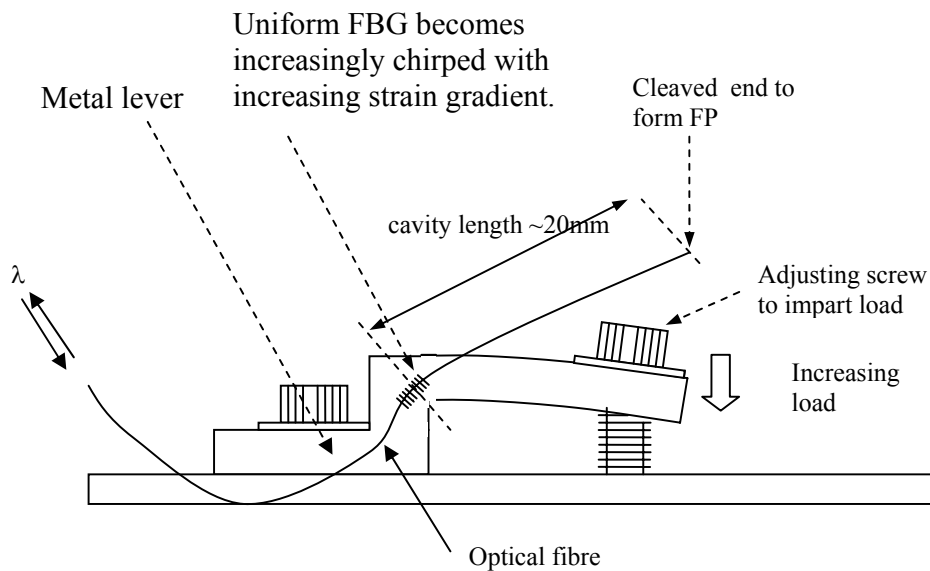


Figure 8.22, illustrates the setup used to apply a strain gradient to a uniform period FBG to induce a chirp. This system was used to form the chirped FBG reflector in the FP cavity.

A uniform period FBG can be chirped by the application of a strain gradient along the grating length [12]. This may be achieved by using a metal lever to impart the strain gradient to the FBG as shown in figure (8.22). A uniform period FBG with centre wavelength of 1553.2nm, and grating length ~ 3 mm, is glued to the side of the metal lever as shown in figure (8.22). The metal lever is secured to the optical table. By adjusting the loading screw, the metal lever is pressed downwards, imparting a non-linear strain along the length of the FBG.

The FBG FP is formed by cleaving the fibre at one end and forming a cavity with the FBG as the reflector. The length of the cavity measured from the centre of the FBG to the fibre end, is ~ 20 mm. The cavity is illuminated by the output from the external cavity laser, over the wavelength range of 1552nm to 1555nm and the reflected signal is recorded at one load level. By tightening the adjustable screw, the metal lever transfers a positional dependent axial strain which changes the period along the grating length, thus creating chirp in the grating [12]. The load is gradually increased by tightening the screw on the lever and the wavelength is scanned for this state of loading. This is repeated for 4 states of loading and the results are shown in figure (8.23).

For a non dispersive cavity such as the uniform period FBG FP, the cavity response will adhere to the conventional FSR response, equation (4.42) where the FSR corresponds to the wavelength detuned cavity length. For a FP formed between a chirped FBG and the cleaved end of the fibre, it is similar to FP formed between chirped FBGs with dissimilar parameters, section (3.9) and section (4.3.3.2). As the dispersive effects in the dissimilar chirped FBG FP do not cancel, it is considered dispersive where the effective cavity length term in the conventional cavity response is modified by the dispersive term of the chirped FBG, equation (4.48). This dispersive chirped FBG FP cavity response will be significantly different to the conventional FP cavity response.

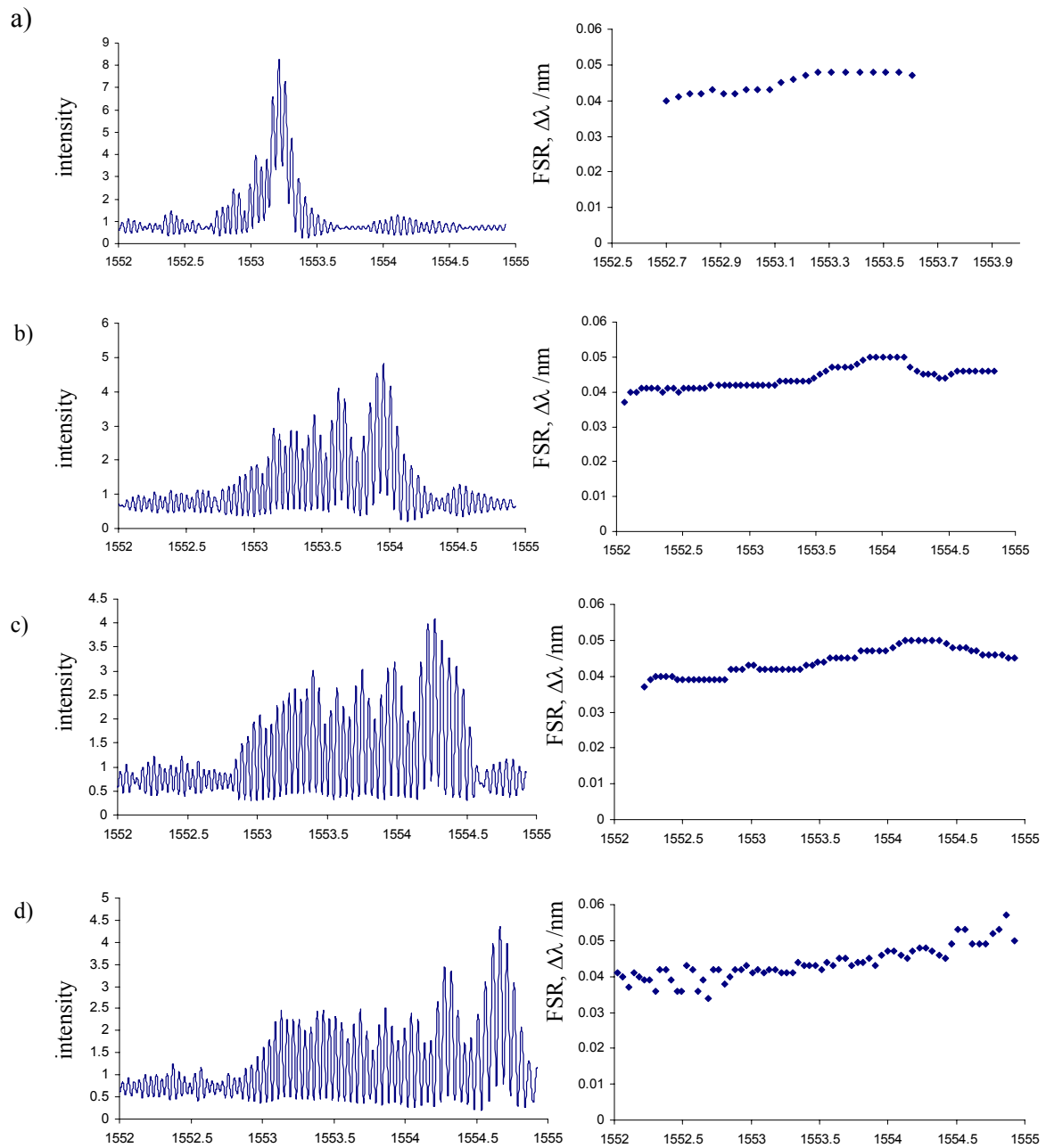


Figure 8.23a, the wavelength response of the uniform period FBG FP which consists of a uniform FBG forming a FP with a fibre end and cavity length ~ 20 mm. b) – d) shows the same cavity when the chirp of the FBG is progressively increased. The bandwidth of the wavelength response is progressively broadened but the change of the chirp rate has no affect on the measured FSR.

Before the applications of any load, the FP formed is that of the uniform period FBG FP formed between the uniform period FBG with the cleaved fibre end. Figure (8.23a) shows the reflected spectrum for the uniform FBG FP when no load is applied to the FBG. The measured FSR of $\sim 0.04\text{nm}$ corresponds to a cavity length of 20mm. As the load is increased, figure (8.23b-d), the bandwidth of the spectrum broadens but there is not significant change to the measured FSR, $\sim 0.04\text{nm}$. Not only does the profile of the grating broaden but the centre wavelength also shifts in response to the increase in the average strain along the grating length. There is no significant difference to the measured FSR value of $\sim 0.04\text{nm}$ and chirping the FBG have no effect on the cavity response.

The chirp in the FBG FP used so far has been derived by different techniques, ie, bending fibre method [13], interference of different wavefront [11] and induced strain gradient to the FBG [12]. Using the chirped FBG created, attempts have been made to observe significant changes in the dispersive FP FSR response, equation (4.48). However all of the FP response of the chirped FBG FP cavities, demonstrate a non dispersive FBG FP response to changes in wavelength with a wavelength dependent cavity length only. The information provided by the wavelength dependent cavity length shows the positional dependent of the reflection positions for wavelength, exist inside the grating. These chirped FBG have the same characteristics as the stepped chirped FBG [14] where there is no continuity in the period but still provide a broadband response. Using the idea that the periods are discontinuous can explain the experimentally derived wavelength response and the interferometric filter response reported in some literatures involving the use of chirped FBGs in interferometric configurations.

To ensure there is continuity of the chirp in the FBG, chirped FBGs fabricated using the continuous chirp phase mask method [15] are sought. Two such gratings were acquired commercially. The FBGs have a central wavelength of 1550nm with a length of 5mm and total chirp of 10nm. The details and specifications of the chirped FBGs are detailed in Appendix F. The experimentally determined reflection spectrum of the 2 chirped FBGs are shown figure (8.24a).

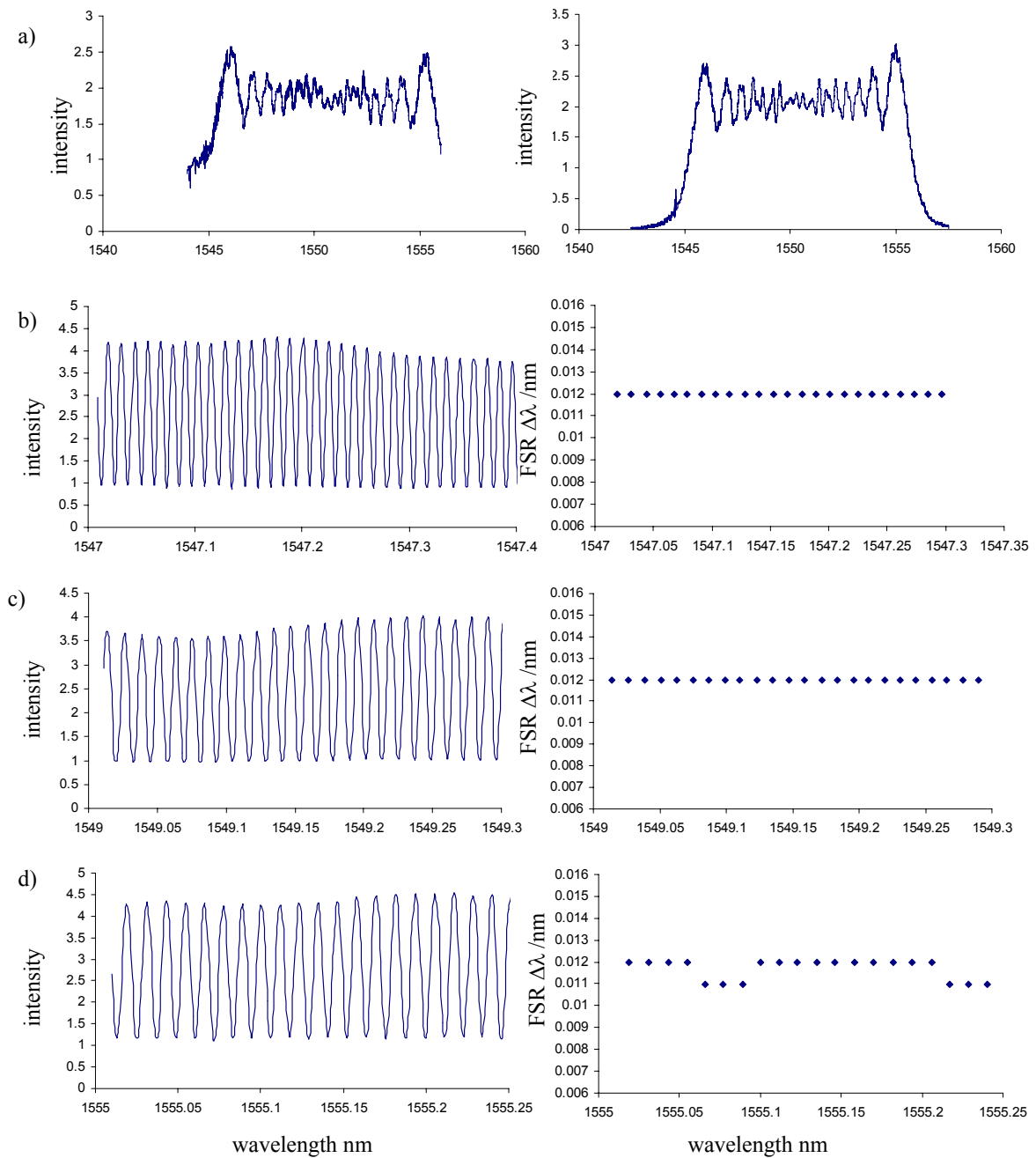


Figure 8.24a) the reflection profile of the 2 chirped FBG written by using a continuous phase mask method, b), the wavelength response @1547nm and the corresponding FSR, c) the wavelength response @1549nm and d) the wavelength response @1555nm. The measured FSR for all wavelengths corresponds to a cavity length ~ 65 mm of a non dispersive FP cavity.

The chirped FBG FP cavity was formed between the chirped FBG and the cleaved fibre end. The cavity length was $\sim 65\text{mm}$, similar to the configuration shown in figure (8.13). The performance of the chirped FBG FP was assessed by scanning the wavelength of the illuminating source and the results are shown in figure (8.24b-d) in 3 wavelength regions, figure (8.24b) @1547nm, c) @1549nm and d)@1555nm. The wavelength scan was repeated in other illuminating wavelength regions as well as reversing the orientation of the chirp of the FBG in the FP configuration. A measured FSR value of $\sim 0.012\text{nm}$ prevailed in all wavelength regions within the bandwidth and for both orientations of the chirped FBG. The measured FSR corresponds to the standard non dispersive FP response with a cavity length $\sim 65\text{mm}$. The chirp rate of the FBG and the orientation of the chirp have no bearing on the FP response. This can be explained if there is no continuity in the period of the chirped FBG and the continuity/dispersive term in equation (4.48) is neglected such as in the stepped chirped FBG or concatenation of many uniform period FBGs. There is no movement of the reflection point when the wavelength is tuned.

8.5 Overlapping cavity chirped FBG FP

The overlapping cavity consists of two co-located chirped FBGs with grating lengths of 4mm and total chirp, $\Delta\lambda_c \sim 100\text{nm}$ (fabricated using the dissimilar wavefronts method [4]), but with chirps oriented in opposite directions, as shown in figure (8.25a). In figure (8.25b), there are two wavelengths, λ_1 and λ_2 for which the cavity length, measured between the reflections positions in the respective FBGs, have the same length. There exists a wavelength whose wavelength dependent cavity length, $l(\lambda)$ equal to zero. For a perfectly overlapping chirped FBG FP, the central wavelength will see a cavity length of zero between the reflection points in the respective FBGs.

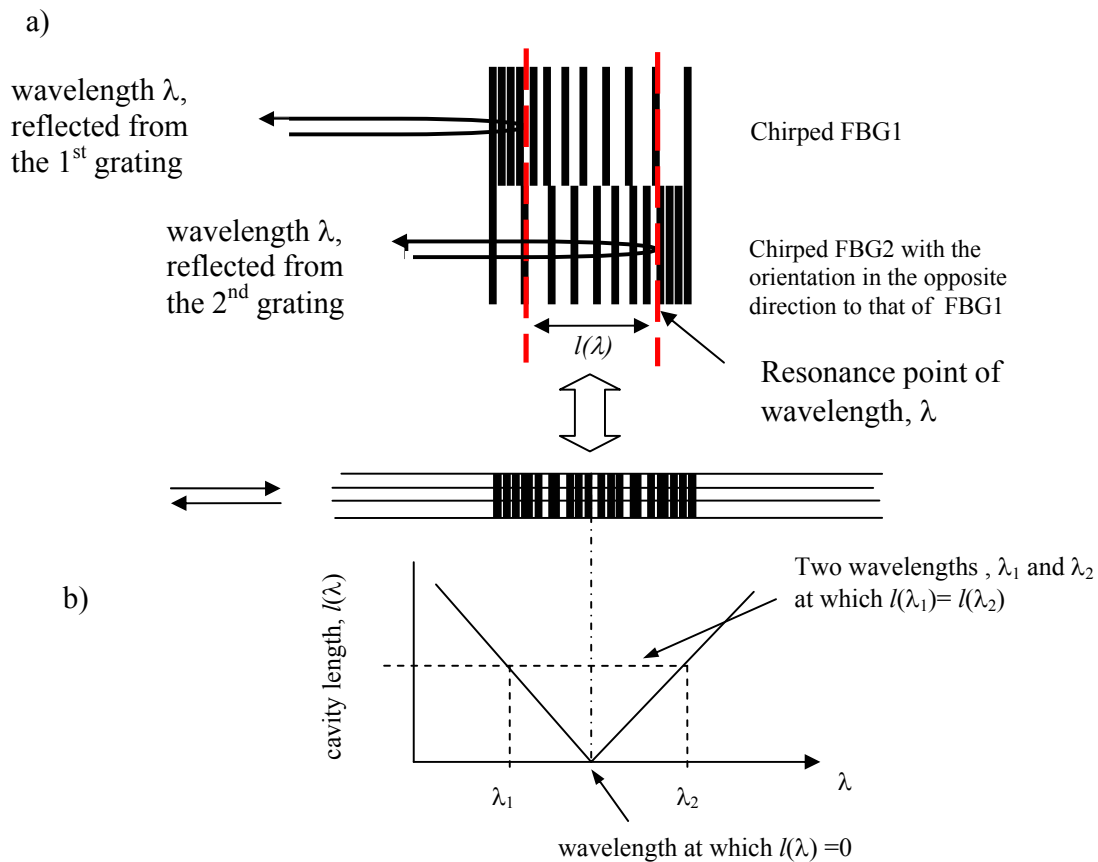


Figure 8.25a), illustration of an overlapping cavity where the respective resonance positions provide the cavity length $l(\lambda)$. b) there exist 2 wavelengths, λ_1 and λ_2 which shares the same cavity length. For a perfectly overlapping chirped FBG FP, the central wavelength will see a cavity length of zero between the reflection points in the respective FBGs.

The collocation of two chirped FBGs in an optical fibre is created by writing two chirped FBG at the same physical location in the fibre. The two chirped FBGs are oriented in the opposite direction. The writing of 2 chirped FBGs in the same location is more likely to disrupt the period of each [16] and therefore, the continuity of the chirp of each FBG, so making the FP more likely to behave like the non-dispersive FBG FP with a response corresponding to the wavelength detuned cavity length, $l(\lambda)$.

8.5.1 Wavelength response of the overlapping cavity

The overlapping chirped FBG FP cavity is illuminated by wavelengths in the 1500-1610nm range. The wavelength is scanned with wavelength steps of 0.002nm and the reflected spectrum of the overlapping chirped FBG FP is shown in figure (8.26).

Using the conventional non-dispersive FP response, equation (4.47) and substituting the wavelength detuned cavity length, $l(\lambda)$ in terms of the chirp rate, C , the FSR can be written about the wavelength where the cavity length is zero (overlapping wavelength), $\delta\lambda$;

$$(\Delta\lambda_{FSR})_{\delta\lambda} = -\frac{\lambda^2}{2nl(\lambda)} = -\frac{\lambda^2}{2n\left(2\frac{\delta\lambda}{C}\right)} \quad (8.6)$$

where the factor 2 indicates that there are 2 gratings involved. At the overlapping wavelength of the 2 chirped FBGs, the FSR, $\Delta\lambda_{FSR}$ will be infinite. From equation (8.6), the FSR will be symmetrical about the overlapping wavelength. From the wavelength response, figure (8.25a), the spectrum is symmetrical about 1526nm. At this wavelength, the FSR is the largest and it progressively decreases on either side of 1526nm. Assuming a chirp rate of 25nm/mm and refractive index $n=1.5$, equation (8.6) is plotted in figure (8.25b) to allow comparison with the experiment data and the two fit closely to each other.

From the measured FSR in figure (8.26b), using the non dispersive FP response with wavelength, equation (8.6) with the assumption that the refractive index, $n = 1.5$, the wavelength detuned cavity length is calculated. The wavelength detuned cavity length, $l(\lambda)$ is plotted as a function of wavelength in figure (8.26c). A linear regression fit to the figure (8.26c) gives a chirp rate of $\sim 27\text{nm/mm}$ which compares well with the designed chirp rate of $\sim 25\text{nm/mm}$. From figure (8.26c), the same cavity length can be accessed by 2 different illuminating wavelengths.

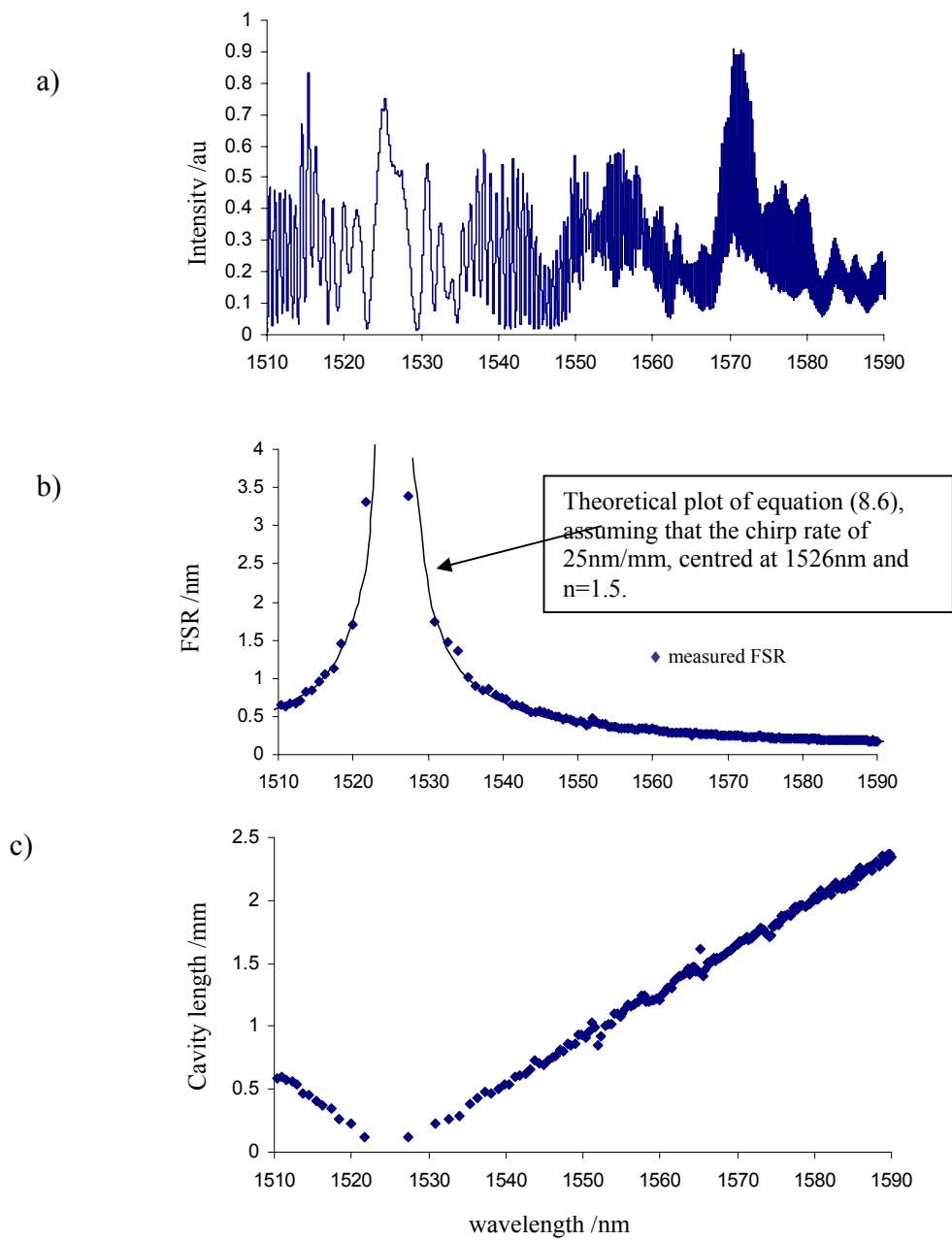


Figure 8.26a) the wavelength response of the overlapping chirped FBG FP cavity where the FSR is the highest at ~ 1526 and decreases on either side, b) the measured FSR is plotted together with equation (8.6) and c) using the FSR data and using equation (8.6) the wavelength detuned cavity length, $l(\lambda)$ is plotted as a function of wavelength. The wavelength at ~ 1526 nm corresponds to a cavity length of zero. A linear fit gives a chirp rate ~ 27 nm. Notice that for a cavity length $l(\lambda)$, can be accessed by 2 illuminating wavelength.

The dimensions of the overlapping chirped FBG FP can be very small, maximum cavity length being equal to that of the FBGs used $\sim 4\text{mm}$. When this cavity is used as a filter, a continuous FSR range from 0.1nm to several nanometers can be accessed by detuning the illuminating wavelength. Both high resolution and large dynamic range can be accessed in a single point sensor head.

8.5.2 Strain response of the overlapping cavity

The overlapping chirped FBG FP grating was subjected to axial strain using the strain rig discussed in section (7.4). The maximum strain imposed was $740\mu\epsilon$, as calibrated with the HeNe source. The cavity was interrogated over the wavelength region of 1510-1610 nm in steps of 5nm by tuning the output of the laser and the strain response was measured at each wavelength.

Figure (8.27) illustrates the strain response for 3 wavelengths. The measured strain response over the entire wavelength range can be found in Appendix G. The phase noise evident on the traces is attributed to the wavelength noise, $<3\text{pm}$, of the laser source [17]. The strain response in figure (8.27) demonstrates the wavelength detuned position of the cavity length in the overlapping chirped FBG FP. By increasing the illuminating wavelength away from the overlapping wavelength at which the cavity length is zero, a larger cavity length can be accessed. The graphs illustrate the dependence of strain sensitivity on the cavity length, $l(\lambda)$. The cavity length, $l(\lambda)$ can be written as the wavelength detuned position about the overlapping wavelength when the cavity length is zero using the Taylor expansion, equation (5.7);

$$l(\delta\lambda) = 2 \frac{1}{C} \delta\lambda \quad (8.7)$$

where $\delta\lambda$ is the detuning from the wavelength at which the cavity length is zero.

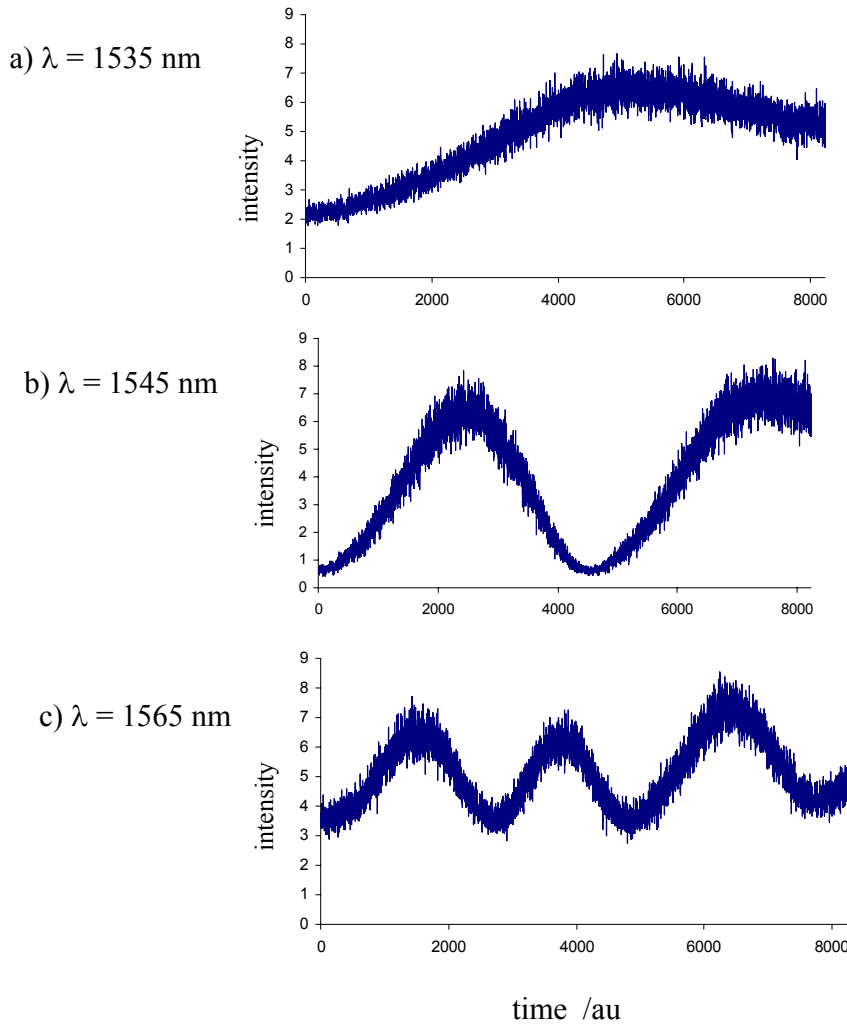


Figure 8.27, shows the strain response of the overlapping chirped FBG FP cavity measured at illuminating wavelength of, a) $\lambda=1535\text{nm}$, b) $\lambda=1545\text{nm}$ and c) $=15650\text{nm}$.

Using the RTSP equation; $\theta = \frac{4\pi n}{\lambda} l$ where l is the length of cavity, and substituting equation (8.7), the strain response is given as [3];

$$\frac{d\theta}{d\varepsilon} = \frac{8\pi n \xi}{\lambda} \frac{1}{C} \delta\lambda \quad (8.8)$$

where ξ is the strain response of the grating/fibre. At the overlapping wavelength when $\delta\lambda = 0$, the strain sensitivity, equation (8.8) becomes zero. At this wavelength, the cavity length measured between the reflection positions in the respective FBG is zero, equation (8.7) but no

matter how much strain is applied, the strain sensitivity at this wavelength is still zero, so there is no movement of the reflection point in the FBG. The wavelength reflection position inside the chirped FBG remains fixed, which is contrary to expectations. The strain response of the cavity is plotted in figure (8.28).

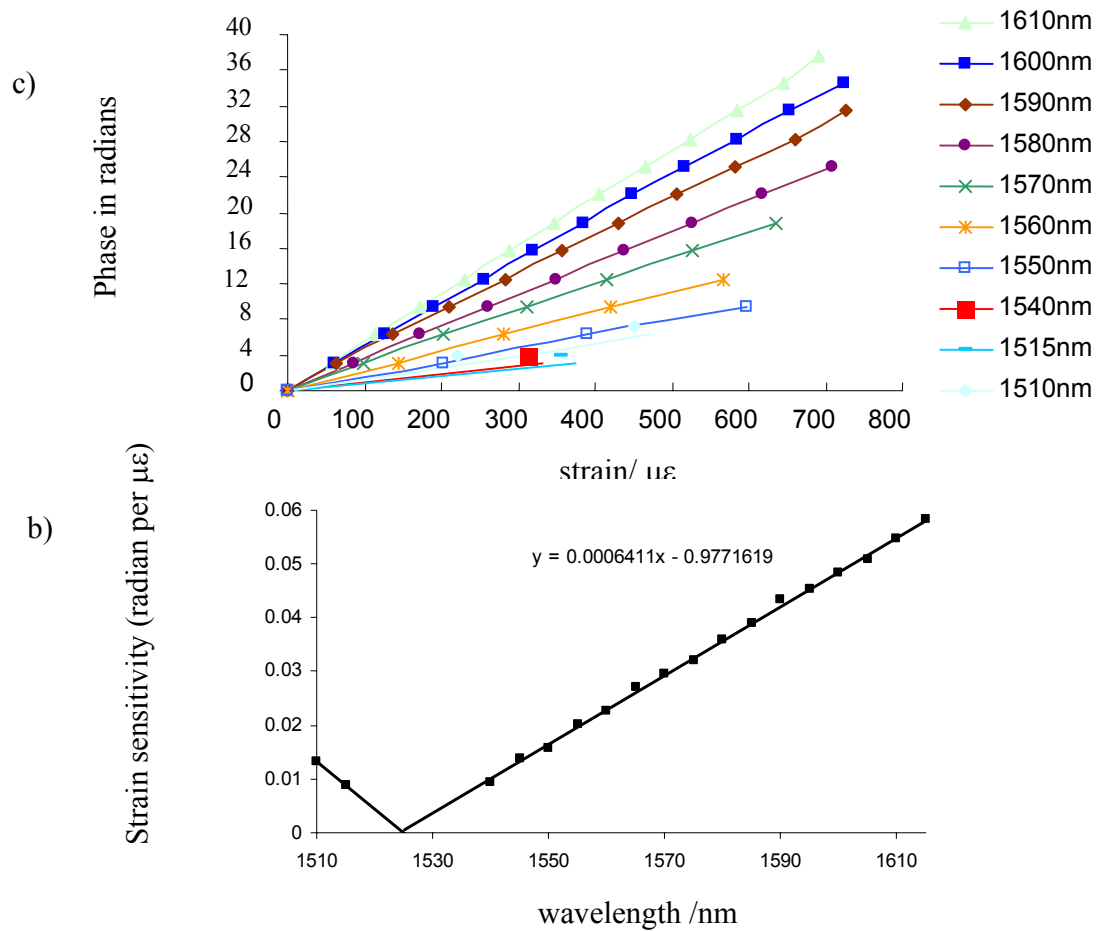


Figure 8.28a) shows the plot of the measured phase shift as a function of the applied strain for different illuminating wavelength and b) is the strain sensitivity of the overlapping cavity as a function of wavelength.

In figure (8.28a), the phase is plotted as a function of the applied strain for different interrogating wavelengths. For each wavelength, the strain sensitivity is seen to be linear. In figure (8.28b), the strain sensitivity is plotted as a function of illuminating wavelength. The linear relationship verifies equation (8.8). As the strain sensitivity is a function of wavelength, the strain sensitivity

of the cavity may be controlled by virtue of the illuminating wavelength. From this graph, the wavelength at which this cavity is insensitive to strain is determined to be $\sim 1526\text{nm}$, the same wavelength as that at which the FSR of the cavity is maximum, figure (8.26).

A least squares fit to the data plotted in figure (8.28b) produces a gradient of $6.666 \pm 0.009 \times 10^{-4}$ radian $\mu\epsilon^{-1} \text{nm}^{-1}$. Using this value, assuming $n = 1.5$, $C = 25\text{nm mm}^{-1}$ and $\lambda = 1550\text{nm}$ in equation (8.8) gives a value for the grating/fibre strain response, $\xi = 0.685 \pm 0.001$ compares to the experiment value $\xi = 0.742$ at 1550nm . The discrepancy is probably due to the change in the material characteristics due to UV exposure when writing the grating at the same place twice.

This chirped FBG FP cavity provides a strain sensor with large dynamic range based on the construction of a single sensor head with a continuous range of wavelength addressable FSR values. Using different illuminating wavelengths, the same sensor allows different strain sensitivity to be employed.

8.5.3 Temperature response of the overlapping chirped FBG FP cavity

The overlapping grating was then placed in the tube furnace described in section (7.6) and the thermal response of the cavity was monitored. The cavity was interrogated in the wavelength region of $1510\text{-}1610 \text{ nm}$ and the temperature of the furnace was increased gradually. Figure (8.29) illustrates the measured responses of the cavity to temperature for 3 interrogating wavelengths. The measured temperature response for the other interrogating wavelengths can be found in Appendix H. As with the strain response, the temperature response of the overlapping chirped FBG FP demonstrates the same wavelength detuned cavity length dependence, figure (8.29). Increasing the detuned wavelength from the wavelength at which the cavity length is zero provide a larger cavity length and thus offers an increased temperature sensitivity.

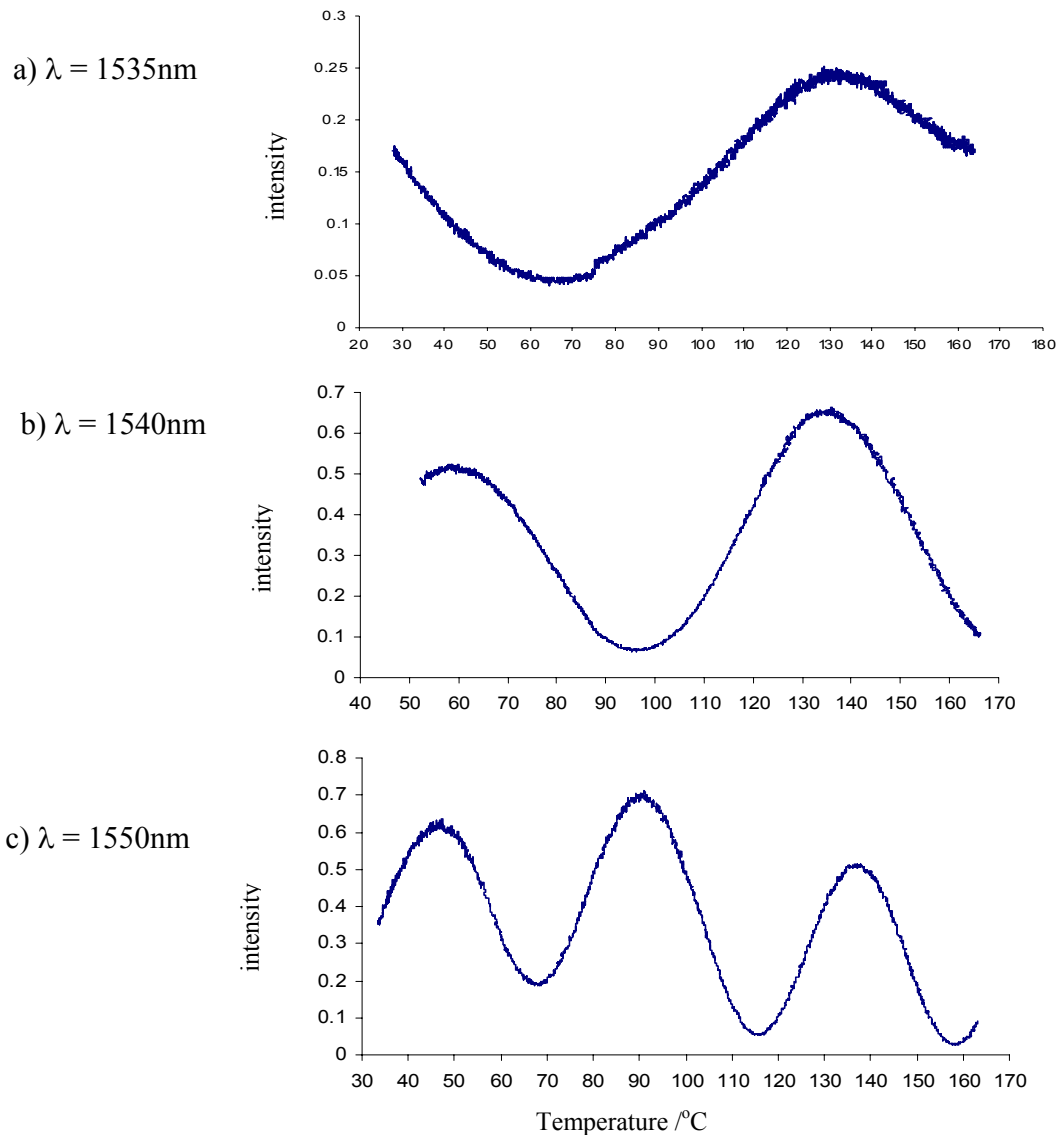


Figure 8.29, measured temperature responses of the overlapping chirped FBG FP cavity with wavelengths a) @1535nm, b) @1540nm, c) @1550nm.

Figure (8.29) illustrates the dependence of temperature sensitivity on the wavelength detuned cavity length, $l(\lambda)$ of the chirped FBG FP. Using equation (8.7), and differentiating the RTSP with respect to temperature, the temperature sensitivity about the detuned wavelength, $\delta\lambda$ can be written as;

$$\frac{d\theta}{dT} = \frac{8\pi n \zeta}{\lambda} \frac{1}{C} \delta\lambda, \quad (8.9)$$

where ζ is the temperature response of the grating/fibre. A plot of the phase shift against temperature for different illumination wavelength (detuned cavity length) is shown in figure (8.30). As the wavelength increases, the phase sensitivity increases. The phase response at each wavelength is seen to be linear, while the sensitivity is a function of wavelength, figure (8.30a). This demonstrates the tuneability of the temperature sensitivity of the cavity by virtue of the illuminating wavelength.

In figure (8.30b), the temperature sensitivity is plotted as a function of illuminating wavelength. The linear relationship verifies equation (8.9). From the graph, the wavelength at which this cavity is insensitive to temperature is determined to be $\sim 1526\text{nm}$ same as the results given in the wavelength and strain response from the previous section.

Again, when the cavity is interrogated at the overlapping wavelength, when $\delta\lambda=0$, the temperature sensitivity is zero, equation (8.9). Increasing temperature has no effect on the cavity at this wavelength, thus no change in the distance between the positions of the reflection point inside the chirped FBG, which constitute the cavity length. The overlapping chirped FBG FP behaves like the bulk type of FP.

A least squares fit to figure (8.30b) gives a gradient of $5.145 \pm 0.034 \times 10^{-3} \text{ radian } ^\circ\text{C}^{-1} \text{ nm}^{-1}$. Using this value together with equation (8.9), assuming $n = 1.5$, $\lambda = 1526\text{nm}$ and $C = 25\text{nm mm}^{-1}$, the temperature responsivity for the fibre/grating is determined to be $\zeta = 5.20 \pm 0.18 \times 10^{-6}$. When this is compared to the accepted value $\zeta = 8.39 \times 10^{-6}$ of a FBG @1550nm, the two have the same order of magnitude and the discrepancy is probably due to fibre type used, and the temperature fluctuations in tube furnace.

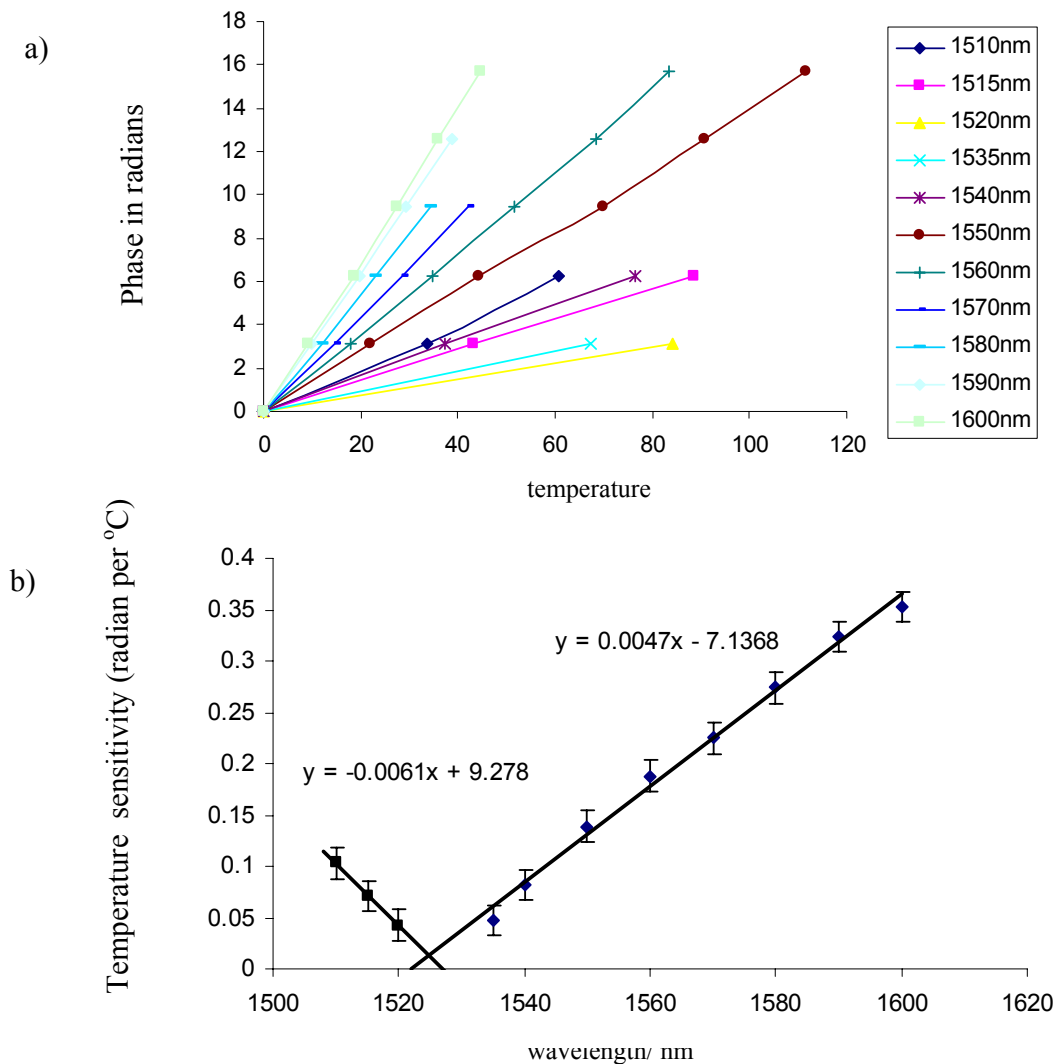


Figure 8.30a) shows the plot of the measured phase shift as a function of the temperature for different illuminating wavelengths and b) is the temperature sensitivity of the overlapping chirped FBG FP cavity as a function of wavelength.

8.6 Summary

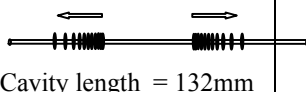
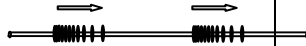
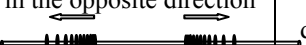
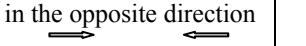

The large group delay experienced by the wavelengths which produces the strain magnification and large path length scanning in the interferometric configuration is caused by the dispersion inside the chirped FBG. Using this dispersive effect, chirped FBG FP cavity configured to have the strain sensitivity reduced has been observed (section (8.2)) at the 800nm wavelength region

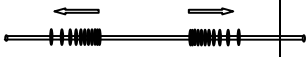
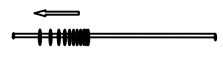
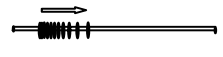
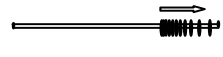
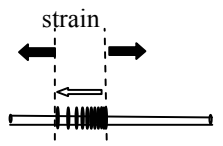

with the chirp created in the FBG by the fibre bending method. Attempts were made to produce dispersive chirped FBG cavities in the 1550nm region which will respond to strain, wavelength and temperature differently to the conventional non dispersive FP response. Different method of creating the chirp in the FBG have been used and different chirped FBG FP configurations have been tried out to observe changes to the FP response but all of which can only indicate a non dispersive response.

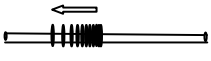
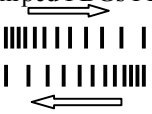
The wavelength detuning of the reflection positions can be seen in the results of the experiments but the continuity of the wavelength with position which gives the dispersive effect is not obvious. The chirped FBG at the 1550nm wavelength region behaved more like the stepped chirped FBG even with the commercially available chirped FBG fabricated with the continuous chirped phase mask. The non dispersive FP response of the chirped FBG has also been demonstrated by other authors too, specifically the wavelength detuned reflection position of the chirped FBG has been utilised in providing a variable FSR in FP filters and in phase based intragrating distributed strain sensing method. The results of the overlapping chirped FBG FP, section (8.5) is one such result where different strain, temperature and strain sensitivity can be accessed by the wavelength detuning in a single sensor head/filter. It is more understandable that the overlapping chirped FBG FP behaved like the non-dispersive cavity as the writing of the gratings at the same physical location disrupts the continuity of the chirp of each.

The different techniques used to create chirp in the FBG in the experiments involved chirping through the change of the period. The observed dispersive effect of the strain magnification in Kersey et al [8] experiment uses chirp created by inducing a temperature gradient along the length of the FBG which uses a different chirping mechanism through the mode refractive index. Perhaps a more accurate method of imparting chirp to the FBG, such as those offered by the direct writing technique using e-beam to create chirped FBGs employed in achieving a large scanning of the path-length mismatch [18]. With the direct writing method, each period is written individually and every period is uniquely defined. On the other hand the fabrication of gratings using the holographic method requires exposure to short duration of UV pulse but the process takes times of orders of minutes. Any fluctuations in temperature or movement of the fabrication system will cause the period of the refractive index modulation to vary. This can be seen in the

wavelength response of the uniform period FBG FP, figure (8.23a). In addition to the FP response within the Bragg wavelength region, there is a broadband response extending a number of nanometres away from the actual Bragg wavelength. This implies that there is a smearing of the refractive index modulation making the periodicity non-unique.

Configuration	Method of chirping	characterised	demonstrates distributed reflective nature	dispersive effect
<p>Chirped FBG FP with chirps in FBG oriented in the opposite direction</p>  <p>Cavity length = 132mm</p>	<p>Bending the fibre Chirp rate of ~20nm/2.6mm</p>	<p>Single wavelength @800nm illumination and characterised by straining</p>	N/A	<p>Reduced strain sensitivity</p>
<p>Chirped FBG FP with Cavity length ~97mm</p> <p>chirps in FBG oriented in the same direction</p>  <p>chirps in FBG oriented in the opposite direction</p>  <p>chirps in FBG oriented in the opposite direction</p> 	<p>Wavelength@1550nm Interference of different wavefronts with chirp rate of 100nm/4mm</p>	<p>Single wavelength @1500nm illumination and characterised by straining</p>	yes	<p>No observed reduction or enhancement of strain sensitivity</p>
<p>Chirped FBG FP with cavity length ~97mm.</p> <p>chirps in FBG oriented in the opposite direction</p> 	<p>Wavelength@1550nm Interference of different wavefronts with chirp rate of 100nm/4mm</p>	<p>Single wavelength @1500nm illumination and characterised by temperature</p>	<p>Can not be resolved due to large fluctuation in temperature</p>	<p>no observed reduction of temperature sensitivity</p>

<p>Chirped FBG FP with cavity length ~97mm.</p> <p>chirps in FBG oriented in the opposite direction</p> 	<p>Wavelength@1550nm Interference of different wavefronts with chirp rate of 100nm/4mm</p>	<p>wavelength @1500nm illumination and characterised by wavelength scanning</p>	<p>yes</p>	<p>no observed reduction of wavelength sensitivity</p>
<p>Chirped FBG FP with dissimilar grating</p>  <p>Cavity length ~6.7mm</p>	<p>Wavelength@1550nm Interference of different wavefronts with chirp rate of 100nm/4mm</p>	<p>Single wavelength @1500nm illumination and characterised by wavelength scanning</p>	<p>yes</p>	<p>no observed reduction of wavelength sensitivity</p>
<p>Chirped FBG FP with dissimilar grating</p>  <p>Cavity length ~7mm</p>	<p>Wavelength@1550nm Interference of different wavefronts with chirp rate of 100nm/4mm</p>	<p>Single wavelength @1500nm illumination and characterised by wavelength scanning</p>	<p>yes</p>	<p>no observed reduction of wavelength sensitivity</p>
<p>dissimilar chirped FBG FP</p>  <p>Cavity length ~2mm</p>	<p>Wavelength@1550nm Interference of different wavefronts with chirp rate of 100nm/4mm</p>	<p>Single wavelength @1500nm illumination and characterised by wavelength scanning</p>	<p>yes</p>	<p>no observed reduction of wavelength sensitivity</p>
<p>Dissimilar chirped FBG FP</p>  <p>strain</p>	<p>Wavelength@1550nm Bending the fibre to create a chirp rate of 12nm/4mm</p>	<p>Single wavelength @1500nm illumination and characterised by strain</p>	<p>yes</p>	<p>No observed enhanced strain sensitivity</p>
<p>Dissimilar chirped FBG FP with cavity length ~20mm</p> 	<p>Wavelength@1550nm Inducing a strain gradient across the grating length to create a chirp in FBG.</p>	<p>wavelength @1500nm illumination and characterised by wavelength scanning</p>	<p>yes</p>	<p>No observed enhanced sensitivity</p>

<p>Dissimilar chirped FBG FP with cavity length ~65mm</p> 	<p>Wavelength@1550nm Commercially purchased chirped FBG with chirp rate of 10nm/5mm</p>	<p>wavelength @1500nm illumination and characterised by wavelength scanning</p>	<p>N/A</p>	<p>No observed enhanced sensitivity</p>
<p>overlap dissimilar chirped FBGs FP</p> 	<p>Wavelength@1550nm Interference of different wavefronts with chirp rate of 100nm/4mm</p>	<p>wavelength @1500nm illumination and characterised by wavelength scanning characterised by staining characterised by temperature</p>	<p>Yes Yes yes</p>	<p>No No no</p>

References:

- 1 K. Sugden, I. Bennion, A. Moloney and N. J. Copner, ‘Chirped grating produced in photosensitive optical fibres by fibre deformation during exposure’, *Elect. Lett.* **30**, 440-441, 1994.
- 2 S. R. Kidd, P. G. Sinha, J. S. Barton and J. D. C. Jones, ‘Fibre optic Fabry-Perot sensors for high speed heat transfer measurements’, *Proc. of SPIE*, **1504**, 180-190, 1991.
- 3 C. D. Butter and G. B. Hocker, ‘Fiber optics strain gauge’, *Appl. Opt.* **17**, 2867-2869, 1978.
- 4 G. E. Town, K. Sugden, J. A. R. Williams, I. Bennion and S. B. Poole, ‘Wide-Band Fabry-Perot-Like Filters in Optical fiber’, *IEEE Photon. Tech. Lett.* **7**, 78-80, 1995.
- 5 I, Bennion, J. A. R. Williams, L. Zhang, K. Sugden and N. J. Doran, ‘UV-written in-fibre Bragg gratings’, *Optical and Quant. Elect.*, **28**, 93-135, 1996.
- 6 A. D. Kersey, M. A. Davis, H. J. Patrick, M. LeBlanc, K. P. Koo, C. G. Askins, M. A. Putnam and E. J. Friebele, ‘Fiber Grating Sensors’, *Journ. of Light. Tech.*, **15**, 1442-1463, 1997.

- 7 Y. J. Rao, 'In-fibre Bragg grating sensors', *Meas. Sci. Tech.*, **8**, 355-375, 1997.
- 8 A. D. Kersey and M. A. Davis, 'Interferometric fiber sensor with a chirped Bragg grating sensing element', *Proc. of SPIE*, **2360**, 319-322, 1994.
- 9 Y. J. Rao and D. A. Jackson, 'Recent progress in fibre Optic low-coherence interferometry', *Meas. Sci. Tech.*, **7**, 981-999, 1996.
- 10 A. D. Kersey and M. A. Davis, 'Interferometric fiber sensor with a chirped Bragg grating sensing element', *Proc. of SPIE*, **2360**, 319-322, 1994.
- 11 M. C. Farries, K. Sugden, D.C. J. Reid, I. Bennion, A. Molony and M. J. Goodwin, 'Very Broad reflection bandwidth (44nm) chirped fibre gratings and narrow Bandpass filters produced by the use of an amplitude mask', *Elect. Lett.* **30**, 891-892, 1994.
- 12 S. Huang, M. M. Ohn and R. M. Measures, 'Phase-based Bragg intragrating distributed strain sensor', *Applied Optics*, **35**, 1135-1142, 1996.
- 13 Sugden, I. Bennion, a. Moloney and N. J. Copner, 'Chipred grating produced in photosensitive optical fibres by fibre deformation during exposure', *Elect. Lett.*, **30**, 440-441, 1994.
- 14 R. Kashyap, P. F. McKee, R. J. Campbell and D. L. Williams, 'Novel method of producing all fibre photoinduced chirped gratings', *Elect. Lett.*, **30**, 996-998, 1994.
- 15 A. E. Willner, K. M. Feng, J. Cai, S. Lee, J. Peng and H. Sun, 'Tunable Compensation of Channel Degrading effects Using Nonlinearly Chirped Passive fiber Bragg Gratings', *IEEE Journ. of Selected Topics in Quant. Elect.* **5**, 1298-1311, 1999.
- 16 S. Doucet, R. Slavik and S. LaRochelle, 'High finesse large band Fabry-Perot fibre filter with superimposed chirped Bragg gratings', *Elect. Lett.*, **38**, 402-403, 2002.
- 17 Photonetics manufacturer's information.
- 18 C. Yang, S. Yazdanfar and J. Izatt, 'Amplification of optical delay by use of matched linearly chirped fiber Bragg gratings', *Optics Lett.*, **29**, 685-687, 2004.

9 Conclusion

In this thesis, the rationale behind the use of chirped FBG in the formation of novel chirped FBG FPs have been presented. Starting from the theoretical understanding behind the principles of FBGs and dispersion in FP cavities, the performance of the dispersive chirped FBG FP have been put forward, drawing on the outcomes and behaviour of reported results involving the use of chirped FBGs in interferometric configuration.

The argument put forward for changes in the FSR of the chirped FBG FP response stems from the fact that the constituents of the FP are dispersive. Dispersion causes the different components of wavelength to travel different optical path lengths whether it is through dispersion in material, where the refractive index changes with wavelength, section (4.3.2) or through a wavelength dependent position of the reflection point such as in the chirped FBG, section (4.3.3.2). Analogous to the material dispersive FP cavity, where the refractive index term is modified by the material dispersion present to become an effective refraction index in the FSR equation (4.40), the length dispersion in the chirped FBG will modify the cavity length term to one of an effective cavity length. Effectively, the sensitivity of the cavity can be changed through the chirp parameters of the FBG used to form the FP. An indication of the wavelength sensitivity of the FP cavity is given by the corresponding effective cavity length. The effective length of the chirped FBG FP could be made longer, thus giving an increased in sensitivity or made shorter, thus a reduced in sensitivity but keeping the physical cavity length of the chirped FBG FP constant. The wavelength sensitivity of the dispersive chirped FBG FP can be extended to the strain sensitivity and temperature sensitivity through the strain and temperature responsivities of the FBG to wavelength change.

The experimental evidence of a reduced strain sensitivity using the chirped FBG FP at 800nm (section 8.2), demonstrate the viability of changing the strain sensitivity using the chirped FBG FP configuration. The physical phenomenon involved can be explained by the dispersive effect of the chirped FBG and it is in support of the physical outcome of the reported strain enhancement of 2000-5000 times of a $500\mu\epsilon$ applied to a 1cm long

grating (extension = $5\mu\text{m}$) produces an optical path length change of 1-3cm in the location of the resonance points, using an interferometric configuration (section (3.11)). It is also evident in the observed large scan of the path length mismatch ($3495\mu\text{m}$), produced in the matched path length interferometer interrogation involving the application of $33\mu\text{m}$ extension to a 1cm chirped FBGs (section (3.11)). Unfortunately this cavity did not survive so that the wavelength response could be verified with the strain response.

Attempts to produce differing sensitivity in the chirped FBG FP formed in the 1550nm wavelength region have proved unsuccessful. Different techniques for creating chirp in the FBG have been used with all the chirped FBGs being periodically chirped. The behaviour of all these chirped FBG FPs adhered to the conventional FP response with the corresponding cavity length equals to the distance between the reflection positions in the FBGs. This wavelength dependence of the reflection position can be discerned from the wavelength, strain and temperature response of these cavities and it is especially so where the cavity length of the chirped FBG FP is small such as the overlapping chirped FBG FP cavity, section (8.5).

If there is no continuity of the period in the chirped FBG such as experienced in the stepped chirped FBG, cavities formed would behave with a conventional FP response. It could happen during the grating writing process where vibration and temperature fluctuations can create a smearing of the periodicity of the FBG, similar to the stepped chirped FBG with a much smaller wavelength step, though the gross chirp is still registered. The smearing of the reflection points makes it non unique and thus the chirp becomes discontinuous. Writing 2 gratings at the same location in the optical fibre disrupts the continuity of the chirp further which causes the overlapping chirped FBG FP to behave like the non dispersive cavity. The reported strain magnification is performed on a FBG whose chirp is created by inducing a temperature gradient along the length of the FBG, which involved a different chirping mechanism of delivering chirp to the FBG. In a chirped FBG induced by temperature gradient, the thermo-optic effect dominates, providing a positional variation in the mode refractive index along the FBG, which is

more akin to refractive index change in material dispersion. Whereas in the case of the observed large group delay in the interferometric scanning, the chirped FBG is created by writing the periodicity directly using e-beam techniques which reduces the smearing of the period and provide continuity in the period.

The scheme using chirped FBG FP offers immense flexibility in determining the sensitivity of the FP. The sensitivity of the chirped FBG FP will not so much depend on the actual cavity length but more reliant on the parameters of the chirped FBG pair. This has huge implications for these cavities to be used as sensors and filters. High wavelength sensitivity means a large phase excursion can be created by a small sweep of the wavelengths and this can create very narrow passband filter whereas a wavelength insensitive cavity will have a very low phase noise. Short gauge length device with high wavelength sensitivity have implications in interferometric demodulation. The sensitive small gauge length device can be used as a processing interferometer where the small length of the cavity will be less stringent on the coherence of the signal source and at the same time providing a high wavelength sensitivity readout such as in the FBG demodulation.

Long or short gauge length sensor can be made possible in the chirped FBG FP to configure systems to exhibit enhanced sensitivity to strain or alternatively, to have reduced or even zero strain sensitivity. High strain sensitivity means a small strain will be needed to create a large phase excursion for use in scanning a much larger path length mismatch before the breaking strength of the optical fibre is reached. Reduced sensitivity to strain increases the dynamic range of the measurement system whereas enhanced strain sensitivity increases the resolution and they are all encompassed within this scheme. This ability to tailor the sensitivity of the FP cavity to strain will enhance the capabilities of FBG for structural monitoring.

9.1 Future work

In this thesis, the performance of the chirped FBG FP has been discussed in the context of dispersion. The theoretical study has shown promise for the development of in fibre FP cavities with variable FSR that may be tailored to a particular application or be used as filter and sensor with controllable sensitivity to wavelength, strain and temperature.

Future work is needed to establish the discrepancy between theory and experiment for the latter chirped FBG FP cavities. This would be in the form of a theoretical study as well as an experimental investigation.

It is envisaged in the future to improve on the TMM model for the dispersive chirped FBG FP cavities so that it will verify and support the predictions that have been made of the responses of dispersive chirped FBG FPs to wavelength, strain and temperature. This would involve the incorporation of the different chirping mechanisms used to create the FBGs. In particular, to predict and verify the cavity response to the reported strain magnification and the large scanning of the path length mismatch in coherence interferometry for the FP, Michelson as well as in the Sagnac/loop configuration by straining of the individual chirped FBG. The realisation of the model could facilitate the prediction of the specification of the chirped FBG cavity requirement for different sensitivity. It will provide a prediction to the performance of chirped FBG FP cavity and of the outcome of future experimental investigation. The success of this wave model will provide a full spectrum as well as the phase information to the wavelength, which can serve as a validation to the theoretical predictions of the performance of the chirped FBG FP, put forward in this thesis.

The observed non dispersive response of the chirped FBG FP cavity to wavelength, strain and temperature, with a corresponding wavelength dependent cavity length can be used with Hi-Bi fibre. By writing the chirped FBG FP in a Hi-Bi fibre, the two polarisation modes will have different sensitivity by virtue of the different effective index, n_{eff} . The sensitivity of the two polarisations can be utilised to separate the strain and temperature

response. It will also be interesting to find out the exact form that these chirped FBGs take. A method of which is by the use of coherence interrogation to look at the refractive index modulation structure inside the FBGs. A resolution of less than $0.5 \mu\text{m}$ of a typical length of a period, is required which needs a very broadband light source. Also in experimental investigating of the chirped FBG FP response, different grating with chirp derived from methods that have been outlined above can be used. The aim of this is to see if the dispersive effect in the chirped FBG does have an effect on the performance on the FPs and also to have repeatable and predictable results which will go some way to verify what has been put forward in this thesis.

The success of this part of the program will enhance the capabilities of FBG as filters and sensors for structural monitoring and for use in other areas where selective sensitivity is required.

Publications arising from this research work

Conference Presentations:

- 1 C.S. Cheung, S.W. James, C.C. Ye, R.P. Tatam, 'Temperature and strain insensitive Fabry-Perot cavities formed using chirped fibre Bragg gratings', In-Fibre Gratings and special fibres, Photonex03, wed. 8th, Oct., 2003.
- 2 C.S. Cheung, S.W. James, C.C. Ye, R.P. Tatam 'The Strain Sensitivity of Fibre Fabry-Perot Cavities Formed between Chirped Fibre Bragg Gratings', OFS -16, International Conference on Optical Fiber Sensors, 13th, Oct., 2003.

Appendix A

The solution to the Maxwell Equation in a cylindrical coordinate system is based on the treatment of Yariv [i]. The propagation of electromagnetic radiation is governed by Maxwell equations:

$$\begin{aligned}\nabla \times E &= -\frac{\partial B}{\partial t}, \\ \nabla \times H &= J_f + \frac{\partial D}{\partial t}, \\ \nabla \cdot D &= \rho_f, \\ \nabla \cdot B &= 0,\end{aligned}\tag{A1}$$

where E and H are the electric and magnetic field vectors and D and B are the corresponding electric and magnetic flux densities. The current density vector J_f and the charge density ρ_f represent the source for the electromagnetic field. In the absence of free charge in the medium such as optical fibres, J_f and $\rho_f = 0$. In a homogeneous and isotropic medium, the Maxwell equations can be reduced to the scalar wave approximation for which the longitudinal field components E_z and H_z must satisfied.

$$\left[\nabla^2 - \mu\epsilon \frac{\partial^2}{\partial t^2} \right] \begin{bmatrix} E_z \\ H_z \end{bmatrix} = 0 \tag{A2}$$

where $k_0 = \frac{\omega}{c} = \frac{2\pi}{\lambda_0}$ and the operator $\nabla^2 = \frac{\partial^2}{\partial x^2} + \frac{\partial^2}{\partial y^2} + \frac{\partial^2}{\partial z^2}$.

E_z and H_z are the longitudinal electric and magnetic field components. The dependency of the other transverse components can be deduced from the standard Maxwell equations (A1). Since the refractive index profiles $n(\rho)$ of most fibre are cylindrically symmetric, it is conveniently to use the cylindrical coordinate system. The index of refraction as a function of the radial distance ρ is given by:

$$\begin{aligned}n(\rho) &= n_1, & 0 \leq \rho \leq a \\ n(\rho) &= n_2, & a < \rho\end{aligned}\tag{A3}$$

where a is the core radius and n_1 and n_2 are the core and the cladding refractive index respectively.

In the cylindrical coordinate system, using the standard trigonometry transformation, the reduced wave equation can be express as:

$$\left[\frac{\partial^2}{\partial \rho^2} + \frac{1}{\rho} \frac{\partial}{\partial \rho} + \frac{\partial^2}{\partial \phi^2} + \frac{\partial^2}{\partial z^2} + n^2 k_0^2 \right] \begin{bmatrix} E_z \\ H_z \end{bmatrix} = 0 \tag{A4}$$

Assuming the general wave equation having the form as shown:

$$\begin{bmatrix} E_z(r,t) \\ H_z(r,t) \end{bmatrix} = \begin{bmatrix} E(\rho, \varphi) \\ H(\rho, \varphi) \end{bmatrix} e^{i(\omega t - \beta z)} \quad (\text{A5})$$

where the transverse field component is given by:

$$\begin{bmatrix} E(\rho, \varphi) \\ H(\rho, \varphi) \end{bmatrix} = F(\rho) e^{\pm i l \varphi}$$

and $F(\rho)$ is the radial dependence of the field and the angular field dependence has a discrete set of angles φ such that $l=0,1,2,\dots$ where the \pm sign indicates the state of circularity. Substituting this general solution into the reduced equation (A4) and assuming that the E_z and H_z are singled-valued function of φ , then (A4) becomes:

$$\frac{\partial^2 F}{\partial \rho^2} + \frac{1}{\rho} \frac{\partial F}{\partial \rho} + (n^2 k_0^2 - \beta^2 - \frac{l^2}{\rho^2}) F = 0 \quad (\text{A6})$$

This is the differential equation for Bessel functions of order l and the general solution can be expressed as a linear combination of the Bessel functions which is written as:

$$F(\rho) = A_1 J_l(h\rho) + A_2 Y_l(h\rho) \quad \text{for } \rho \leq a$$

where $h^2 = n_1^2 k_0^2 - \beta^2$

and $F(\rho) = B_1 I_l(\kappa\rho) + B_2 K_l(\kappa\rho) \quad \text{for } \rho \geq a$

where $\kappa^2 = \beta^2 - n_2^2 k_0^2$.

J_l and Y_l are the Bessel function of the first and second kind respectively in the core region and that I_l and K_l are the modified Bessel functions of the first and second kind respectively in the cladding region. These are the general solutions and the number of constants can be reduced when appropriate consideration for viable solution exist in the core and cladding regions. These conditions require the solution be finite in the core and that the field distribution should trail off towards zero when ($\rho \rightarrow \infty$). Some of the constants are eliminated and the solution is simplified to:

$$\begin{bmatrix} E(\rho, t) \\ H(\rho, t) \end{bmatrix} = \begin{bmatrix} A \\ B \end{bmatrix} J_l(h\rho) e^{\pm i l \varphi} \quad \text{for } \rho \leq a$$

and (A7)

$$\begin{bmatrix} E(\rho, t) \\ H(\rho, t) \end{bmatrix} = \begin{bmatrix} C \\ D \end{bmatrix} K_l(\kappa\rho) e^{\pm i l \varphi} \quad \text{for } \rho \geq a$$

Solution to the Bessel differential equation (A6) required that h and κ be positive so that:

$$n_2 k_0 < \beta < n_1 k_0 \quad (A8)$$

and

$$h^2 + \kappa^2 = (n_1^2 - n_2^2) k_0^2$$

$$V^2 = (ah)^2 + (a\kappa)^2$$

and

$$V = \frac{2\pi a}{\lambda} \sqrt{n_1^2 - n_2^2}$$

where V is the normalised frequency. A relationship between the various fields can be derived by writing the Maxwell Equations (A1) in its differential form. A set of simultaneous equation involving, E_ϕ , H_ϕ and E_ρ , H_ρ in terms of E_z and H_z can be expressed in terms of the set of solution (A7). Applying the boundary condition required the continuity of the tangential fields components across the core-cladding interface such that the E_z , H_z , E_ϕ and H_ϕ be the same at $\rho = a$. For a non-trivial solution to this set of simultaneous equations, the determinants involving these many Bessel functions to be zero. This produces the eigenvalue equation whose solutions determine the propagation constant β for the fibre modes:

$$\left(\frac{J'_l(ha)}{hJ_l(ha)} + \frac{K'_l(\kappa a)}{\kappa K_l(\kappa a)} \right) \left(\frac{J'_l(ha)}{hJ_l(ha)} + \frac{n_2^2 K'_l(\kappa a)}{n_1^2 \kappa K_l(\kappa a)} \right) = \left(\frac{l\beta k_0 (n_1^2 - n_2^2)}{a\kappa^2 h^2 n_1} \right)^2 \quad (A9)$$

This has a quadratic form in $\left(\frac{J'_l(ha)}{hJ_l(ha)} \right)$ and the solution of which produce two

different equations corresponding to the two quadratic roots. The resulting equations yield two classes of solution, one of which is designated conventionally as the EH_{lm} mode and the other the HE_{lm} modes. These are hybrid modes involving all six field components and the field distribution is very complex but under certain condition, the especially the low order mode, the field distribution is predominantly polarised in certain direction. When $l = 0$, when there is no angular dependency on the transverse field distribution, equation (A9) can be reduced to a simple form with the help of some Bessel functions identities, for Transverse Electric (TE) mode:

$$\frac{J_1(ha)}{haJ_0(ha)} = -\frac{K_1(\kappa a)}{\kappa a K_0(\kappa a)} \quad (A10)$$

where the non vanishing terms are H_ρ , H_z and E_ϕ . and for Transverse Magnetic (TM) mode:

$$\frac{J_1(ha)}{haJ_0(ha)} = -\frac{n_2^2 K_1(\kappa a)}{\kappa a n_1^2 K_0(\kappa a)} \quad (A11)$$

where the non vanishing terms are E_ρ , E_z and H_ϕ . The solution for $l = 0$ are a special case as they are radial symmetric and produce completely transverse solutions. The graphical solution of the above by plotting each side of the equation (A10) or (A11) against ha , reveal that for TM and TE mode. The onset of the propagation mode is when, κa is near zero and not quite attain a positive value such that the field in the fibre is still un-guided as $ha \rightarrow V$. When modes approaching the cut-off condition, the fields extend well into the cladding layer, thus near cut-off the modes are poorly confined. For TE or TM modes, there is no propagation until $V = 2.405$ is reached. This value comes about from the first root of $J_0(V)$ when $V = 2.405$. Before the onset of the TM_{01} or the TE_{01} mode, there exists the fundamental mode so called HE_{11} which do not have a cut-off value. This mode have all six nonzero components of the field exist and it is the so called the hybrid mode. Some of these components can be ignored and can be considered as highly polarised. For single mode operation, the operating value of V is below 2.405.

i A. Yariv, 'Optical Electronics', Chapter 3, 4th edition, International edition, 1991.

Appendix B

The phase response of the insensitive chirped FBG FB cavity in section (4.3.3.6) is written as;

$$d\theta = -\frac{8\pi m}{C} \left(\frac{\Delta\lambda}{\lambda^2} \right) d\lambda \quad (C1)$$

when it is integrated from the central wavelength λ_0 to $\lambda_0 + \Delta\lambda$, then (C1) becomes;

$$\int d\theta = -\frac{8\pi m}{C} \int_{\lambda_0}^{\lambda_0 + \Delta\lambda} \frac{\Delta\lambda}{\lambda^2} d\lambda \quad (C2)$$

The phase response going from λ_0 to $\lambda_0 + \Delta\lambda$, is given by;

$$\theta = -\frac{8\pi m}{C} \int_{\lambda_0}^{\lambda_0 + \Delta\lambda} \frac{\Delta\lambda}{\lambda^2} d\lambda \quad (C3)$$

The integral can be simplified by;

$$\begin{aligned} \int_{\lambda_0}^{\lambda_0 + \Delta\lambda} \frac{\Delta\lambda}{\lambda^2} d\lambda &= \int_{\lambda_0}^{\lambda_0 + \Delta\lambda} \frac{\lambda - \lambda_0}{\lambda^2} d\lambda \\ &= \int_{\lambda_0}^{\lambda_0 + \Delta\lambda} \frac{\lambda}{\lambda^2} d\lambda - \lambda_0 \int_{\lambda_0}^{\lambda_0 + \Delta\lambda} \frac{1}{\lambda^2} d\lambda \\ &= \left[\ln(\lambda) + \frac{\lambda_0}{\lambda} \right]_{\lambda_0}^{\lambda_0 + \Delta\lambda} \\ &= \ln(\lambda_0 + \Delta\lambda) - \ln(\lambda_0) + \frac{\lambda_0}{\lambda_0 + \Delta\lambda} - 1 \\ &= \ln\left(\frac{\lambda_0 + \Delta\lambda}{\lambda_0} \right) + \frac{\lambda_0}{\lambda_0 + \Delta\lambda} - 1 \\ &= \ln\left(1 + \frac{\Delta\lambda}{\lambda_0} \right) - \frac{\Delta\lambda}{\lambda_0 + \Delta\lambda} \end{aligned}$$

using $\ln(1+x) = x - \frac{1}{2}x^2 + \dots$ $|x| < 1$

$$\begin{aligned} &= \frac{\Delta\lambda}{\lambda_0} - \frac{1}{2} \left(\frac{\Delta\lambda}{\lambda_0} \right)^2 - \frac{\Delta\lambda}{\lambda_0} + \left(\frac{\Delta\lambda}{\lambda_0} \right)^2 \\ &= \frac{1}{2} \left(\frac{\Delta\lambda}{\lambda_0} \right)^2 \end{aligned}$$

equation (C3) becomes;

$$\theta = \frac{4\pi m}{C} \left(\frac{\Delta\lambda}{\lambda} \right)^2 \quad (C4)$$

Appendix C

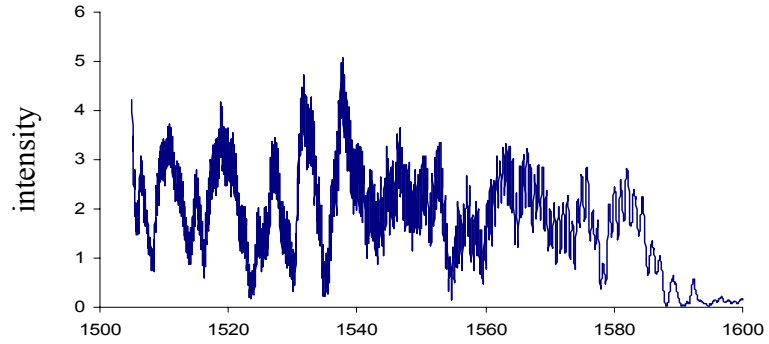
The specifications of the SEO TITAN-CW Series, Ti:sapphire Tunable Laser.

Output Power (at 800mw) (Standing-wave or ring cavity)	
250mW	(3W Pump Power)
500mW	(5W Pump Power)
750mW	(7.5W Pump Power)
Minimum Tuning Ranges (Pump power 5W or greater)	
Mirror Set	
Short-band	700-820nm
Mid-band	780-900nm
Long-band	890-1020nm
Spectral Linewidth (5W pump power)	
Standing-wave Cavity	<2GHz
Unidirectional Ring Cavity	<40MHz
Output Beam	
TEM ₀₀	
Horizontally Polarized	
Diffraction-Limited Beam Diameter (approx. 1mm@ exit)	
Coherence Length, $l_c = 0.64 \frac{c}{\delta\nu}$	
Standing-Wave:	$\delta\nu = 2 \times 10^9 \text{ Hz}$ $l_c \approx 10\text{m}$
Ring Cavity:	$\delta\nu = 40 \times 10^6 \text{ Hz}$ $l_c \approx 500\text{m}$
Divergence:	$\Theta_d = 2\lambda/\pi w_0$ $w_0 = 0.47\text{-}0.53\text{mm}$ $\Theta_d = 0.96\text{-}1.08\text{mrad}$

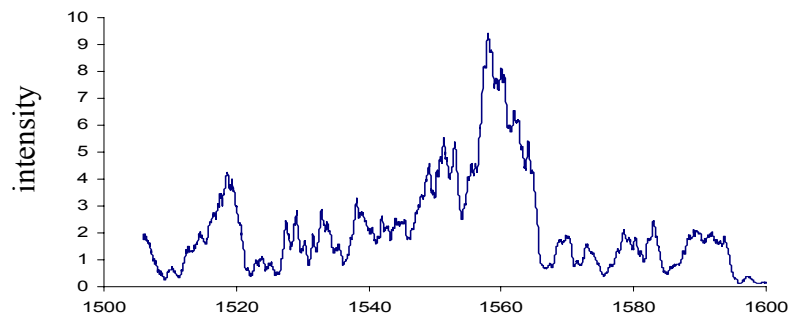
Appendix D

The reflection profile of the chirped FBGs used in the experiments

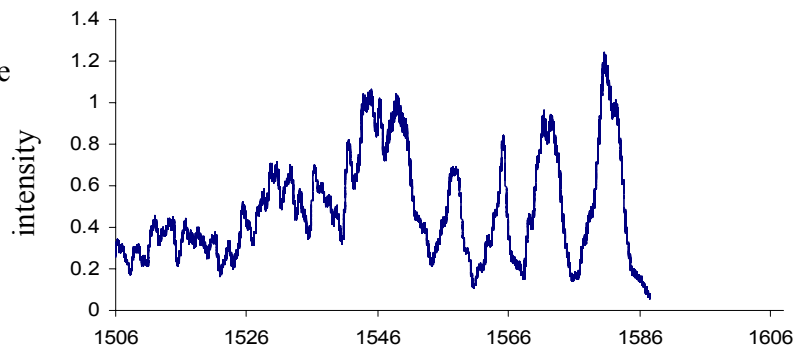
a) the grating profile of FBG no.1



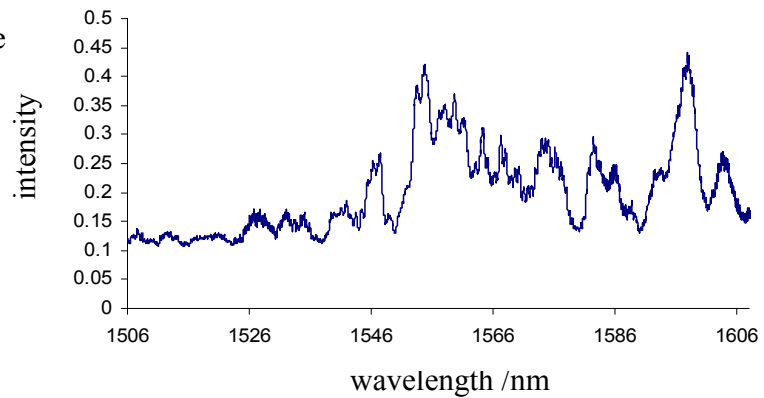
b) the grating profile of FBG no.2



c) the grating profile of FBG no.S3

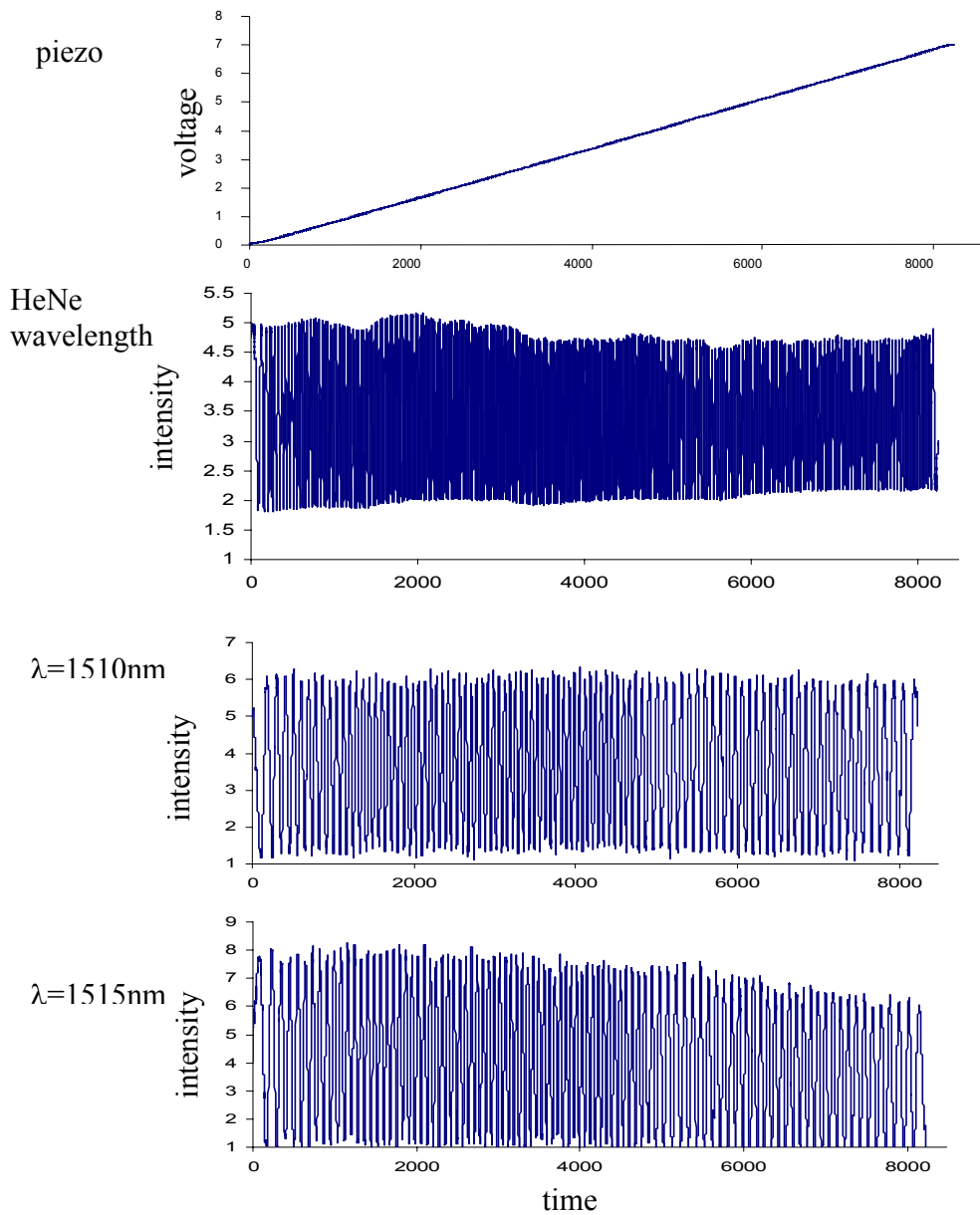


c) the grating profile of FBG no.S8

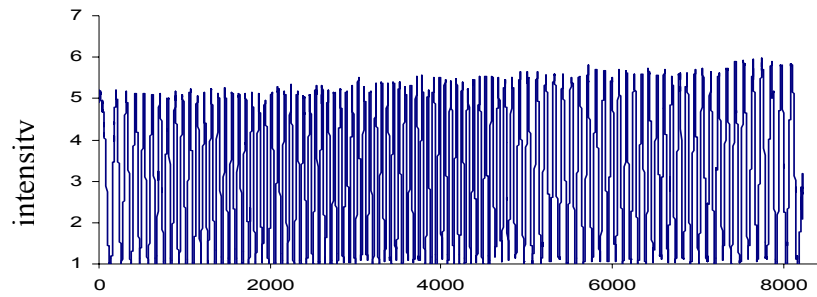


Appendix E

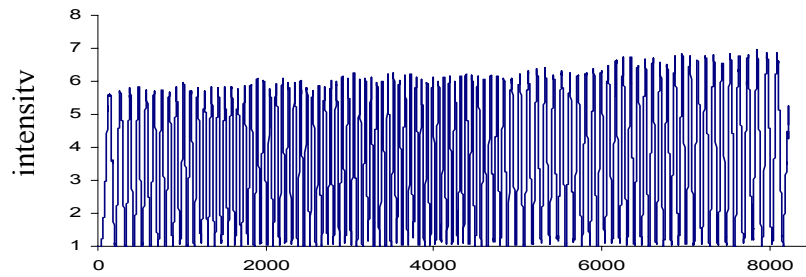
Phase response of the chirped FBG FP with designed chirp of 25nm/mm arranged so that the direction of increasing chirp is oriented in same way separated by a cavity length of 97mm between the gratings centres, figure (8.6a).



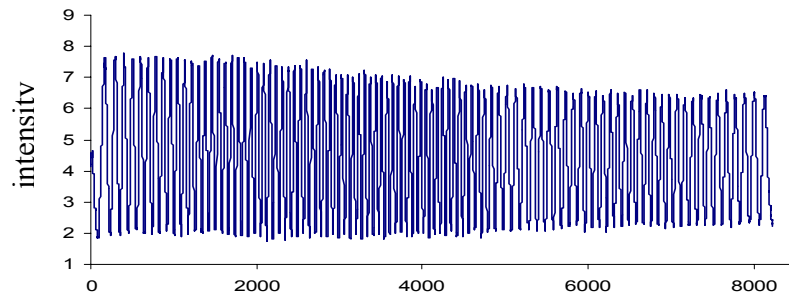
$\lambda = 1530\text{nm}$



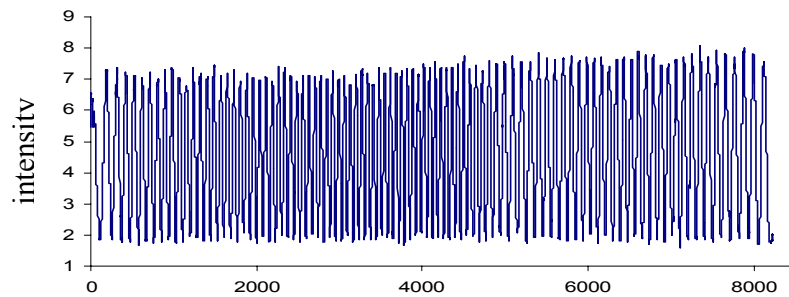
$\lambda = 1520\text{nm}$



$\lambda = 1540\text{nm}$

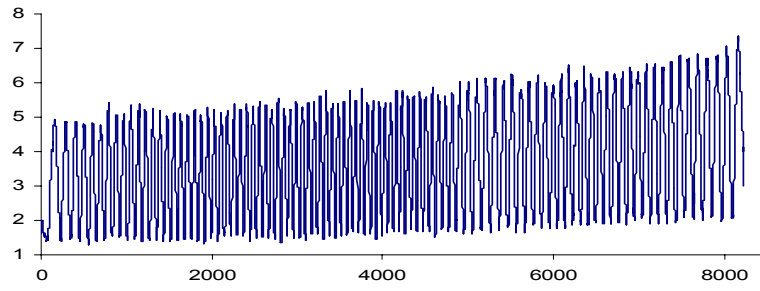


$\lambda = 1550\text{nm}$

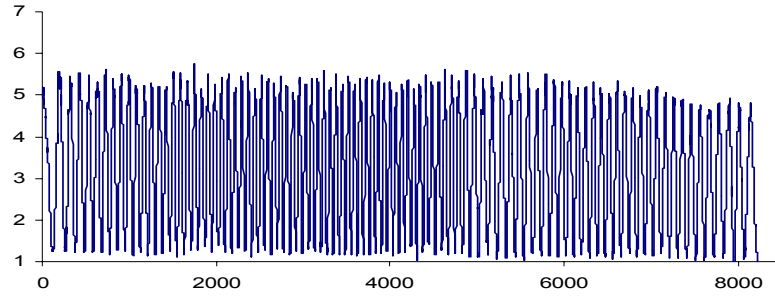


time

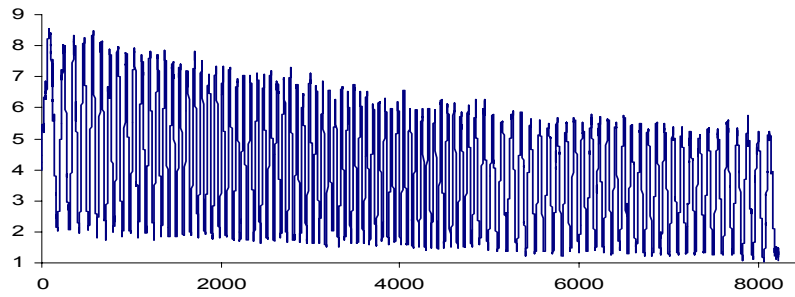
$\lambda = 1560\text{nm}$



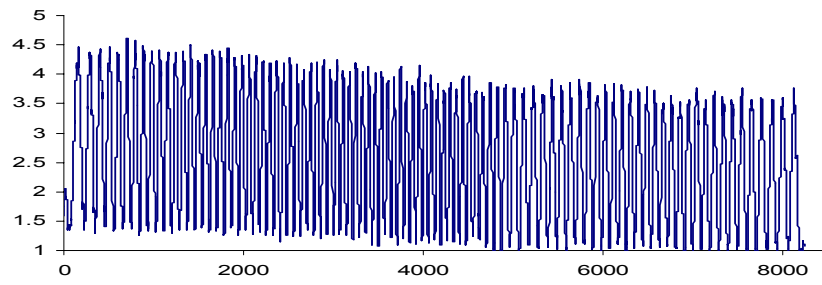
$\lambda = 1570\text{nm}$



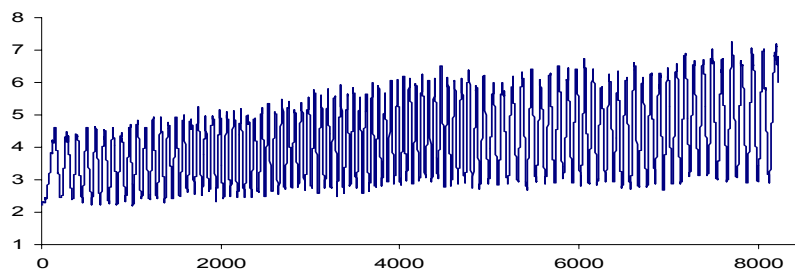
$\lambda = 1580\text{nm}$



$\lambda = 1590\text{nm}$

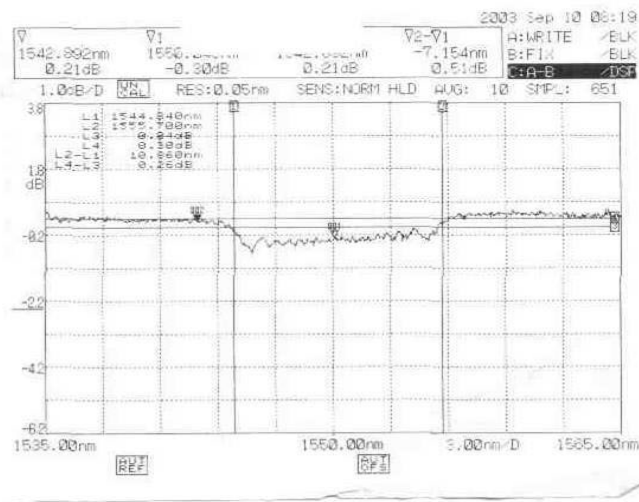
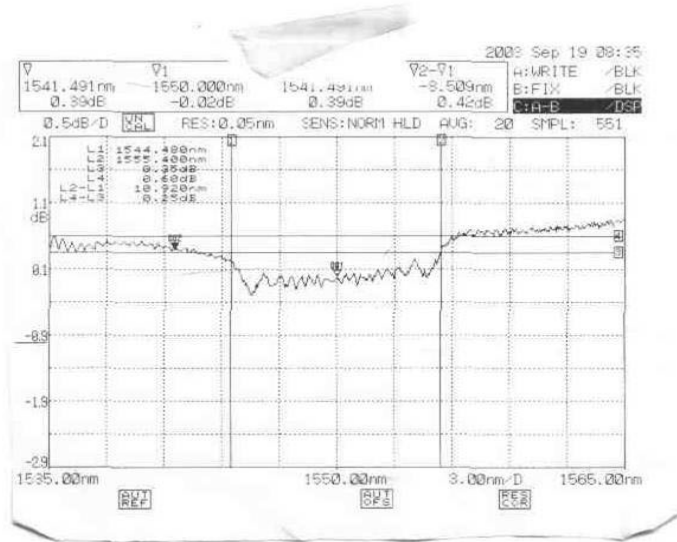


$\lambda = 1600\text{nm}$



Appendix F

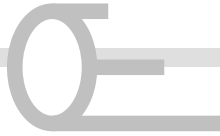
Details and profiles of the chirped FBGs written using continuous chirped phase mask bought commercially.



O/E LAND INC.

4321 Garand, St-Laurent, Quebec, H4R 2B4, CANADA

Tel: (514)334-4588, Fax: (514)334-0216, Email: sales@o-eland.com



Quotation

Attn: S Cheung

Quote No. 30622

To: Cranfield

E-mail: <S.Cheung.2000@Cranfield.ac.uk>

From: George

Date: 21/4/2004

Re: Stock chirped FBGs

Pages: 1

Item	specification	Qty	unit price	Total
1	Inventory chirped FBGs, wl : ~1550nm, grating length : 5mm, refl : 5-10%, bw : 11.01nm, fiber type : SM, fiber length : 1.5m, no connector, spectrum included	1	USD250.-	USD250.-
2	Inventory chirped FBGs, wl : ~1550nm, grating length : 5mm, refl : 5-10%, bw : 5.07nm, fiber type : SM, fiber length : 1.5m, no connector, spectrum included	1	USD250.-	USD250.-
3	Handling, one time fee	1	USD20.-	USD20.-

Total: USD520.-

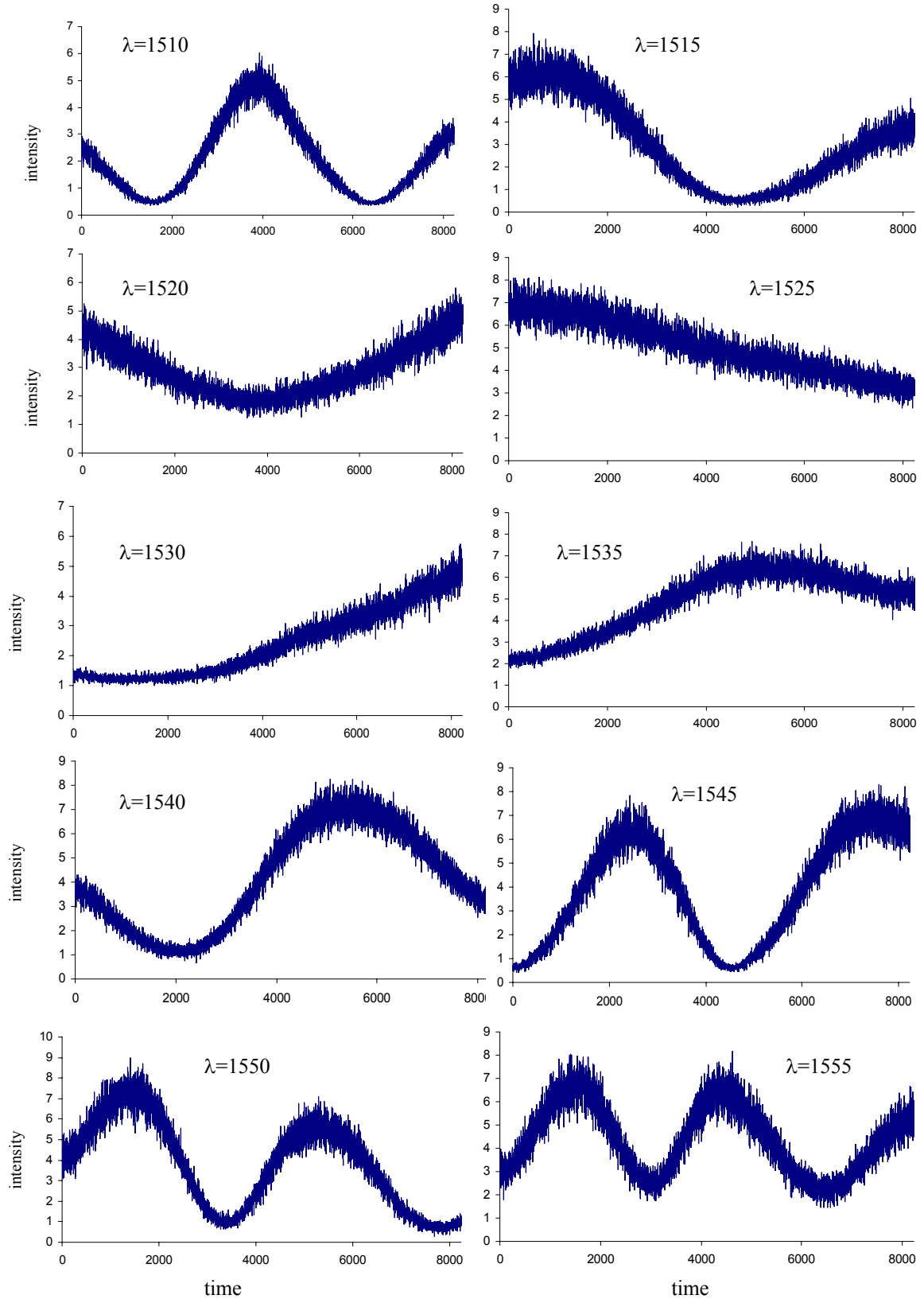
- Term: FOB Montreal, QC, Canada
- Delivery time: 2 to 5 days
- Freight: Paid by the customer
- Payment: **Net 30 days**
- This quotation is valid for 30 days

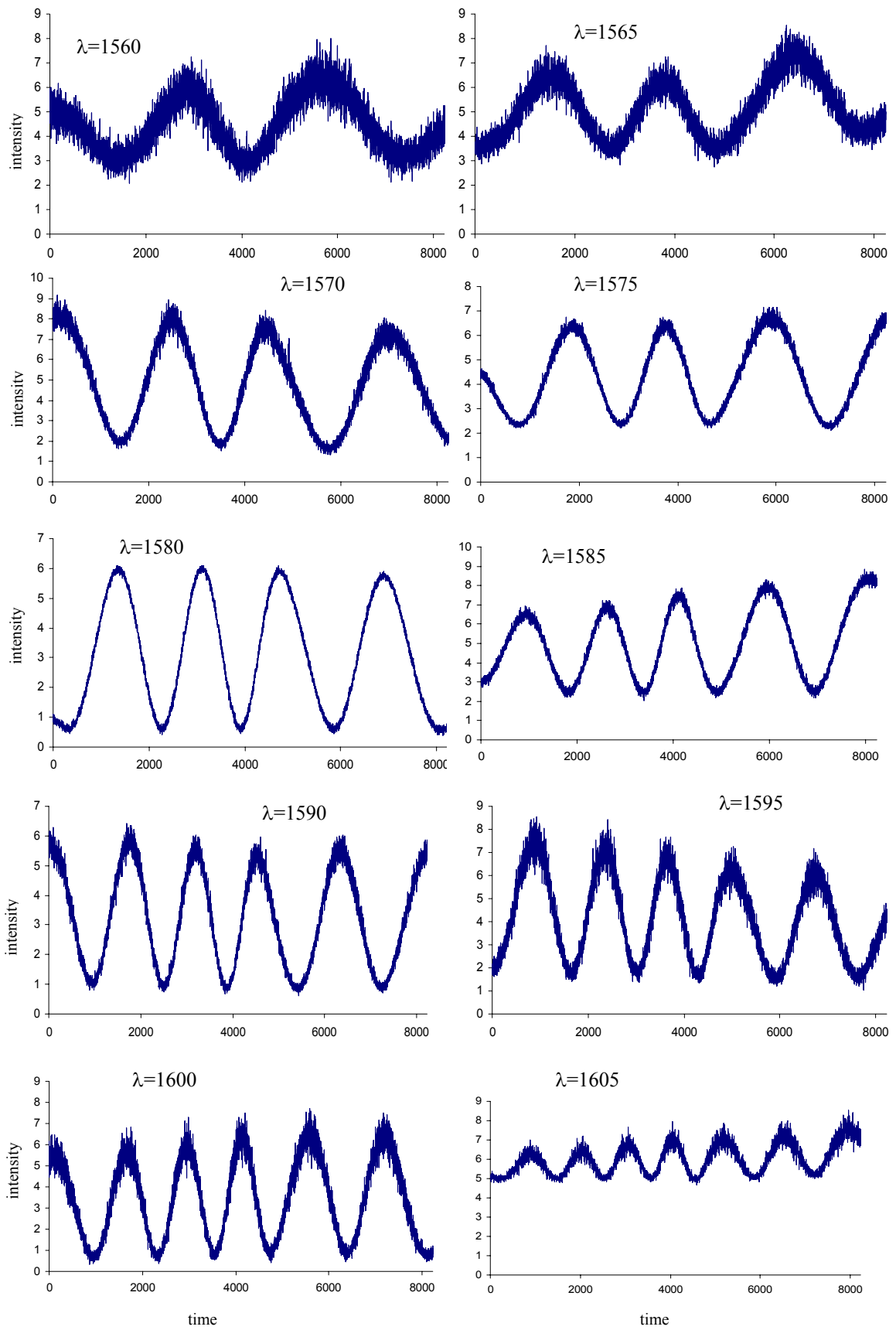
With Best Regards,

George
O/E Land Inc.

Appendix G

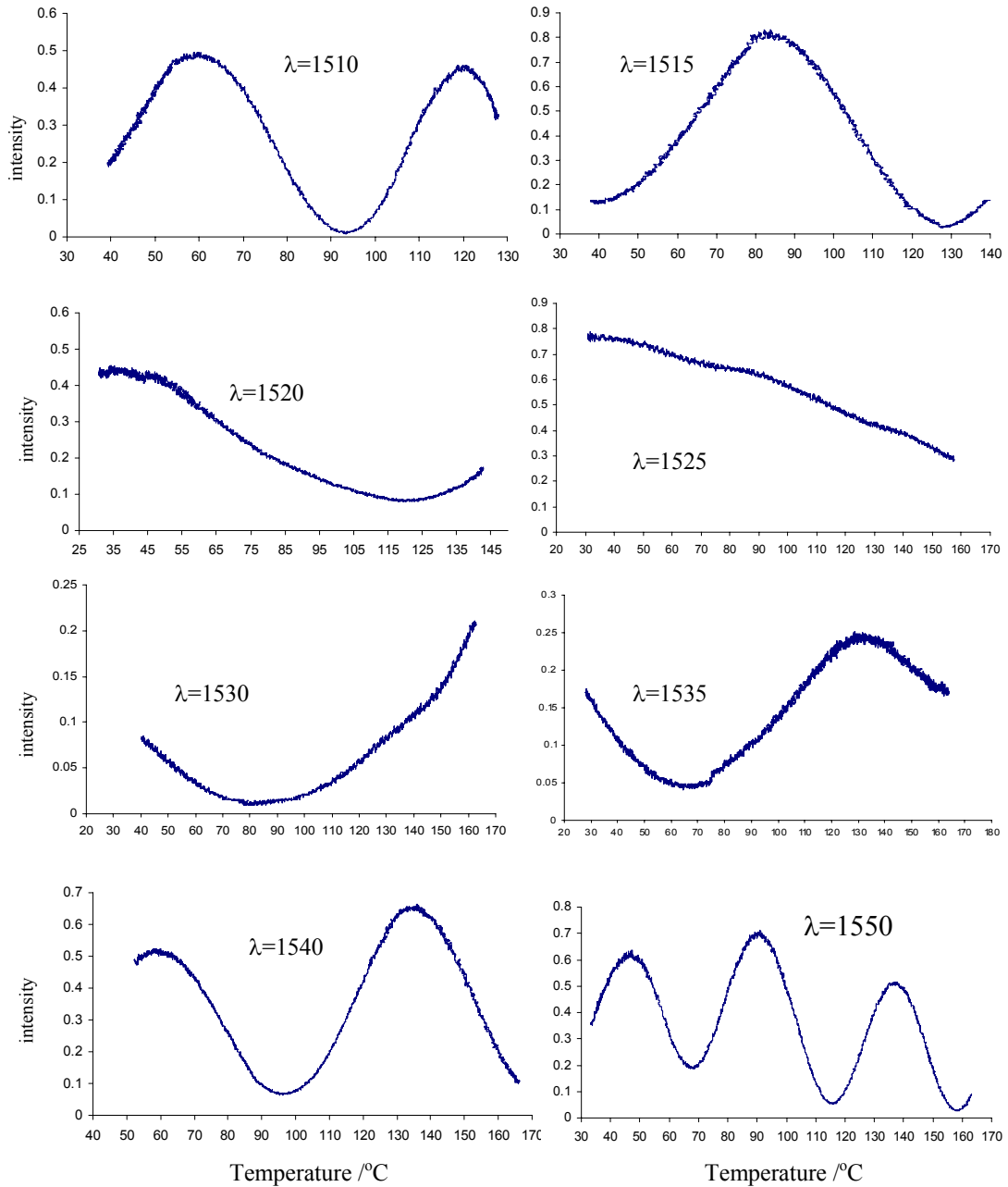
Strain response of the overlapping chirped FBG FP with grating length of 4mm and chirp rate of 25nm/mm with the orientation of the chirp opposite to each other.

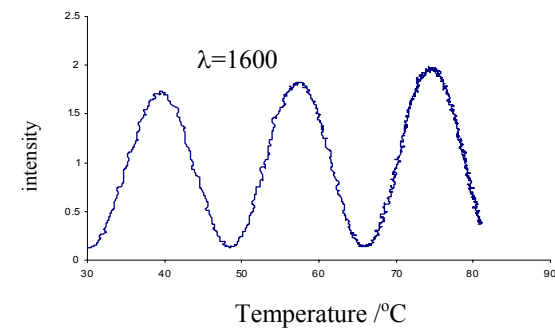
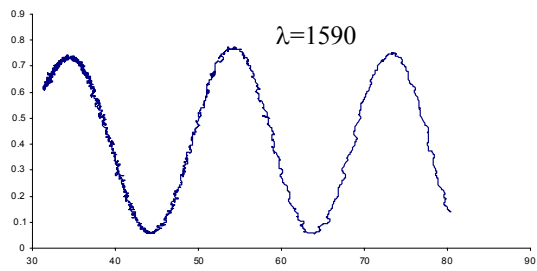
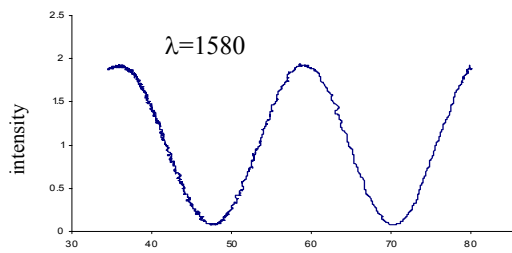
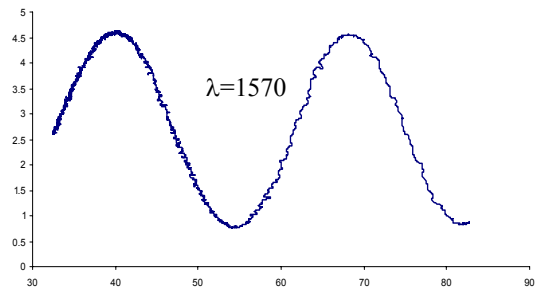
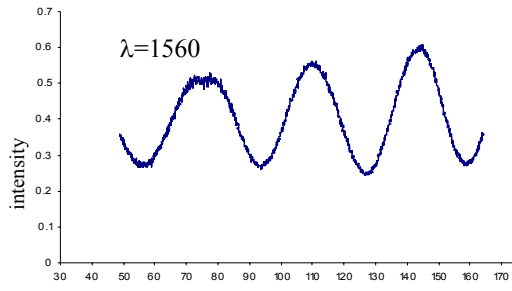




Appendix H

Temperature response of the overlapping chirped FBG FP with grating length of 4m and designed chirped rate of 25nm/mm with the chirp oriented opposite to each other.





Temperature /°C